Impact Behaviour of Model Prestressed Concrete Beams

Thesis submitted to
the University of Sheffield
for
the degree of Doctor of Philosophy
in
the Department of Civil and Structural Engineering
of
the Faculty of Engineering

by
Andrew Kay Ching Chan

April, 1986

To Lucy

Summary

This research work investigates the impact behaviour of prestressed concrete beams. A total number of forty 1000 mm long model beams with a rectangular section of 44 x 65 mm were cast. The beams were divided into four series with ten beams in each series. Each beam was prestressed by four 1.6 mm diameter piano wires and the shear reinforcement was varied from series to series.

The test rig available was modified so that the beam could have pin-end supports with a span of 600 mm and a static or impact load could be applied at the midspan. A total number of 40 static tests (8 static and 32 post-impact-static) and 32 impact tests were performed. The static load was applied by a screw jack via a one meter long steel pressure bar. The impact load was produced by the impact of a 350 mm steel cylinder projected at velocities of 4 to 17 m/s by compressed air onto the same pressure bar.

In each impact test, the impact force-time history was recorded by the electrical resistance foil strain gauges attached on the pressure bar. The transient deflections at various positions along the span were measured by linear variable differential transducers and the reaction was measured by aluminium load cells on which electrical resistance strain gauges were fixed.

A dynamic plastic model proposed by Ezra[90] was developed and applied in conjunction with the one-degree of freedom system to evaluate the maximum dynamic midspan deflection, reactions, energy absorption capacity and the initial impact beam velocity. A comparison was made between the predicted and the experimental results.

Acknowledgements

The author wishes to thank the Croucher Foundation, Hong Kong for the financial assistance.

The author would like to thank Dr A J Watson for his supervision, comment and encouragement in this research.

The author also acknowledges the co-operation of the staff of the Civil and Structural Engineering Department, the Mechanical Engineering Department and the Metallurgy Department, University of Sheffield.

Contents

Notations

A	area
C_L	longitudinal wave velocity
E	Young's modulus; output voltage
E_d	Young's modulus (dynamic)
E_s	Young's modulus (static)
F	force
F_{im}	impact load
G_k	dead load
I	moment of inertia of transformed elastic section; impulse
I_A	moment of inertia about A
K	deformation constant of impact zone; beam stiffness
L	half span
M	mass of strike; moment
M_e	equivalent mass including mass of pressure bar
M_p	ultimate moment of resistance (prestressed concrete beam)
M_p'	ultimate reverse moment of resistance (prestressed concrete beam)
M_u	ultimate moment of resistance (reinforced concrete beam)
P	dynamic load
P_e	effective prestressing force
P_u	ultimate design load
Q	physical quantity
Q_k	imposed load
R	reaction (normal); resistance (electrical)
R'	uplift reaction
R_e	resistance in one-degree of freedom system
S	scale factor
S_g	gauge factor of electrical resistance strain gauge
T	duration of a dynamic load
T_1	period of vibration of first mode
U	energy
V	excitation voltage

W weight of falling mass; load (static); work done

W_l weight of beam

X_i ith free vibration mode

Z midspan deflection; uncracked elastic section modulus

b width of beam

d depth of tendon

d' depth to centroid of all tension steel

e eccentricity of tendon group

f natural frequency; stress

f_c' cylinder crushing strength of concrete

f_c'' concrete compresssive strength in beam

f_{cu} concrete cube strength

f_p acceleration of point P

f_{py} yield stress of prestressing steel

f_y yield stress of normal reinforcement in tension

h height of fall

k deflection constant; number of fundamental dimensions

l span

l_e effective span

m mass per unit length of beam

m_b beam mass

m_e equivalent mass

m_s striker mass

r arm resistance ratio

$1/r$ curvature

t time

t_r rise time of a dynamic load

v impact velocity

v_0 impact velocity of striker

v_p velocity of point P

x distance of moving plastic hinge from midspan; beam co-ordinate at point of impact

x_d depth to neutral axis

Δ deflection as if the falling mass is applied statically: change

Π pi-term

α energy reduction factor; moment of resistance ratio

β mass ratio

ϵ strain

ϵ_0 concrete strain at maximum stress

ϵ_u ultimate concrete strain

η ratio of bullet energy absorbed by hinges

θ angle of rotation at support

λ arbitrary length from midspan

ρ density

σ stress

τ pulse duration

τ_- pulse duration when beam is massive compare to striker mass

ϕ' angle of rotation at moving plastic hinges

ω_i angular frequency of ith free vibration mode

Subscripts

B at point B

I incident

L geometric; length

O at point O

R reflected

T transmitted

b bottom

c concrete

e of equivalent system

f stress

m model; measured

max peak; maximum

p prototype; of prestressing steel

s of normal reinforcing steel

t top; in tension

0 initial

0,1,2... material; order; stage

γ acceleration

Superscript

' in compression

Mathematical symbols

f(x) function of x

F, Φ function

· derivative with respect to time

·· double derivatives with respect to time

List of Figures

List of Tables

List of Plates

CHAPTER ONE

INTRODUCTION

1.1 Development of Prestressed Concrete[1,2]

The basic principle of prestressing was applied to construction centuries ago, when ropes or metal bands were wound around wooden staves to form barrels. When the bands were tightened, they were under tensile prestress which in turn created compressive prestress between the staves and thus enabled them to resist hoop tension produced by internal liquid pressure.

This idea was applied to concrete and was first patented by P H Jackson in California in 1886, and later by C E W Doehring of Germany. The concrete was put into compression by tensioning the steel and holding it against the concrete. Yet these patented methods were not successful because of of the low tensile strength of steel. E Freyssinet of France in the early twentith century used high strength concrete and high strength steel and this resulted in a much better utilization of the two materials (steel and concrete). However, it was not until the late 1940s that prestressed concrete really began to develop.

Prestressed concrete is widely used nowadays in buildings, bridges, sea structures (e.g. harbours, offshore terminals and oil platforms) and in nuclear containment structures.

1.2 Dynamic Loads

1.2.1 Characteristics of a Dynamic Load

A dynamic load, unlike a static load, is time dependent and cannot be described by a single load parameter. A force (or pressure) and time relationship is shown in fig. 1.1. The significant features are the ratio of rise time t_r, duration T and peak load P_{max}. Even if the impulse $\int P.dt$ or energy sent into a structure is known, the dynamic response of the structure cannot be derived from its response under a low speed (static) loading because

(a) many common materials behave differently at high strain rates,

(b) local plastic region near the contact zone can be formed while other parts

of the member remain elastic or even undeformed, and

(c) inertia forces are generated at high rates of loading and these are sufficent to alter the mode of deformation.

1.2.2 Classification of Dynamic Loads

From the external viewpoint, dynamic loads can be divided into three types.

(a) Impact - The peak load and the variation of force with time are dependent on the masses of colliding objects. e.g. vehicle collision.

(b) Impulse - The pressure-time history is produced by an explosion or deflagration which depends upon the source and the type of explosion or the striking object is considered to have no mass. i.e. mass is not involved in an impulse. e.g. gaseous explosion.

(c) Cyclic loading - A part of a structure undergoes a rapidly changing displacement. e.g. earthquake.

Figure 1.2 gives the typical load-time curves of impact and impulsive loads. The rise time of an impact load is generally longer than that for an impulsive load.

1.3 Dynamic Loads Applying to Structures

In addition to static loads, structures are often subjected to dynamic loads accidentally or deliberately. Industrial or transportation accidents, demolition contracts, terrorist activities are just a few examples. The consequencies could be devastating.

1.4 Design for Impact Resistance

The major considerations in design for impact are as followed.[3]

(a) The characteristics of the impact. Typical load-time histories of different types of impact were given by Struck and Voggenretier.[4]

(b) The probability of occurrence. At present, there are little reliable data.[5]

(c) The behaviour of structures under high rate loading. The inherent impact resistance of structures designed for static loads has been investigated for years (see chapter 2). Yet there is limited information on prestressed concrete beams.[6]

Design recommendations are not usually found in civilian codes of practice for structural design but do exist in a few text books and military manuals.[7]

1.5 Scope of Present Investigation

The objective of this investigation is to carry out a theoretical and experimental study of the behaviour of pin-ended pre-tensioned prestressed concrete beam during and after being impacted at midspan. From the results of the investigation, it is expected that design recommendations could be formulated.

In the experiment programme, the model beams were 44 mm wide x 65 mm deep x 600 mm span and were impacted at midspan by a steel rod (bullet) 28 mm diameter x 350 mm long driven by compressed air. In total, 32 beams were impacted by a single blow and 8 beams were tested under static rate of loading for comparison. Each impacted beam was also tested statically in order to study post-impact behaviour. The independent variables were the amount of shear reinforcement and the impact velocity.

A literature review on the relevant subjects is presented in chapter 2.

Chapter 3 describes the fabrication of the model beams and the test procedure. The layout of the experimental programme is also included.

The test results are given in chapter 4.

A theoretical analysis is made in chapter 5 and includes :
(a) beam behaviour under static load,
(b) one dimensional stress wave theory,
(c) beam behaviour under impact load.

The theoretical predictions are compared against the experimental results and discussed in chapter 6.

Chapter 7 gives the conclusions drawn and suggestions for future work.

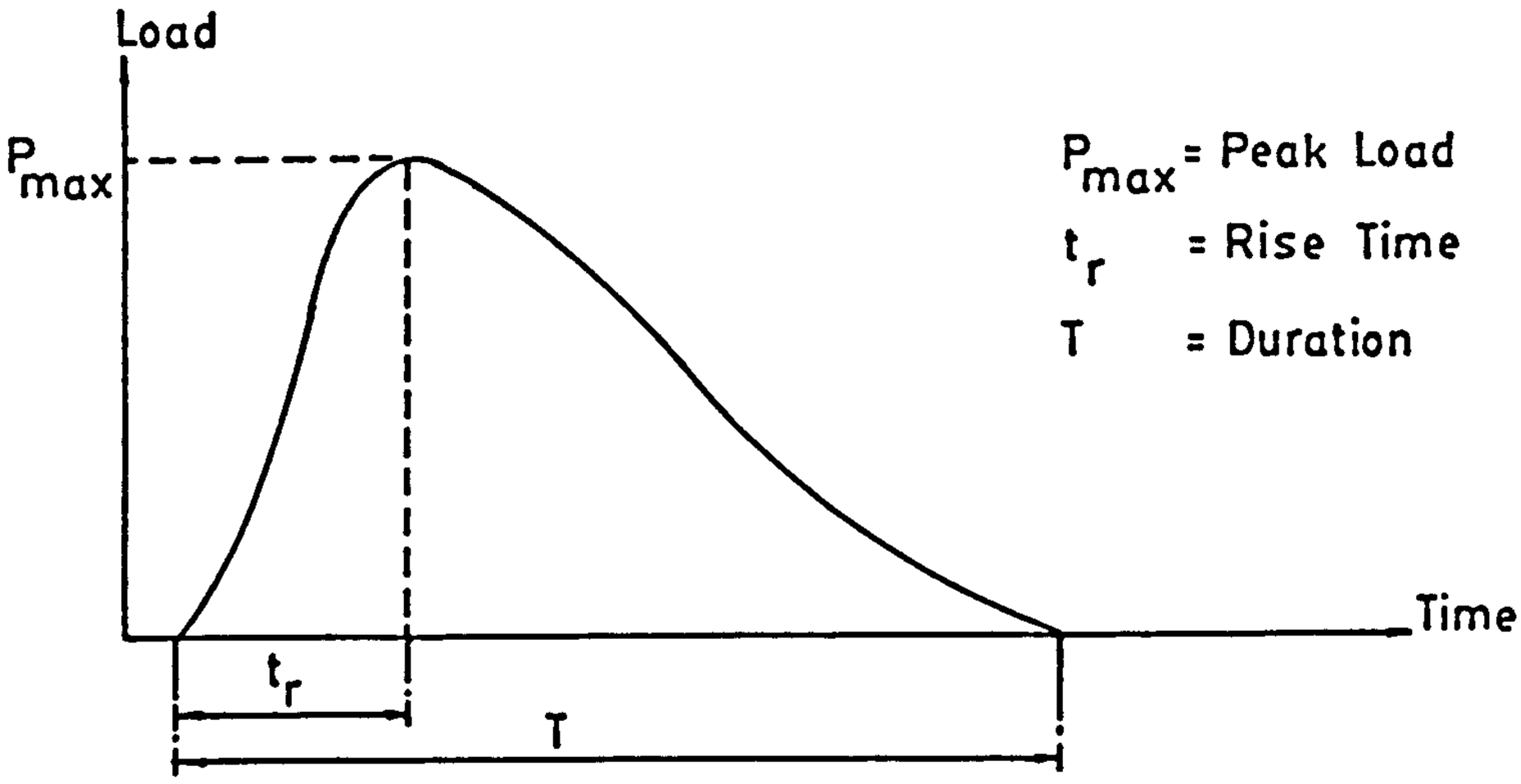

FIG. 1.1 CHARACTERISTICS OF DYNAMIC LOADS

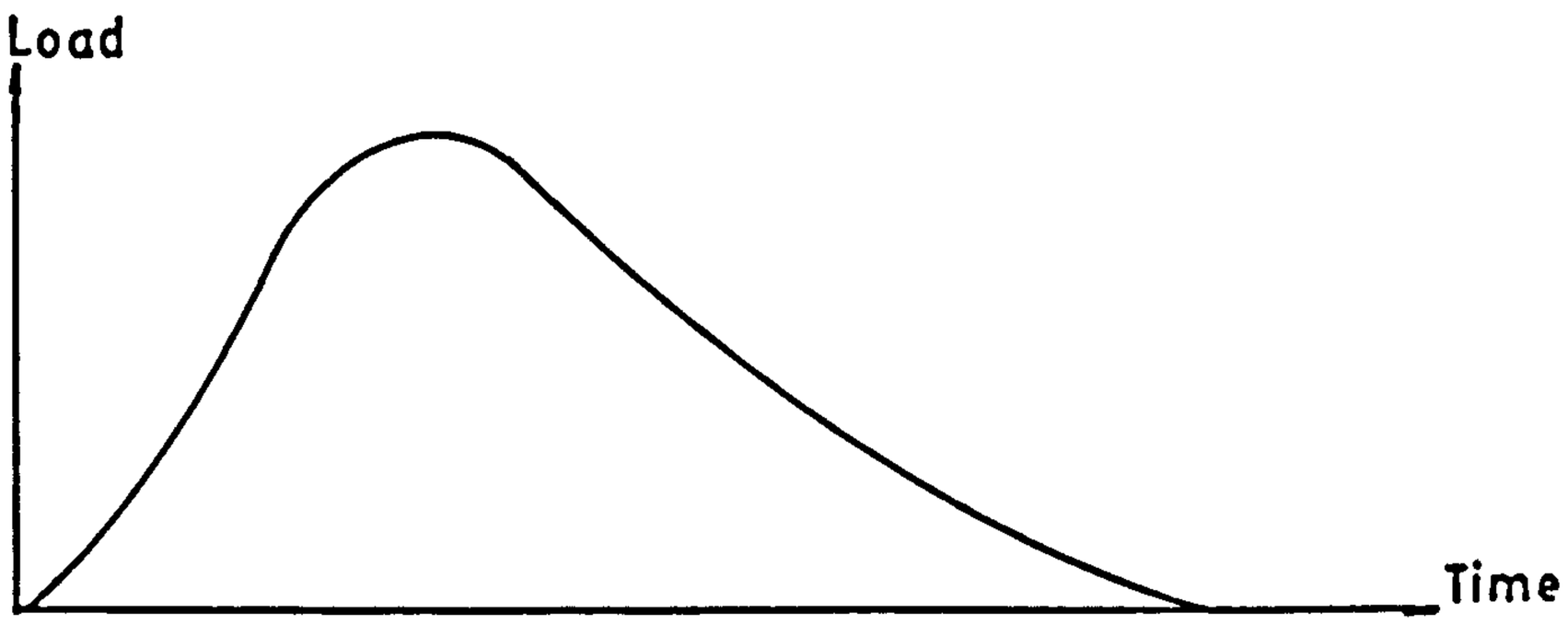

(a) Impact

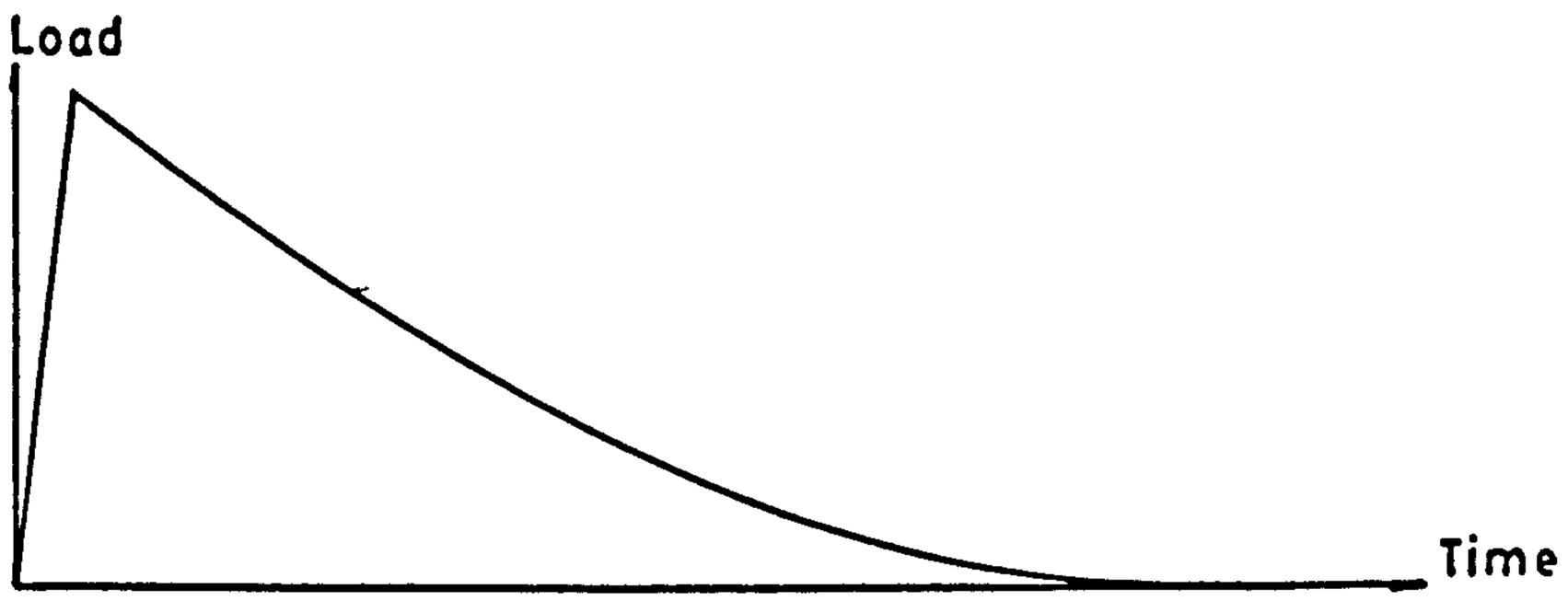

(b) Impulse

FIG. 1.2 TYPICAL DYNAMIC LOADINGS

CHAPTER TWO

LITERATURE REVIEW

2.1 Introduction

The literature survey in this chapter covers briefly the following aspects.

(a) Behaviour of prestressed concrete beams failing in flexure under static condition.
(b) Strain rate sensitivities of steel and concrete.
(c) Some theoretical approaches to structural dynamics problems.
(d) Previous experiments on the beam-impact problem.
(e) Problems encountered in modelling.

2.2 Response of Prestressed Concrete Beams under Static Loads

The behaviour of prestressed concrete beams under static loadings presented in this section provides a platform to compare with beam under impact loadings. The performance of simply supported prestressed concrete beams subjected to a point-load at midspan was studied by many investigators.[8,9,10] A typical load-deflection curve of such a beam failed in flexure is shown in fig. 2.1. There are three distinct stages of deformation.

In the first stage (stage I), the relationship between load and deflection is linear and the deformation is very largely elastic. This stage is terminated by the commencement of cracking. The energy of deformation (area under the curve) associated with this stage is small by comparison with the total.

During the second stage (stage II), the deflection increases rapidly and disproportionately with increasing load. Apart from cracking of the concrete, the deformation is still largely elastic and recoverable on unloading. This stage commences with the start of cracking and ends when the maximum load is reached and the deformation becomes localised. i.e. a hinge forms under the loading point. The energy of deformation in this stage is substantial and largely recoverable.

In the final stage (stage III), the local damage at the hinge becomes

progressively more severe as the capacity of the member to support load decreases with increasing deformation until finally complete collapse ensues. In the absence of secondary effects, failure occurs as a result of progressive fracture of the prestressing tendons with little damage to the concrete if the amount of steel in the section is small; if the amount of steel is greater, more severe damage to the concrete precedes the fracture of the tendons; and if the amount of steel is still greater, crushing of the concrete without fracture of the tendons may occur. The energy in this stage is absorbed by the permanent deformation and the damage of the materials.

Throughout the application of the loading up to failure, there is only one hinge formed within the span and is at the midspan.

2.3 Strain Rate Sensitivities of Steel and Concrete

Many materials possess properties which are dependent on the rate of straining. The strain rate sensitivities of the two materials associated with prestressed concrete structures, i.e. reinforcing steel and concrete, under different orders of strain rate were studied by numerous researchers and are summarised in this section and in table 2.1 (after Al-Azawi[5]). The dynamic increase factors (DIF's) in the strengths of these materials presented in table 2.2 are given by the American Concrete Institute[11] as a rough guide line. These figures are not related to strain rate and hence they may not be safe to be used without checking the strain rate involved in the view of the earlier investigations. The actual DIF for concrete depends on the mix proportions, materials, method of casting, curing and testing while the DIF for steel depends on the static strength and method of testing.

2.3.1 Sensitivity of Reinforcing Steel to High Rates of Straining

The results of some twenty independent experiments carried out in the period from 1941 to 1972 on testing the uniaxial tensile strength of steel under different strain rates were summarised by Mainstone[12] and eight sets of experimental data obtained from 1942 to 1982 were studied by Al-Azawi.[5] The general conclusions are

(a) the Young's modulus is insensitive to strain rate,

(b) the yield and ultimate strengths are increased at high strain rates,

(c) low strength steel shows more enhancement in strength than high

strength steel at the same strain rate.

(d) the ultimate strain and ductility are slightly increased at high strain rate in some tests while some other shows no change at all. i.e. the extra allowance in this aspect should be treated with extreme care.

2.3.2 Sensitivity of Concrete to High Rates of Straining

Mainstone[12] and Al-Azawi[5] again studied a total of twenty three research works in the period from 1936 to 1982 on the strain rate effect on concrete. The conclusions deduced are

(a) the Young's modulus increases with strain rate. Mainstone[12] proposed that this was probably due to viscosity of the liquid phase of cement gel and inertial resistances to the deformation associated with internal cracking.

(b) the strain rate sensitivity is possibly affected by the type of aggregate in the concrete.

(c) McHenry and Shideler[13] found that the modulus of rupture increased by about 20 % for an increase in rate of stressing by two orders of magnitude. Their data were related to rates of stressing below 10^{-1} N/mm^2s.

(d) shear strength increases under rapid loading.

(e) moisture content and temperature may be expected to affect the sensitivity to strain rate.

(f) strain at maximum stress is greater at higher strain rate.

(g) the stronger the concrete, the less sensitive it is to the rate of straining.

(h) the bond resistance of deformed bars increases at high strain rate.

Hughes and Watson[14] measured the transient applied load away from the specimen and calculated the actual transient load by using the one-dimensional stress wave analysis (section 5.3). Their results indicated that the average ratio of the impact strength to the static strength were lower than that found in the earlier investigations. This discrepancy is due to the fact that the earlier researchers took the load registered on the load cell as the actual transient load which is the integration of all the reflected and transmitted load pulses which is not the actual load resisted by the specimen.

2.4 Previous Theoretical Approaches as a Design Aid for Dynamic Loading

In principle, the behaviour of prestressed or reinforced concrete structures under high rate loading can be deduced from the individual properties of concrete and steel. However, the dynamic response (e.g. higher modes of vibration, etc.) and the other failure modes may be overlooked (e.g. unless higher bond strength can be developed, the increased strengths of steel and concrete are likely to lead to bond failure). There are various approaches to help in the design of structural members to resist dynamic loadings. In this section, some classical methods are presented and discussed followed by a general summary.

2.4.1 Dynamic Load Factor (DLF) Method

This method considers a falling mass as the dynamic load. The structure, e.g. beam, is designed to resist a static force equal to the weight of the falling mass multiplied by a dynamic load factor, DLF.

The method employed by Mylrea[15] is to idealise the beam to an elastic model with the following assumptions.

(a) No inelastic deformation. i.e. no energy dissipation from local plastic strain or fracture.

(b) No inertia forces resisting movement or displacement.

(c) Linear and same force-deflection relationship for static and dynamic loading conditions.

(d) Energy conserved at the instant when the velocity of the impacting body is zero, then the internal strain energy (deflection) is maximum.

The DLF is given by

$$DLF = 1 + \sqrt{1 + \frac{2h}{\Delta} \cdot \frac{1}{1 + \frac{17\,W_1}{35\,W}}} \qquad \text{equ. 2.1}$$

where h - height of fall,
Δ - deflection as if the force (weight of the falling mass) is applied statically,
W_1 - weight of beam,
W - weight of the falling mass.

Knowing the DLF. the dynamic deflection can be easily calculated. However. being bounded by the assumptions, equation 2.1 is of limited use. In the case when it is applicable, the result will be conservative as the dynamic effects (e.g. vibrations, enhancement in material strengths, etc.) are ignored.

2.4.2 Energy Method

This method assumes that all or a portion of the energy carried by the impacting body is transferred to the structure. and by comparing it with the static load-deflection curve, the deflection will be obtained.

Simms[16] employed the method for a simply supported beam being impacted by a falling mass at midspan with the following assumptions.

(a) The load-deflection curve is identical for static and impact loads.
(b) The falling hammer (mass) remains in contact with the beam throughout the period of impact.
(c) There is no deformation at the point of contact. i.e. this point is infinitely rigid.

By considering the conservation of momentum and energy and assuming an elastic beam, the reduction factor α (= energy transferred to beam/ falling mass energy) is

$$\alpha = \frac{1 + \frac{17\ W_1}{35\ W}}{\left(1 + \frac{5\ W_1}{8\ W}\right)^2} \qquad \text{equ. 2.2a}$$

and Simms(16) justified that this equation could be simplified to

$$\alpha = \frac{1}{1 + \frac{4\ W_1}{5\ W}} \qquad \text{equ. 2.2b}$$

where W_1 and W are defined as in section 2.4.1.

Using this reduction factor, the amount of energy transferred to the beam and hence the deflection can be evaluated. Cracknell and Jarman[17] proposed this method to be used in design. However, all the assumptions are questionable or only valid in a very special case.

2.4.3 Equivalent Dynamic (Lump Mass) System

The structure which is under consideration is transformed into lump masses at the points of interest and connected by elastic springs. The dynamic load may need to be modified in this method to predict the response of these particular points. The equivalent mass factors and the dynamic load factors in different conditions (e.g. type of structure and shape of the dynamic pulse) which are obtained from rigorous solution[18,19,20] are in terms of the force-time function of the dynamic load, natural frequency and the ductility of the member. More than one degree of freedom (hence higher modes of vibration) can be considered in this method. However, if this is the case, this method will then become very tedious even with the design charts produced by Norris el at[18] or Biggs.[20] The other major set back is that the force-time function of the dynamic load is not often well defined though some typical examples are obtainable from Struck and Voggenretier.[4]

2.4.4 Finite Element Method (Mathematical Model)

The structure under investigation is divided into small rigid segments joined by springs in this method. At each time step, a set of simultaneous equations is generated by considering the equilibrium of each segment. The dynamic response of the structure can be obtained by solving these equations numerically in a computer. However, as in the model developed by Van der Veen and Blaauwendraad[21], this method requires some hypotheses on the failure mechanism (hence criteria), dynamic response of the material (e.g. steel and concrete), suitable nodal points positions (size and orientation of each segment). etc, which may lead to inaccuracy.

2.4.5 Approach of Hughes and Speirs[21] and Hughes and Beeby[7]

In this approach, the response of a beam impacted by a rigid striker is analysed by considering the local impact deformation and all the possible modes of vibration. If the beam remains elastic throughout, the beam impact

equation derived is

$$\left(\frac{F}{K}\right)^{\frac{2}{3}} = v_0 t - \frac{1}{m_s}\int_0^t d\bar{\tau}\int_0^{\bar{\tau}} F(\bar{t})\,d\bar{t}$$

$$- \left\{\frac{X_0^2(\bar{x})}{\rho A \int_0^L X_0^2\,dx}\int_0^t d\bar{\tau}\int_0^{\bar{\tau}} F(\bar{t})\,d\bar{t}\right\}$$

$$- \sum_{i=1,2}^{\infty} \frac{X_i^2(\bar{x})}{\rho A\,\omega_i \int_0^L X_i^2\,dx}\int_0^t F(\bar{t})\sin\{\omega_i(t-\bar{t})\}\,d\bar{t}$$

equ. 2.3

where F = impact force

K = deformation constant for impact zone

v_0 = impact velocity of striker

t = time

m_s = striker mass

X_i = ith free vibration mode

τ = pulse duration

ρ = beam density

A = area of beam cross section

$\bar{x}$ = beam co-ordinate at point of impact

ω_i = angular frequency of ith free vibration mode

L = span

It is obvious from equation 2.3 that the beam is considered as a continuous body. The response (displacement, moment, shear, etc.) of each beam section with respect to time can be calculated or deduced from this equation. Numerical techniques have to be used to solve this equation as it cannot be solved in closed form. After a dimensional analysis, equation 2.3 contains two important parameters. They are

(a) the mass ratio = m_b/m_s, and

(b) the pulse ratio = τ_{--}/T_1

where m_b - beam mass

τ_∞ - pulse duration when beam is massive compared to m_s

T_1 - period of vibration of first mode ($2\pi/\omega_1$)

The limitations to the applicability of this approach are

(a) if the pulse ratio is small, a wave-travel solution is necessary.

(b) if the pulse ratio is large, errors can occur since the vibration solution does not, as it should, approach static solution exactly.

The actual bounds of applicability can really only be found experimentally.

2.4.6 Design Guides (Load Factor and Dynamic Increase Factor)

According to CP 110 part 1[24], the ultimate design load P_u in the case of accidental impact load F_{im} is

$$P_u = 1.05 (G_k + Q_k + F_{im}) \qquad \text{equ. 2.4}$$

where G_k - dead load

Q_k - imposed load

The partial safety factors for concrete and steel are 1.3 and 1.0 respectively instead of the more commonly used values of 1.5 and 1.15. The kinetic energy of the striker is assumed to be completely transformed into strain energy in the impacted member.

The Home Office published a guide for nuclear shelters in 1982[23] to resist blast loading (nuclear explosion). The ultimate load capacity of a structural member subjected to blast loading is determined by considering its capacity for sustaining external load by relatively large plastic deformations. The design rules in this guide limit the magnitude of the plastic deformations and thus the level of damage to the structural elements to a condition of moderate damage, where there will be considerable yielding of steel and concrete, but no impairment of the resistance to further loading. Load factors for different types of elements in different degree of exposure (table 2.3) and dynamic increase factors for steel and concrete in different aspect (same as those values in table 2.2) can be found in this publication. Yet no explanation is given for the derivation of the values of the load factors.

2.4.7 Summary and Motive of a New Approach

Each of the approach mentioned so far (from section 2.4.1 to section 2.4.6) is restricted to certain particular cases in the view of design purpose. The cause of the limitation on the usefulness of the individual method is due to one or more of the following reasons.

(a) The assumption(s) is/are valid only in a special case.
(b) It is an elastic approach and invalid in plastic response.
(c) The vibration response of the structure and the dynamic increase factors of materials are ignored.
(d) Only certain points on the structure can be studied and there are transformation problems. e.g. equivalent dynamic system (section 2.4.3).
(e) The equation(s) derived is/are complicated and tedious.

A simple plastic model is therefore developed (section 5.4) in this research and hopefully will provide some useful information on beam impact problem to designers.

2.5 Previous Investigations on Beam Impact Problem

The experimental works carried out on reinforced or prestressed concrete beams under impact loading are listed briefly in this section. Some major findings of the individual study are summarised at the end of the subsection under the name(s) of the investigator(s).

2.5.1 Mylrea 1940[15]

In this study, simply supported reinforced concrete beams 250 mm wide x 400 mm deep x 2400 mm span with different grades and amount of steel and no shear reinforcement were loaded at the midspan by a 225 kg or 930 kg hammer falling from heights ranging from 0.23 m to 2.3 m.

Mylrea concluded that

(a) the analytical approach as described in section 2.4.1 was good.
(b) no noticeable difference in impact resistance was displayed by any of the grades of steel used.

2.5.2 Simms 1945[16]

In this test, two types of simply supported reinforced concrete structures (beams and slabs) were impacted at the midspan by a falling mass. The beam dimensions were 100 mm wide x 200 mm deep x 1830 mm span while the corresponding values for slab were 500 mm x 150 mm x 1524 mm. In general, the longitudinal reinforcement in the beams consisted of either mild steel bar or high strength steel while cold worked steel and ribbed mesh sheet steel were employed in the slabs. The test conditions were

(a) all specimens were designed to fail in bending. i.e. shear stirrups were provided.
(b) the impact was characterised by local deformation.
(c) the weight of the falling mass was equal to that of the specimen.
(d) the striking velocity ranged from 2.44 m/s to 8.53 m/s.

Simms concluded that

(a) in general, the form of damage of these units was roughly the same under static loading or impact, and in such cases, the damage to beams and slabs due to impact was reasonably predicted from considerations of the energy absorbed under static loading, used in conjunction with a simple energy equation (equation 2.2a or equation 2.2b, section 2.4.2).
(b) in contrast to Mylrea[15] (section 2.5.1), the performance of beams with high strength steel was not as good as those beams reinforced with mild steel bars.

2.5.3 Mavis and Greaves 1957[25]

In this study, simply supported beams 100 mm wide x 150 mm deep x 1980 mm span were loaded at the midspan by a dynamic spring load. The beams were reinforced with different types of steel (hard grade or intermediate-grade). Mavis and Greaves reported that

(a) the performance of a beam under dynamic loading were different from the corresponding static performance of a similar beam by
    (i) the dynamic load capacity was higher,
    (ii) the limiting dynamic strain was greater,
    (iii) the dynamic reactions varied differently from the load,
    (iv) the dynamic stress distributions was different.
(b) beams with hard-grade steel outperformed beams with intermediate-grade

steel.

However, in the discussion paper by Fey, Hansen, Johnstone, Newmark and White[26], it was pointed out that the pulse generated by the spring in this study had a duration always higher than the natural period of the beam and consequently, tests with pulses of short durations would also be required to validate the conclusions.

2.5.4 Bate 1961[10]

The experiments carried out by Bate were an extension of the investigation by Simms (section 2.5.2). A total number of 54 reinforced concrete beams and 306 prestressed concrete beams, all simply supported, were loaded at the midspan by either a static load or a falling mass. Only the details for prestressed concrete beam tests are reviewed here.

The independent variables were

(a) dimensions of specimens (width, depth and span),
(b) type, amount and position of prestressing steel,
(c) effective prestressing force,
(d) weight of the falling mass,
(e) height of fall,
(f) concrete strength.

Bate concluded that

(a) the energy of deformation (area under the load-deflection curve) determined in static loading gave an approximate indication of resistance to the impact of a single blow, provided that the failure modes under both cases were similar.
(b) when failure occurred in bending, there was a particular proportion of steel which gave greatest resistance to impact,
(c) the effects of slip of pre-tensioned wires and of shear failures had an important influence on performance. e.g. it might lead to different modes of failure under static and impact test.
(d) the shear effect was enhanced and stirrup reinforcement became much more important in impact tests. This was also reported later by Seabold[27] for reinforced concrete beams under impulsive loads.
(e) the impact resistance could be estimated by comparing the energy of

deformation with the energy transferred from the striker to the beam using a simple energy equation (equation 2.2a or equation 2.2b,section 2.4.2).

2.5.5 Karim 1977[28]

A total number of 48 simply supported post-tensioned prestressed concrete beams were tested either statically or dynamically by a drop hammer. The variables were

(a) size of beam,

(b) area of prestressing steel,

(c) initial prestressing force,

(d) amount of web reinforcement.

Karim's conclusions are similar to those of Simms (section 2.5.2). In addition, Karim also reported that

(a) the energy reduction factor calculated using equation 2.2a was always higher than the one deduced by measuring the midspan deflection and comparing with the static load-deflection graph. i.e. this calculation method is conservative.

(b) in the case of bond slip, the extra amount of energy absorption capacity which occurred in static test did not reproduce under impact, hence there was a danger of over-estimating the impact resistance from the knowledge of static test results.

2.5.6 Lai 1980[6] and Hughes 1981[29]

A total of 57 beam specimens were tested by Lai under the similar condition as in Karim's study (section 2.5.5). In addition to Karim's variables, polypropylene or steel fibre was introduced to some beams. Eight special terms were proposed and defined as following.

(a) Energy unit (EU) - area under the calculated 'dynamic' load-deflection curve upto the point corresponding to a compressive strain of 0.0055 in concrete.

(b) Deflection unit (DU) - initial camber plus the deflection corresponding to 0.0055 concrete strain.

(c) Prestressing index (PI) - $PI = P_e/(f_{cu}bd)$

where P_e = effective prestressing force,

f_{cu} = static concrete cube strength,

b = width of beam,

d = depth to tendon.

(d) Apparent impact energy (AIE) - product of the efficiency of the hammer, the weight of hammer and the height of fall.

(e) Energy ratio (ER) = AIE/ EU

(f) Deflection ratio (DR) = measured dynamic deflection/ DU

(g) Maximum impact capacity (MIC) - impact resistance without 'collapse'.

From the experiment data and the calculated values of EU and DU, a unique ER vs DR curve was produced for same type of beams and of identical PI. A family of such curves (different types of beams and PI's) was therefore generated and was readily applied to the evaluation and design of impact-susceptible beams. In contrast to the previous studies, it can be seen that the weight of the hammer (in relation to the weight of beam) on its own has no noticeable effect on the dynamic response. In this investigation, it was also found that for identical PI, the performance of steel-fibre beams was better than that of the polypropylene-fibre beams which were better than that of plain beams on the basis of impact capacity.

2.5.7 Watson and Ang 1981[30], 1982[31]

One eighth model microconcrete structures were impacted by a steel cylinder of 1.78 kg at a velocity of 16 m/s. Longitudinal and transverse reinforcement and span-depth ratios were varied for beams simply supported and with column continuity. Watson and Ang concluded that

(a) impact loads up to 40 times larger than the static strength of beams, produced punching shear fractures and higher mode flexural cracks which were quite distinct from the lower mode flexural cracks under static load.

(b) the impact fractures from a load up to 40 times greater than the static strength of beams designed for ultimate loads, did not reduce the residual static strength below that required for static service loads.

(c) the peak and residual deflections under impact load were reduced as the

volume of shear reinforcement increased. Spiral stirrups produced a stiffer beam than conventional tied reinforcement, comparing with the conclusion of Seabold[27] that inclined (spiral) stirrups were not recommended to resist impulsive loading.

2.5.8 Hughes and Speirs 1982[22] and Hughes and Beeby 1982[7]

Some 92 pin-ended reinforced concrete beams of different span and reinforcing details were impacted by a falling mass at midspan. Different types of padding were used. The results were compared to the theoretical approach as described in section 2.4.5. They concluded that

(a) the theory showed good agreement with the experiment in the early stage (i.e. beam remained elastic). However, the solution involved some computational difficulties.

(b) the solution could be described in terms of dimensionless parameters which were depended on the mass ratio and the pulse ratio as defined in section 2.4.5.

(c) the limitations of the applicability were already described in section 2.4.5.

2.5.9 Mahmood 1983[32] and Hughes and Mahmood 1984[33]

Post- tensioned prestressed concrete beams of 1/4 and 1/2-scale were tested in a manner similar to Lai (section 2.5.6). In addition to Lai's terminologies, the following terms are added or modified.

(a) Reinforcement index (RI) - $RI = (A_p f_{py} + A_{st} f_y)/(f_c' bd)$

where A_p = area of prestressing steel,
f_{py} = yield stress of prestressing steel,
A_{st} = area of normal reinforcement in tension,
f_y = yield stress of normal reinforcement in tension,
f_c' = cylinder crushing strength of concrete,
b = width of beam,
d' = depth to centroid of all tension steel.

(b) Prestressing index (PI) - PI = $P_e/(f_c'bd)$

where P_e = effective prestressing force.

(c) Reference toughness (RT) = EU as in Lai's terms.

(d) Reference deflection (RD) = DU as in Lai's terms.

(e) Nominal impact capacity (NIC) - the impact energy of the impact which just produdes an excessive residual central deflection which lies within a range 1/300 to 1/250 of the span.

The impact data were generalised through these terms. Data of beams of similar PI and RI at different impact intensities were plotted (i.e. ER vs DR) and provided a comprehensive indication of the behaviour of beams under the effect of impact loading (e.g. NIC). Beams impacted with an intensity equal to or below their NIC retained more than 85 % of their static ultimate strength and beams impacted by a single blow having an intensity equal to the NIC could generally resist a greater total energy if it was delivered as the sum of energies of two or more impacts.

2.5.10 Ang 1984[34]

This work on model structures was the base of the work of Watson and Ang[30,31] (section 2.5.7). From the high speed films, Ang observed that only part of the structure (reduced effective span) might respond to an impact before the response of the whole structure, depending on the material properties (e.g. dimensions,etc.) and the pulse characteristics (e.g. duration, etc.). Using this reduced effective span concept and the experimental data, a set of design curves involving parameters of beam properties and materials properties were produced and successfully predicted the energy absorption capacities of some test specimens.

2.6 Modelling

Physical models are very often used for developing new methods of design and in checking the performance of corresponding prototypes because they are less expensive and less time-consuming than testing the prototypes. However, as it is pointed out by Mirza[35], care must be exercised throughout all stages of the modelling process and testing of the models. i.e. modelling

laws must be observed.

2.6.1 Laws of Similitude[36,37]

The structural response of a full scale structure can be predicted from the response of a model by using as appropriate scale factor. i.e.

$$Q_p = S \times Q_m$$

where Q = physical quantity; S = scale factor;
and subscripts p = prototype; m = model.
The scale factors can be obtained from the laws of similitude which can be determined by using the method of dimensional analysis. The fundamental dimensions of this research involved in the famous Buckingham Π theory[36] are mass (M), length (L) and time (T). The Buckingham Π theory states that the expression

$$F(Q_1, Q_2, Q_3, \ldots\ldots\ldots\ldots, Q_n) = 0$$

can be reduced to the form

$$\Phi(\Pi_1, \Pi_2, \Pi_3, \ldots\ldots\ldots\ldots, \Pi_{n-k}) = 0$$

where Q = physical quantity,
Π = dimensionless quantity which is a product of Q's,
k = number of fundamental dimensions.
A list of the relationships between the prototype Q terms and model Q terms is presented in table 2.4. The full derivation of these relationships by using the Buckingham Π theory can be found in Brideman[38], Inkester[39] and Al-Azawi[5]. It can be seen that only two scale factors are needed to determine all the relations. They are the stress factor S_f and the geometric (length) factor S_L.

2.6.2 Materials for model and Associated Problems

A direct model which is used to predict the behaviour of the prototype up to failure must be of a material whose entire stress-strain curve is homologous to that of the prototype material. Since prestressed concrete beam consists of concrete and steel, it is necessary to have the same stress factor for both the substitudes for concrete and steel. To satisfy this condition, cement mortar (microconcrete) and steel wires are often used. Accordingly, the stress factor for the two material will be near to unity. i.e. $S_f \simeq 1$.

In some aspects of the model or material, the geometric factor S_L cannot be truly satisfied. They are

(a) in table 2.4, it requires the model to have a density equal to S_L times that of the prototype (S_f -1) which is difficult to achieve and is ignored in this research.

(b) the constituents of the microconcrete should be scaled down. Finely ground cement is rare and expensive. Accordingly, ordinary rapid hardening Portland cement was used in this research. The requirements for the aggregate and mix design will be discussed in section 3.2.2.2.

(c) small size of high yield steel wire is difficult to manufacture. Mild steel wires are often further treated by cold working, knurling (indentating), etc. before they are used as a substitute. The details and effects of these treatments can be found in Brock[40], Harris et al[41,42], Clark[43], Sabedi and Garas[44] and Evans and Clarke[45].

Modelling of bond is seriously hindered because of the limited knowledge of the bond mechanism in prototype prestressed or reinforcement concrete. Intensive study on the bond behaviour in prototypes and models was carried out by Harris et al[41], Vos[46], Sabedi and Garas[44], White and Clark[49], Clark[48], Mirza[49] and Noor and Khalid[50]. Their conclusions are summarised below.

(a) The ultimate bond strength decreases as embedment length increases.

(b) Deformed wire is better than plain wire in crack simulation.

(c) Deformed wire has a higher peak value for ultimate bond stress than plain or plain corroded wire.

(d) Wire of smaller diameter and rougher surface requires smaller anchorage length.

(e) Plain wire and prestressing strand are not affected by high rate of loading.

The phenomenon known as size effect was investigated by Johnson[51], Litle and Paparoni[52], Syamal[53], Evans, Clark and Beeby[54] and Sabnis and Mirza[55]. It is concluded that the strengths (compressive, tensile, etc.) of concrete are increased and is more variable as the size of the specimen decreases. This effect becomes apparent when the size is smaller than a certain critical size depending on the type of behaviour being studied.

e.g.Chowdhury and White[56] successfully predicted the moment rotation relationship of a prototype beam-column joint by 1/10-scale models, and McCutcheon[57] produced satisfactory results on prestressed concrete beams by 1/4 and 1/8 models while Alexander[58] reported that the ultimate bending moment obtained from a 1/22-scale microconcrete beam was 40 % higher than the theoretical predicted value.

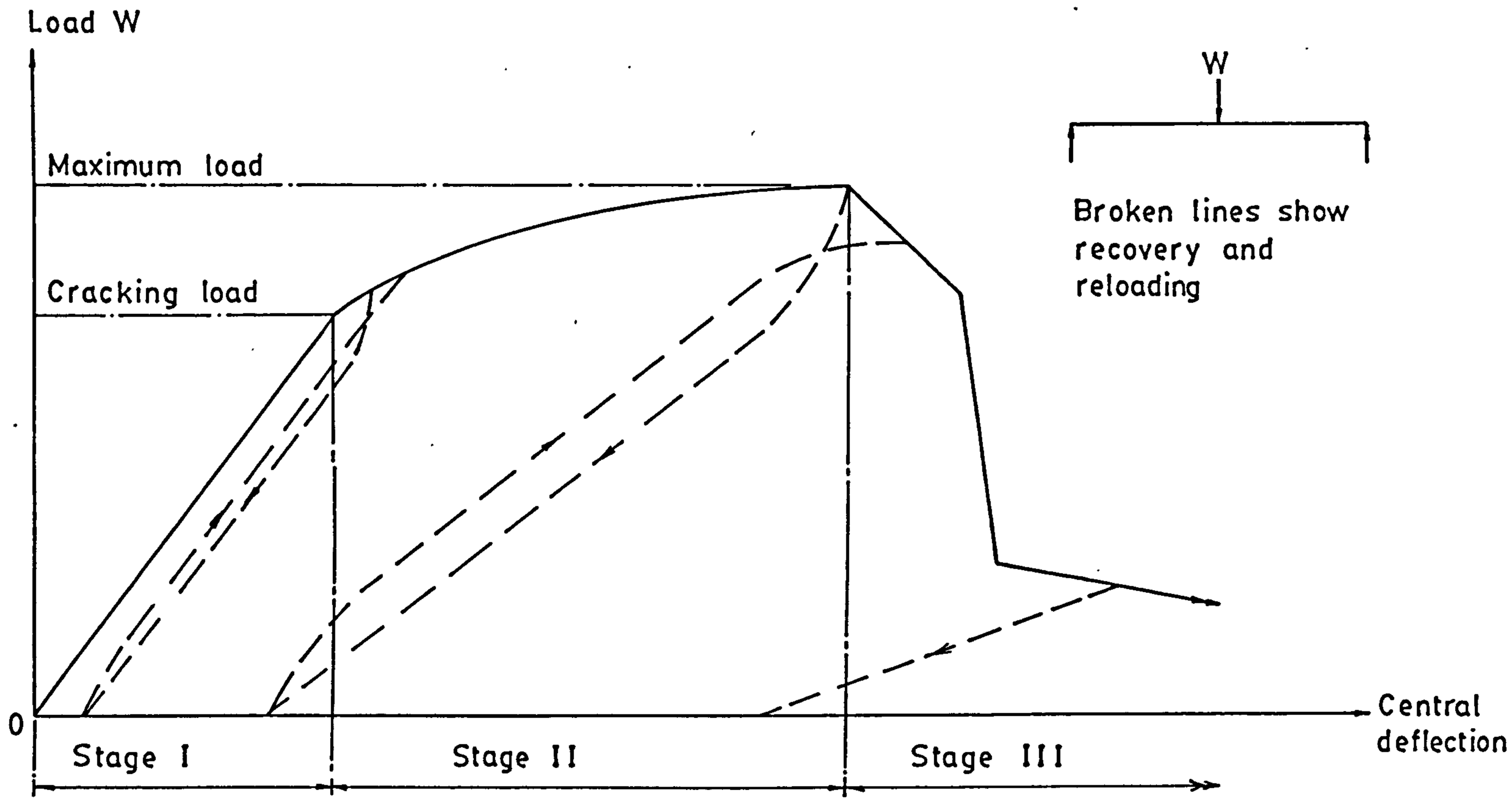

FIG. 2.1 TYPICAL STATIC LOAD-DEFLECTION CURVE OF A PRESTRESSED CONCRETE BEAM

	CONCRETE			STEEL		
	Tensile Strength	Compressive Strength	Young's Modulus	Yield Stress	Ultimate Strength	Young's Modulus
Dynamic Increase Factor	1.0 - 4.0	1.0 - 2.0	1.0 - 1.5	1.0 - 2.5	1.0 - 1.5	1.0
Order of Strain Rate (S^{-1})	10^{-9} - 10	10^{-4} - 10^{2}	10^{-4} - 10	10^{-4} - 10^{2}	10^{-2} - 10^{3}	Any

TABLE 2.1 DYNAMIC INCREASE FACTORS FOR CONCRETE AND STEEL (AFTER AL-AZAWI[5])

Material	DIF
<u>Reinforcing Steel</u>	
fy = 267 N/mm²	1.20
fy = 345 N/mm²	1.15
fy = 414 N/mm²	1.10
Prestressing Steel	1.00
<u>Concrete</u>	
Axial and Flexural Compression	1.25
Shear	1.10

NOTES DIF - Dynamic increase factor which may be applied to static material strengths

fy - yield stress

TABLE 2.2 DYNAMIC INCREASE FACTORS FOR CONCRETE AND REINFORCING STEEL (AFTER ACI[11])

	Shallow Buried		Surface
	In Dry Ground	High Water Level	
Roofs and Floors	Pso	Pso	Pso
Walls	0.5 Pso	Pso	2.3 Pso

NOTES Pso - overpressure

TABLE 2.3 LOAD FACTORS FOR BLAST LOAD[23]

Parmeter	Symbol	Fundamental Dimension	Relationship to Prototype
Mass	M	M	$M_p = S_L^2 M_m$
Length	L	L	$L_p = S_L L_m$
Acceleration	γ	L/T^2	$\gamma_p = S_\gamma \gamma_m$
Force	F	ML/T^2	$F_p = S_f S_L^2 F_m$
Time	T	T	$T_p = S_L^{1/2}/S_\gamma^{1/2} T_m$
Stress	σ	M/LT^2	$\sigma_p = S_f \sigma_m$
Strain	ϵ	-	$\epsilon_p = \epsilon_m$
Young's Modulus	E	M/LT^2	$E_p = S_f E_m$
Deformation	u	L	$u_p = S_L u_m$
Density	ρ	M/L^3	$\rho_p = S_f/S_L \rho_m$
Velocity	v	L/T	$v_p = S_\gamma S_L^{1/2} v_m$
Poisson's Ratio	ν	-	$\nu_p = \nu_m$

Notes : S_L = geometric scale factor

S_f = stress scale factor

S_γ = acceleration scale factor = $1/S_L$ (5)

Subscripts p = prototype

m = model

TABLE 2.4 RELATIONSHIPS OF PROTOTYPE QUANTITIES AND MODEL QUANTITIES

CHAPTER THREE

TEST SPECIMENS - FABRICATION AND TESTING

3.1 Introduction

In this chapter, the details and fabrication of the model prestressed concrete beams are described, followed by the description of the test equipment and procedure. Data of the material properties required for the one-dimensional stress wave analysis (chapter 5, section 5.3) are also presented at the end of this chapter.

3.2 Test Specimen

3.2.1 Dimensions of Model Beam

The test rig available was first used by J E Inkester[39] and T H Ang[34] for a rectangular beam section of 65 x 44 mm based on a geometric scale factor of about 1/8. For convenience, the same size of beam section was used. The span was set at a constant length of 600 mm and the overall length was 1000 mm (section 3.4) for all beams.

3.2.2 Model Materials

3.2.2.1 Prestressing Wire

Piano wire with a diameter of 1.6 mm was used as the model prestressing wire and was obtained from McArthur Young Ltd., Barnsley in a single batch. The wire was cut into pieces of 1.5 m long. Since the wire had a very smooth surface, each piece of wire was sand-blasted to improve the bond. A Super 6 Guyson sand blast cleaner, borrowed from the Mechanical Engineering Department, University of Sheffield, was used with Salfigrain of size 60/ 80. Each wire was sand-blasted for approximately four minutes under a pressure of 7 bar.

Five pieces of treated wire (1500 mm) were choosen at random. The stress-strain characteristics and relaxation were determined from a 300 mm and a 500 mm piece cut from each 1500 mm wire. Each 300 mm piece was tested

in an Amsler loading machine with a 50 mm gauge length. The stress-strain obtained from the average of five wires is shown in figure 3.1. The average 0.1 % proof stress, ultimate strength, Young's modulus and percentage of maximum elongation were found to be 1625 N/mm^2, 2200 N/mm^2, 208.8 kN/mm^2 and 1.6 % respectively. Each 500 mm piece was stressed to a tension of 2.5 kN by a prestressing device (section 3.5.2). The average relaxation after 14 days was found to be 2.0 %.

With a geometric scale factor of 1/8, the piano wire represents a wire of 12.8 mm in diameter.

3.2.2.2 Microconcrete and Mix Proportions

In order to satisfy the similitude conditions, the concrete constituents should also be scaled down by the same factor. Since finer ground cement was not available, ordinary graded cement was used. Rapid hardening Portland cement (Ferrocrete), a product of the Blue Circle Group, was used throughout the experimental programme to achieve a high early strength. Accordingly, the time of the programme was shortened. Sabnis, Harris, White and Mirza[59] concluded that if a mean size of coarse aggregate exists in the prototype concrete, then a corresponding scaled-down mean size of (sand) particles should exist in the model concrete. However, scaling down the maximum size is also acceptable as it is implicitly assumed that the scale ratio between the maximum size aggregate of model and prototype materials has the same ratio as the mean sizes of the two. Secondly, the finer particles are limited to less than 10 % passing the US no. 100 sieve (= BS no. 100) to avoid the necessity for very high water/ cement ratios in order to obtain a workable mix. The maximum size of sand used in the present investigation was chosen to be 2.36 mm (BS sieve no. 7), which compares with 19 mm for the normal prototype maximum size aggregate.

The gradation curves (before and after all sizes larger than 2.36 mm were omitted) of the available river sand obtained by sieving according to BS 410[60] are shown in figure 3.2. After sieving, all sizes larger than 2.36 mm were omitted and the sand shifted from zone 2 to zone 3 (BS 882[61]).

Sand/ cement and water/ cement ratios of 2.5 and 0.55 by weight were chosen respectively after testing several different mixes. This mix achieved an

average 14-day compressive strength of 39.7 N/mm^2 from 50 mm diameter x 100 mm control cylinders and 32.6 N/mm^2 from 100 x 100 x 300 mm prisms. The stress-strain relation is shown in figure 3.3. The axial strain indicated is the average strain on two prisms. The strain at the centre of two opposite faces of each prism were measured by a 200 mm demec gauge extensometer. These tests were carried out using as ELE crushing machine. The saturated density measured according to BS 1881 part 5[62] was 2240 kg/m^3. The logitudinal wave velocity, C_L, was measured by a commerically available PUNDIT equipment, CNS Instruments Ltd., London and also using a pair of 50 mm diameter, 54 kHz probes placed 100 mm and 300 mm apart on the prisms, using the direct method given in BS 4408 part 5[63]. The average value found was 3340 m/s.

3.2.2.3 Shear Reinforcement and Carrier Bars

Black annealed mild steel wire of 2.0 mm diameter was used as shear reinforcement and carrier bars while 0.45 mm diameter wire was used as binding wire.

The 2.0 mm wire was purchased from McArthur Young Ltd., Barnsley in a single batch. Since the wire came in a coil, it was straightened out and had the kinks removed by drawing. This operation was done in the Metallurgy Department, University of Sheffield. The drawing machine was that described by J E Inkester[39] and T H Ang[34]. A 0.079 inch (2.0 mm) die was used. The length of each piece of wire was cut to 1.2 m approximately and all the wire was drawn in the same day. The stress-strain curve was obtained in a similar manner as the piano wire (section 3.2.2.1) and is shown in figure 3.4. The average 0.2 % proof strength, ultimate strength and Young's modulus were found to be 300 N/mm^2, 350 N/mm^2 and 199 kN/mm^2 respectively.

With a geometric scale factor of 1/8, this wire represented the 16 mm diameter prototype wire.

3.3 Experimental Programme

The details of the experimental programme are shown in table 3.1. Four series of beams were tested. Beams in the same series were reinforced similarly. The details of the reinforcement are described in section 3.4. Each series contained five pairs of beams. One pair was tested statically while the

other four pairs were tested under various impact velocities by using different air gun pressures (section 3.7.6). A post-impact-static test was carried out on each impacted beam to determine its residual static load resistance.

3.4 Reinforcing Details[24,64,65,66,67]

For convenience, four piano wires with a diameter of 1.6 mm and a straight profile were used and each wire was pre-tensioned to 56.5 % (2.5 kN) of its ultimate strength in all beams. The four 1.6 mm diameter wires gave a steel ratio of 0.28 % which satisfied the requirement to ensure gradual failure as stated in CP 110 part 1[24].

Closed rectangular stirrups were used in all beams. According to the same code of practice[24], the maximum stirrup spacing should be 0.75 x effective depth in shear = 44.3 mm. From the previous studies mentioned in section 2.5, the shear effect is enhanced under a dynamic load. The stirrup spacings in series 1, 2, 3 and 4 were set at 40, 80, 20 and 10 mm respectively. An extra stirrup was introduced in the end region to avoid development of horizontal cracks[64,65].

CP 110[24] only gives a vague recommendation on the transfer length for pre-tensioned tendons. Accordingly, the recommendation in the ACI code[66] of 100 x wire diameter (160 mm) was used. In order to achieve a constant bending moment within the span, the beam was extended by a conservative length of 200mm beyond each support. The total embedment length, and hence the total length of the beam, was 1000 mm. This length was checked against the values recommended in the ACI code[66] and by Zia and Mosatafa[67]. It was found to be satisfactory.

A minimum microconcrete cover of 4 mm was provided to all sides of the stirrups. This was accomplished by the binding wires which were cut to protrude 4 mm alternatively in vertical and lateral directions from the sides of the stirrups.

Figure 3.5 shows the reinforcing details of all four series.

3.5 Fabrication of Model Beams

3.5.1 Reinforcing Cages

Since the black annealed wire was too small for a normal steel bender, the template descibed by Ang[34] was used so that the internal dimensions of the stirrups would be 32 x 53 mm with little variation. The rest of the fabrication of the reinforcing cages was then quite straight forward.

3.5.2 Prestressing Tools and Method

A simple prestressing device made from 8.0 mm diameter mild steel threaded rods shown in figure 3.6 was developed to pre-tension the piano wire. One free end of the wire was flattened after threading it through a 1.6 mm diameter hole in a 20 mm rod (fig. 3.6d). It was then joined to a 100mm or a 200 mm rod (fig. 3.6c) by a coupler (fig. 3.6b). This coupler was either a 50 mm internally threaded, 16 mm diameter mild steel rod with two flats on the shaft to accommodate a 13 mm spanner for the locking operation or simply a 30 mm nut. The final part which is basically a 170 mm rod (fig. 3.6a) was connected to the rest directly or via a 100 mm extension rod by a similar coupler(s). A length of 25 mm on this 170 mm rod was thinned down to a rectangular cross section of 6 x 3 mm. On this smooth section, two 5 mm Kyowa KFC-5-C1-11 electrical resistance foil strain gauges were installed on opposite surfaces so that the bending strain introduced in the calibration and load measurement would be eliminated. Each gauge was connected to form an active arm of a Wheatstone bridge circuit in a P-350A strain indicator, Vishay Instruments Inc., and was calibrated on a Hounsfield extensometer to read the applied prestressing force. The other free end of the piano wire was passed through a 1.6 mm hole in a 30 mm rod (fig. 3.6d) and was flattened. A total number of four 170 mm rods and the associated parts for casting four beams at a time were made.

The prestressing bed consisted of a 1.6 m long 305 x 102, 46.2 kg/m RSC section with four 160 mm long 90 x 90 RSA 10. Each angle was bolted down onto the channel section by two 20 mm diameter black bolts, grade 4.6 as shown in plate 3.1(a). One of the angles at the prestressing end had one of its legs cut to 43 mm to give access for the locking operation. Three 10 mm thick stiffeners were welded to the angle at the fixed end. Holes of 9 mm diameter were drilled

at the appropriate positions on the angle to let the parts of the prestressing device pass through. A total number of two prestressing beds were constructed. Each bed could accommodate a formwork consisting of two beam moulds.

The piano wires were fed through the reinforcing cage and the 3 mm diameter holes on the aluminium end panels of the form. The free ends were connected up to the end bits as described previously. The end panels were then connected to the perspex base of the form by brass screws. After placing this arrangement in the correct position on the prestressing bed, the rest of the prestressing device was added on and the 30 mm rods were locked against the fixed end angle by M8 nuts (plate 3.1(b)). The desired prestressing force was applied in two stages by tightening the nut mounted at the free end of the 170 mm rod and reading the load from the calibrated strain gauges (plate 3.1(b) and plate 3.1(c)). About 50 % of the required force was achieved at the first stage. When the prestressing force was steady, the appropriate M8 nut on the 100 mm or 200 mm rod was then adjusted to transfer the prestress to the appropriate angle and release the prestressing device for the next tensioning operation. In each tensioning operation, four wires were stressed.

3.5.3 Casting and Curing

Four beams and nine 50 mm diameter x 100 mm long cylindrical control specimens were cast at a time. This size of control specimen was chosen following the recommendation of the ACI committee 444[68] and Sabnis and Mirza[55] to avoid size effects. The aluminium side forms and the cylinder moulds were cleaned prior to the application of a thin film of mould oil. The side forms were then joined to the perspex base by brass screws before the prestressing beds and cylinder moulds were transferred to a vibration table. The cylinder moulds were put on the prestressing beds so that they were compacted to a similar degree as the beams by the vibration table. The position of the reinforcing cage was checked at several sections to ensure accuracy.

The sand was oven dried 24 hours prior to mixing. When it cooled down, all sizes greater than 2.36 mm were taken out by sieving and the rest was stored in dry room. The inner surface of a non-tilting 0.02 m^3 electric mixing pan was moistened with extra water before the correct amount of sand and cement was poured into it. The dry materials were poured into the pan in five layers

alternately with sand first, and were then mixed for 90 seconds. The correct volume of water was added in gradually with the mixing pan switched on. The whole content was mixed for a further two minutes after all the water was in.

The wet concrete was deposited in the forms and cylinder moulds in two or three layers. After each pour, the vibration table was switched on and a vibration poker was run along the outside surfaces of all the moulds for two minutes or until the wet concrete began to bleed. The tops of the moulds were overfilled by one mm and left for 90 minutes away from direct sunlight to allow for initial shrinkage before being trowelled smooth. All the moulds were then enclosed by polystrene sheets and left to set (on the vibration table when possible) in the laboratory.

After being demoulded carefully 24 hours later, all the specimens were covered by damped sacks and polystrene sheets for a curing period of six days in the laboratory. At the seventh day, the covers were removed and the specimens were air-dried for a few hours. Three cylinders were then tested to determine the 7-day compressive strength. Five pairs of 200 mm gauge length demec studs were installed across the midspan of each beam using plastic padding (fig. 3.7) and the readings were taken. The prestressed piano wires were then carefully released in two stages. The beams had been whitewashed so that cracks would be more clearly seen and the identification number and the positions of the shear links were marked with a felt pen on the trowelled surface of each beam. The demec readings were taken each day with the trowelled face of the beam facing up. Together with the rest of the control cylinders, the beams were left in the laboratory until they were tested at 14 days.

3.6 Measurements Prior to Test

The 14-day compressive strength and tensile splitting strength of each batch of the concrete mix were determined by taking the average of three control cylinders. The results can be found in table 3.2.

The weights of some beams were measured just before testing in order to find out the mass per unit length. This value is important in the later analysis (chapter 5, section 5.4) and the results were tabulated also in table 3.2.

The effective prestressing force P_e in each beam prior to testing was estimated from the strain profile at midspan established by the difference in the readings of the demec points before release and just before testing. In this research, the stress at the top and bottom fibre is given by

$$\left.\begin{aligned} \frac{P_e}{A} + \frac{P_e e}{Z_b} &= \sigma_b = \epsilon_b E_c \\ \frac{P_e}{A} - \frac{P_e e}{Z_t} &= \sigma_t = \epsilon_t E_c \end{aligned}\right\} \qquad \text{equ. 3.1}$$

where P_e - effective prestressing force,

A - cross section area - 2860 mm^2

e - eccentricity of tendon group - 16.5 mm,

Z - uncracked elastic section modulus (- 33381 mm^3 top and 34213 mm^3 bottom),

σ - stress,

ϵ - strain,

E_c - Young's modulus of concrete - 22.3 kN/mm^2 (fig. 3.3)

and subscripts t - top,

b - bottom.

Substituting the known values in equation 3.1, and knowing the overall depth is 65 mm, the effective prestressing force is related to the curvature, 1/r, which is equal to the difference of the strain at the top and the strain at the bottom divided by the overall depth, by

$$P_e = 1.57 \times 1/r \qquad \text{equ. 3.2}$$

where P_e in kN, and

1/r in 10^{-6}/mm.

The result for each beam is given in table 3.2. The measured effective prestressing force varied from 3.19 kN to 10.05 kN and this suggested that the bond strength was not consistent.

3.7 Testing Equipment

3.7.1 Introduction

All the recording equipment was checked by comparing their response times and band-widths with the natural frequency of the beam (section 5.2.3) and the rise times and durations of the output signals (chapter 4 and chapter 5)[69,70]. Screened cables were used when possible to cut down the interferences from noise and extraneous vibration.

The general layout for the different tests is shown in figures 3.8 and 3.9 and details of each individual measuring equipment are described below.

3.7.2 Beam Supporting Rig

The beam was supported in a horizontal plane by two supporting towers (plate 3.2) designed by J E Inkester[39] and modified by T H Ang[34], and bolted onto a steel table. In this investigation, they were fixed at a distance 600 mm apart. Each tower is designed to allow rotational and translation movement in the longitudinal and lateral directions. However, in this research, each beam was preloaded to 3.0 ± 0.1 kN at each support by tightening the spring-load mechanism mounted on the tower against the reaction load cell (section 3.7.3) after checking its position carefully and this would restrict the longitudinal and the lateral movements but not the rotation and a near pinned-end support was simulated. This preloading was important because it enabled the uplift (reverse) reaction to be measured and prevented uplift of the beam during the impact test while simulating pinned-end condition.

3.7.3 Reaction Measurement

The reactions or preloadings were measured by the 250 mm long, 18 mm diameter aluminium load cells (LC2 and LC3) described by Ang[34] (fig. 3.10a). A total of 8 TML FLA-3-23 electrical resistance foil strain gauges were used in each load cell. They were arranged in a full Wheatstone bridge circuit in such a way that any bending stress was eliminated (figs. 3.10b and 3.10c). The output signals were amplified by Fylde FE-359-TA bridge amplifiers[71]. Each amplifier supplied a 5.0 V d.c. to energise its corresponding bridge circuit. The load cells were calibrated by an NPL proving ring and the conversion factor

deduced was 0.975 V/kN with an amplification factor of 2500.

The amplified output signals were connected directly to a digital voltmeter (Solartron 7045 Digital Multimeter[72]) at the preloading stage.

In static or post-impact-static test, both reaction signals were connected to a recording system[73] which consisted of a Commodore microcomputer 4032, a Bentham 266F analogue to digital convertor, a transducer interface box, a Commodore disk drive 2031 and software V.34 A-D-C. The interface box has the facilities which allows 1/4, 1/2 and full strain gauge bridge to be used and can trim the output signal from a transducer to a desirable initial value. The energising power for the transducer can also be obtained from the interface box if it is required. The software V.34 A-D-C recorded the signals on a floppy disk and in data recovery mode, a numerial hard copy and/ or graphs of the data could be obtained from the Teletype model 43 printer and/ or the Hewlett-packard 7470A plotter available in the department.

For the impact tests, LC3 was connected to a storage type oscilloscope (T912-Tektronix[74]) which was triggered by the strain gauge station on the pressure bar (section 3.7.4). An ordinary camera was used to photograph the stored trace on the screen.

3.7.4 Applied Load Measurement and Pressure Bar

A pressure bar was chosen to measure the impact load from a projectile propelled by an air gun (section 3.7.6). This technique simplifies the theoretical analysis because the force-time pulse produced in the bar is a one dimensional stress wave with a plane wavefront[84] and the incident pulse can be recorded before reflections reach the gauge if the bar is sufficiently long. In these experiments, the pressure bar is 25 mm diameter x 1000 mm long and is made from 830M31 (previously EN 27) steel (BS 970[75]). The bar was ground to fit in two sets of linear bearings so that its longitudinal axis was perpendicular to the longitudinal axis of the beam and in contact at midspan. Its ends were ground flat and smooth to ensure good contact during the test. Two sets of electrical resistance foil strain gauges were installed on the pressure bar at the positions shown in figure 3.11. Each strain gauge station contains 12 x Kyowa KFC-5-C1-11 foil gauges to complete a full Wheatstone bridge circuit. The two active arms were cemented onto the pressure bar by

CC-15A adhesive while the other two were on a 70 mm dummy made from the same material as the pressure bar to compensate for possible temperature effects. Their arrangement is shown in figure 3.11. The gauge stations were named PB1 and PB2. PB1 is also known as LC1 in the static tests. Each gauge station was connected to and received a supply voltage of 5.0 V d.c. from the Fylde FE-359-TA amplifier[71]. The dummies were calibrated by an NPL proving ring and the conversion factor found was 33.2 mV/kN with an amplification factor of 666.7. This was assumed to be the same as testing the pressure bar. The Wheatstone bridge circuit equation is

$$\Delta E = V \frac{r}{(1+r)^2} \left(\frac{\Delta R_1}{R_1} - \frac{\Delta R_2}{R_2} + \frac{\Delta R_3}{R_3} - \frac{\Delta R_4}{R_4} \right) \qquad \text{equ. 3.3}$$

where ΔE = output voltage,

V = excitation voltage (= 5.0 V),

r = arm resistance ratio (=1),

Δ = change,

R_1, R_3 = resistance in active arm (= 360 Ω),

R_2, R_4 = resistance in passive arm (= 360 Ω).

and the electrical resistance strain gauge equation is

$$\frac{\Delta R}{R} = S_g \epsilon \qquad \text{equ. 3.4}$$

where S_g = gauge factor (= 2.10)

ϵ = strain,

R = resistance (= 360 Ω),

Δ = change.

The numerical values used in equations 3.3 and 3.4 are given above. The Young's modulus of the pressure bar could be calculated and was found to be 208.0 kN/mm^2.

In the static or post-impact-static tests, a screw (car) jack was installed to apply a static load to the beam via the pressure bar. The amplified output from LC1 was connected to the recording system[73] mentioned in section 3.7.3.

In the impact test, the amplified output signals of PB1 and PB2 were

stored in digital storage oscilloscope (OS 4020 Gould[76]) which was triggered by the signal from PB2. The signals were then transferred to a floppy disk via a Commodore microcomputer 4032 and software 4020. Using software HP 4020 or HP 4020.1[77], a digital printout and a hard copy of the traces (section 4.3.1) were obtained from the equipment mentioned in section 3.7.3. By inspecting the digital printouts, the average time for a stress wave to travel the 300 mm distance between PB1 and PB2 was measured as 57.5 μs. Accordingly, the longitudinal wave velocity for the pressure bar was calculated as 5217 m/s.

3.7.5 Deflection Measurement

One RDP[78] D2/2000 d.c. LVDT (linear variable differential transformer) was used to measure the midspan deflection in static or post-impact-static test. It was energised by a steady 6.0 V d.c. supply (Farnell E30/2 power supply unit) and connected to the beam as shown in figure 3.12 which allowed the beam section to rotate as it deformed during the test. A stand with a magnetic base was used to hold the LVDT in position. The output was recorded and stored by the system[73] described in section 3.7.3. The LVDT reading was calibrated by a dial gauge.

Three d.c. LVDT's (RDP[78] D2/500A, D2/1000 and D2/2000) were used to measure the dynamic displacements at 1/6, 1/3 and 1/2 span (fig. 3.9). They were energised and connected to the beam as in a static test and the output from these LVDT's and from PB2 on the pressure bar (as a time reference) were fed directly to a 4-channel Racal Store 4 high speed tape recorder[79] at a recording speed of 1524 mm/s (60"/s). At the end of each impact test, the output from the tape recorder was played back at 762 mm/s (30"/s) and fed to an SE 3006 DL ultra-violet recorder[80] with a paper speed of 1250 mm/s. This produced a time base of 400 μs/mm on the paper record. The galvonometers used were A1000 for the LVDT's and A8000 for PB2 (SE Laboratories (Engineering) Ltd.). Three external adjustable resistors were introduced in the tape recorder/ ultra-violet recorder transmission circuit (fig. 3.9) so that this system could be calibrated by a dial gauge and the external resistors were adjusted until a magnification factor 2.5 in the deflection measurement of each LVDT was achieved on the final paper record.

3.7.6 Air Gun and Bullet Velocity Measurement

The impact force applied to the beam was produced from a steel bullet accelerated by the pressure of compressed air (fig. 3.9). Details of each part of this system was described below.

The air was compressed by an Airmate WM 40 system with a maximum pressure of 10 bar (145 psi). The outlet of the reservoir was connected to the gun barrel in two routes. One was via a 3-way solenoid valve and the other via an ordinary 3-way valve. The solenoid valve is described by Ang[34]. The air pressure was released for a preset time and vented from the gun barrel after impact to let the bullet rebound. The ordinary valve was added so that the bullet could be transported in the gun barrel at a safe speed[81]. In this research, the air pressure was set at 15, 20, 25 and 30 psi (0.103, 0.138, 0.172 and 0.207 N/mm^2) and released for a duration of 0.52 second for consistency in impact (bullet) velocity and venting reasons (see later in this section).

The bullet was a 28.03 mm diameter x 350 mm long x 1.687 kg steel rod made of the same material as the pressure bar. Accordingly, the Young's modulus and the longitudinal wave velocity were 208.0 kN/mm^2 and 5217 m/s respectively. Its ends were ground flat and smooth to ensure good impact contact. It was placed at a chosen position to give a launching distance of 2.775 m before impacting the pressure bar in every test.

The gun barrel (fig. 3.9) was a precision machined 2.8 m x 28.3 mm internal diameter mild steel pipe mounted on base plates at close intervals. The breech was sealed by a screw cap after it was loaded.

The bullet velocity measurement device[39] timed the bullet over 100 mm just before impact. It consists of two sets of photodiodes with 12 V light bulbs set at a distance of 100 mm apart housed inside a bakelite casing. This device was mounted in a fixed position on the end of the gun barrel so that the two sets of photodiodes were placed at 145 mm and 45 mm from the impact end of the pressure bar and all the longitudinal axes were in line (fig. 3.13). Just before impact, the bullet cut the two light paths of the photodiodes and triggered the start and stop signals in a Racal counter timer 9903[82] via the photo-electic switches[34]. The time interval was then registered and the velocity of the bullet calculated.

Before the main experimental programme, the air gun system was checked for repeatability. It was found that a 'constant' bullet velocity (± 0.3 m/s) could be achieved and was directly proportional to the magnitude of the applied constant air pressure, only if this pressure was greater than 14 psi (0.096 N/mm^2) before release. After release, the pressure in the reservoir usually dropped by 5 psi.

3.7.7 Consistency Between Applied Load and Reaction Measurement

The applied load and reactions were compared in a preliminary test on a steel beam of the same size as the model concrete beam. The dummy and the reaction load cells were set up as described in section 3.7.2 and section 3.7.3. A static load was applied at the midspan as described in section 3.7.4. The maximum difference between the sum of the reactions and applied load was 0.16 kN (5%) and the reactions agreed with each other with a maximum difference of 0.08 kN (5%) (fig. 3.14). This discrepancy was probably due to friction in the roller bearings in the supporting towers. These results showed that the recording systems and position of the equipment were good.

3.8 Test Procedure

The beam was placed in the test rig and preloaded as described in sections 3.7.2 and 3.7.3. Before every test, at least 15 minutes was allowed for the electrical equipment to warm up. All the electrical connections, equipment sensitivities and the squareness of the pressure bar axis to the beam were then checked carefully.

The loading in the static or post-impact-static test was monitored from the instant display of the load-deflection curve on a visual display unit. The reactions, applied load and the deflection were recorded as described in sections 3.7.5, 3.7.4 and 3.7.3 and all the visible cracks were marked at every load step of 0.3 kN until the linearity of the load-deflection curve started to deteriorate, then at every load step of 0.1 kN or deflection step of 5 mm until the applied load dropped suddenly (failure) or the deflection reached 25 mm. The crack pattern, tendon conditions and the failure mode were all recorded.

Before each impact test, the beam was tested statically as in a normal

static test up to a load of 1.0 kN to determine the initial beam stiffness. The static equipment was then disconnected and the impact equipment connected. If necessary, the positions of the pressure bar and/ or the beam were adjusted so that the end of the pressure bar was touching the beam. After the recordng equipment had been switched on, the bullet was loaded in the correct position and the breech of the gun barrel was sealed. The tape recorder was then switched on to record. Two seconds later, i.e. when the tape recorder reached the preset speed, the bullet was fired. The transient reaction, load and deflections were recorded as described in sections 3.7.3, 3.7.4 and 3.7.5 during the test. After the test, the pressure in the reservoir, bullet times, crack pattern and tendon conditions were all recorded. The necessary equipment was then changed and a post-impact-static test was carried out on the impacted beam.

The results of these tests are reported and discussed in chapters 4 and 6 respectively.

3.9 Data required in the One Dimensional Elastic Stress Wave Analysis

The data required for the analysis (chapter 5, section 5.3) are the cross sectional areas, densities and longitudinal wave velocities of the bullet, the pressure bar and the beam.

The areas of the bullet and pressure bar were calculated from their diameters. The static Young's modulus, E_s, was 208.0 kN/mm^2 (section 3.7.4) and was assumed to equal the dynamic Young's modulus, E_d, since this value is not very sensitive to strain rate (chapter 2, section 2.3.1). The wave velocity, C_L, already calculated in section 3.7.4, was 5217 m/s. The density, ρ, is given by[83]

$$\rho = (E_d / C_L)^{1/2} \qquad \text{equ. 3.5}$$

and substituting for E_d and C_L, ρ is obtained as 7643 kg/m^3.

The initial concrete (beam) area involved in the analysis was assumed to equal that of the pressure bar. From section 3.2.2.2, the density of the concrete beam was 2240 kg/m^3 and the wave velocity was 3340 m/s. This gave a dynamic Young's modulus of 25.0 kN/mm^2 using equation 3.5 which was higher than

the static value of 22.3 kN/mm^2 (fig. 3.3). This was expected because of the strain rate sensitivity of concrete (chapter 2, section 2.3.2).

Table 3.3 gives a summary of these data.

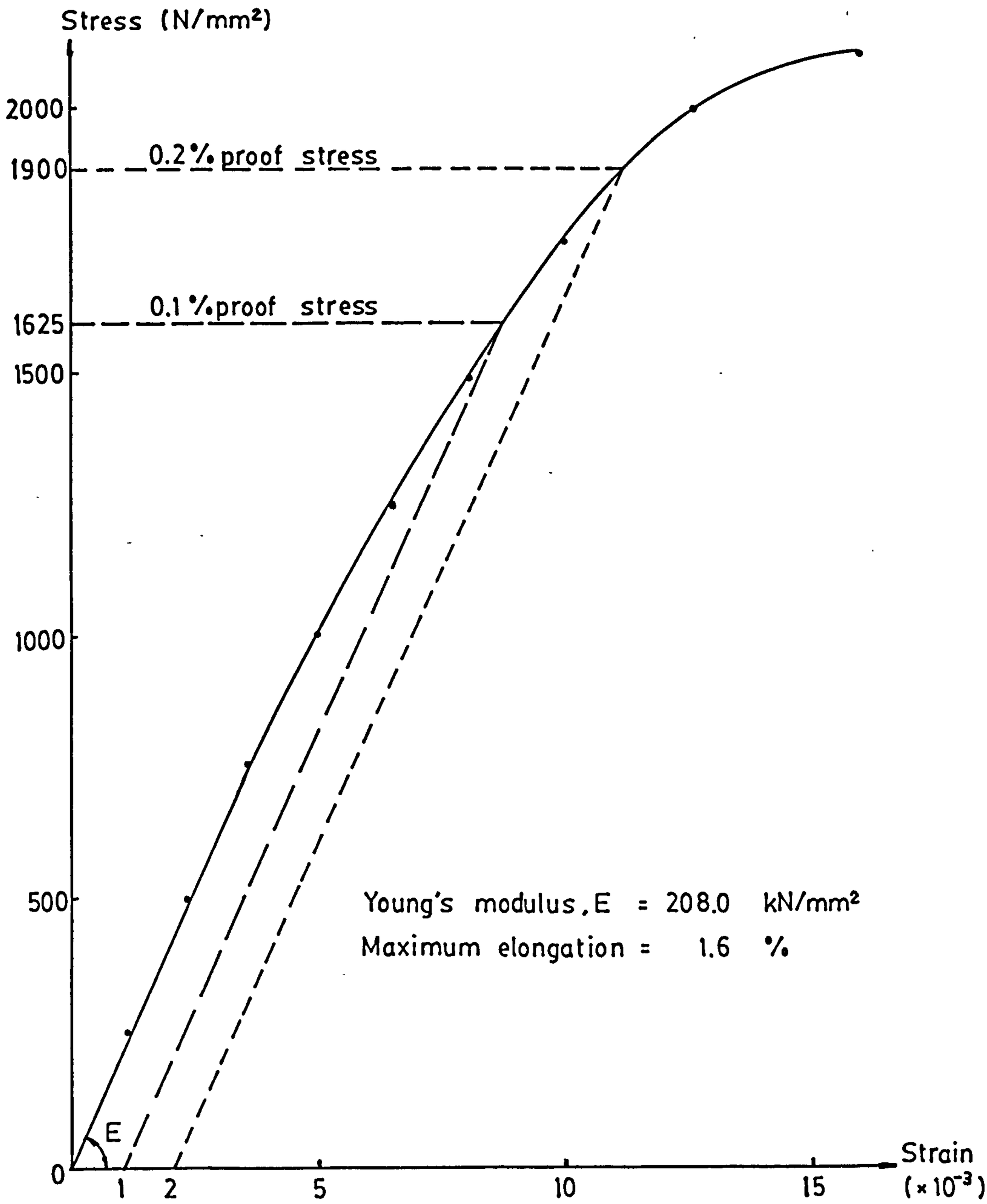

FIG. 3.1 STRESS STRAIN CURVE OF 1.6 mm DIAMETER PIANO WIRE

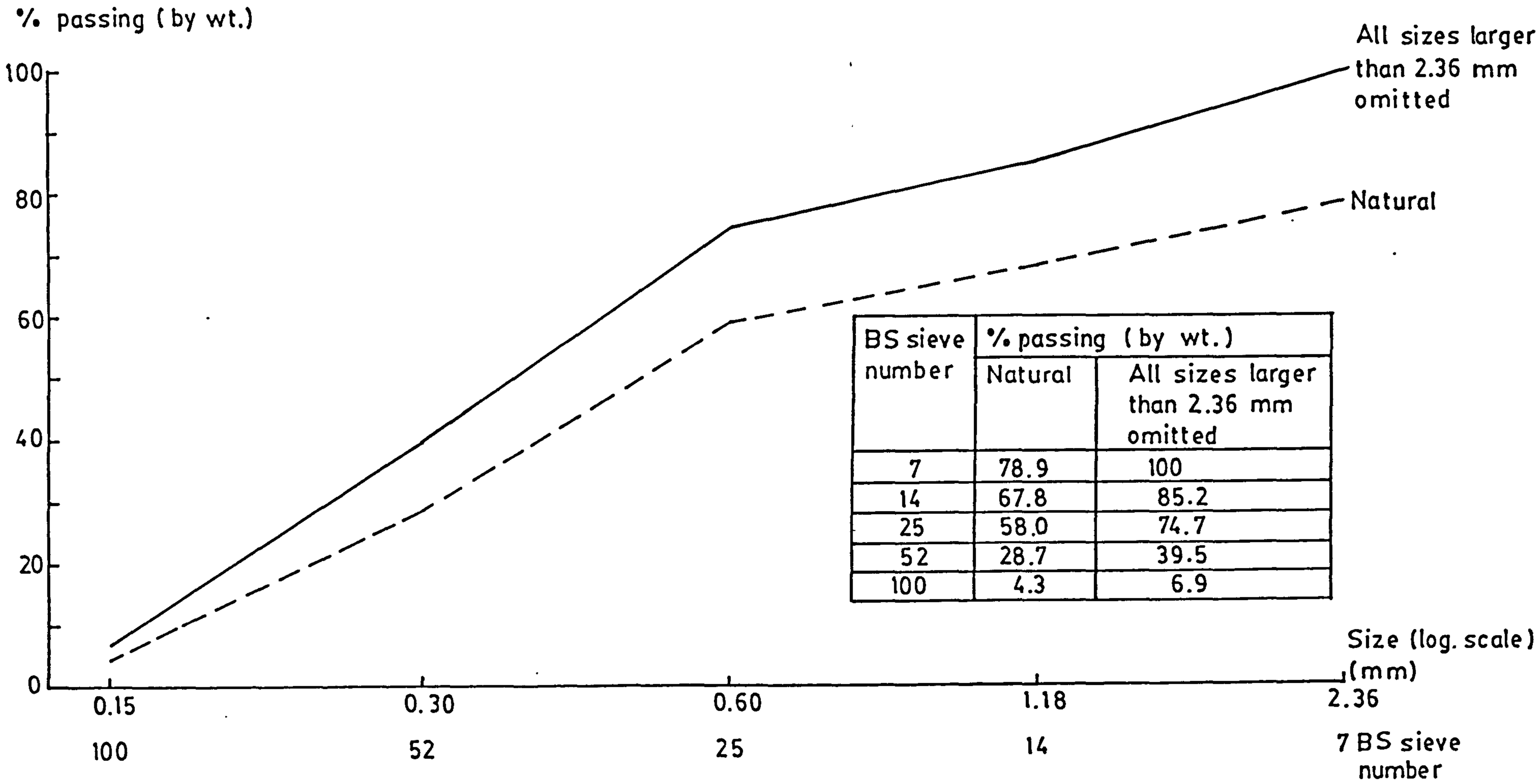

BS sieve number	% passing (by wt.)	
	Natural	All sizes larger than 2.36 mm omitted
7	78.9	100
14	67.8	85.2
25	58.0	74.7
52	28.7	39.5
100	4.3	6.9

FIG. 3.2 GRADATION CURVE OF SAND

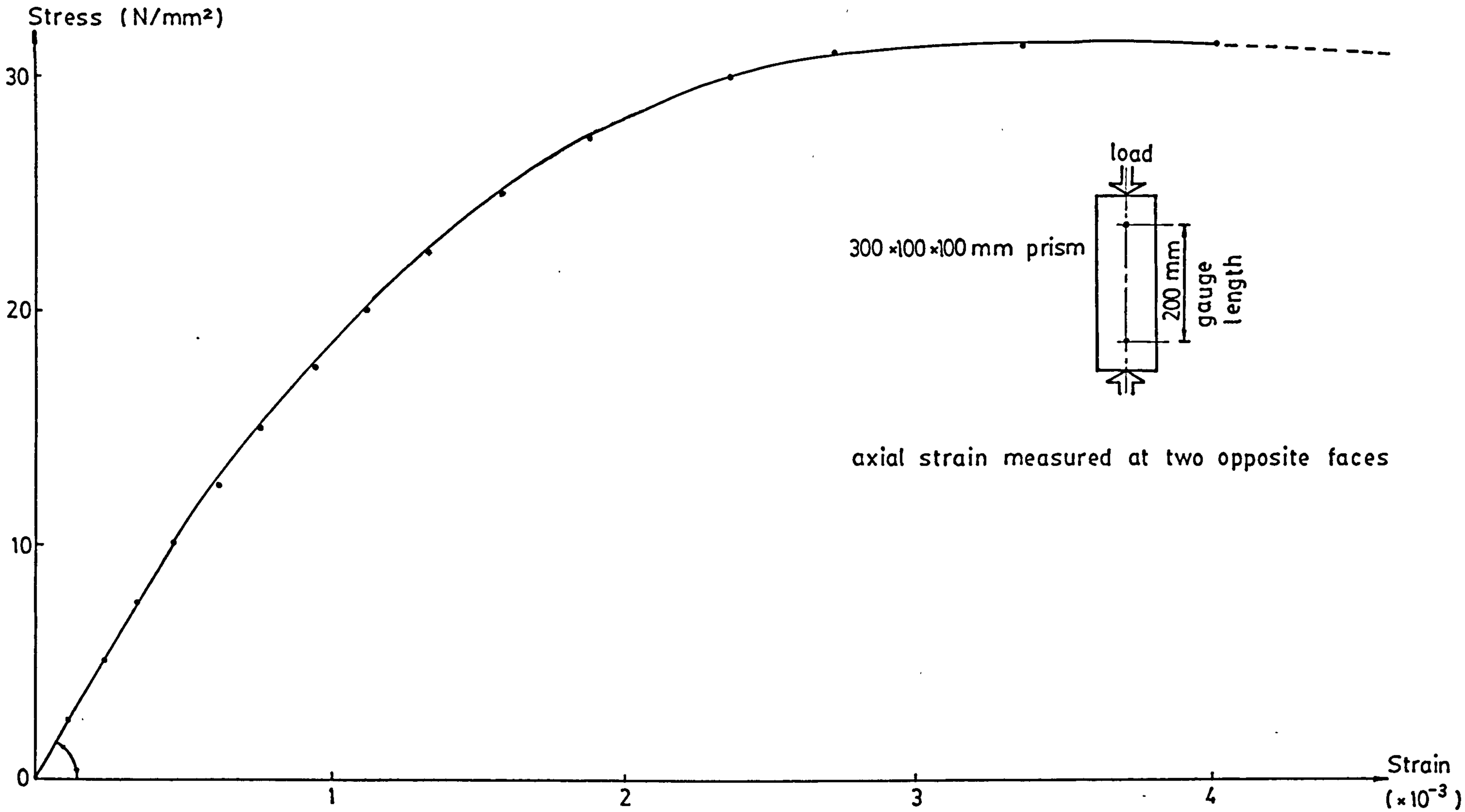

FIG. 3.3 STRESS STRAIN CURVE OF MICROCONCRETE

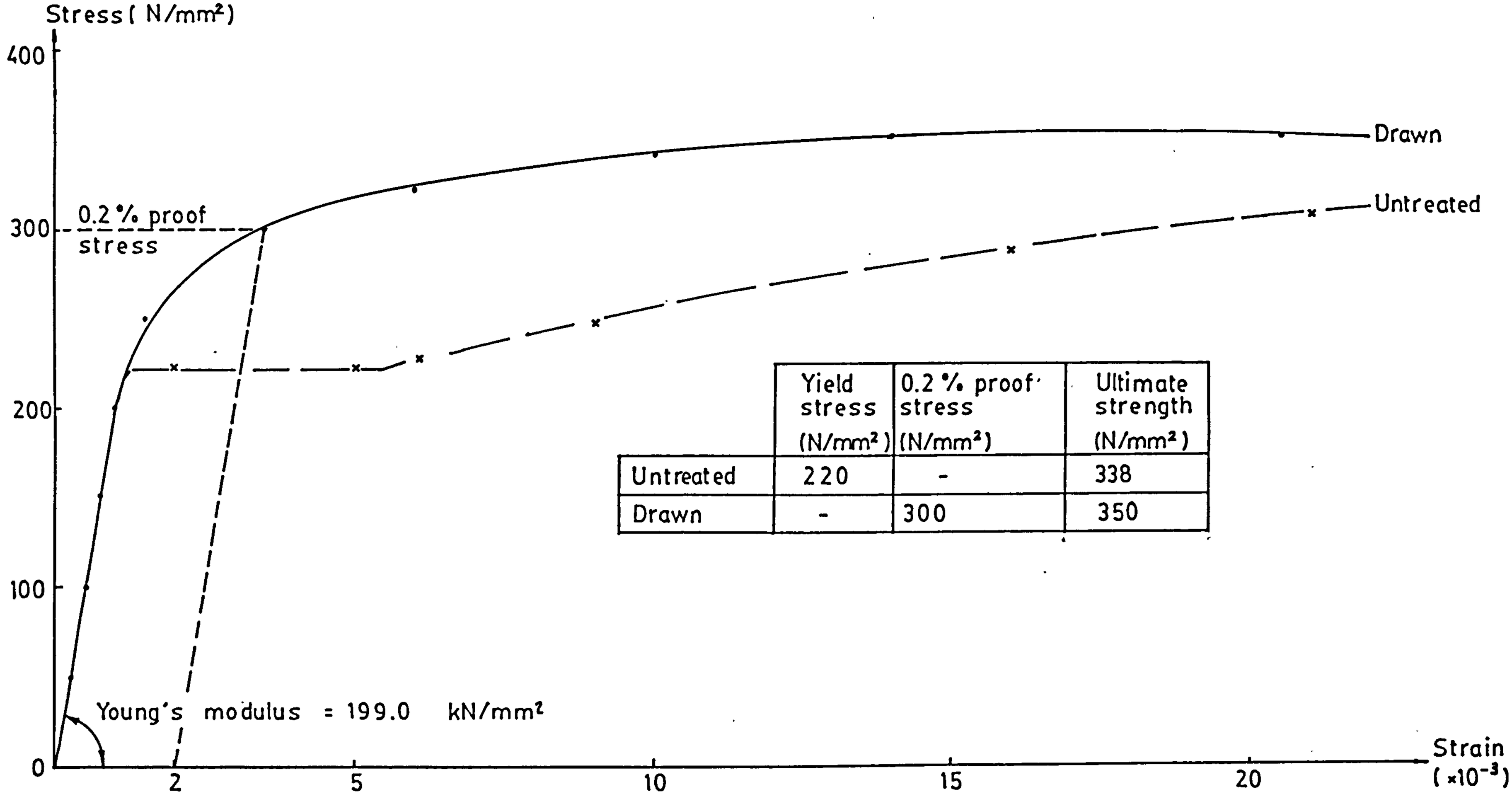

	Yield stress (N/mm²)	0.2 % proof stress (N/mm²)	Ultimate strength (N/mm²)
Untreated	220	-	338
Drawn	-	300	350

FIG. 3.4 STRESS STRAIN CURVE OF 2.0 mm BLACK ANNEALED MILD STEEL WIRE

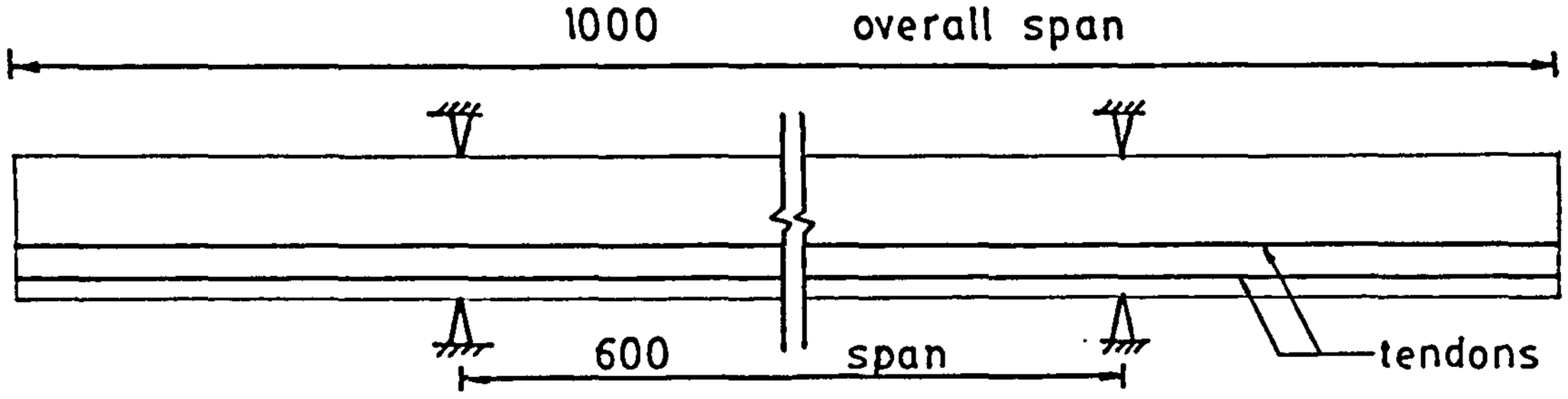

(a) Tendon Profile for All Series

24R2-40 series 1
12R2-80 series 2
47R2-20 series 3
93R2-10 series 4

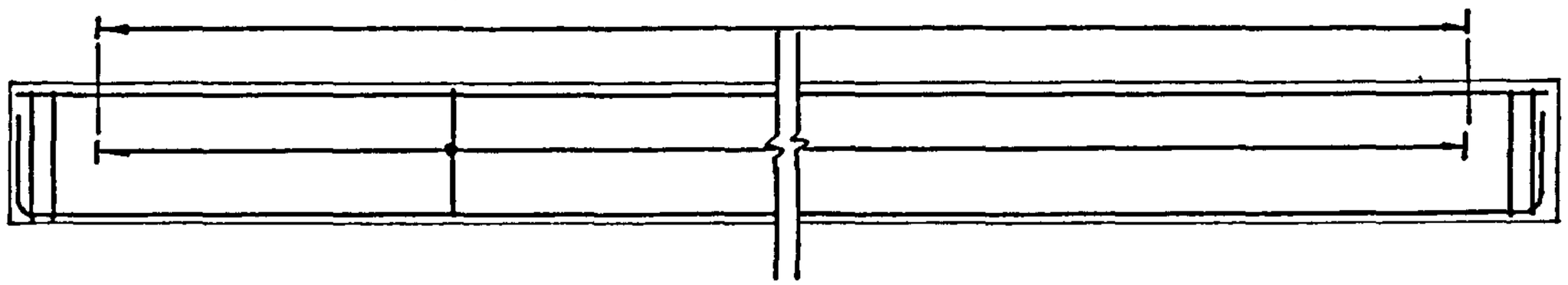

(b) Shear Reinforcing

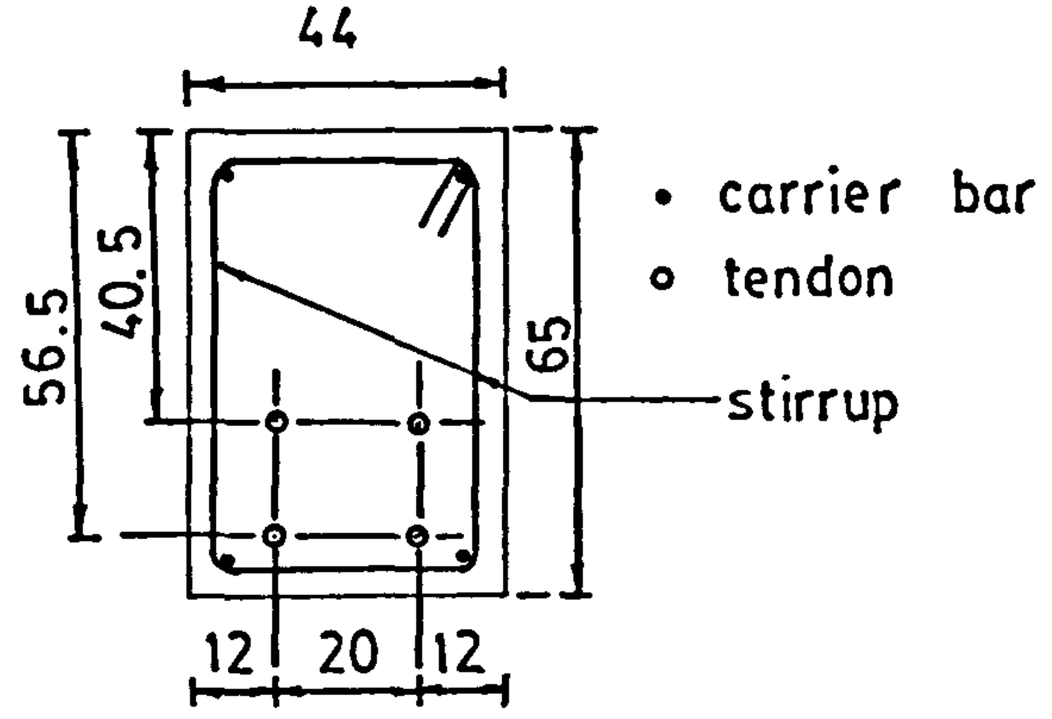

(c) Cross Section for All Series

Notes:
1. All dimensions in mm.
2. Reinforcing symmetric about midspan.
3. Cover 4 mm.
4. Tendon 1.6 mm diameter piano wire.
5. Stirrup and carrier bar 2.0 mm black annealed mild steel wire.

FIG. 3.5 REINFORCING DETAILS

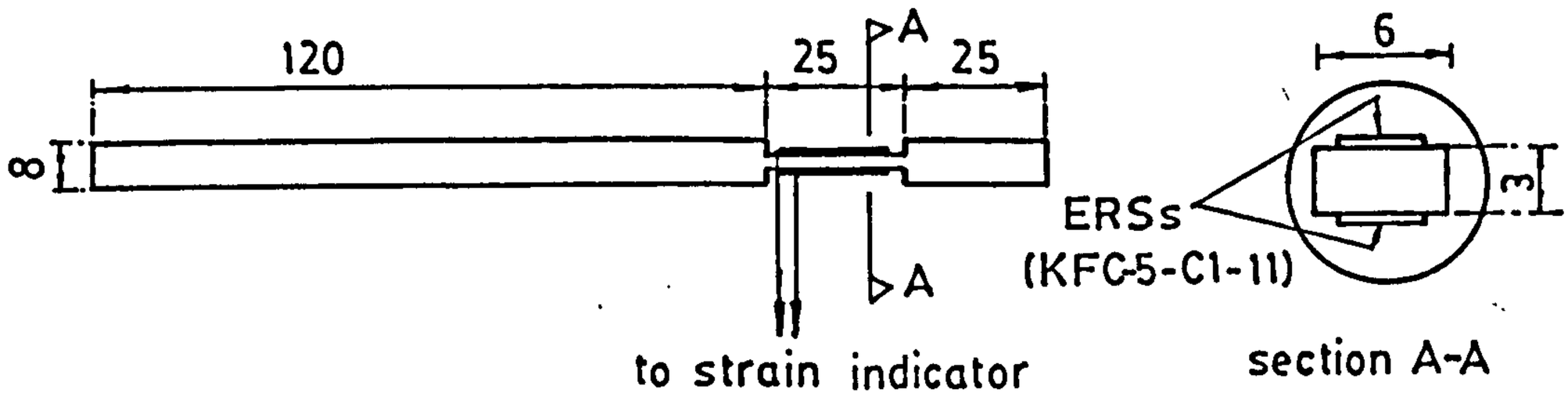

(a) 170 mm Rod

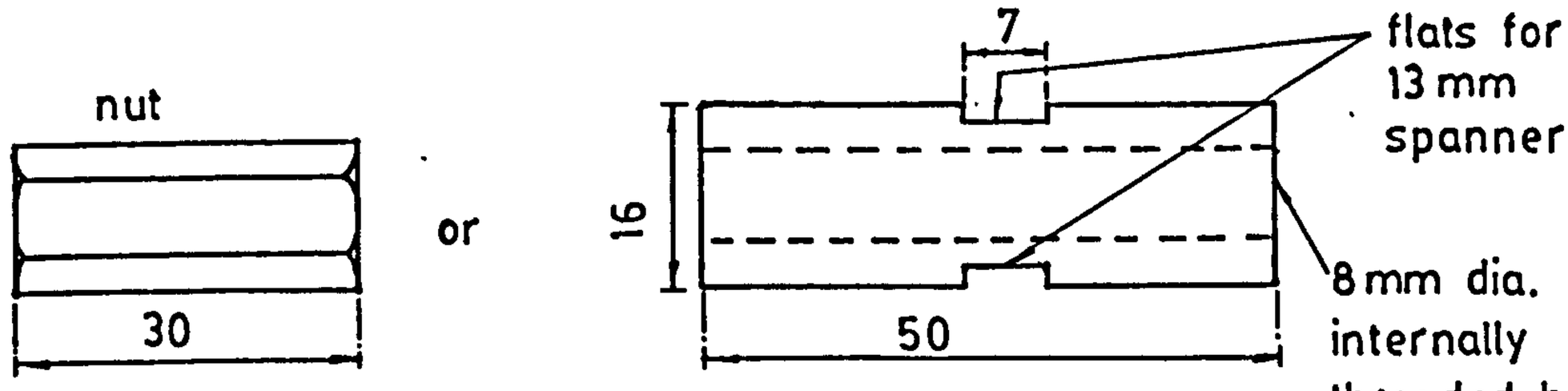

(b) Coupler

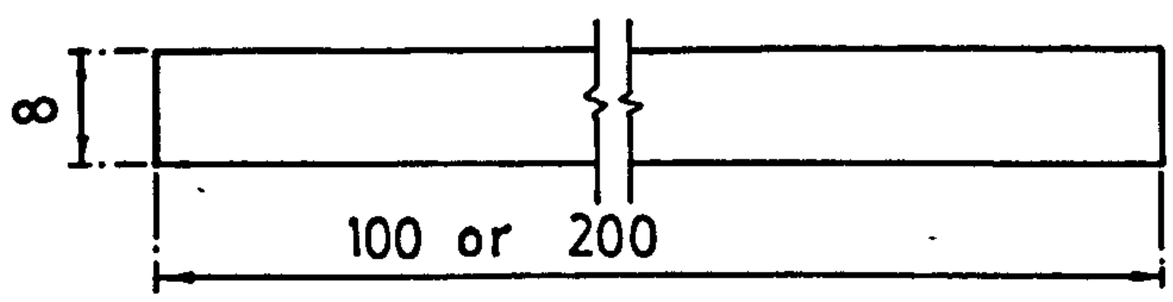

(c) 100 mm or 200 mm Rod

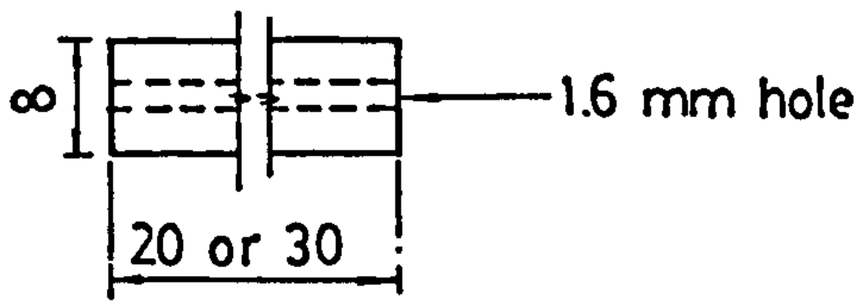

(d) 20 mm or 30 mm Rod

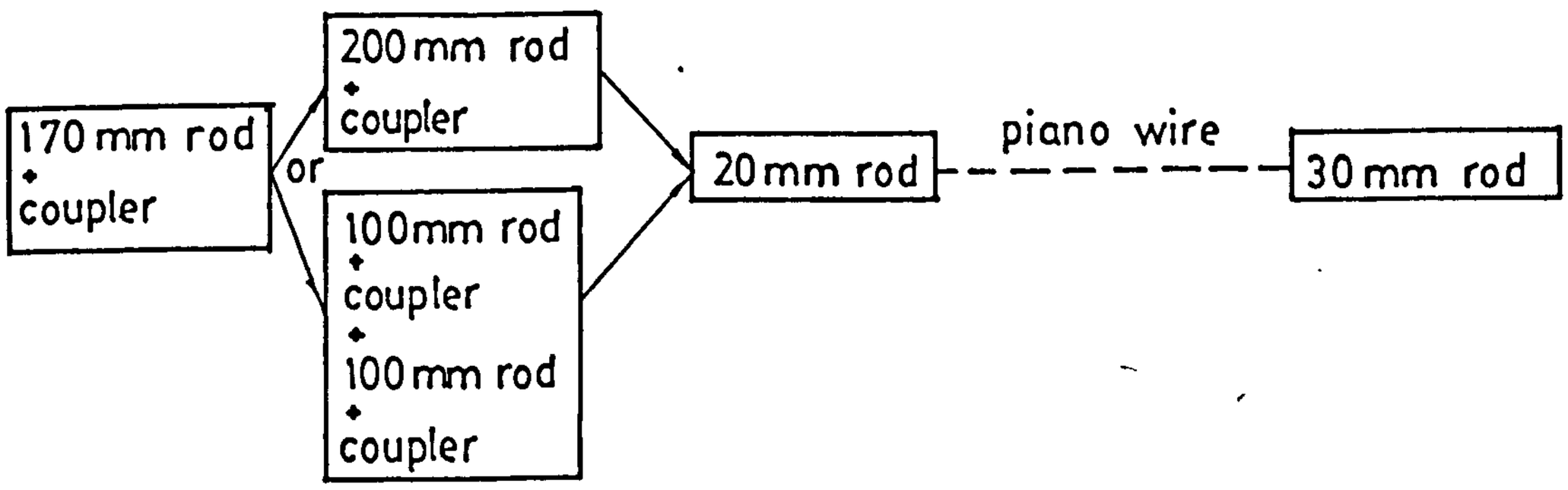

(e) Arrangement

Notes: 1. All dimensions in mm
2. All rods threaded

FIG. 3.6 PRESTRESSING DEVICE - PARTS AND ARRANGEMENT

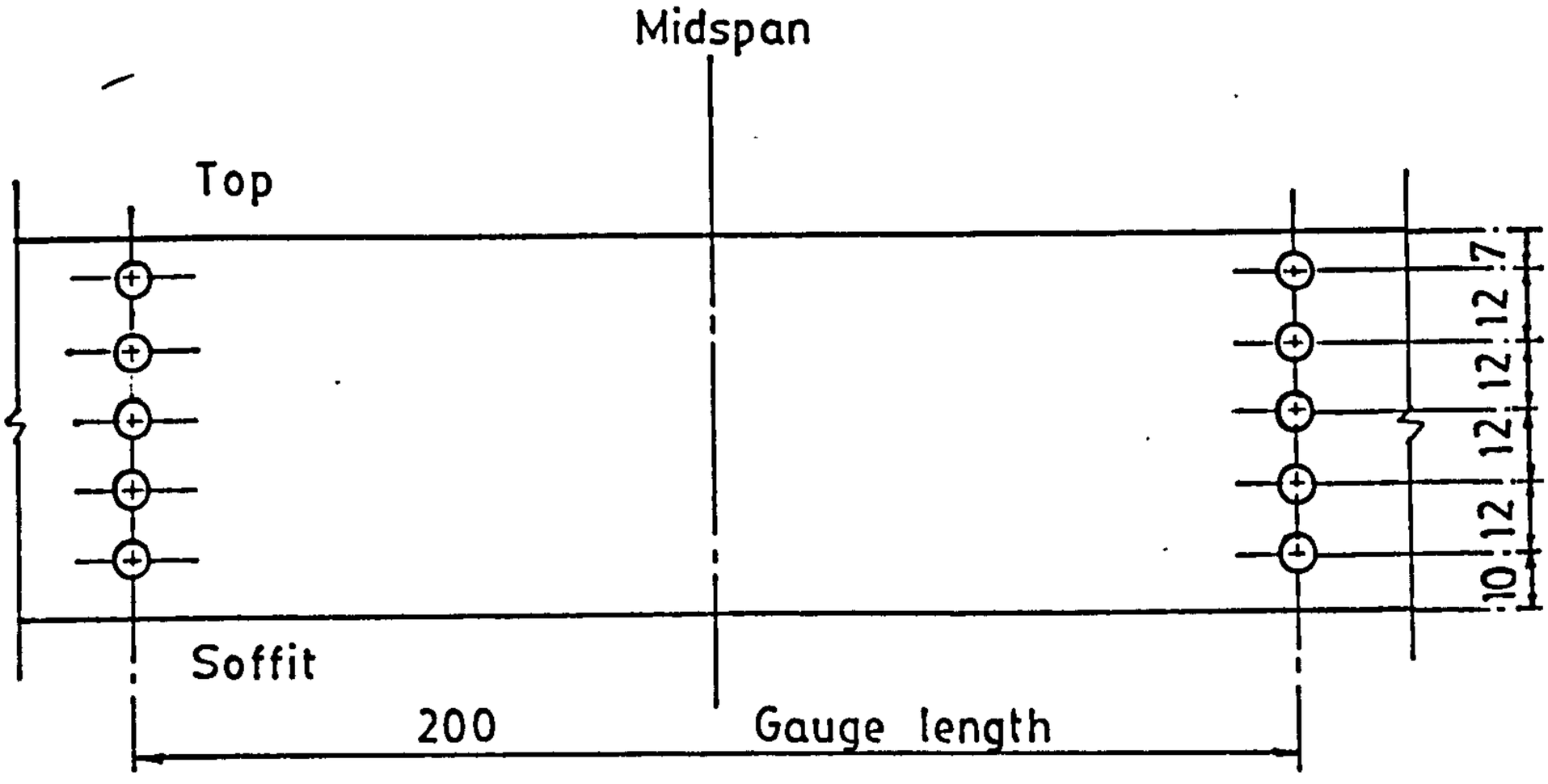

Notes: 1. All dimensions in mm
2. O - Demec stud

FIG. 3.7 DEMEC STUDS POSITIONS

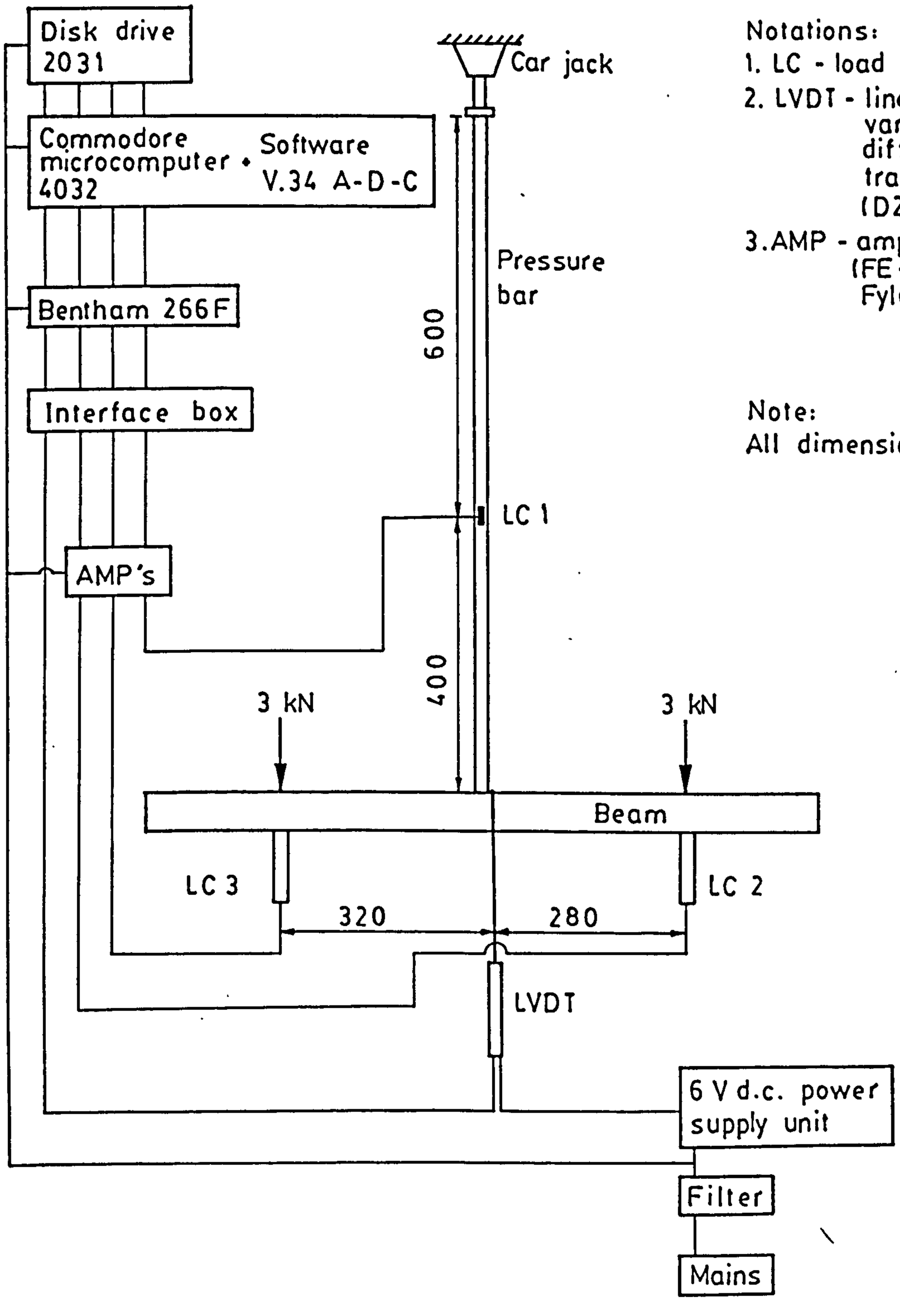

Notations:

1. LC - load cell
2. LVDT - linear variable differential transformer (D2/2000, RDP)
3. AMP - amplifier (FE-359-TA, Fylde)

Note:
All dimensions in mm

FIG. 3.8 GENERAL LAYOUT OF STATIC / POST-IMPACT STATIC TEST

All dimensions in mm

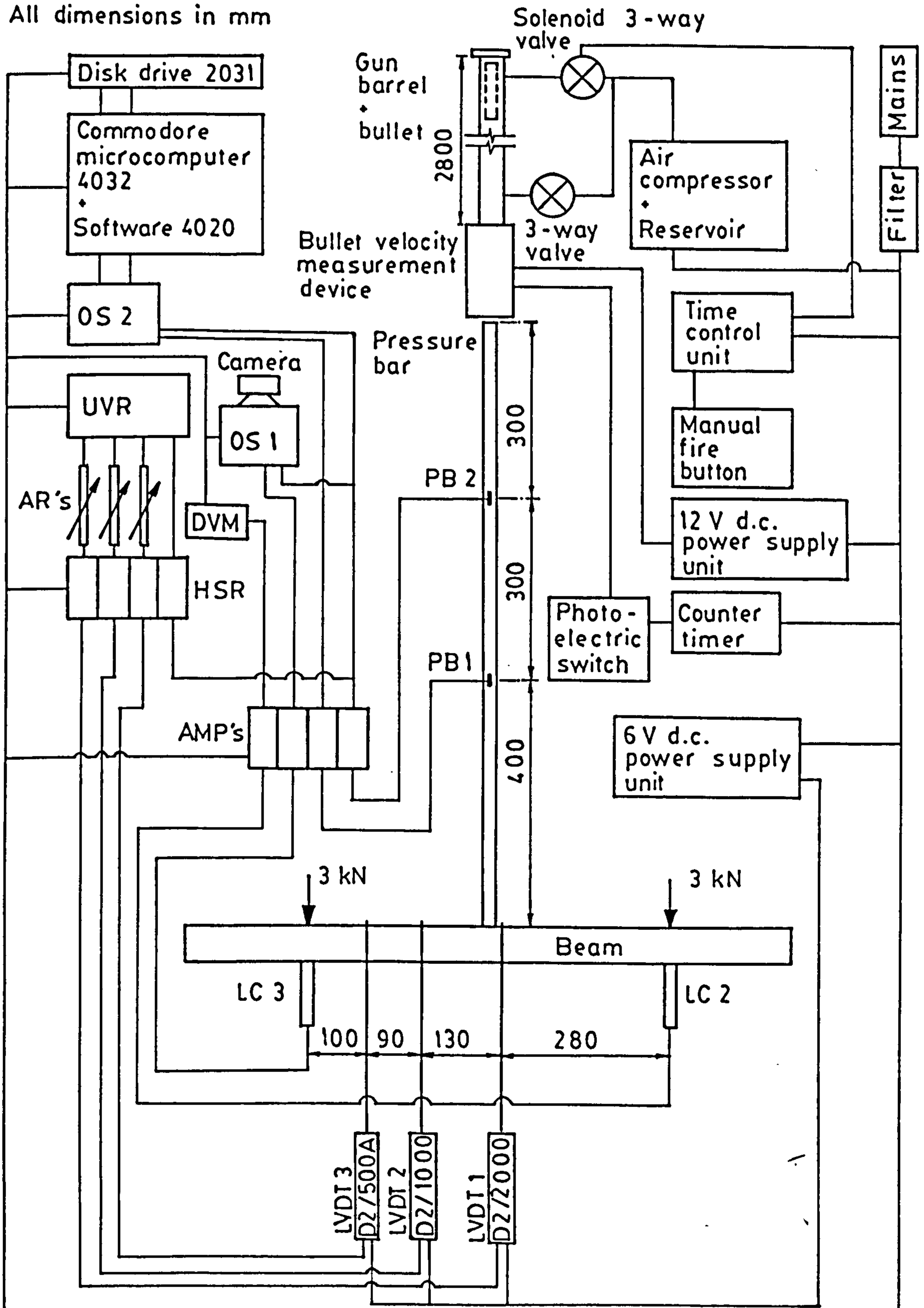

Notations:

1. OS - oscilloscope
   1 - T912, Tekronics
   2 - OS4020, Gould
2. UVR - ultraviolet recorder
3. HSR - high speed tape recorder
4. AR - adjustable resistor
5. DVM - digital voltmeter
6. AMP - amplifier
7. LC - load cell
8. PB - strain gauge station
9. LVDT - linear variable differential transformer

FIG. 3.9 GENERAL LAYOUT OF IMPACT TEST

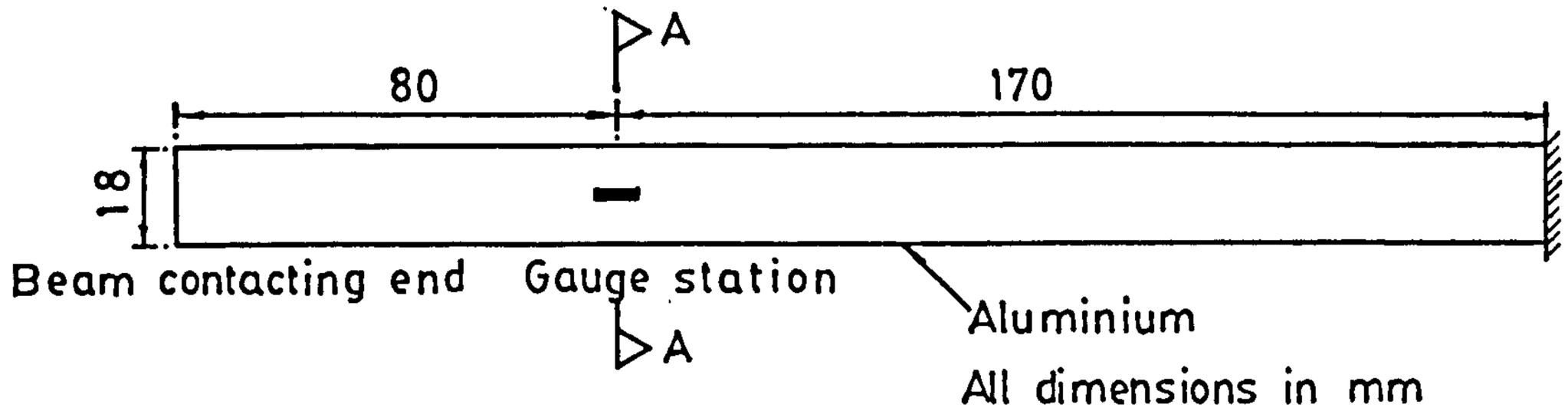

(a) Elevation

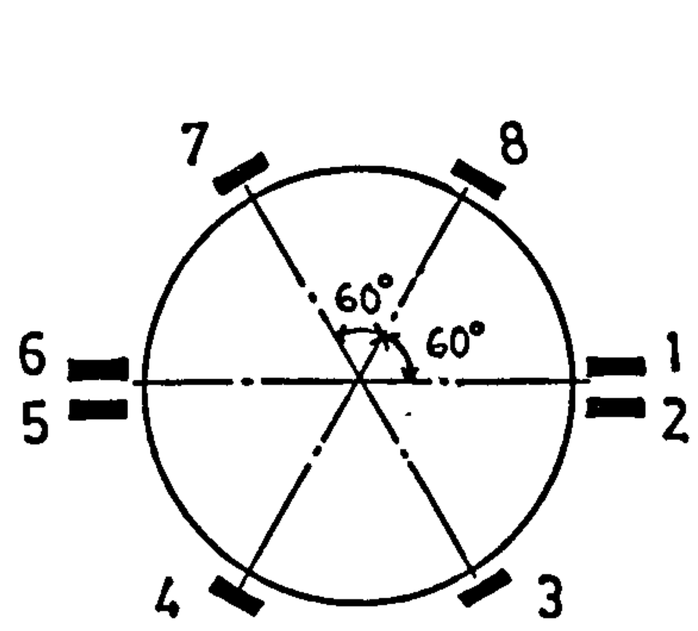

All gauges TML-FLA-3-23

(b) Gauges Orientations
Section A-A

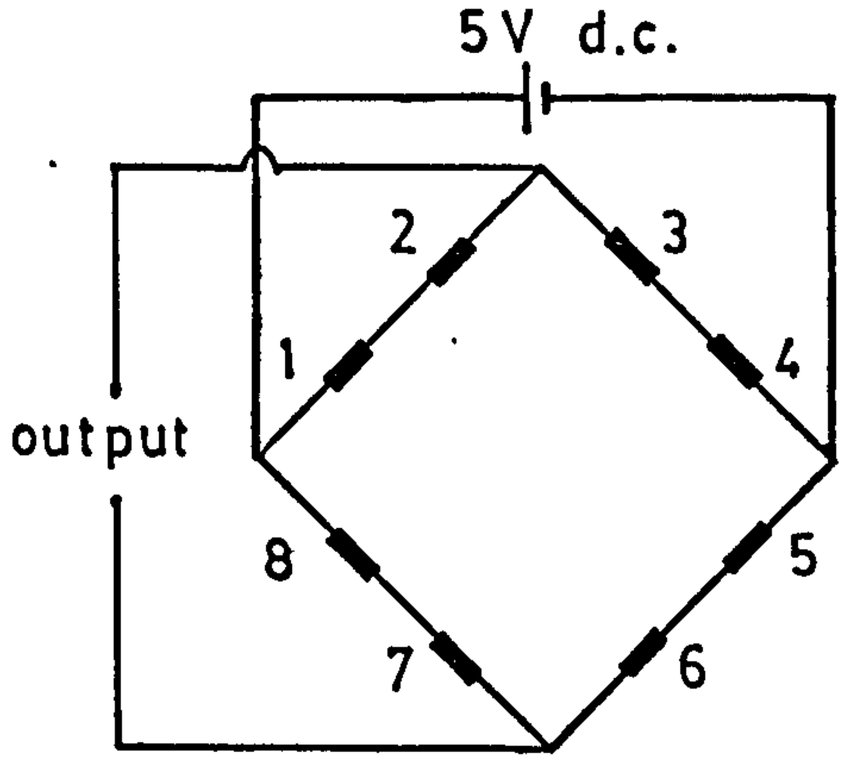

(c) Wheatstone Bridge Circuit

FIG. 3.10 REACTION LOAD CELL - LC 2 / LC 3

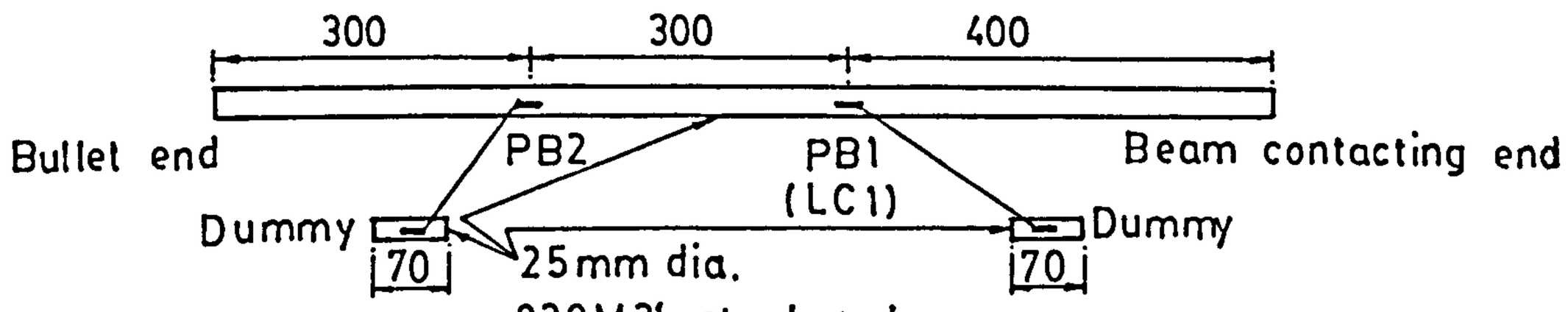

(a) Elevation

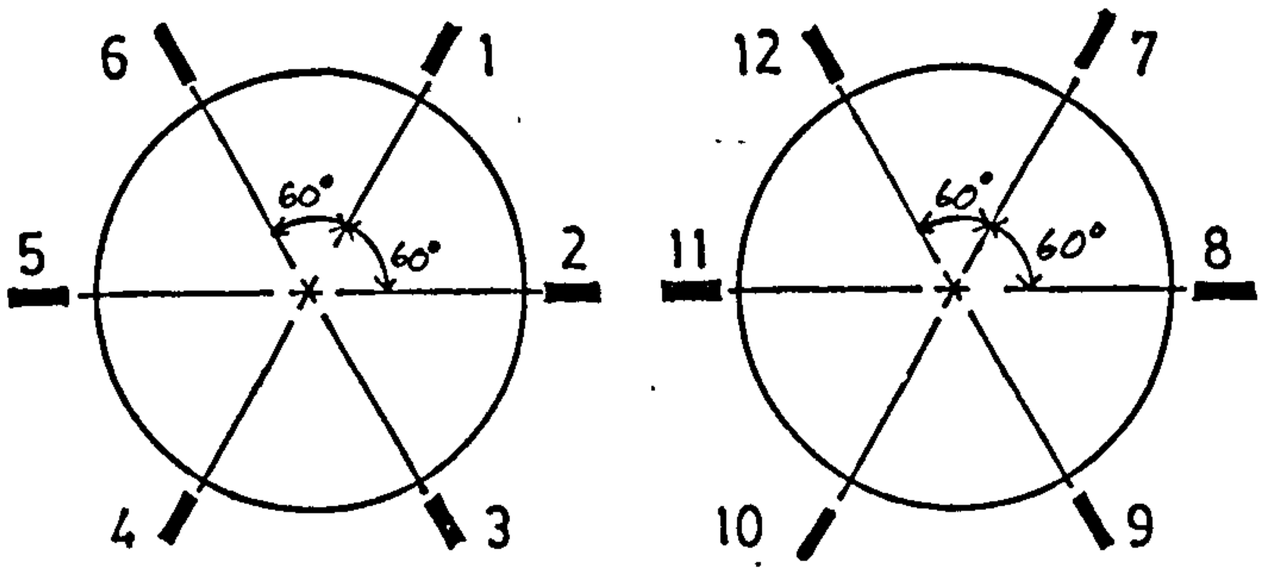

Pressure bar Dummy

All gauges KFC-5-C1-11

(b) Gauges Orientations PB1/PB2

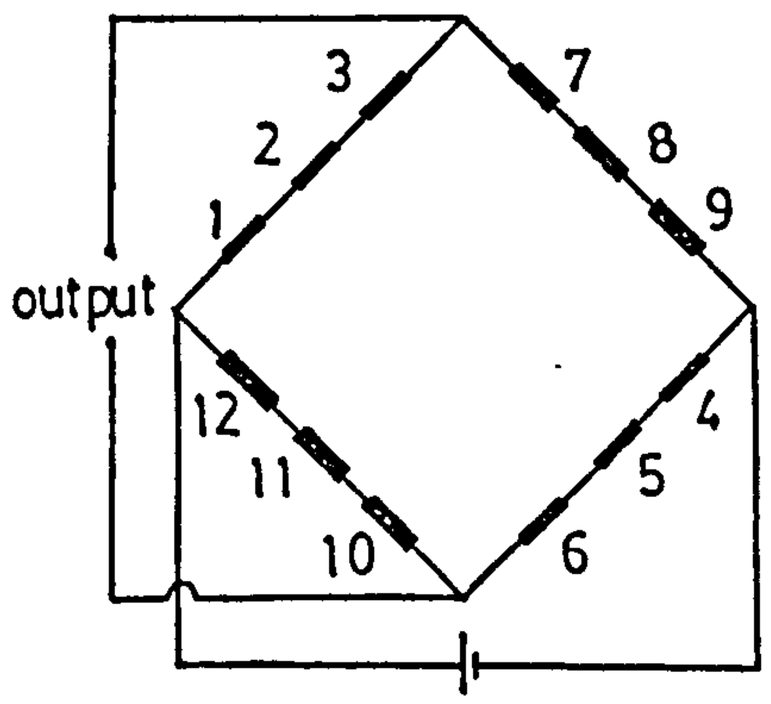

(c) Wheatstone Bridge Circuit

FIG. 3.11 PRESSURE BAR AND STRAIN GAUGES ARRANGEMENT

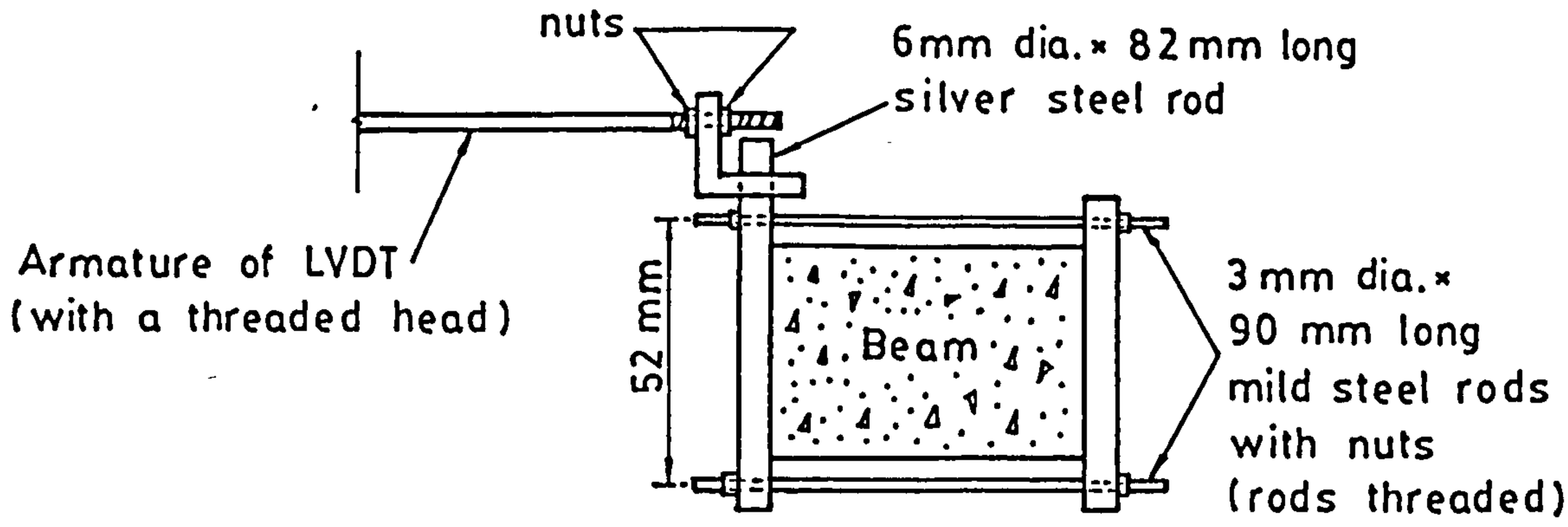

(a) Elevation

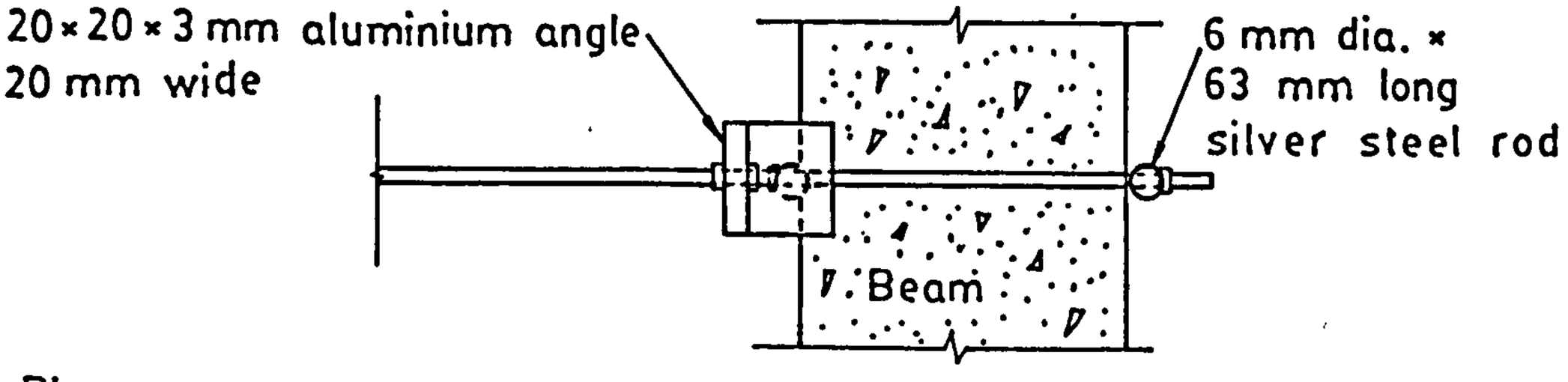

(b) Plan

FIG. 3.12 LVDT/BEAM CONNECTION

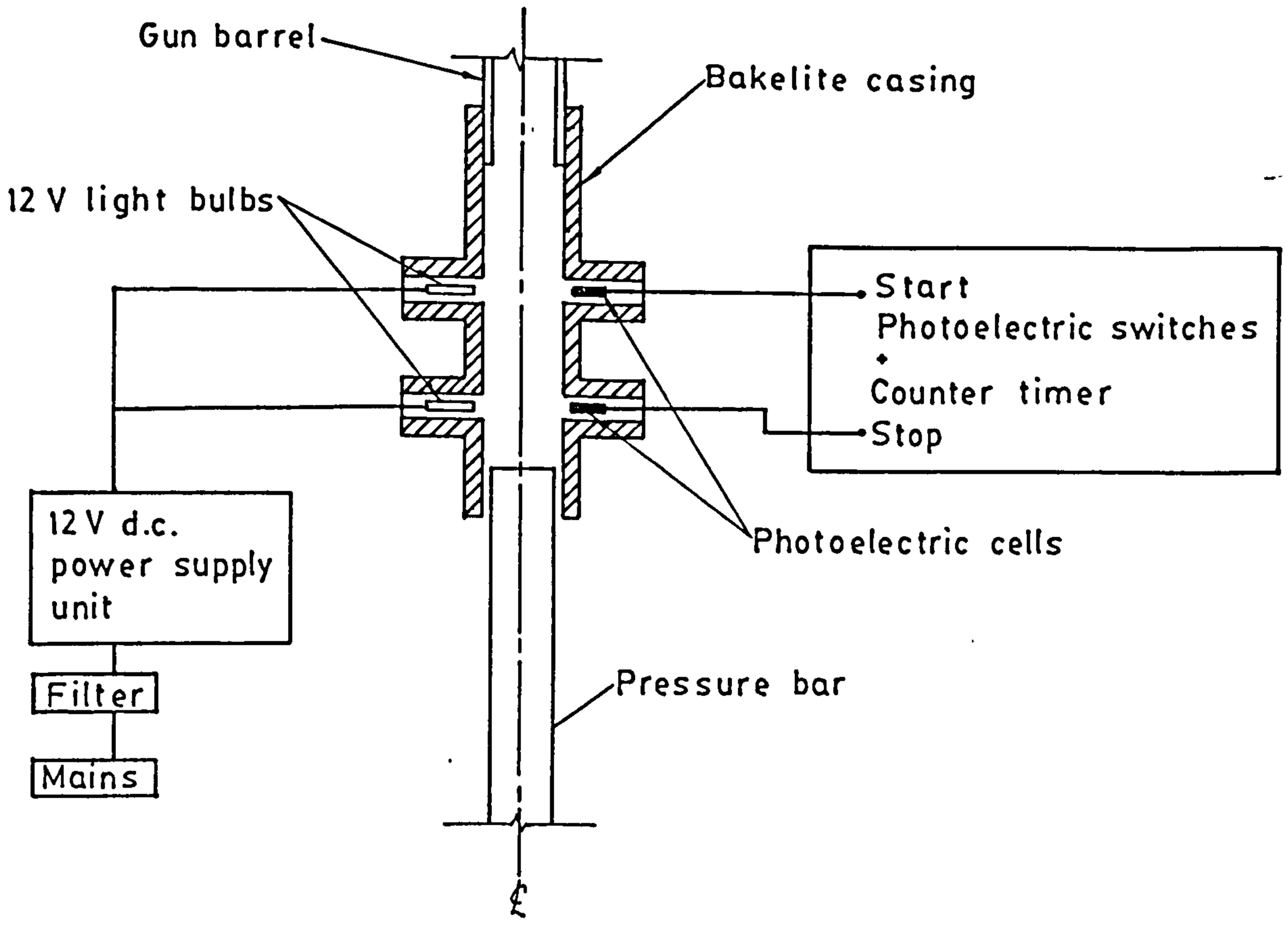

FIG. 3.13 BULLET VELOCITY MEASUREMENT DEVICE

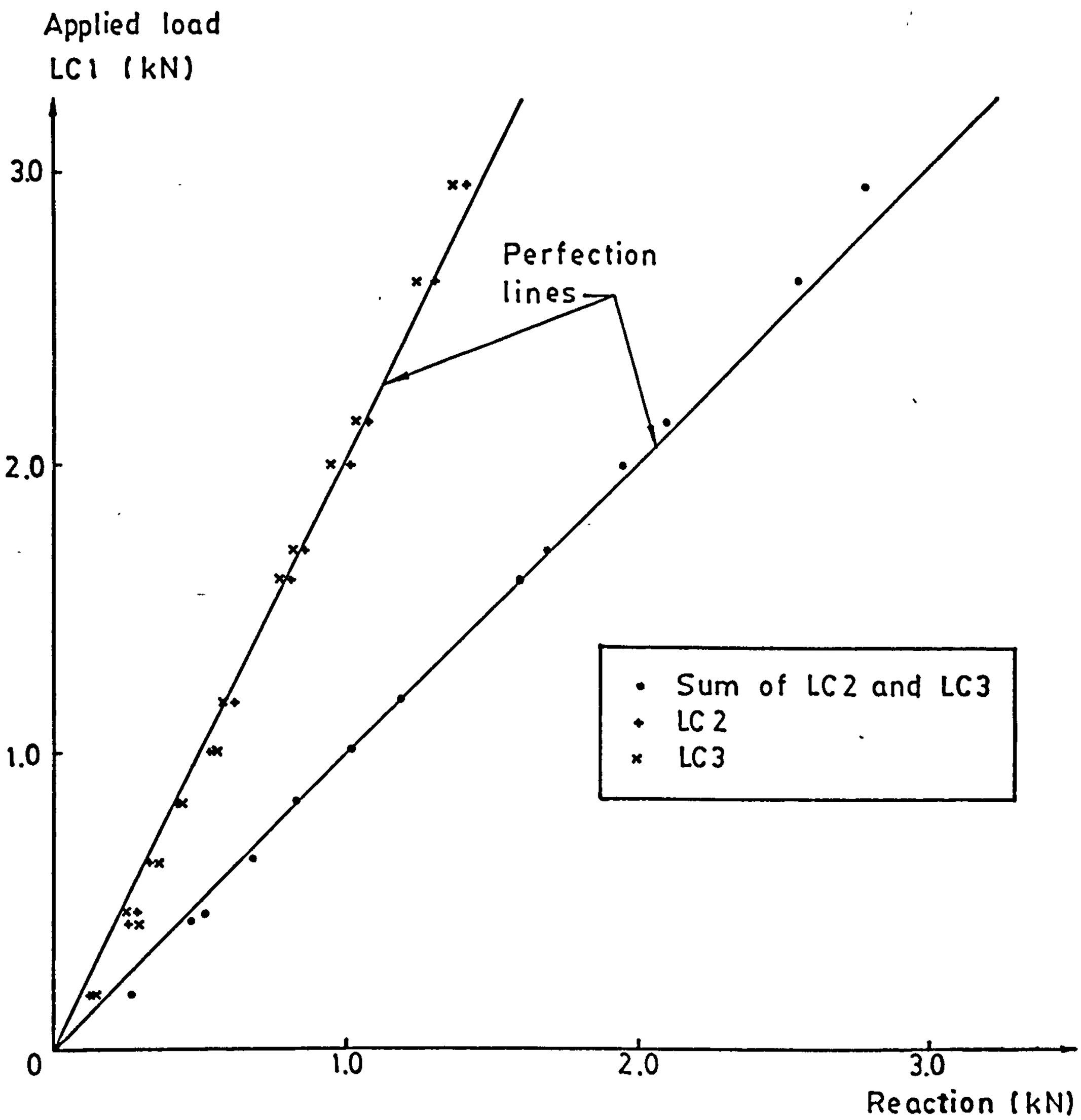

FIG. 3.14 CONSISTENCY TEST RESULTS ON APPLIED LOAD AND REACTION MEASUREMENTS

Series	Beam Number	Stirrup Spacing (mm)	Static Test	Impact Test Air Gun Pressure (psi)	Post-Impact Static Test
1	2 3	40	✓ ✓		
	1 4			15	✓ ✓
	5 6			20	✓ ✓
	7 8			25	✓ ✓
	9 10			30	✓ ✓
2	2 4	80	✓ ✓		
	1 3			15	✓ ✓
	5 6			20	✓ ✓
	7 8			25	✓ ✓
	9 10			30	✓ ✓
3	2 3	20	✓ ✓		
	1 4			15	✓ ✓
	5 6			20	✓ ✓
	7 8			25	✓ ✓
	9 10			25	✓ ✓
4	2 3	10	✓ ✓		
	1 4			15	✓ ✓
	5 6			20	✓ ✓
	7 8			25	✓ ✓
	9 10			25	✓ ✓

Span = 600mm, Pin-Ended for all Beam

TABLE 3.1 EXPERIMENTAL PROGRAMME

Series	Beam Number	(a) fc' (N/mm²) 7-day	(a) fc' (N/mm²) 14-day	(b) f_t (N/mm²) 14-day	(c) m (kg/m) Individual	(c) m (kg/m) Average	(d) P_e (kN)
1	1	32.4	39.9	4.41	-	(e) 6.717	4.44
	2				-		4.63
	3				-		4.44
	4				-		4.44
	5	34.1	38.5	5.43	-		5.02
	6				-		4.93
	7				-		4.93
	8				-		4.73
	9	35.5	40.3	4.96	-		6.56
	10				-		5.49
2	1	29.2	38.5	5.56	-	(e) 6.662	3.19
	2				-		3.19
	3				-		9.28
	4				-		8.30
	5				-		5.65
	6				-		7.53
	7	30.4	37.4	5.68	-		6.37
	8				-		6.95
	9				-		8.70
	10				-		6.37
3	1	38.7	43.5	5.64	-	6.822	10.05
	2				-		9.65
	3				-		9.47
	4				-		9.65
	5	32.4	41.0	5.54	-		5.60
	6				-		5.60
	7				-		5.79
	8				-		7.35
	9	34.5	38.2	5.60	6.800		4.84
	10				6.845		6.09
4	1	32.3	37.9	5.22	6.980	7.032	6.19
	2				7.060		5.12
	3				6.965		6.28
	4				7.095		6.28
	5				7.035		6.28
	6				7.045		7.05
	7	33.3	42.1	5.39	7.050		6.86
	8				7.045		6.47
	9				7.020		6.57
	10				7.030		4.54

AVERAGE 33.9

AVERAGE 39.7

AVERAGE 5.34

Remarks : a - compressive strength, average of three 50mm dia x 100mm cylinder
b - tensile splitting strength, average of three 50mm dia x 100mm cylinder
c - mass per unit length
d - effective prestressing force
e - estimation

TABLE 3.2 MEASUREMENTS PRIOR TO TEST

	Bullet	Pressure Bar	Microconcrete
Young's Modulus E (kN/mm^2)	208.0	208.0	22.3 (Static) 25.0 (Dynamic)
Density ρ (Kg/m^3)	7643	7643	2240
Cross Section Area A (mm^2)	617.1	506.7	Varies
Longitudinal Wave Velocity C_L (m/s)	5217	5217	3340
Impedance $A\rho C_L$ (kg/s)	24606	20204	Varies

TABLE 3.3 MATERIAL PROPERTIES IN ONE-DIMENSIONAL ELASTIC STRESS WAVE THEORY

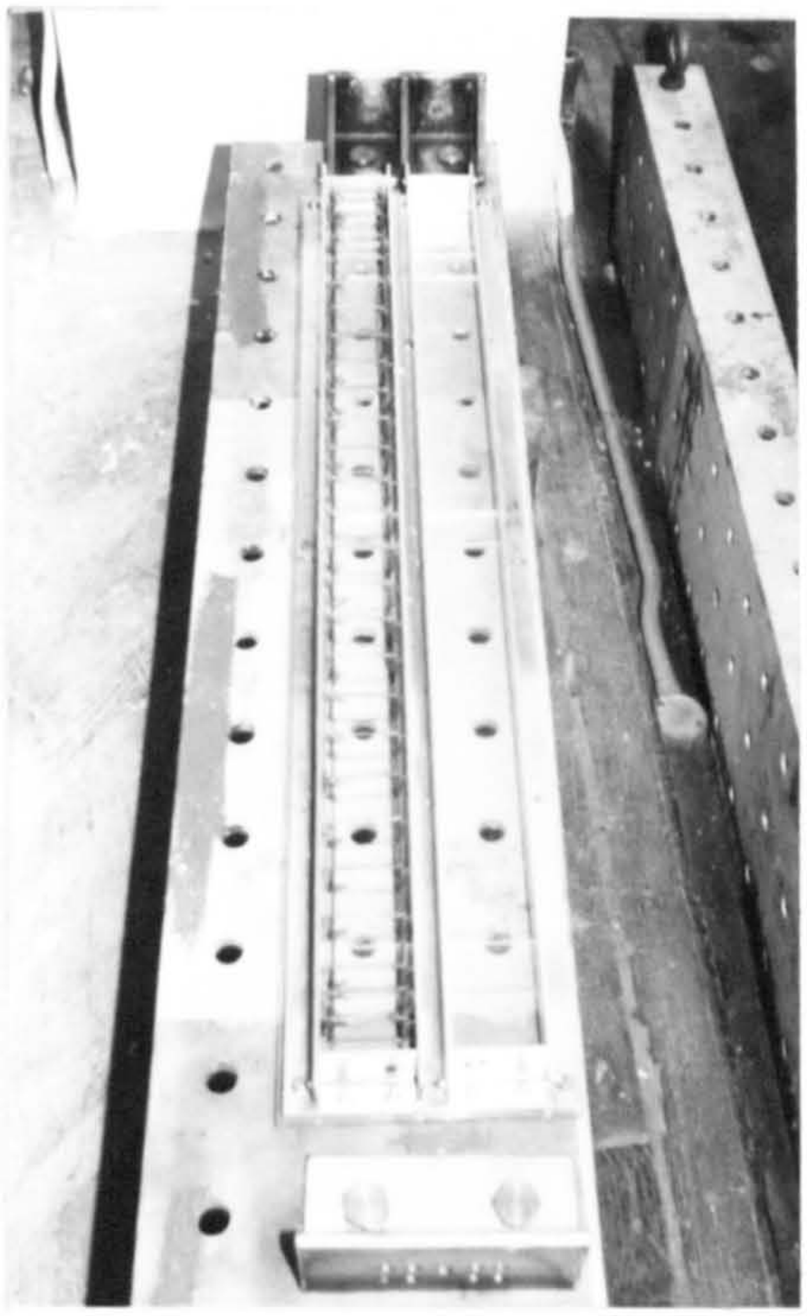

(a) Prestressing Bed

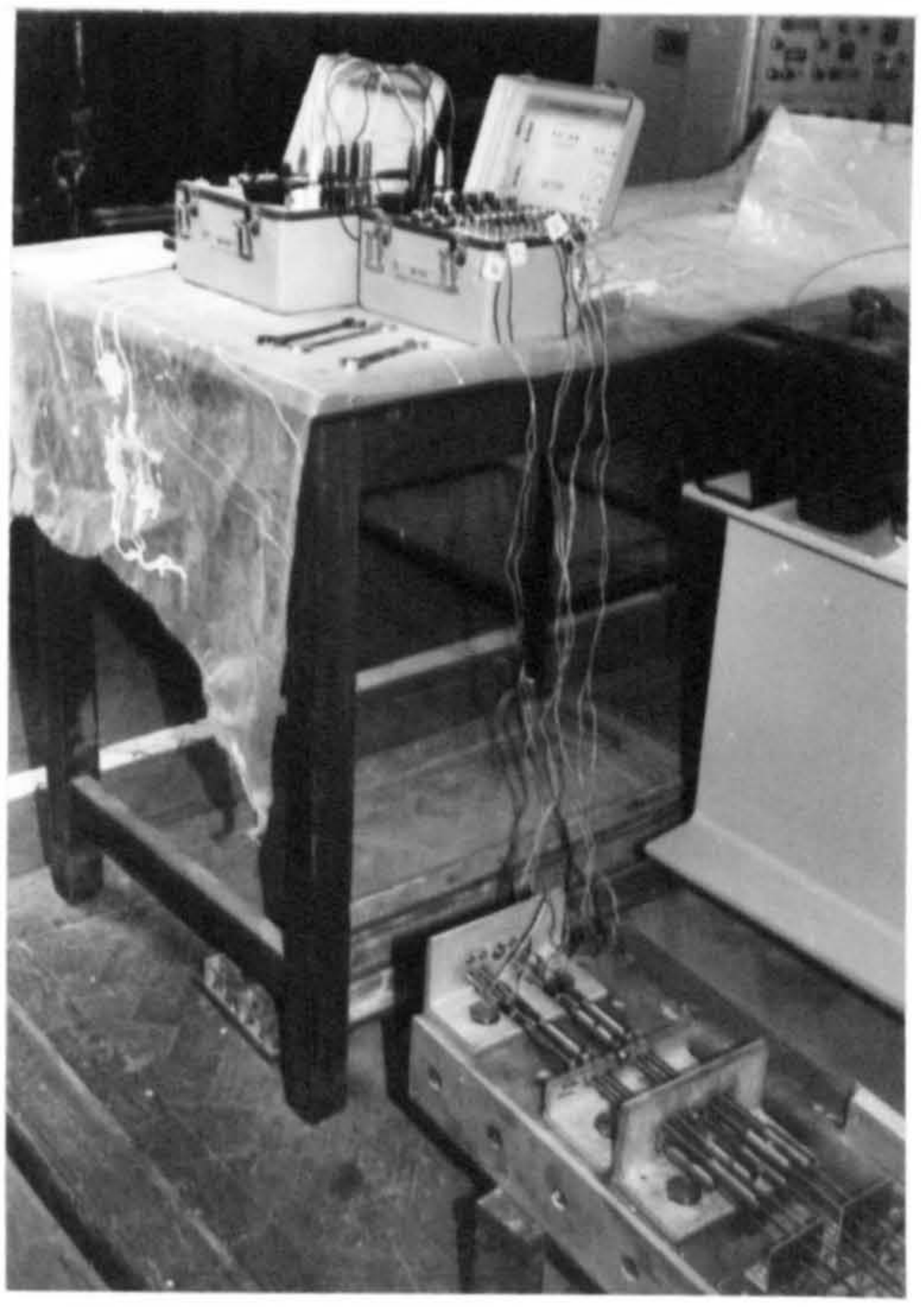

(b) Stressing Equipment

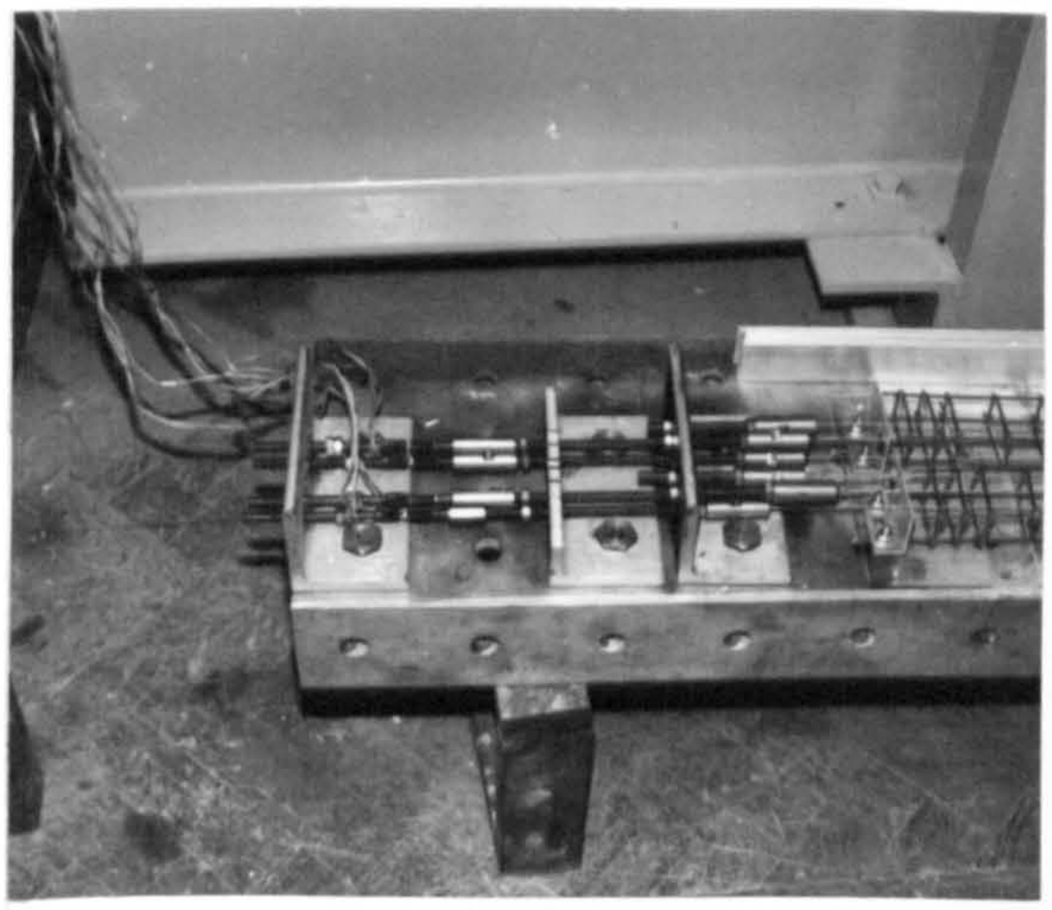

(c) Stressing End

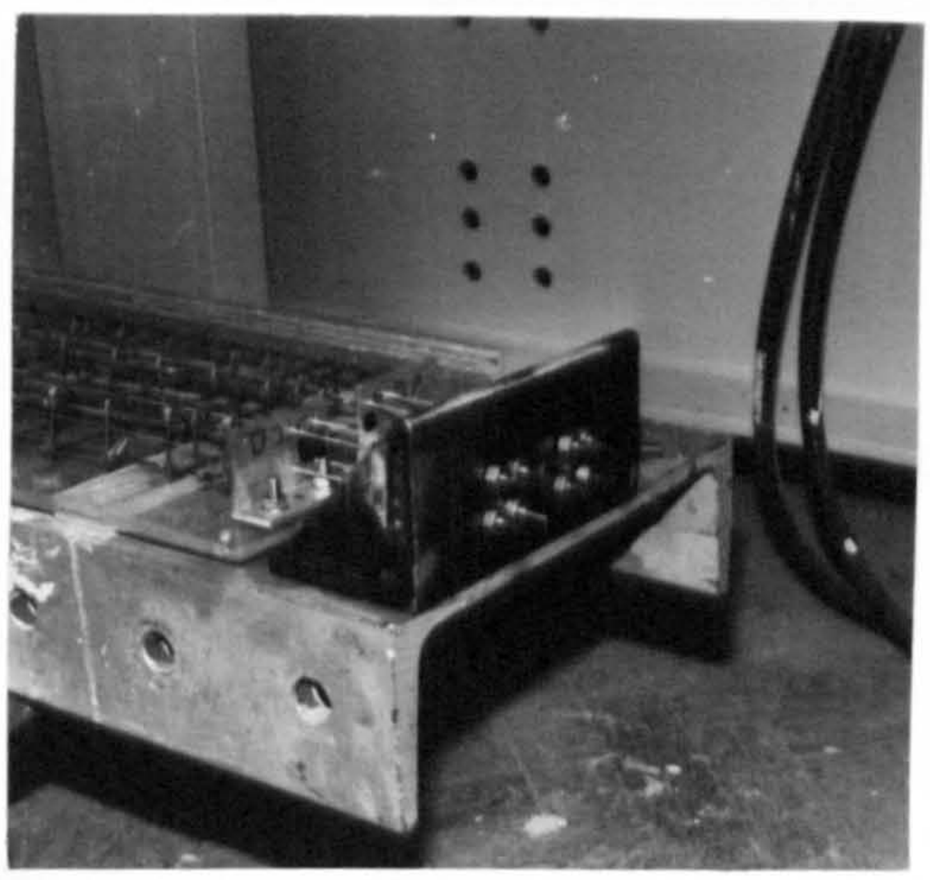

(d) Fixed End

PLATE 3.1 PRESTRESSING EQUIPMENT

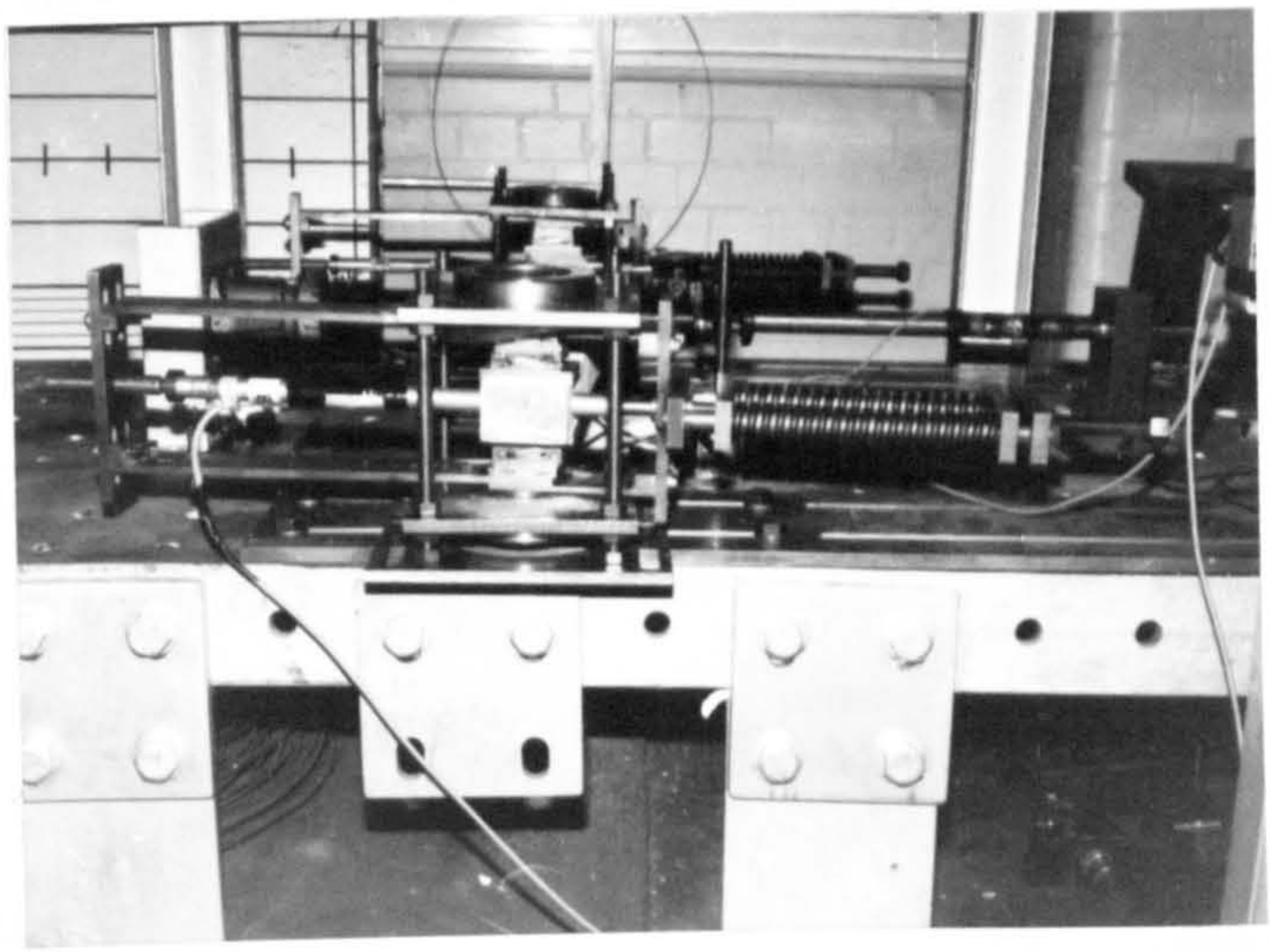

PLATE 3.2 GENERAL VIEW OF THE SUPPORTING TOWER

CHAPTER FOUR

TEST RESULTS

4.1 Introduction

This chapter presents the static, impact and post-impact-static test results. Calibration and material property results are given in chapter 3.

4.2 Static Test

A total of eight static tests were carried out as described in section 3.8. The results are tabulated in table 4.1.

The lowest initial beam stiffness was 1.6 kN/mm and the highest was 3.3 kN/mm. The average of all eight beams was 2.33 kN/mm. The stiffness was maintained until the first flexural crack appeared under the loading point. The stiffness then decreased rapidly and flexural or flexural-shear cracks developed near the loading region up to the ultimate load. The flexural crack under the loading point was always vertical and the largest. The spacing of the cracks was about 40 mm for all series (plate 4.1a).

Beyond the ultimate load, there was little further deflection before the prestressing tendons either fractured or slipped suddenly. This was marked by the sudden drop in load in the load-deflection curve (fig. 4.1) except for beams 1.3 and 2.2. For these two beams, the tendons slipped at the early stage and the residual bond strength was responsible for maintaining load support.

The area under the load-deflection curve was used to determine the energy absorption capacity. Since beam 3.2 had the highest ultimate load carrying capacity (5.98 kN) which was the closest to that predicted (table 5.1), it was used to estimate the maximum energy absorption capacity for all beam. The area measured was 40.0 J.

The load-deflection curve of each beam is given in appendix A.

4.3 Impact Test

A total of 32 beams were impacted as described in section 3.8. The results of these impact tests were tabulated in table 4.2. Observations and findings are presented in this section.

4.3.1 Incident Impact Pulse and Force

The incident pulse in all the impact tests was measured as decribed in section 3.7.4.and had the shape of a trapezium as shown in figures 4.2a and 4.2b. The average duration was 164 μs and the rise time (10 % - 90 %) was 22 μs. It was found that the magnitude of the incident force varied linearly with the impact velocity (fig. 4.3) and had an empirical relationship

$$\text{incident force, } F_I = 11.6 \times \text{impact velocity, } v \qquad \text{equ. 4.1}$$

where F_I was in kN and v in m/s.

The individual force-time (pulse) trace is in appendix B.

4.3.2 Crackings

There were two basic types (flexural and shear) of cracks in four different appearances. They were flexural, punching shear (shear), flexural shear and inverted flexural cracks, in the order of appearance moving from the impact point towards the supports (fig. 4.4). The flexural shear crack seemed to be initiated by an inverted crack in most cases.

For similar shear reinforcement spacing, more cracks and a higher degree of crushing up under the impact point occurred at the higher impact velocity.

For similar impact velocity, the total number of cracks was higher but the crack widths were smaller when the shear reinforcement spacing was small. This phenomenon was also reported by Ang[34].

Plates 4.1b and 4.1c give the typical crack pattern with and without the punching shear plug. This plug was bounded by two shear cracks which

inclined at an angle of about 45° to the soffit. The plug width on the impact face was slightly larger than 25 mm (the diameter of the pressure bar) and had a value of 28 ± 2 mm. The plug width at the opposite face was 180 ± 20 mm. The size of the plug seemed to have no relationship to the amount of shear reinforcement. From table 4.2 that this plug formed if the bullet energy was higher than about two and a half times the static beam energy absorption capacity (section 4.2).

The crack pattern of each beam is presented in appendix C.

4.3.3 Transient Deformation

A typical LVDT's record and deformation profile are shown in figure 4.5. The deformation profile showed that there were two reverse bending regions about 200 mm on either side of the point of impact and beyond which the beam remained stationary at the early stage. This mode of deformation has been observed by many investigators (section 2.5). At a later stage, these two reverse bending regions disappeared and the beam deformed as if it was loaded statically and with a plastic hinge at the centre.

The peak deflection at midspan was plotted against the impact velocity both in linear and logarithm scale (figs 4.6a and 4.6b). The empiric relationship found was

$$\text{peak dynamic deflection, } Z_{max} = 0.092 \times (\text{impact velocity, } v)^2 \qquad \text{equ. 4.2}$$

where Z_{max} in mm and v in m/s.

The initial beam velocity was found to be linearly proportional to the impact velocity (fig. 4.7) for each individual series.

The recovery of the beam as a percentage of the peak deflection is plotted against the bullet energy in figure 4.8 and it shows that there was a better percentage of recovery at lower bullet energy.

Individual set of LVDT's traces and deformation profile are given in appendix D.

4.3.4 Transient Reaction

The reaction traces were similar in all the test series using different impact velocities. A typical result is shown in figure 4.9 and the individual traces can be found in appendix E. The negative (uplift) reaction had a magnitude of 2.6 ± 0.2 kN at a time 0.5 ms after trigger. i.e. time = 0 when the wavefront of the incident pulse reached the gauge station PB2 on the pressure bar (section 3.7.4) and time = 0.13 ms when this wavefront arrived at the pressure bar/ beam interface. The maximum reaction was 4.7 ± 0.3 kN and occurred at 2.0 ms. After this, the reaction dropped linearly to nearly zero. At about 3.8 ms, it rose again until it reached 2.3 kN at 6.0 ms. This value was maintained for about 2 ms. It then fell to zero at 10 ms and oscillated about the time axis.

4.3.5 Other Observations

It was difficult to inspect the tendons after impact because in most cases they were not visible. The number of tendons which either slipped or fractured is recorded in table 4.2 and were those which were either visible or the condition was estimated from the post-impact-static test load-deflection curves (section 4.4)

There was a sign of local damage (crackings) at the point of impact.

4.4 Post-Impact-Static Test

A post-impact-static test was carried on each impacted beam (section 3.8) and the results are shown in table 4.3. The individual load-deflection characteristics can be found in appendix F.

All the impacted beams had a constant stiffness up to the point just below the ultimate load. Beams 2.4, 3.1 and 3.4 developed additional flexural cracks. Once the ultimate load was reached, it either remained unchanged or decreased gently as the deflection increased (fig. 4.10), except for beams 2.3, 2.5, 2.6, 4.4, 4.6 and 4.7. For these beams, there was a sudden drop in load, which indicated that there was further tendon slip or fracture.

The stiffness, as a percentage of initial beam stiffness before impact, and

the peak strength were plotted against the bullet energy in figures 4.11 and 4.12. These figures indicated that

(a) for similar bullet energy, the smaller the shear reinforcement spacing, the higher was the percentage of the initial stiffness preserved,

(b) the higher the bullet energy, the lower was the peak strength and beam stiffness.

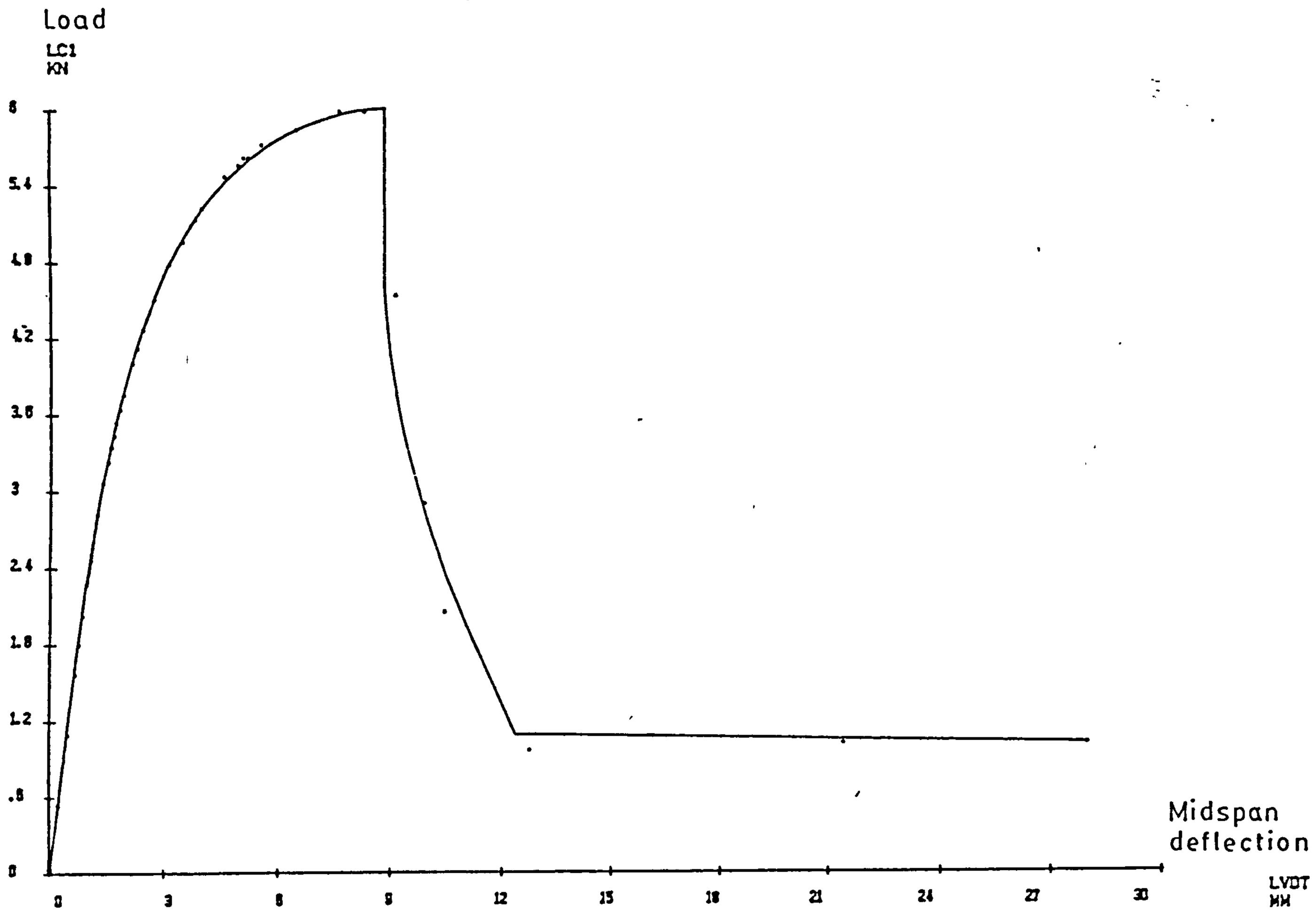

FIG. 4.1 LOAD-DEFLECTION CURVE OF BEAM 3.2 - STATIC TEST

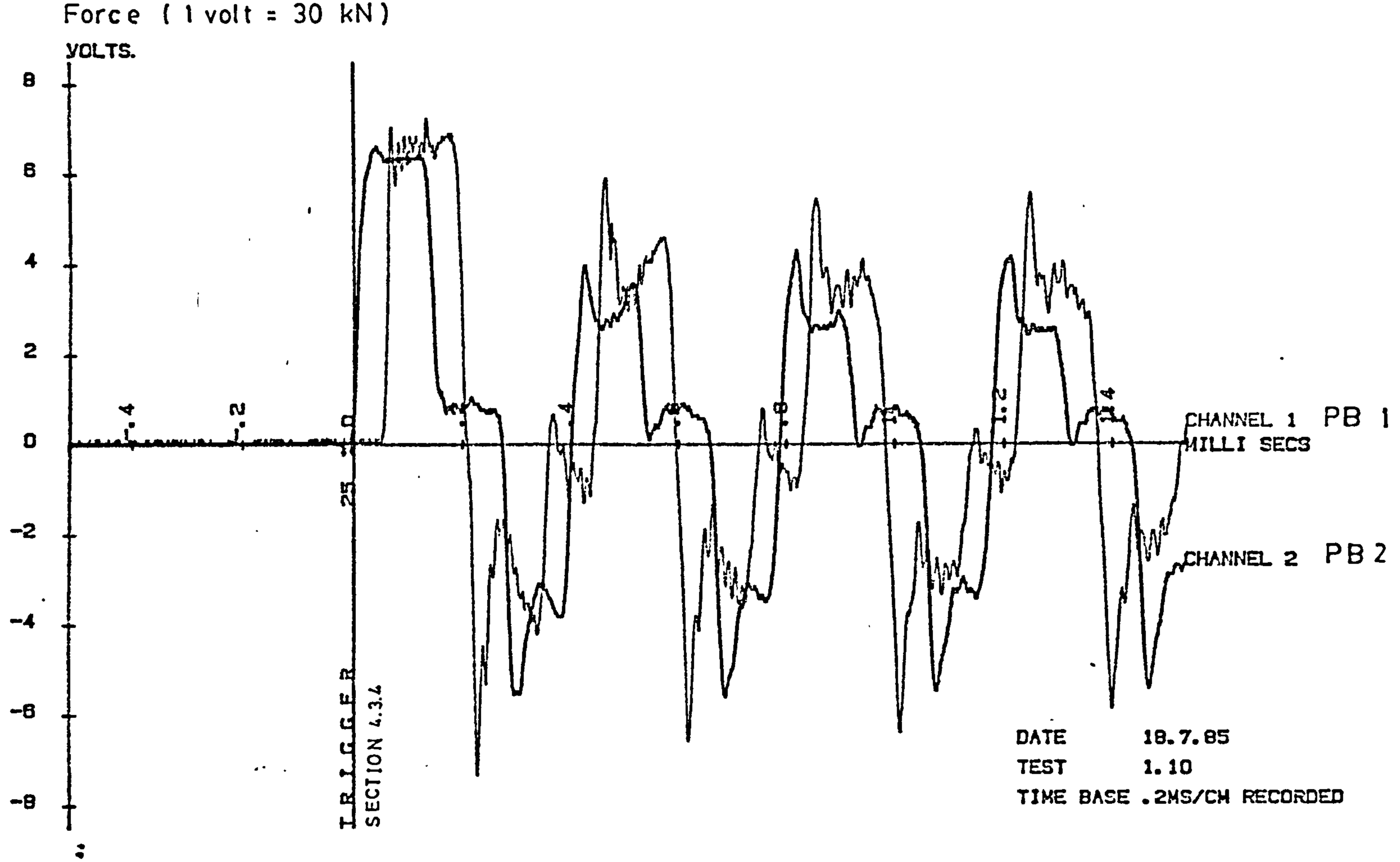

FIG. 4.2 (a) IMPACT PULSE TRACE

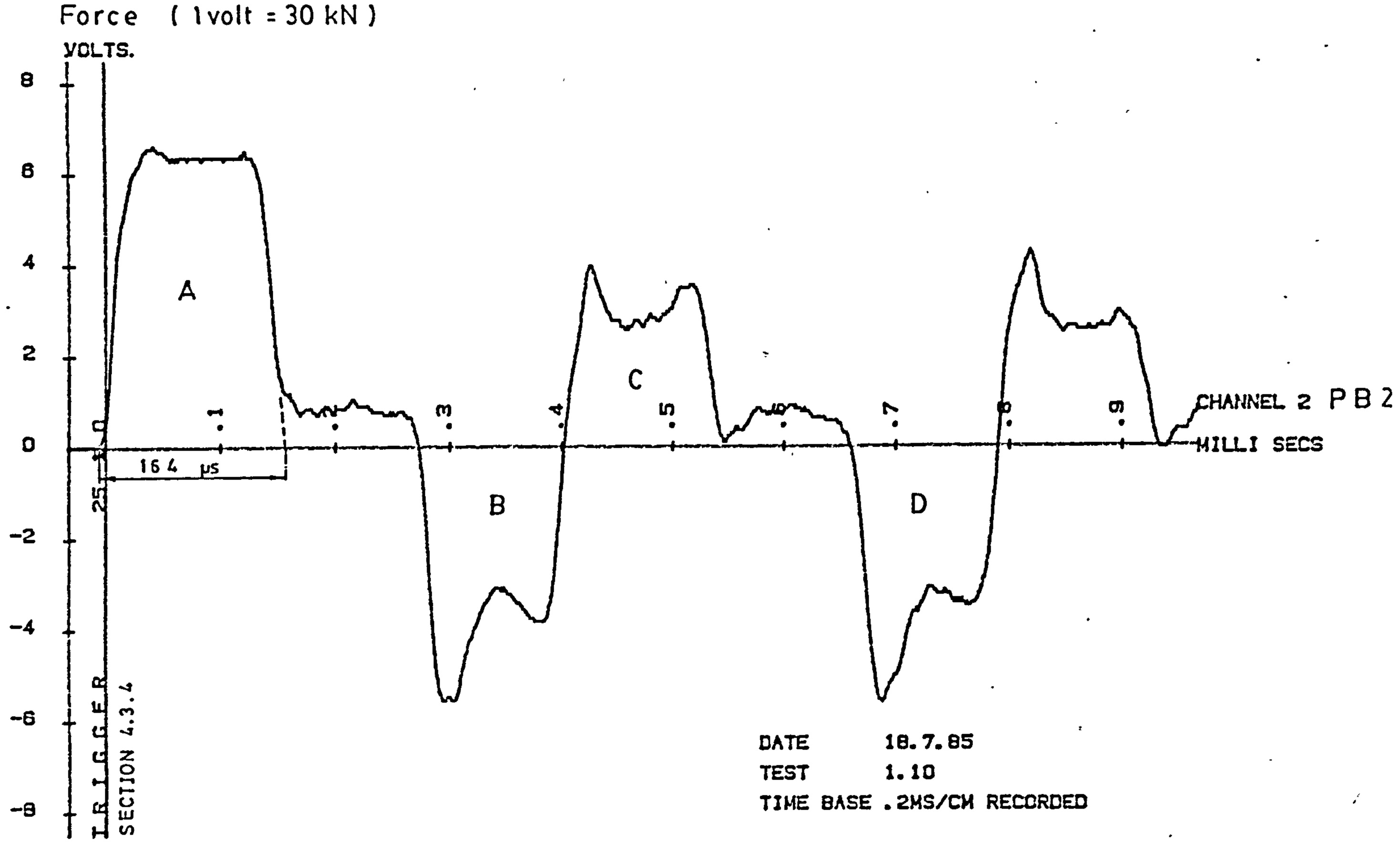

FIG. 4.2 (b) IMPACT PULSE TRACE

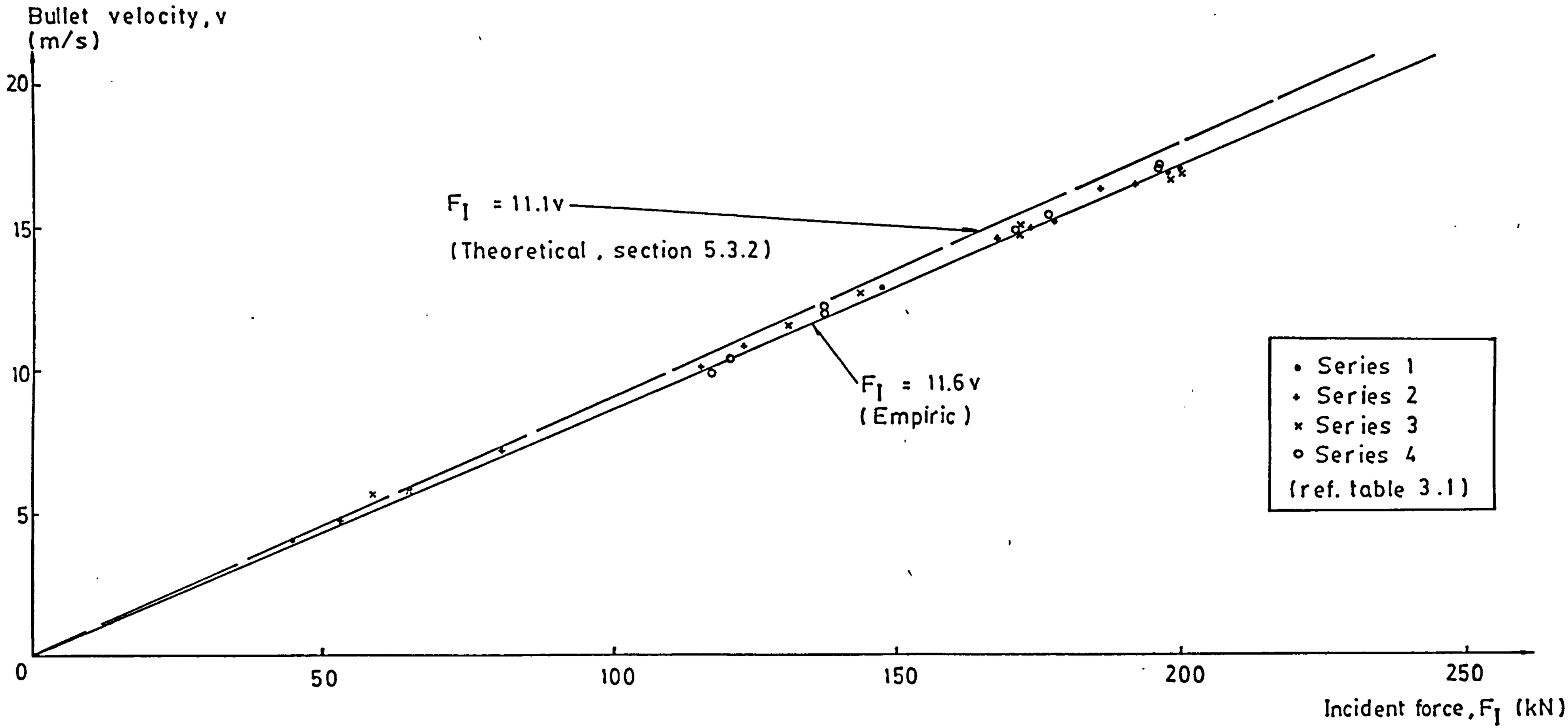

FIG. 4.3 BULLET VELOCITY AND INCIDENT FORCE RELATIONSHIP

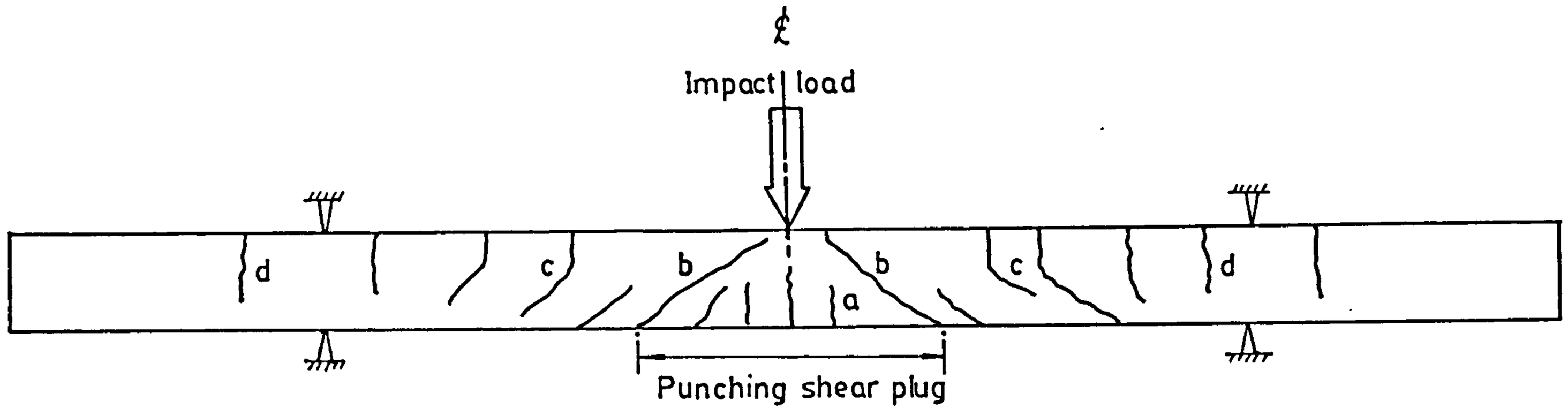

Notes : 1. Crack classification
a. - flexural
b. - shear
c. - flexural shear
d. - inverted flexural

FIG. 4.4 CRACK CLASSIFICATION

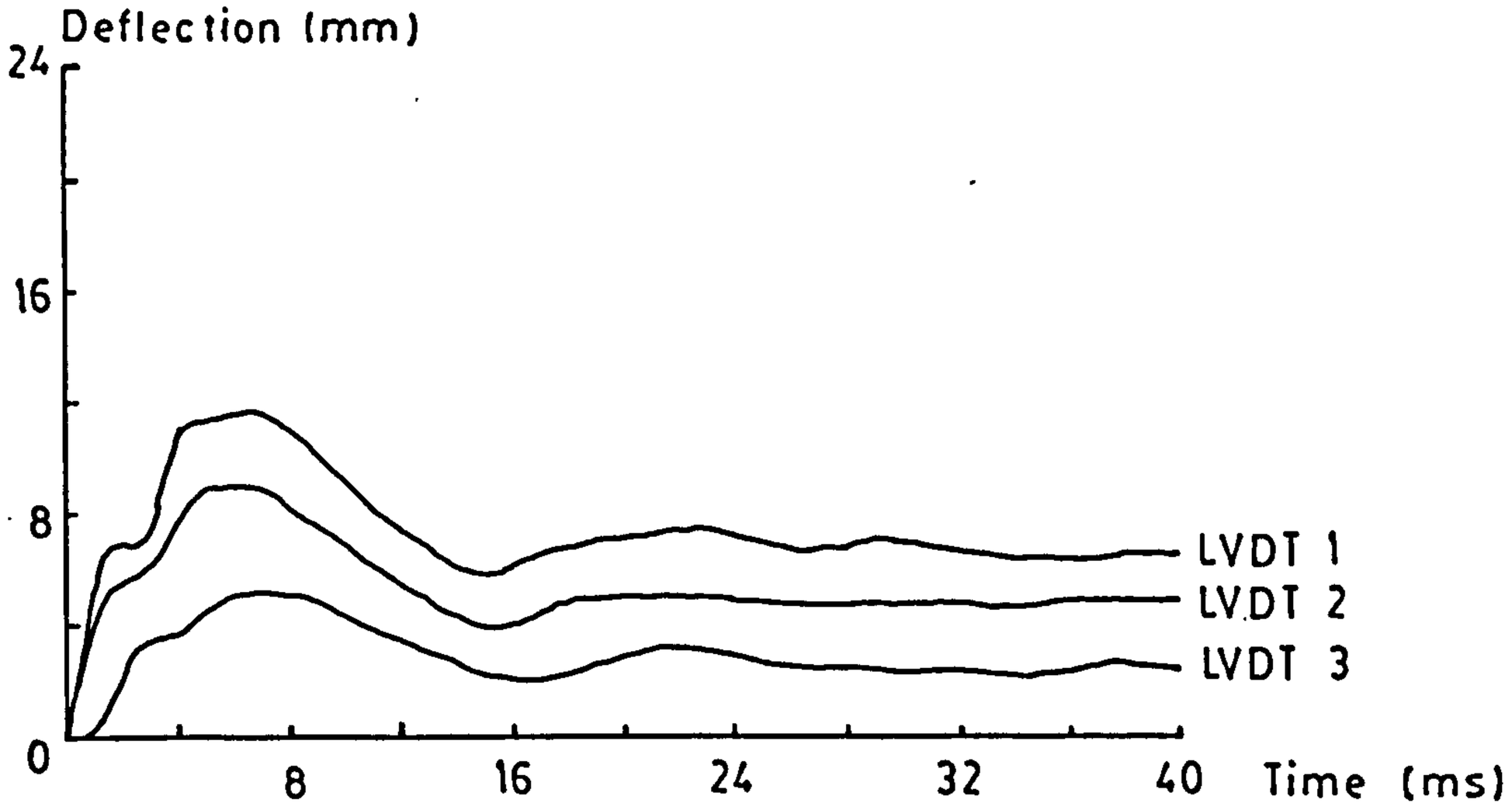

(a) LVDT record

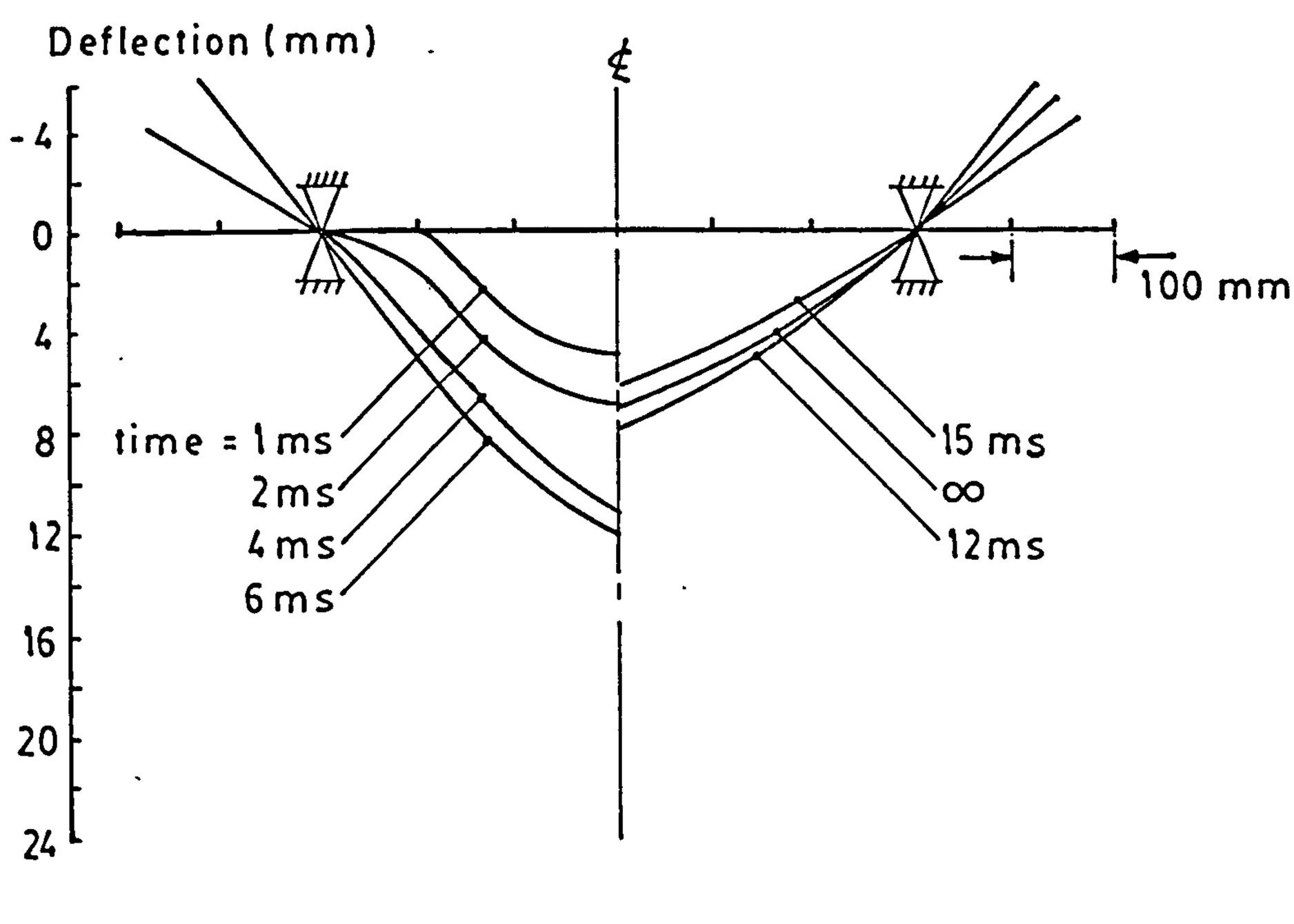

(b) Deformation profile

Notes:
1. Time = 0 at trigger (section 4.3.4).
2 Positions of LVDT's refer to fig. 3.9.

FIG. 4.5 LVDT RECORD AND DEFORMATION PROFILE OF BEAM 1.5 - IMPACT TEST

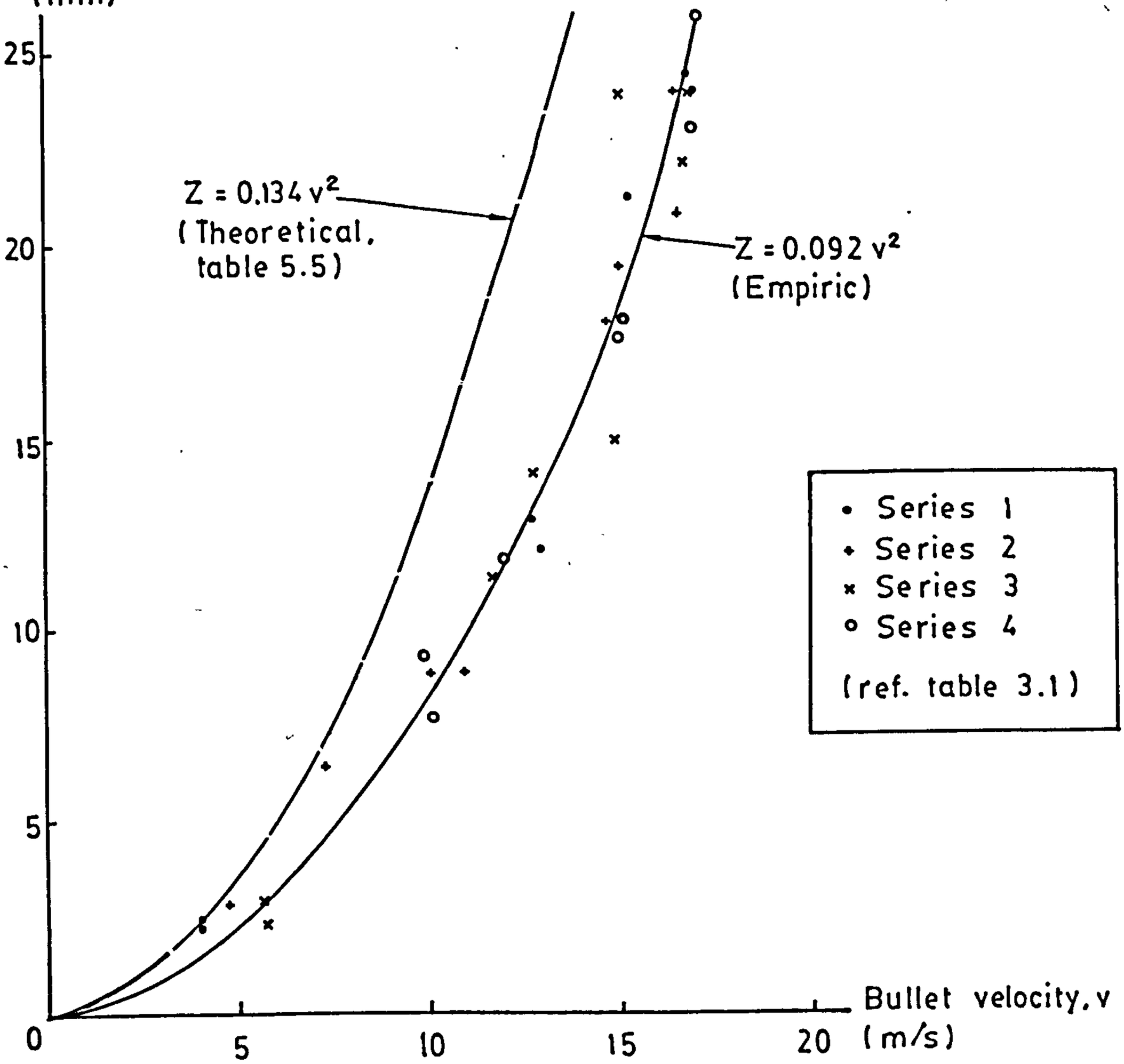

(a) Normal scale

FIG. 4.6 PEAK DYNAMIC DEFLECTION AT MIDSPAN AND BULLET VELOCITY RELATIONSHIP

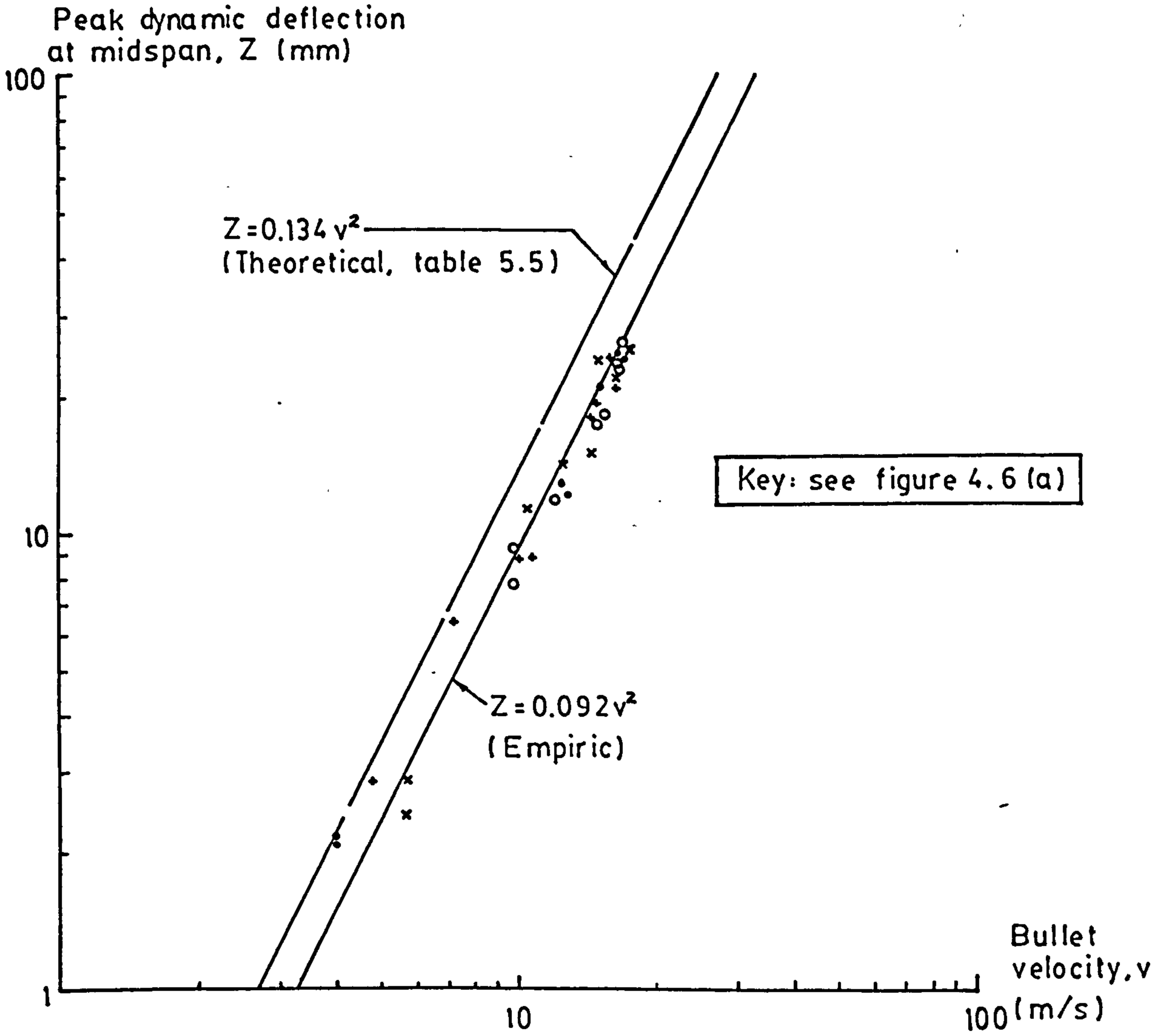

(b) Log. scale

FIG. 4.6 PEAK DYNAMIC DEFLECTION AT MIDSPAN AND BULLET VELOCITY RELATIONSHIP

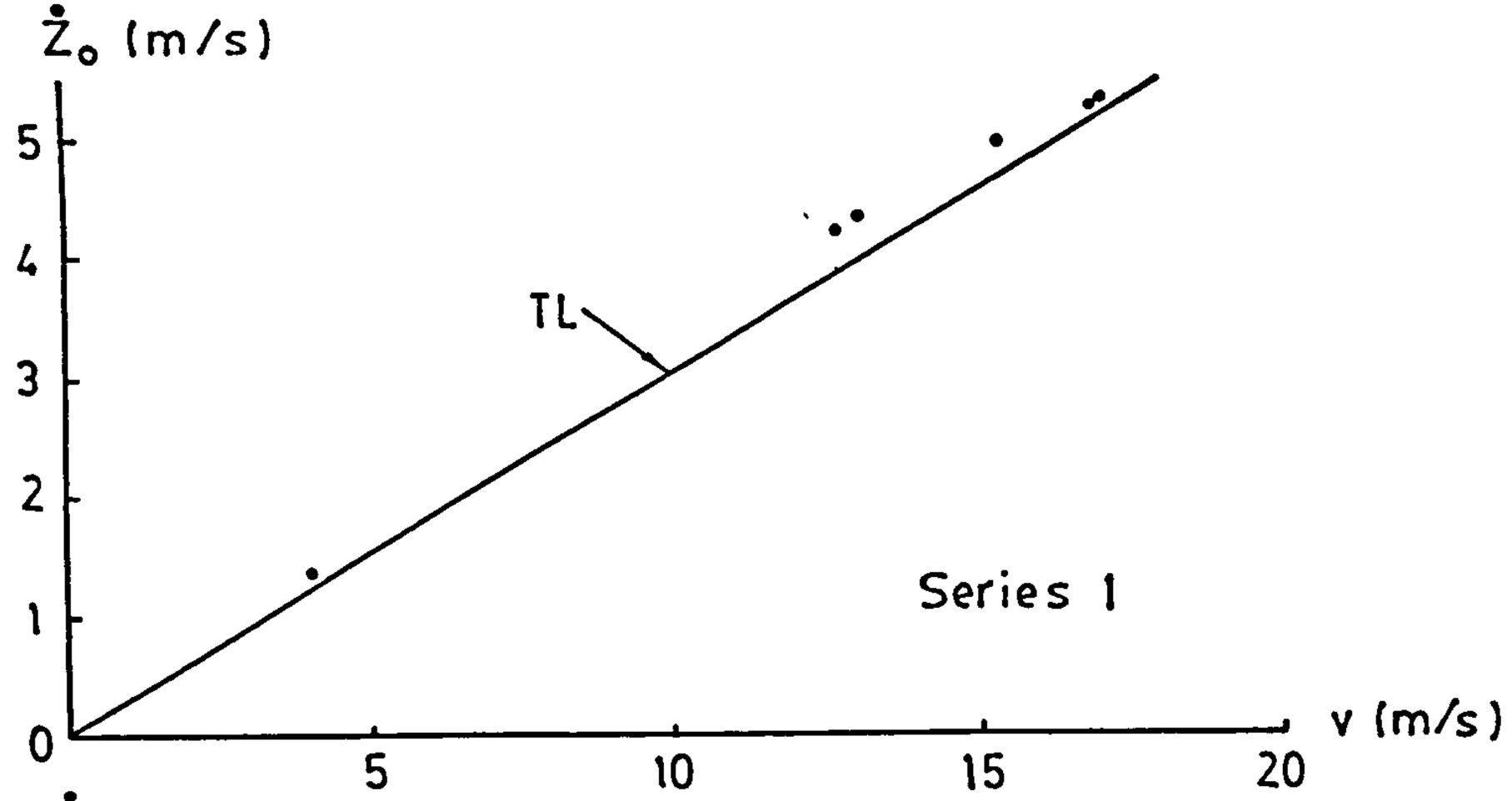

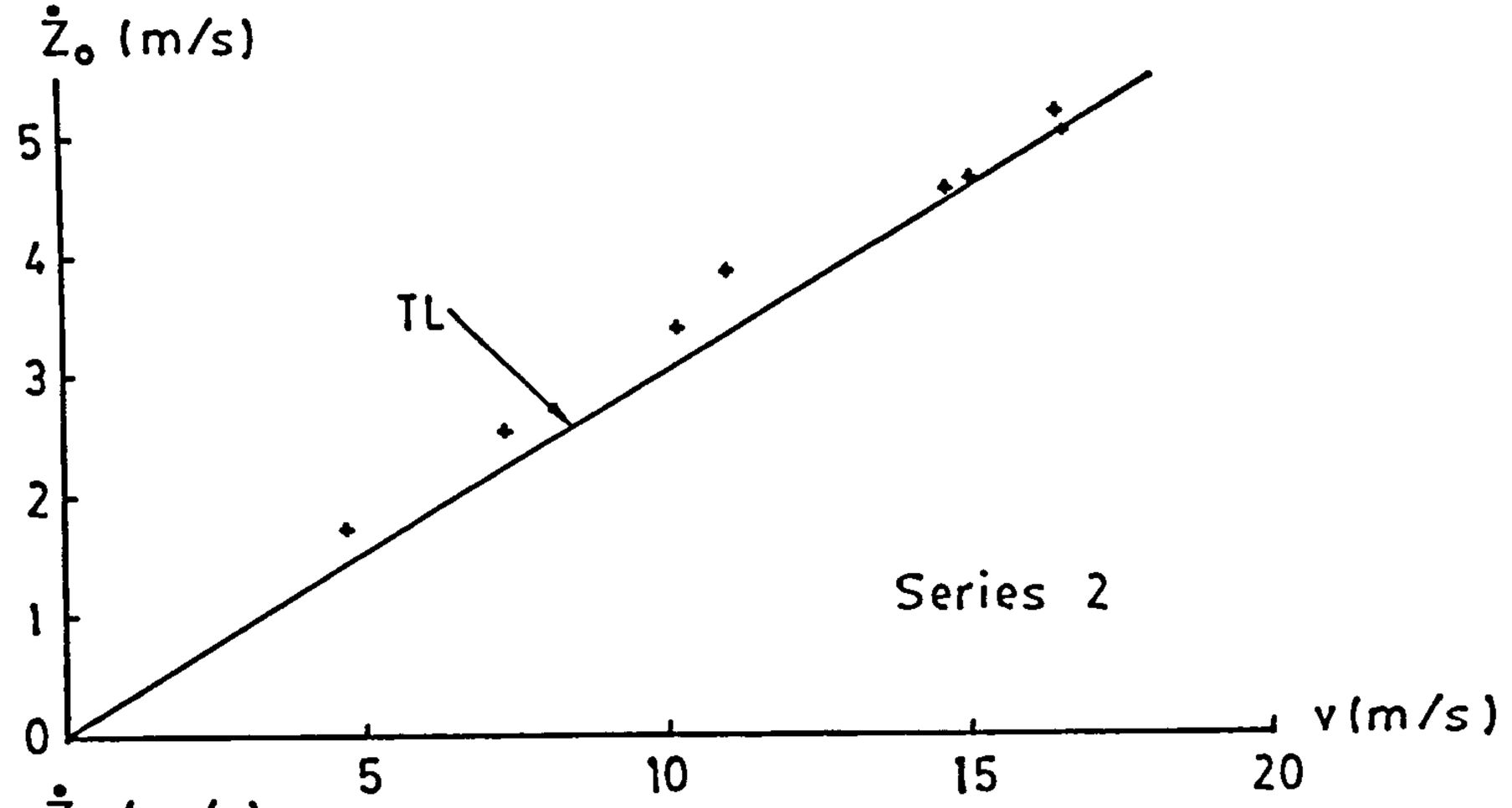

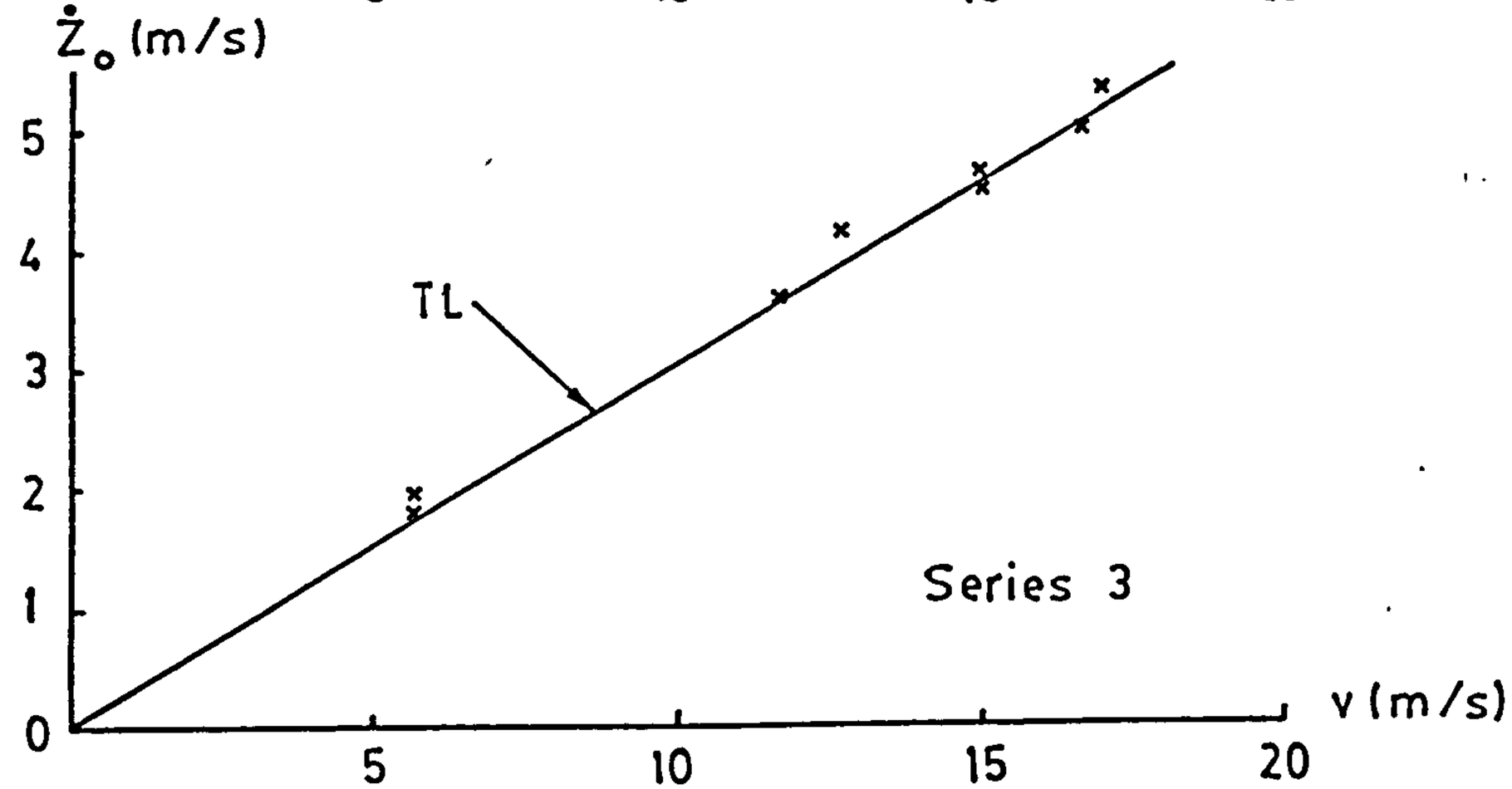

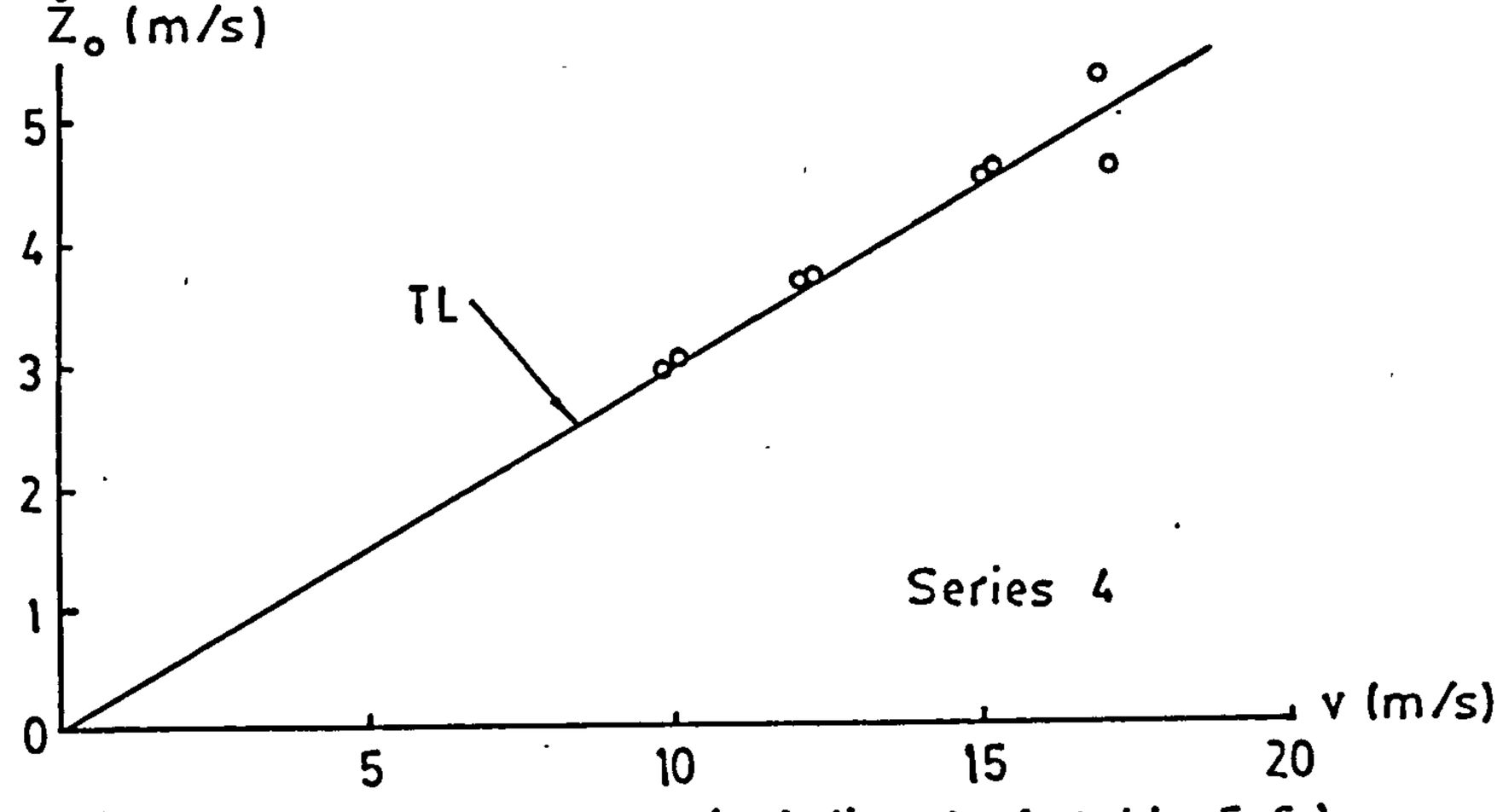

Notations: 1. $\dot{Z}_o$ - beam initial velocity 2. v - bullet velocity 3. TL - theoretical line (ref. table 5.6)
4. Series - ref. table 3.1

FIG. 4.7 BEAM INITIAL VELOCITY AND BULLET VELOCITY RELATIONSHIP

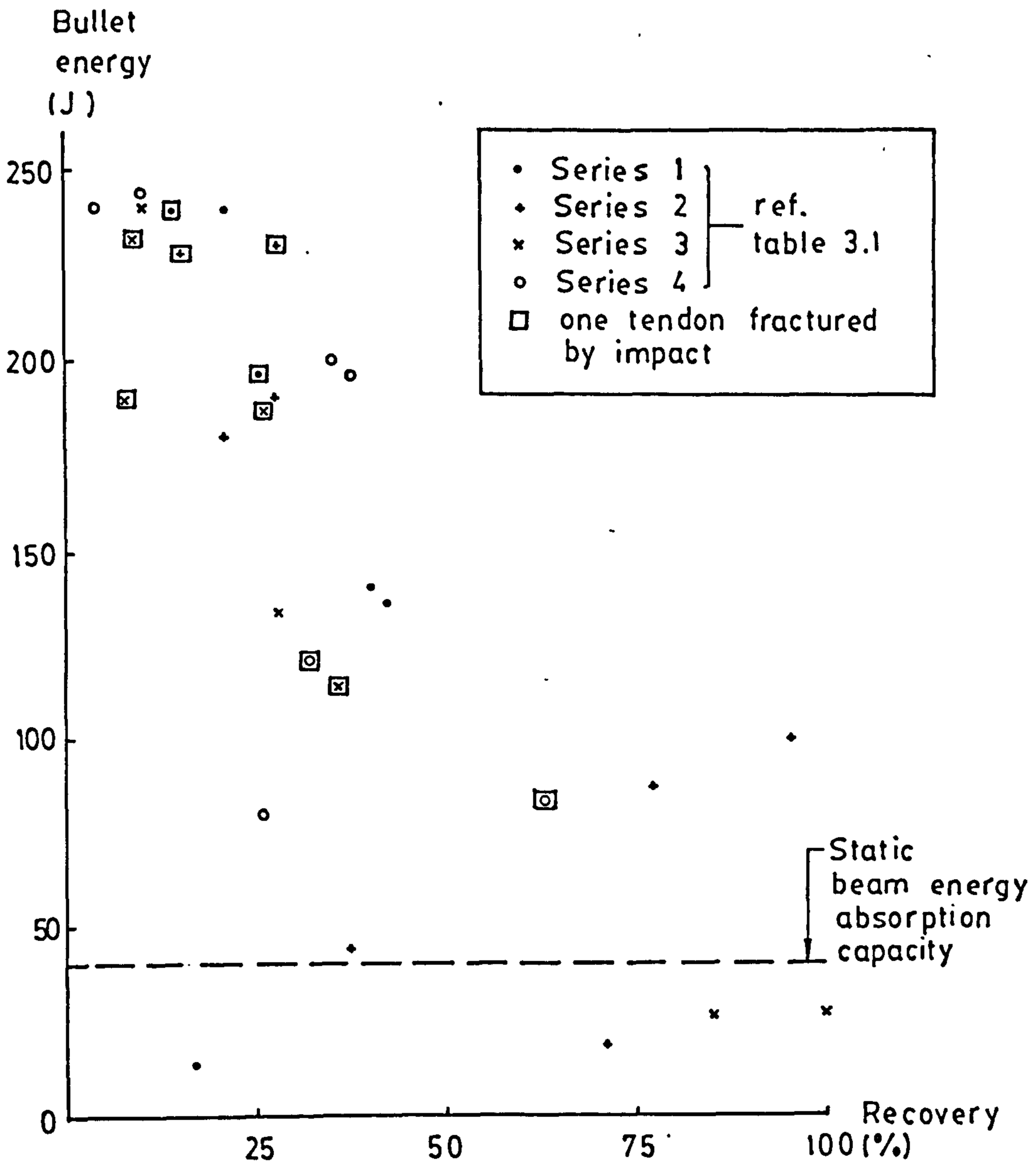

FIG. 4.8 BULLET ENERGY AND RECOVERY RELATIONSHIP

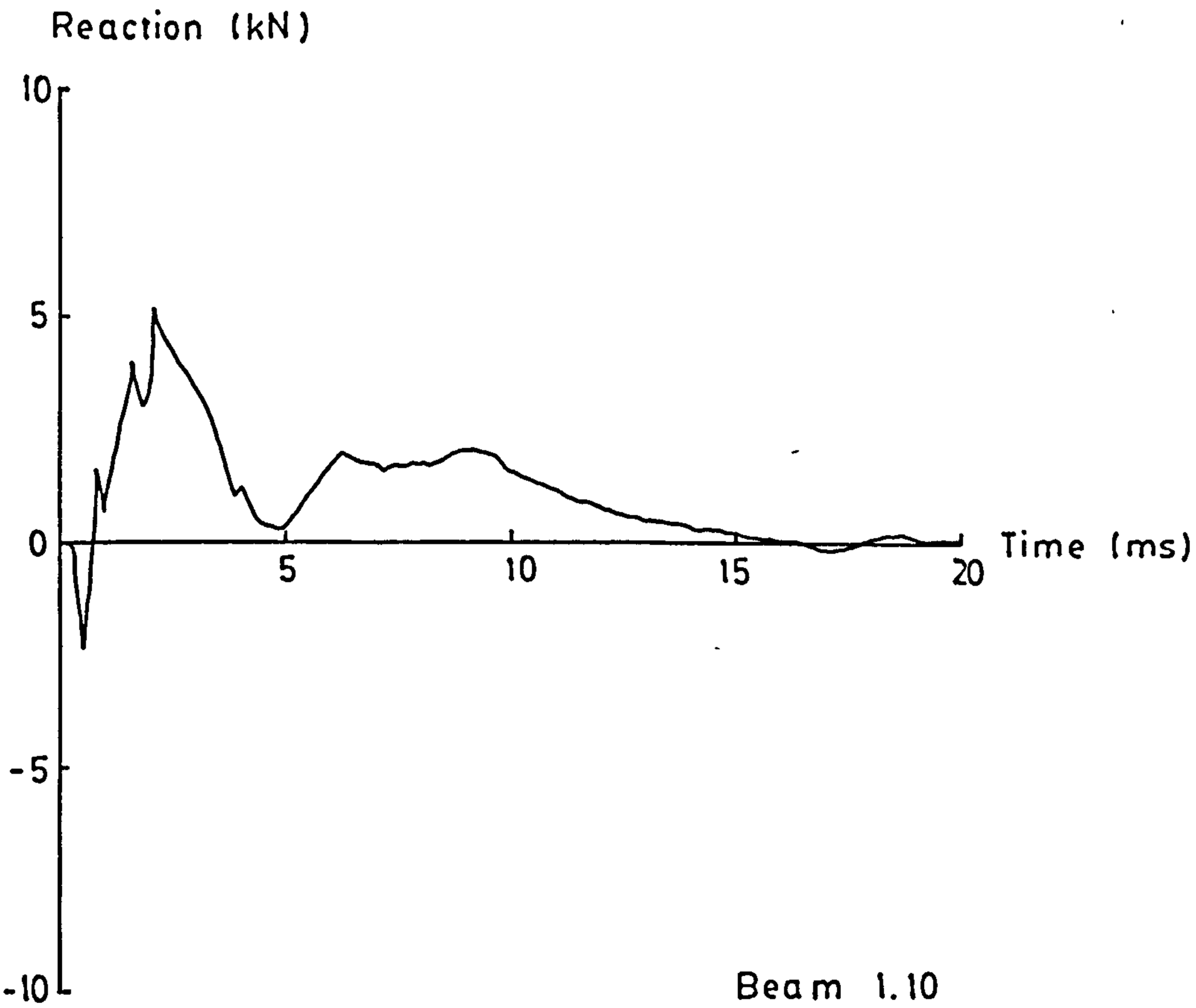

Notes: 1. Normal reaction positive.
2. Triggered at time = 0 (section 4.3.4)

FIG. 4.9 REACTION TRACE

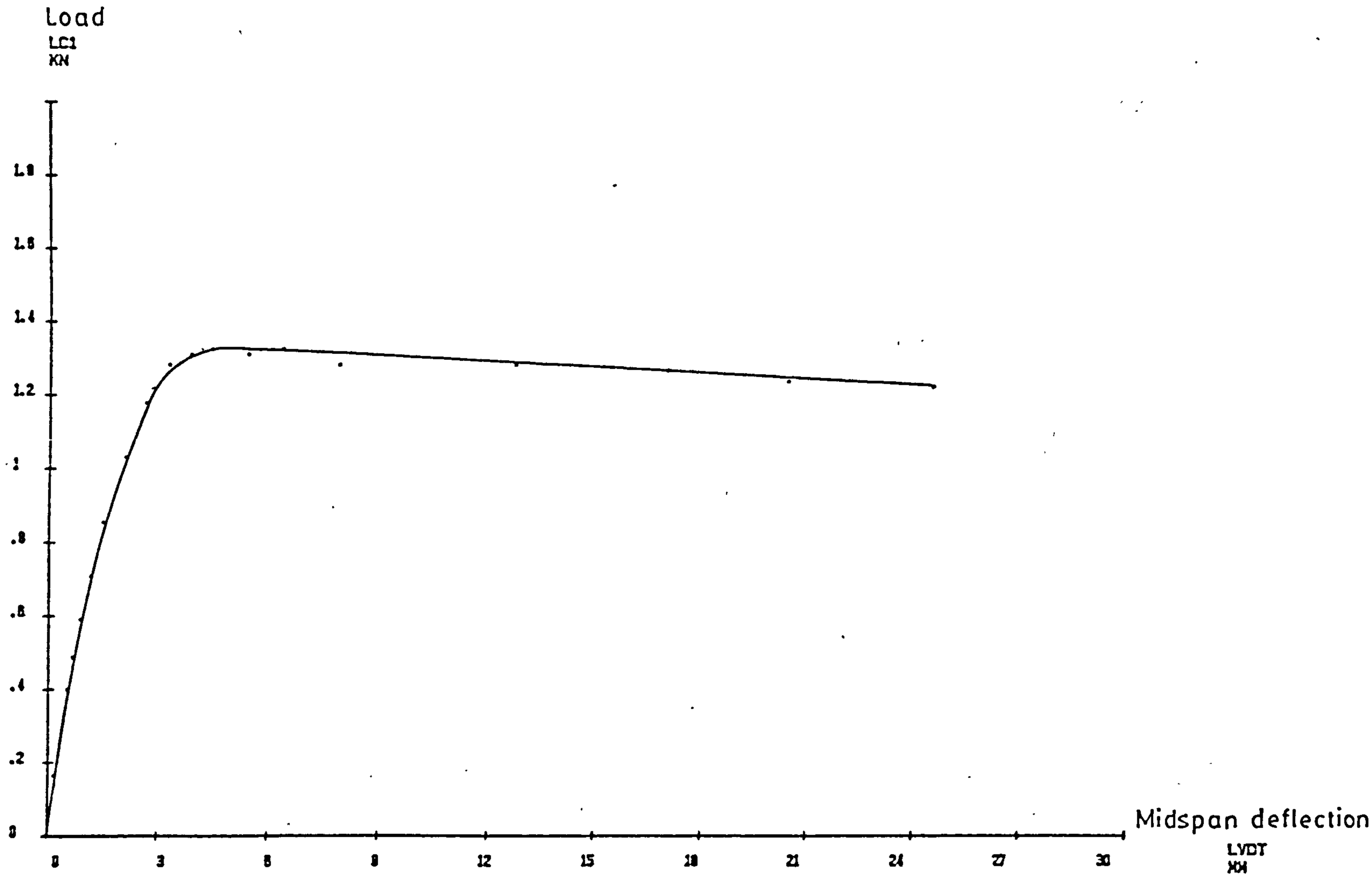

FIG. 4.10 LOAD-DEFLECTION CURVE OF BEAM 1.7 - POST-IMPACT-STATIC TEST

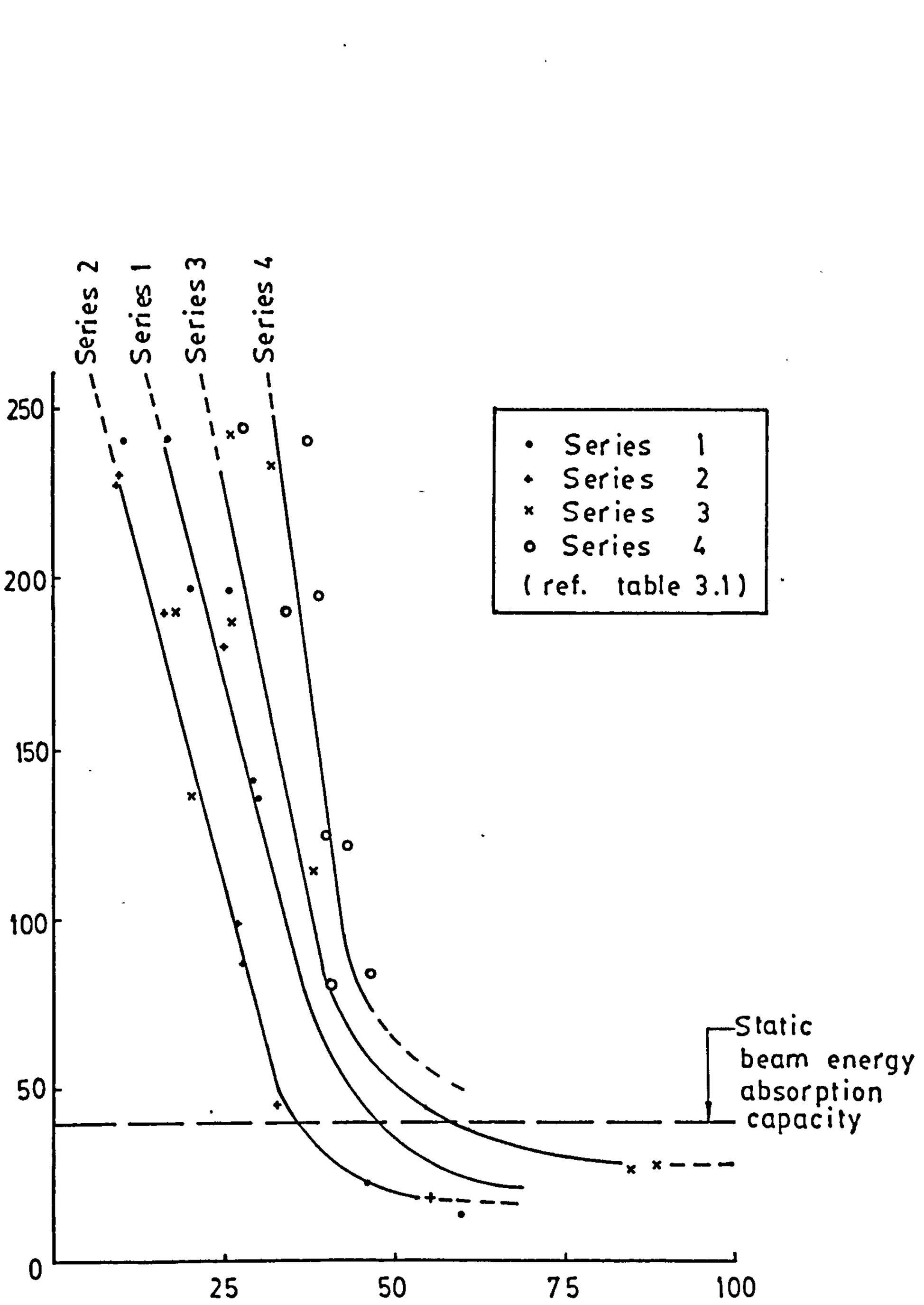

FIG. 4.11 BULLET ENERGY AND IMPACTED BEAM STIFFNESS RELATIONSHIP

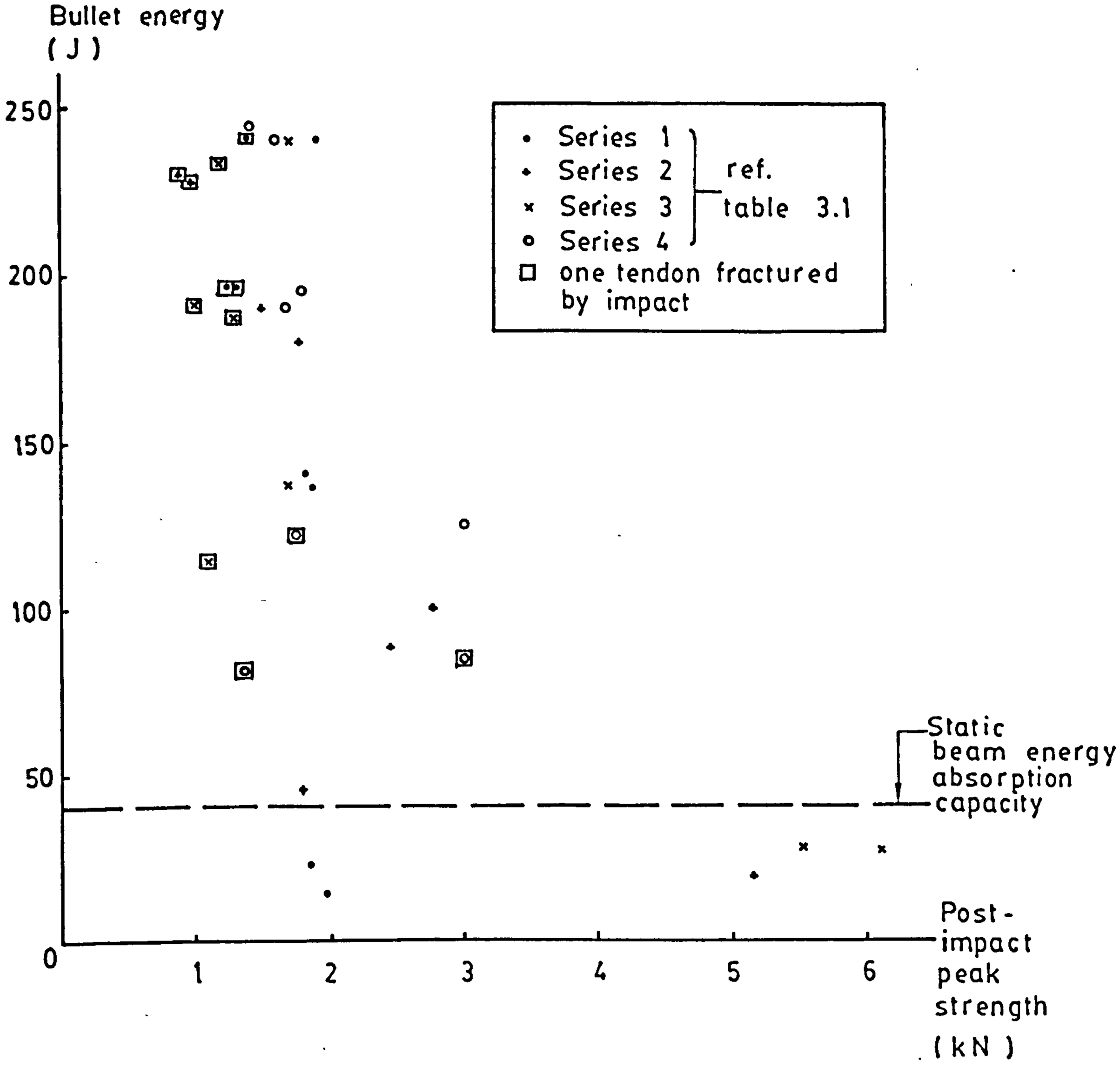

FIG. 4.12 BULLET ENERGY AND POST-IMPACT PEAK STRENGTH RELATIONSHIP

Series	Beam Number	Beam Stiffness (kN/mm)	Peak Load (kN)	Midspan Deflection at Peak Load (mm)	Number of Flexural or Flexural-Shear Crack	Crack Spacing (mm)	* Number of Tendon Fractured	Number of Tendon Slipped
1	2	2.3	3.30	7.23	4	40	0	4
	3	1.7	2.42	2.96	2	40	0	4
2	2	2.3	1.67	4.75	1	—	0	4
	4	2.4	3.32	3.14	3	40	0	4
3	2	2.4	5.98	7.64	4	40	4	0
	3	2.6	4.48	2.86	2	40	3	1
4	2	1.6	3.16	5.64	1	—	0	4
	3	3.3	3.70	4.75	3	50	1	3

* Bottom tendon always fractured before top ones

TABLE 4.1 STATIC TEST RESULTS

Series	Beam Number	Impact Velocity (m/s)	Incident Force (kN)	Rise Time of Incident Pulse (μs)	Bullet Energy (J)	Crack Pattern					Dynamic Deflection					Initial Beam Velocity (m/s)	** Number of Tendons Fractured	Number of Tendons Slipped
						Punching Shear Plug	Flexural	Shear	Flexural Shear	Inverted Flexural	Peak (mm)	Time to Peak After Triggered (ms)	Residual (mm)	Recovery (mm) (Peak-Residual)	Recovery / Peak %			
1	1	5.17	*60	-	*22.54		✓				-	-	-	-	-	-	0	4
	4	4.07	44.4	22	13.97		✓	✓	✓	✓	2.4	2	2.0	0.4	16.7	1.38	0	4
	5	12.94	147.3	20	141.24	✓	✓	✓	✓	✓	12.0	6	7.2	4.8	40.0	4.35	0	4
	6	12.70	*147.3	-	136.05	✓	✓	✓	✓	✓	12.8	6	7.4	5.4	42.2	4.24	0	4
	7	15.26	177.6	21	196.42	✓	✓	✓	✓	✓	-	-	-	-	-	-	1	3
	8	15.28	*177.2	-	196.94	✓	✓	✓	✓	✓	21.2	10	15.8	5.4	25.5	4.98	1	3
	9	16.92	199.8	22	241.48	✓	✓	✓	✓	✓	24.0	10	20.6	3.4	14.2	5.30	1	3
	10	16.87	197.8	22	240.08	✓	✓	✓	✓	✓	24.4	10	19.4	5.0	20.5	5.30	0	4
2	1	7.29	80.7	23	44.86		✓		✓	✓	6.4	5	4.0	2.4	37.5	2.54	0	4
	3	4.72	52.5	29	18.79		✓			✓	2.8	2	0.4	2.0	71.1	1.70	0	?
	5	10.16	115.0	20	87.07		✓	✓	✓	✓	8.8	6	2.0	6.8	77.3	3.40	0	?
	6	10.87	123.1	20	99.67		✓	✓	✓	✓	8.8	5	0.4	8.4	95.5	3.85	0	?
	7	14.98	173.6	21	189.28	✓	✓	✓	✓	✓	19.4	10	14.0	5.4	27.8	4.66	0	4
	8	14.59	167.5	21	179.55	✓	✓	✓	✓	✓	18.0	8	14.2	3.8	21.1	4.56	0	4
	9	16.49	191.7	21	229.25	✓	✓	✓	✓	✓	20.8	8	15.0	5.8	29.9	5.09	1	3
	10	16.45	185.7	21	228.25	✓	✓	✓	✓	✓	24.0	12	20.4	3.6	15.0	5.19	1	3
3	1	5.64	58.5	26	26.83					✓	2.8	2	0.4	2.4	85.7	1.91	0	0
	4	5.69	64.6	25	27.31						2.4	2	0.0	2.4	100.0	1.80	0	0
	5	12.75	147.3	26	137.12	✓	✓	✓	✓	✓	14.0	8	10.0	4.0	28.5	4.13	0	4
	6	11.65	131.2	30	114.48	✓	✓	✓	✓	✓	11.2	8	7.2	4.0	35.7	3.60	1	3
	7	15.02	173.6	28	190.30	✓	✓	✓	✓	✓	24.0	12	22.0	2.0	8.3	4.45	1	3
	8	14.90	173.5	22	187.26	✓	✓	✓	✓	✓	15.0	8	11.0	4.0	26.6	4.66	1	3
	9	16.92	199.8	20	241.48	✓	✓	✓	✓	✓	24.0	10	21.4	2.6	10.8	5.30	0	4
	10	16.63	195.8	22	233.28	✓	✓	✓	✓	✓	22.2	10	20.0	2.2	9.9	4.88	1	3
4	1	9.80	117.0	22	81.01		✓		✓	✓	9.2	8	6.8	2.4	26.1	3.29	1	3
	4	10.04	121.1	22	84.52	✓	✓	✓	✓	✓	7.6	4	2.8	4.8	63.3	3.39	1	?
	5	12.05	137.2	20	122.48	✓	✓	✓	✓	✓	11.8	8	8.0	3.8	32.2	3.82	1	3
	6	12.18	137.2	20	125.14	✓	✓	✓	✓	✓	-	-	-	-	-	-	0	?
	7	15.23	177.6	22	195.65	✓	✓	✓	✓	✓	18.0	8	11.4	6.6	6.6	4.77	0	?
	8	14.99	171.5	20	189.53	✓	✓	✓	✓	✓	17.6	8	11.4	6.2	6.2	4.88	0	4
	9	16.89	195.8	21	240.62	✓	✓	✓	✓	✓	23.0	9	22.0	1.0	1.0	5.30	0	4
	10	17.01	195.8	22	244.06	✓	✓	✓	✓	✓	26.0	12	23.2	2.8	2.8	4.50	0	4

** Bottom Tendons Fractured

? Unknown

* Failed to Record, Estimated

TABLE 4.2 IMPACT TEST RESULTS

Series	Beam Number	Initial Beam Stiffness (kN/mm)	Stiffness of Impacted Beam (kN/mm)	Stiffness of Impacted Beam / Initial Beam Stiffness (%)	Peak Load (kN)	Deflection at Peak Load (mm)	Number of Additional Flexural Crack Developed	Crack Spacing (mm)	* Final Count: Number of Tendons Fractured	* Final Count: Number of Tendons Slipped	Remarks
1	1	2.4	1.1	45.8	1.85	2.55	0	-	0	4	-
	4	2.5	1.5	60.0	1.92	1.88	0	-	0	4	-
	5	2.4	0.7	29.2	1.83	4.27	0	-	0	4	-
	6	2.3	0.7	30.4	1.88	7.80	0	-	0	4	-
	7	2.5	0.65	26.0	1.32	4.45	0	-	1	3	-
	8	2.5	0.5	20.0	1.26	3.45	0	-	1	3	-
	9	2.6	0.4	15.4	1.35	6.64	0	-	1	3	-
	10	2.5	0.25	10.0	1.69	5.93	0	-	0	4	-
2	1	2.4	0.8	33.3	1.60	7.28	0	-	0	4	-
	3	3.9	2.2	56.4	5.15	6.77	1	-	0	4	-
	5	2.5	0.7	28.0	2.45	5.96	0	-	0	4	-
	6	2.4	0.65	27.1	2.79	8.85	0	-	0	4	-
	7	2.4	0.4	16.7	1.49	5.63	0	-	0	4	-
	8	2.4	0.6	25.0	1.77	4.40	0	-	0	4	-
	9	2.0	0.2	10.0	0.92	7.97	0	-	1	3	-
	10	2.6	0.25	9.6	0.98	5.81	0	-	1	3	-
3	1	2.6	2.2	84.6	6.12	7.33	5	40	4	0	-
	4	2.6	2.3	88.5	5.45	5.54	3	40	2	2	-
	5	2.5	0.5	20.0	1.71	7.91	0	-	0	4	-
	6	1.7	0.65	38.2	1.17	8.33	0	-	1	3	-
	7	2.2	0.4	18.2	0.99	4.62	0	-	1	3	-
	8	2.3	0.6	26.1	1.30	6.56	0	-	1	3	-
	9	2.3	0.6	26.1	1.73	3.81	0	-	0	4	-
	10	1.6	0.55	34.4	1.19	5.04	0	-	1	3	-
4	1	2.4	1.0	41.7	1.35	2.98	0	-	1	3	-
	4	2.6	1.2	46.2	2.99	4.93	0	-	1	3	-
	5	2.1	0.9	42.9	1.49	3.34	0	-	1	3	-
	6	2.6	1.05	40.4	3.02	9.44	0	-	0	4	-
	7	2.3	0.9	39.1	1.83	3.85	0	-	0	4	a
	8	2.5	0.85	34.0	1.67	3.62	0	-	0	4	-
	9	2.4	0.9	37.5	1.61	3.31	0	-	0	4	b
	10	1.8	0.5	27.8	1.44	8.30	0	-	0	4	-

Notes :

a-One bottom carrier bar fractured during test

b-One bottom carrier bar necked during test

* Results due to impact included

TABLE 4.3 POST-IMPACT-STATIC TEST RESULTS

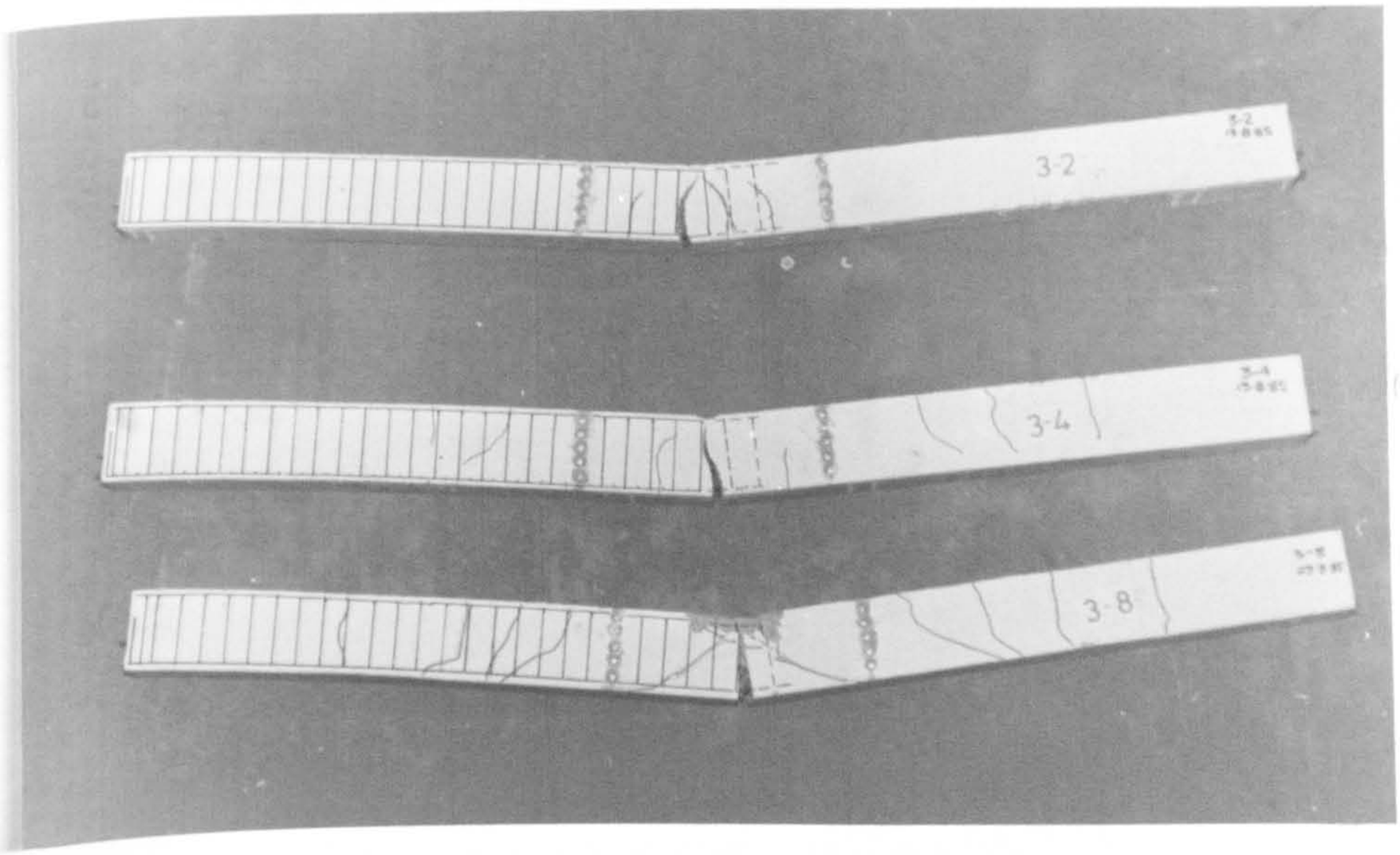

(a)

(b)

(c)

(a) Static test

(b) Impact test - without punching shear plug

(c) Impact test - with punching shear plug

PLATE 4.1 CRACK PATTERN

CHAPTER FIVE

THEORETICAL ANALYSIS

5.1 Introduction

This chapter gives a theoretical analysis of the beam impact problem based on a plastic model. The beam properties and stress wave theory concerned in this investigation are also presented at the beginning of this chapter.

5.2 Beam Properties

The theoretical results concerning the beam properties in this section are summarized in table 5.1 and 5.2.

5.2.1 Load Carrying Capacity

The ultimate moment of resistance of the beam section is found by balancing the internal forces[2,8] (figs. 5.1a and 5.1b). The assumptions are

(a) plane sections remain plane in bending,

(b) the tendons and the concrete are bonded up to failure,

(c) the stress in steel is given by the appropriate stress-strain curve (figs. 3.1 and 3.4),

(d) the stress in concrete is given by the Hognestad's formula[85], modified by Pfrang, Siess and Sozen[86] (fig. 5.2) and assuming that concrete cannot carry any tensile stress. Accordingly, with the cylinder strength f_c' of 39.7 N/mm^2 (section 3.3.2), the compressive strength in the beam is $f_c'' = 0.85\, f_c' = 33.7$ N/mm^2. Since the stress-strain curve obtained from a prism (section 3.2.2.2) has a compressive strength of 32.0 N/mm^2, this curve (fig. 3.3) is used for determining the concrete strain at maximum stress ϵ_0 and at ultimate ϵ_u. The compressive strain corresponding to the maximum stress is $\epsilon_0 = 3000\ \mu$ strain, and the ultimate strain $\epsilon_u = 5500\ \mu$ strain. This high value of ϵ_u is justified by Corley[87] and Hughes[30].

(e) under normal bending, the bottom tendons in the model beam are assumed to fracture at failure because the ductility of the piano wire is small and

the percentage of elongation is only 1.6 % (section 3.2.2.1)

In the analysis, the ultimate strain in the bottom tendons is set to 16000 μ strain and the depth to the neutral axis x_d is then found by trial and error until the sum of internal compressive forces is equal to the sum of internal tensile forces, within ± 2 %. When x_d is found, the ultimate moment of resistance M_p can be evaluated by taking the moment of all the internal forces about the top fibre. An example of this calculation can be found in appendix G.

Under reverse bending, the top carrier bars are assumed to achieve their ultimate stress of 350 N/mm^2 and therefore a strain of 14000 μ strain (fig. 3.4). Following the same method, the ultimate reverse moment of resistance M_p' can be found.

By assuming that the loss in the prestressing force varies from 5 to 100 %, M_p has a value of 0.81 ± 0.01 kNm and M_p' is 0.23 ± 0.03 kNm.

If the tendons and the concrete are not bonded, or the bonding is completely destroyed due to impact, the load is then carried by the bottom carrier bars. Using the same method and assuming that the concrete strain reached the ultimate strain of 5500 μ strain at the extreme fibre at failure, the ultimate moment of resistance M_u is 0.13 kNm.

The strain rate effects (section 2.3) on steel and concrete are not considered separately in these calculations because

(a) all the beams were tested under the same order of loading rate and the differences in the dynamic increases factors (DIFs) is small (table 2.1),
(b) the solutions obtained by considering the separate DIF are not neccessary correct (section 2.4).

The American Concrete Institute Code of Practice[11] (ACI 349-76) recommends that the dynamic increase factors for axial compressive strength in concrete and high strength steel (prestressing steel) should be taken as 1.25 and 1.00 respectively. The maximum strain rate in the experimental programme is estimated to be 3.76 s^{-1} (appendix H). From the data collected by Mainstone[12], the DIFs are the same as the ACI recommendations. The average of these DIFs is therefore used to give some idea of the ultimate moment of resistance under impact.

The ultimate moment of resistance can be converted into load carrying capacity and is given in table 5.1.

5.2.2 Beam Stiffness

The beam stiffness K (unit kN/mm) is given by

$$K = (48 E_c I)/ l^3 \qquad \text{equ. 5.1}$$

where E_c = Young's modulus of concrete (kN/mm^2),

l = span (mm),

I = second moment of area of the transformed elastic section (mm^3).

The stiffness varies from 0.73 to 5.44 kN/mm under different conditions. i.e. cracked or uncracked sections and the bonding condition between steel and concrete (table 5.2).

5.2.3 Natural Frequency of Beams

The natural frequency, f (unit kHz), is given by[88]

$$f = (K_e/m_e)^{1/2}/(2\pi) \qquad \text{equ. 5.2}$$

where K_e = equivalent stiffness = K for beams (kN/mm),

m_e = equivalent mass (kg), section 5.5.2.

The maximum equivalent stiffness is 5.44 kN/mm and minimum is 0.73 kN/mm (section 5.2.2). The maximum equivalent mass is 1.116 kg in series 4 and the minimum is 1.056 kg in series 2 (table 5.6). Thus, the range of the natural frequency of the beam is from 129 to 361 Hz.

5.3 One Dimensional Elastic Stress Wave Theory

5.3.1 Basic Equations

The magnitudes of the force and stress generated by an impact and their distributions can be analysed by the one dimensional elastic stress wave theory[83]. Assuming the force and the particle velocity in the impacting body and the impacted body are the same at the common plane of impact, and using the initial conditions provided in this test (fig. 5.3), the theory gives

$$\sigma_I = \frac{A_2\rho_2 C_{L2}\cdot \rho_1 C_{L1}}{A_2\rho_2 C_{L2} + A_1\rho_1 C_{L1}} v, \quad F_I = \frac{A_2\rho_2 C_{L2}\cdot A_1\rho_1 C_{L1}}{A_2\rho_2 C_{L2} + A_1\rho_1 C_{L1}} v \qquad \text{equ. 5.3}$$

$$\sigma_T = \frac{2A_1\rho_2 C_{L2}}{A_2\rho_2 C_{L2} + A_1\rho_1 C_{L1}}\sigma_I, \quad F_T = \frac{2A_2\rho_2 C_{L2}}{A_2\rho_2 C_{L2} + A_1\rho_1 C_{L1}} F_I \qquad \text{equ. 5.4}$$

$$\sigma_R = \frac{A_2\rho_2 C_{L2} - A_1\rho_1 C_{L1}}{A_2\rho_2 C_{L2} + A_1\rho_1 C_{L1}}\sigma_I, \quad F_R = \frac{A_2\rho_2 C_{L2} - A_1\rho_1 C_{L1}}{A_2\rho_2 C_{L2} + A_1\rho_1 C_{L1}} F_I \qquad \text{equ. 5.5}$$

where σ = stress, C_L = longitudinal wave speed = $(E/\rho)^{1/2}$,

F = force, E = Young's modulus,

A = area, v = impact velocity,

ρ = density,

and subscripts I = incident, R = reflected,

T = transmitted,

1 = body from which the stress wave is travelling,

2 = body to which the stress wave is travelling.

Equation 5.5 yields

(a) the reflected stress is equal in magnitude but opposite in sign to the incident stress at a free end; and

(b) the reflected stress is equal in magnitude and of the same sign to the incident stress at a fixed end.

5.3.2 Incident Pulse

By substituting the properties of the bullet and the pressure bar (table 3.3) in equation 5.3, it gives

$\sigma_I = 17.98\, v$ and $F_I = 11.1\, v$ equ. 5.6

and considering a stress wave travelling from the bullet to the pressure bar, equations 5.4 and 5.5 give

$\sigma_T = 1.098\, \sigma_I$ and $F_T = 0.902\, F_I$ equ. 5.7

$\sigma_R = -0.098\, \sigma_I$ and $F_R = -0.098\, F_I$ equ. 5.8

where σ is in N/mm^2, F is in kN and v is in m/s.

From the space time diagram (fig. 5.4), the reflected tensile wave from the free end of the bullet will start to unload the stress wave in the pressure bar at a time = (2 x length of bullet/ C_L of bullet) = 134 μs after impact. Because of the subsequent reflected and transmitted waves (fig. 5.4), a tensile force is eventually generated at the bullet/ pressure bar interface after 383 μs, at which the bullet will separate from the pressure bar (table 5.3).

The portion of a pulse which is less than 10 % of its incident peak amplitude is generally considered to be insignificant and is ignored in the analysis[89]. The theoretical incident pulse is thus simplified to be a rectangle with a peak amplitude as predicted by equation 5.6 and has a duration of 134 μs (fig. 5.5).

5.3.3 Impulse Transmitted

The technique used to calculate the impulse transmitted was developed by Inkester[39] and was employed by Ang[34] afterwards.

Rearranging equations 5.3 to 5.5 with subscripts 1 and 2 representing the pressure bar and the beam respectively, it gives

$$A_2 = \frac{A_1 \rho_1 C_{L1}}{\rho_2 C_{L2}} \left(\frac{F_I + F_R}{F_I - F_R} \right) \qquad \text{equ. 5.9}$$

where F_I is a constant and can be easily evaluated from the digital printout (section 3.7.4), and F_R can be evaluated from the first reflected wave form B in figure 4.2b. Yet from the space time diagram (fig. 5.4), the pulse reflected inside the beam interferes with the oscilloscope record at a time

t = (2 x beam depth / C_{L2}) = 39 μs

after the pulse is reflected from the pressure bar/ beam interface. Taking this interference into account,

$$F_{R(measured)} = F_{RM} = \left(\frac{2 A_1 \rho_1 C_{L1}}{A_2 \rho_2 C_{L2} + A_1 \rho_1 C_{L1}} F_I' \right) + \left(\frac{A_2 \rho_2 C_{L2} - A_1 \rho_1 C_{L1}}{A_2 \rho_2 C_{L2} + A_1 \rho_1 C_{L1}} F_I \right)$$

equ. 5.10

where F_I' = incident force from beam to pressure bar

= $-F_T$ at a time 39 μs earlier (section 5.3.1).

Rearranging equation 5.10. it yields

$$A_2 = \frac{A_1 \rho_1 C_{L1}}{\rho_2 C_{L2}} \left(\frac{F_I + F_{RM} - 2F_I'}{F_I - F_{RM}} \right) \qquad \text{equ. 5.11}$$

Substituting equations 5.9 and 5.11 at the appropriate time in equation 5.4, the transmitted force is found.

An example of calculation sheet is presented in table 5.4. To simplify the calculation, equation 5.11 is used at time = 40 μs instead of 39 μs and the time interval is 5 μs. Since the rise time varied from 20 to 30 μs (table 4.2), A_2 was assumed to vary in a linear manner in this period. At the start of the reflected wave form B, A_2 is set equal to A_1 (= 506.7 mm^2) as the pressure bar is initially touching the beam.

5.4 Dynamic Plastic Model

5.4.1 Introduction

This model was developed by Ezra[90] for mild steel with a rectangular section, using the concept of moving plastic hinges introduced by Parkes[91]. This model is modified and extended in this thesis to cope with the test conditions.

Figure 5.6 shows a beam which is pin-ended and is dynamically loaded at its midspan by a rigid striker. The deflections induced are everywhere supposed small, but the kinetic energy delivered by the striker and dissipated in the plastic hinges is taken to be an order of magnitude greater than the elastic strain energy which the beam can store. At the moment of impact a plastic hinge forms under the striker and two plastic hinges travel outwards from the midspan. The portions AB and A'B' rotate about the supports. These rotations must occur because the free body diagram (fig. 5.7) indicates only the yield moment acts on OB. There is no shear force at B because the bending moment is the greatest and there is no concentrated load between O and A. i.e. the shear force diagram is continuous. The deflection is

divided into two stages by the time when the hinges B and B' cease to move.

Table 5.5 tabulates the theoretical results derived from this section. All the notations are as defined in figure 5.6.

5.4.2 Effective Span

The effective span l_e is defined as the maximum distance between the moving hinges. i.e. when they become stationary.

The downwards velocity v_p at a point P between O and B is given by (fig. 5.6),

v_p = velocity of B + velocity of P relative to B

$$= (L-x)\dot{\theta} + [\,\dot{Z} - (L-x)\,\dot{\theta}\,]\left(\frac{x-\lambda}{x}\right)$$

$$= \dot{Z}\left(1-\frac{\lambda}{x}\right) + \frac{\lambda}{x}(L-x)\,\dot{\theta} \qquad \text{equ. 5.12}$$

Thus the acceleration at P, f_p is

$$f_p = \frac{dv_p}{dt} = \ddot{Z}\left(1-\frac{\lambda}{x}\right) + \dot{Z}\left(\frac{\dot{x}\lambda}{x^2}\right) - \frac{\lambda}{x^2}(L-x)\,\dot{\theta}\,\dot{x} - \frac{\lambda}{x}\dot{\theta}\,\dot{x} + \frac{\lambda}{x}(L-x)\ddot{\theta} \qquad \text{equ. 5.13}$$

Balancing the force acting on OB (fig. 5.7), yield :

$$\frac{M}{2}\ddot{Z} + \int_0^x m f_p\, d\lambda = 0$$

$$\Rightarrow \frac{M}{2}\ddot{Z} + m\left[\,\ddot{Z}\frac{x}{2} + \dot{Z}\frac{x}{2} - \frac{(L-x)\,\dot{\theta}\,\dot{x}}{2} - \frac{x\dot{\theta}\,\dot{x}}{2} + \frac{x(L-x)\ddot{\theta}}{2}\,\right] = 0$$

$$\Rightarrow (M+mx)\ddot{Z} + mx\ddot{\theta}(L-x) + m\dot{x}(\dot{Z}-L\dot{\theta}) = 0 \qquad \text{equ. 5.14}$$

The equation of rotation for OB is, taking moments about O, (fig. 5.7)

$$M_p + M_p' = \int_0^x m f_p \lambda\, d\lambda \qquad \text{equ. 5.15}$$

and substituting for f_p from equation 5.13,

$$M_p + M_p' = m\int_0^x [\ddot{Z}(1 - \frac{\lambda}{x}) + \dot{Z}(\frac{\dot{x}\lambda}{x^2}) + (L-x)\ddot{\theta}\frac{\lambda}{x} - \frac{\lambda}{x}\dot{\theta}\dot{x}$$

$$- \frac{\lambda}{x^2}(L-x)\dot{\theta}\dot{x}]\lambda\, d\lambda$$

$$\Rightarrow 6(M_p + M_p') = m[\ddot{Z}x^2 + 2x^2(L-x)\ddot{\theta} + 2x\dot{x}(\dot{Z} - L\dot{\theta})] \qquad \text{equ. 5.16}$$

For portion AB, the moment of inertia of AB about A is

$$I_A = \frac{m(L-x)^3}{3} \quad \text{and since } I_A\ddot{\theta} = M_p', \text{ then :}$$

$$m(L-x)^3\ddot{\theta} = 3M_p' \qquad \text{equ. 5.17}$$

If equation 5.14 is multiplied by 2x and subtracted from equation 5.16, it gives

$$6(M_p + M_p') = -(2Mx + mx^2)\ddot{Z}$$

$$\Rightarrow \ddot{Z} = \frac{-6(M_p + M_p')}{(2Mx + mx^2)} \qquad \text{equ. 5.18}$$

Substituting equation 5.17 and equation 5.18 into equation 5.14, it is found that

$$\dot{x}(\dot{Z} - L\dot{\theta}) = \frac{3M_p'}{m}\{(1 + \frac{M_p}{M_p'})(\frac{1}{x} + \frac{1}{2\frac{M}{m} + x}) - \frac{x}{(L-x)^2}\} \qquad \text{equ. 5.19}$$

When the plastic hinges cease to move, then

$$\dot{x} = 0 \quad \text{and} \quad \dot{Z} = L\dot{\theta}$$

and putting $\alpha = M_p/M_p'$, moment of resistance ratio; and

$\beta = M/(mL)$, mass ratio,

equation 5.19 becomes

$$(1 + \alpha)(\frac{1}{x} + \frac{1}{2\beta L + x}) = \frac{x}{(L-x)^2} \qquad \text{equ. 5.20}$$

$$\text{Let } f(x) = (1+\alpha)\left(\frac{1}{x} + \frac{1}{2\beta L + x}\right) - \frac{x}{(L-x)^2} \qquad \text{equ. 5.21}$$

then when (a) $x \to -0$, $f(x) \to -\infty$,

(b) $x \to +0$, $f(x) \to \infty$,

(c) $x \to L$, $f(x) \to -\infty$,

(d) $x \to \infty$, $f(x) \to 0$,

which indicates that x in equation 5.20 has three solutions. The first one x_0 is close to zero, i.e. before the hinges start to move, the second one x_1 lies between 0 and L, and the third one x_2 is at infinity. Obviously the effective span l_e is given by

$$l_e = 2x_1 \qquad \text{equ. 5.22}$$

5.4.3 Dynamic Deflection

High speed photographs[34] of simply supported beams impacted at midspan show that in the early stage of deformation, the two portions of the beam which will rotate about the supports at the later stage (fig. 5.8) are almost straight and undeflected. Thus assuming that
at t = 0, then

$\dot{\theta} = \ddot{\theta} = 0$,

$x = 0$, and

$\dot{Z} = V$,

the approximate deflection can be found.
Equation 5.14 becomes

$$(M + mx)\ddot{Z} + m\dot{x}\dot{Z} = 0$$

$$\Rightarrow \frac{d(M\dot{Z} + mx\dot{Z})}{dt} = 0 \qquad \text{equ. 5.23}$$

Equation 5.16 becomes

$$m\ddot{Z}x^2 + 2mx\dot{x}\dot{Z} = 6(M_p + M_p')$$

$$\Rightarrow \frac{d\,mx^2\dot{Z}}{dt} = 6(M_p + M_p') \qquad \text{equ. 5.24}$$

Hence integrating and putting in the initial conditions to find the integration constant, equation 5.23 gives

$$\dot{Z} = \frac{Mv}{M + mx} \qquad \text{equ. 5.25}$$

and equation 5.24 gives

$$mx^2\dot{Z} = 6(M_p + M_p')t \qquad \text{equ. 5.26}$$

Substituting for $\dot{Z}$ in equation 5.26 from equation 5.25,

and differentiating with respect to t,

$$\dot{x} = \frac{6(M_p + M_p')}{Mmv} \cdot \frac{(M + mx)^2}{x(2M + mx)} \qquad \text{equ. 5.27}$$

Dividing equation 5.25 by equation 5.27.

$$\frac{dZ}{dx} = \frac{Mv}{M + mx} \cdot \frac{Mmv}{6(M_p + M_p')} \cdot \frac{x(2M + mx)}{(M + mx)^2} \qquad \text{equ. 5.28}$$

Put $S = M + mx$ and equation 5.28 becomes

$$Z = \int_{M}^{M+mx} \frac{M^2 v^2}{6(M_p + M_p')m} \cdot \frac{S^2 - M^2}{S^3} dS$$

Solving

$$Z = \frac{M^2 v^2}{6(M_p + M_p')m}\left[\ln\left(1 + \frac{m}{M}x\right) - \frac{mx(2M + mx)}{2(M + mx)^2}\right] \qquad \text{equ. 5.29}$$

Assuming the beam deforms as in figure 5.8a, then equation 5.29 indicated that the maximum deflection at midspan Z_1 is proportional to the square of the impact velocity at this stage. i.e.

$$Z_1 = k_1 v^2 \qquad \text{equ. 5.30}$$

where $k_1 = \frac{M^2}{6(M_p + M_p')m}\left[\ln\left(1 + \frac{m}{M}x_1\right) - \frac{mx_1(2M + mx_1)}{2(M + mx_1)^2}\right]$; and

$$\phi' = \frac{Z_1}{x_1} \qquad \text{equ. 5.31}$$

The work done by the hinge at B, U_B is given by

$$U_B = M_p'\phi'$$

$$= \frac{M_p' k_1}{x_1} v^2 \qquad \text{equ. 5.32}$$

Assuming the beam deforms as in figure 5.8b at later stage and ABO is near enough to be considered as a straight line (see appendix D, part b, Deformation Profiles).

At $Z = Z_{max}$, then

$\dot{\theta} = 0, \dot{Z} = 0$ and

$$\theta = \frac{Z_{max}}{L} \qquad \text{equ. 5.33}$$

Thus the work done by the hinge at midspan U_0 is given by

$$U_0 = M_p 2\theta$$

$$= \frac{2M_p Z_{max}}{L} \qquad \text{equ. 5.34}$$

Equating the energy supply (bullet energy), U_I, to the total work done by the hinges and assuming the energy absorbed by the hinges = U_I and negligible elastic energy.

$$U_I = U_0 + 2U_B$$

$$\Rightarrow \frac{Mv^2}{2} = \frac{2M_p Z_{max}}{L} + \frac{2M_p' k_1}{x_1} v^2 \qquad \text{equ. 5.35}$$

Rearranging

$$Z_{max} = \frac{L}{4}\left\{\frac{M}{M_p} - \frac{4k_1}{\alpha x_1}\right\} v^2 \qquad \text{equ. 5.36}$$

From equation 5.36, again, the maximum deflection, Z_{max}, at midspan is proportional to the square of the impact velocity, v. i.e

$$Z_{max} = k_2 v^2 \qquad \text{equ. 5.37}$$

where $k_2 = \frac{L}{4}\left\{\frac{M}{M_p} - \frac{4k_1}{\alpha x_1}\right\}$

5.4.4 Dynamic Reactions

At the early stage, the maximum uplift reaction R' is given by (fig. 5.9a)

$$R'(L - x) = M_p'$$

$$\Rightarrow R' = M_p'/(L - x) \qquad \text{equ. 5.38}$$

At the later stage (i.e. when the moving hinges become stationary), there is an inertia force acting on the beam (fig. 5.9b). From the standard text books[18], the lever arm under plastic conditions is 2/3 L. Thus the maximum reaction R is given by

$$2RL/3 = M_p$$

$$\Rightarrow R = (3M_p)/(2L) \qquad \text{equ. 5.39}$$

5.5 Equivalent One-degree of Freedom System[18,88,92]

5.51 Introduction

When dealing with dynamic problems on beams, the beam under study is very often transformed into one-degree of freedom system (fig. 5.10). All the

equations derived in this section are true at the early stage of impact. Table 5.6 gives the theoretical results calculated from these equations.

5.5.2 Equivalent Mass

The assumptions are

(a) the beam vibrates in simple harmonic motion,

(b) the deflected shape is constant with time so that the ratio of any two ordinates of deflection along the beam is always constant.

(c) the deflected shape is the same as that which would be caused by the load applied statically.

From Norris et al[18] and Bolton[88], the equivalent mass m_e for a beam dynamically loaded at midspan is

$m_e = 0.49\, ml_e$ for a simply supported / pin-ended beam in the elastic range equ. 5.40a

$m_e = 0.37\, ml_e$ for a fix-ended beam in the elastic range equ. 5.40b

$m_e = 0.33\, ml_e$ for all beams in the plastic range equ. 5.40c

5.5.3 Energy Asorbed by Beam

This analysis is based upon the principle of conservation of energy. i.e. the work done by the externally applied load must be equal to the sum of the internal strain energy and the kinetic energy of the beam. Referring to figure 5.10,

$$\int_0^Z F_e(t)dZ = \frac{1}{2} m_e \dot{Z}^2 + \int_0^Z R_e(Z)dZ \qquad \text{equ. 5.41}$$

where $F_e(t)$ = external load as a function of time

$R_e(Z)$ = beam resistance as a function of deflection

The equation of motion is

$$m_e \ddot{Z} = F_e(t) - R_e(Z) \qquad \text{equ. 5.42}$$

and the external work done $W_e(t)$ up to time t is

$$W_e(t) = \int_0^{Z(t)} F_e(t)\, dZ$$

$$= \int_0^t F_e(t) \frac{dZ}{dt}\, dt \qquad \text{equ. 5.43}$$

Integrating equation 5.42 and substituting into equation 5.43,

$$W_e(t) = \int_0^t F_e(t) \{ \frac{1}{m_e} \int_0^t F_e(t) - R_e(Z)\, dt \} dt \qquad \text{equ. 5.44}$$

Since in the present experiments, the impact pulse duration T is 134 μs (section 5.3.2) and the minimum time to peak deflection is 2 ms (table 4.2), the beam resistance can be deleted[18] in equation 5.44 which becomes

$$W_e(T) = \int_0^T F_e(t) \{ \frac{1}{m_e} \int_0^T F_e(t)\, dt \} dt \qquad \text{equ. 5.45}$$

Putting $I_T = \int_0^T F_e(t)\, dt$ = transmitted impulse,

then equation 5.45 becomes

$$W_e(T) = \frac{I_T^2}{2 m_e} \qquad \text{equ. 5.46}$$

The maximum energy transferred into the beam U_T is equal to the work done by the external load (= $W_e(T)$). Since the impulse transmitted and the equivalent mass can be evaluated as described in sections 5.3.3 and 5.5.2, the energy transferred U_T can be readily calculated using equation 5.46.

5.5.4 Initial Beam Velocity

After the application of the load, the beam has acquired a kinetic energy equal to the maximum work done W_{max}.i.e.

$$W_{max} = \frac{I_I^2}{2M_e} = \frac{\dot{Z}_0^2 M_e}{2} \qquad \text{equ. 5.47a}$$

$$\Rightarrow \dot{Z}_0 = \frac{I_I}{M_e} \qquad \text{equ. 5.47b}$$

where I_I = incident impulse,

$\dot{Z}_0$ = initial beam velocity,

M_e = equivalent mass including mass of pressure bar.

and $I_I = F_I T$ equ. 5.48

Since equation 4.1 gives $F_I = 11.6v$ and section 5.3.2 gives $T = 134\ \mu s$, equation 5.48 becomes

$$I_I = 11.6v \times 134 \times 10^{-3}$$

$$= 1.55v \qquad \text{equ. 5.49}$$

Substituting equation 5.49 into equation 5.47b,

$$\dot{Z}_0 = \frac{1.55\,v}{M_e} \qquad \text{equ. 5.50}$$

where $\dot{Z}_0$ and v are in m/s and

M_e in kg.

Equation 5.50 indicates the beam initial velocity is proportional to the impact velocity.

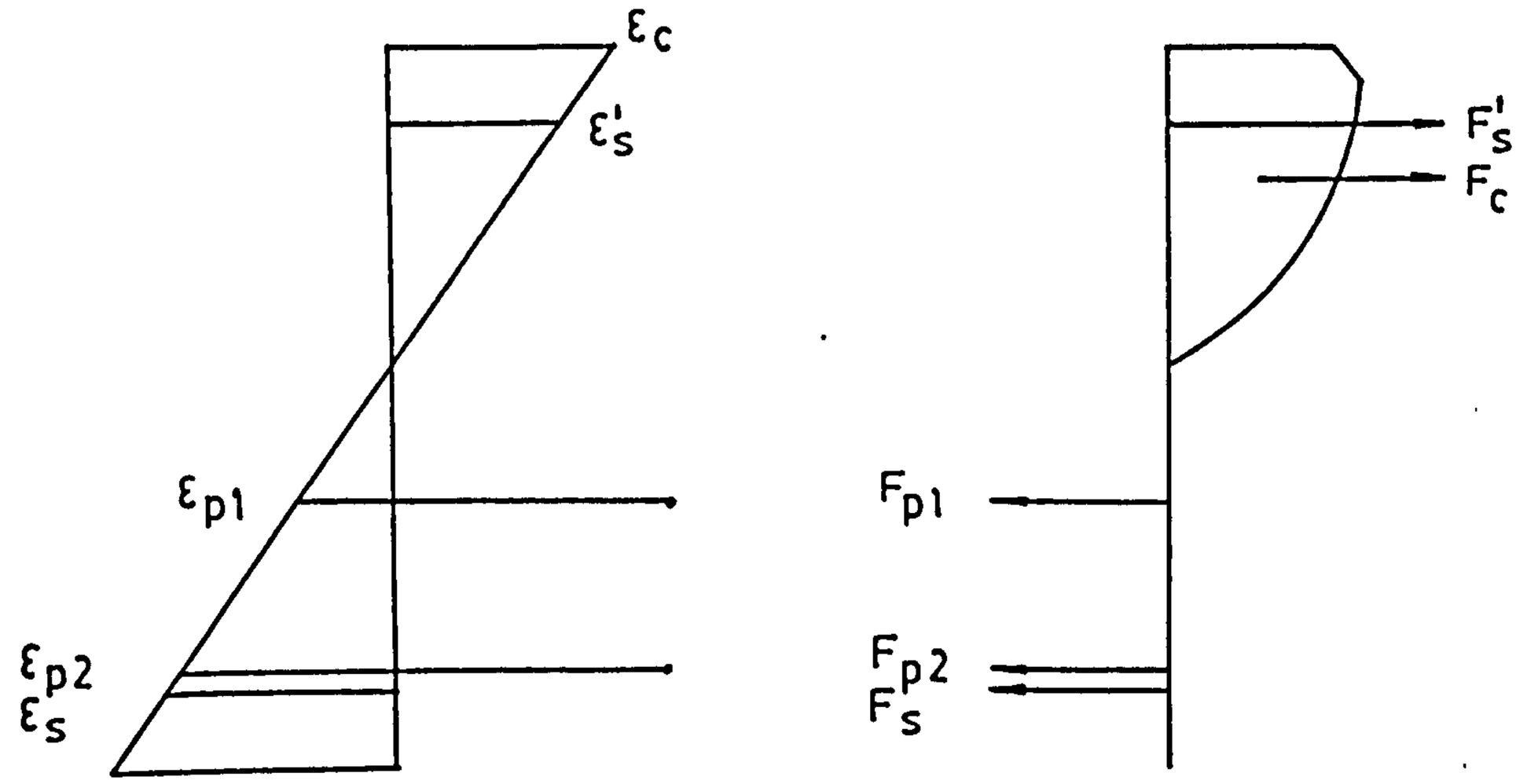

(a) Strain (b) Force

Notations: 1. ε = strain
2. F = force

Subscripts:
1. c = concrete
2. 's = top (in compression) steel
3. s = bottom (in tension) steel
4. p1 = top (in tension) tendon
5. p2 = bottom (in tension) tendon

FIG. 5.1 FORCE AND STRAIN DISTRIBUTION IN BEAM SECTION

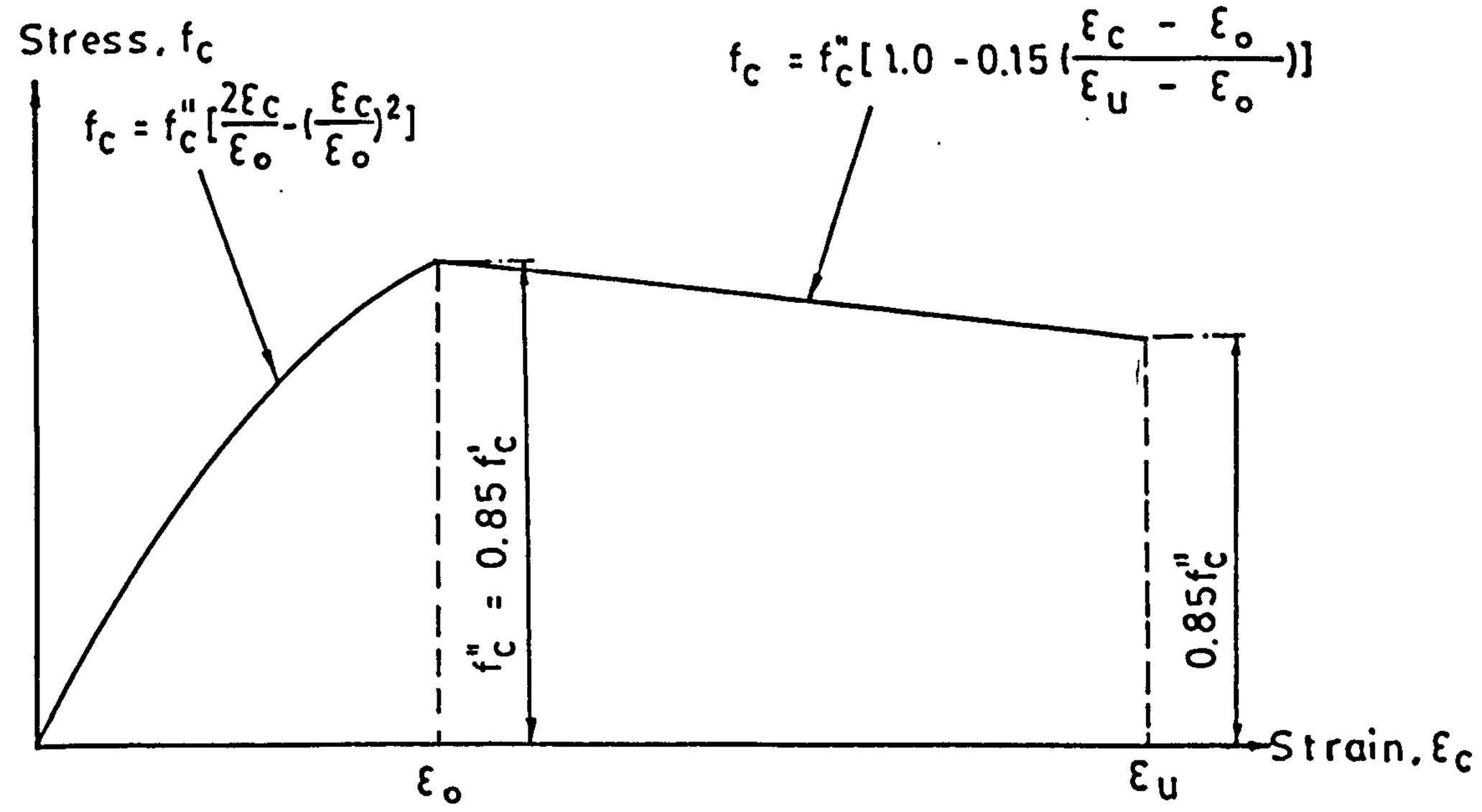

Notations: see section 5.2.1

FIG. 5.2 STRESS STRAIN CHARACTERISTICS OF CONCRETE IN COMPRESSION[86]

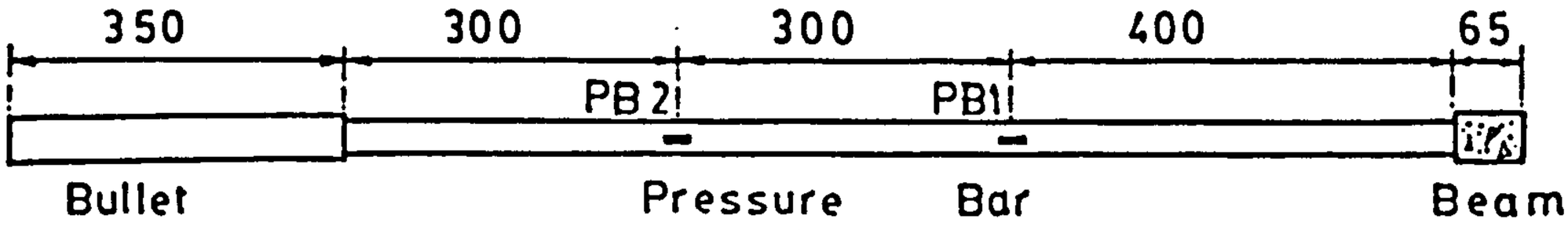

Note: all dimensions in mm

FIG. 5.3 BULLET / PRESSURE BAR / BEAM DIAGRAM

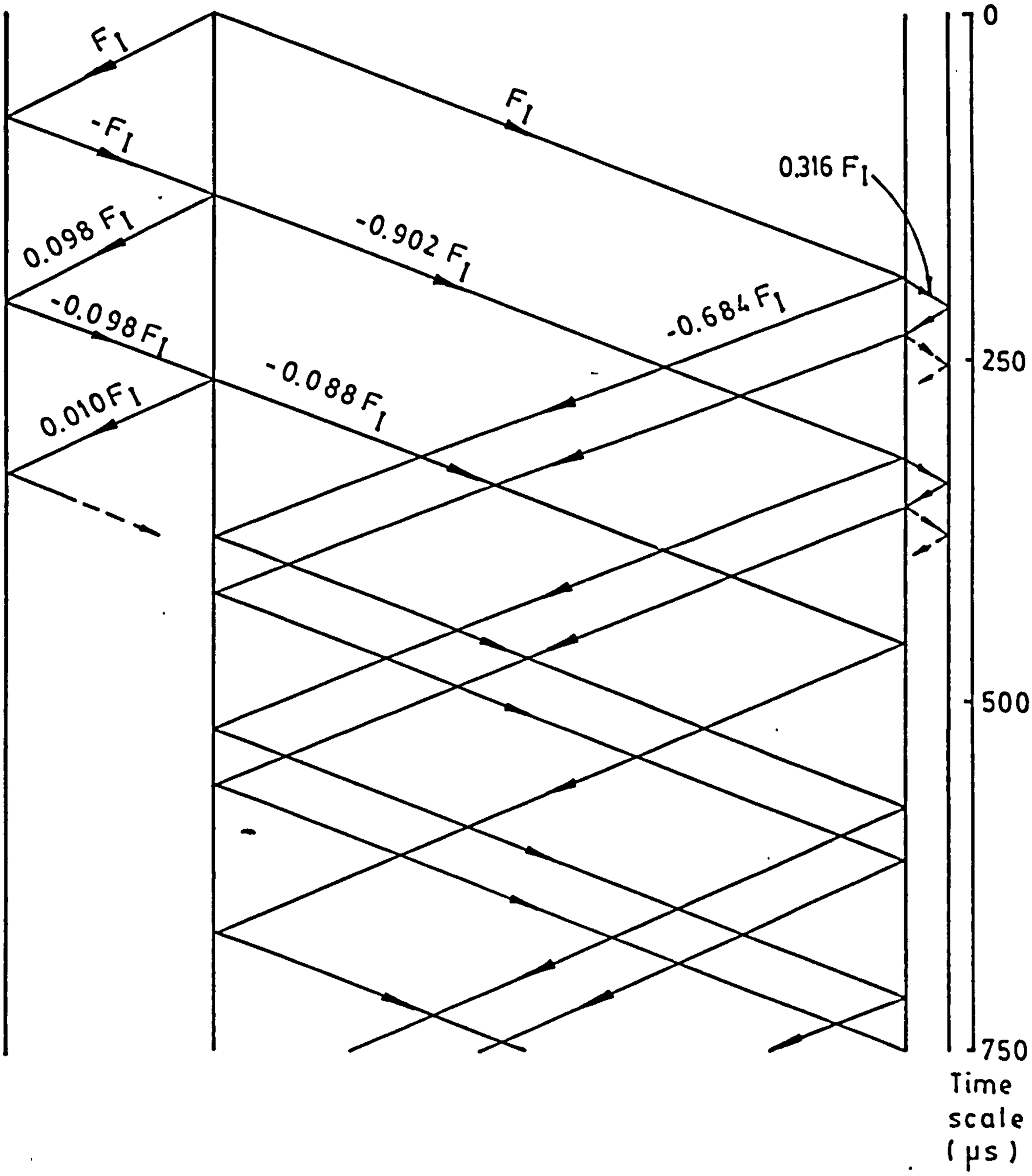

FIG. 5.4 SPACE TIME DIAGRAM

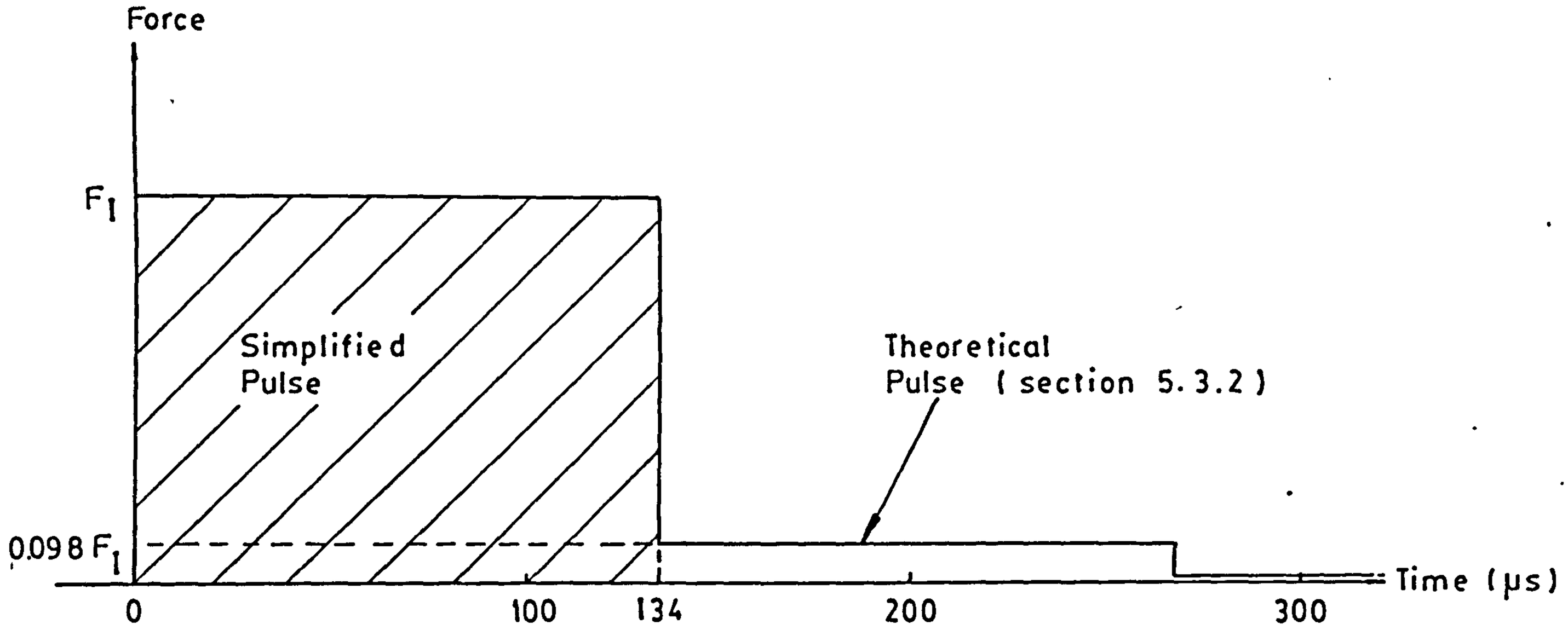

FIG. 5.5 THEORETICAL IMPACT PULSE SHAPE

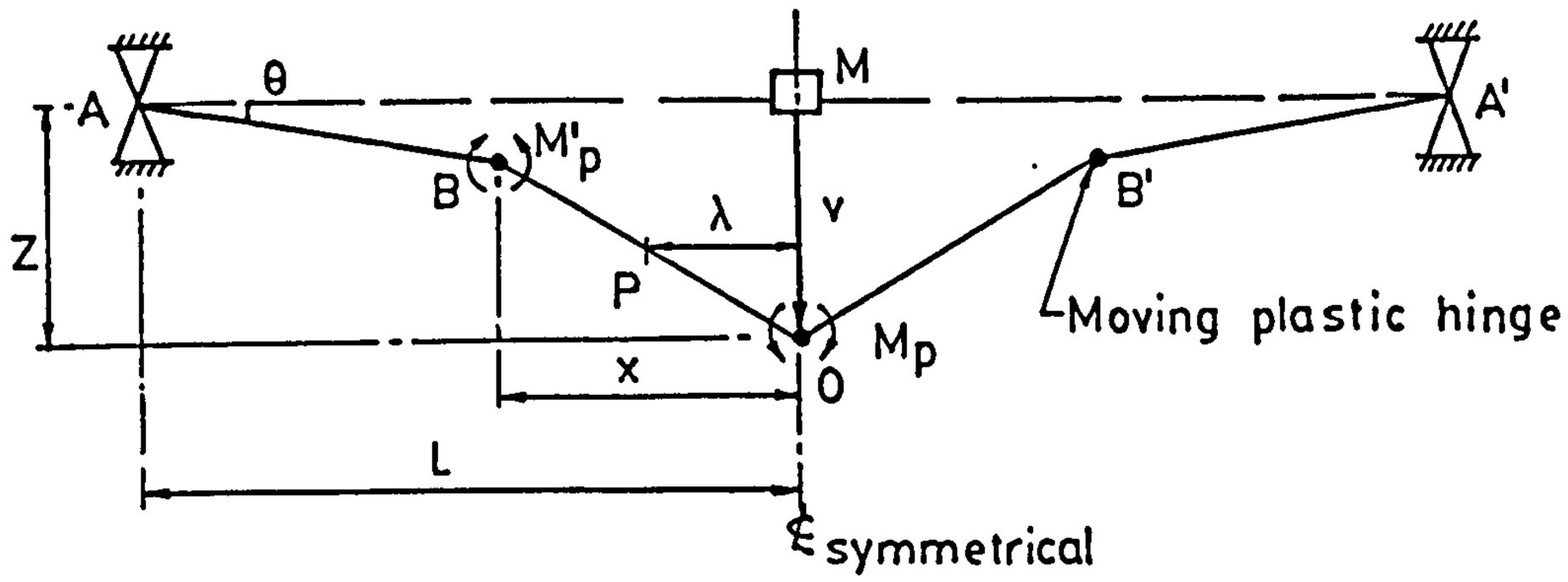

Notations: 1. M = mass of striker
2. v = impact velocity
3. x = distance between moving plastic hinge and midspan
4. λ = distance between point P and midspan
5. Z = deflection at midspan
6. M_p = ultimate moment of resistance
7. M'_p = ultimate reverse moment of resistance
8. θ = angle of rotation at support
9. L = half span

FIG. 5.6 DYNAMIC PLASTIC MODEL

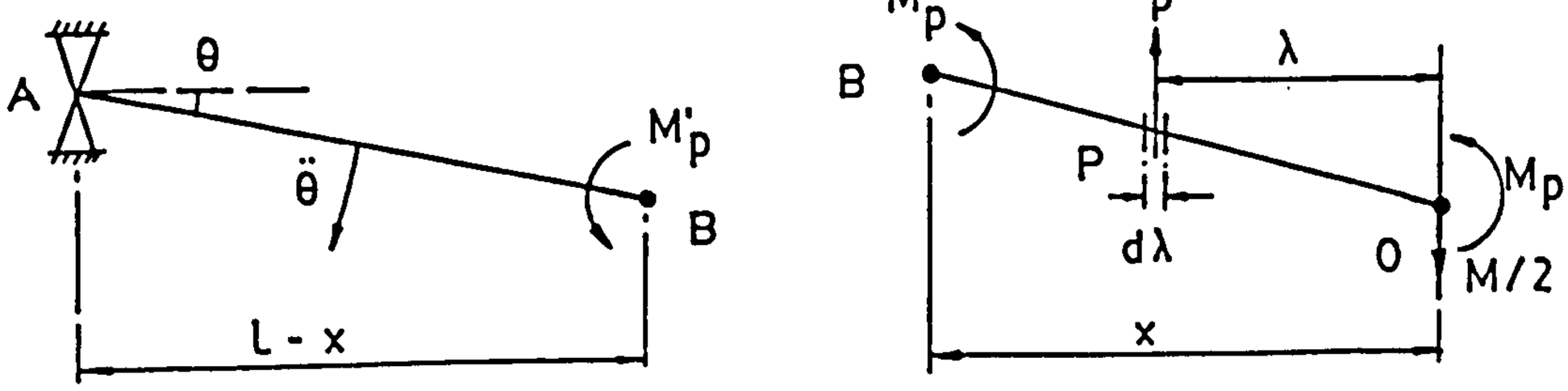

(a) AB (b) BO

Notations: see section 5.4.2

FIG. 5.7 FREE BODY DIAGRAM

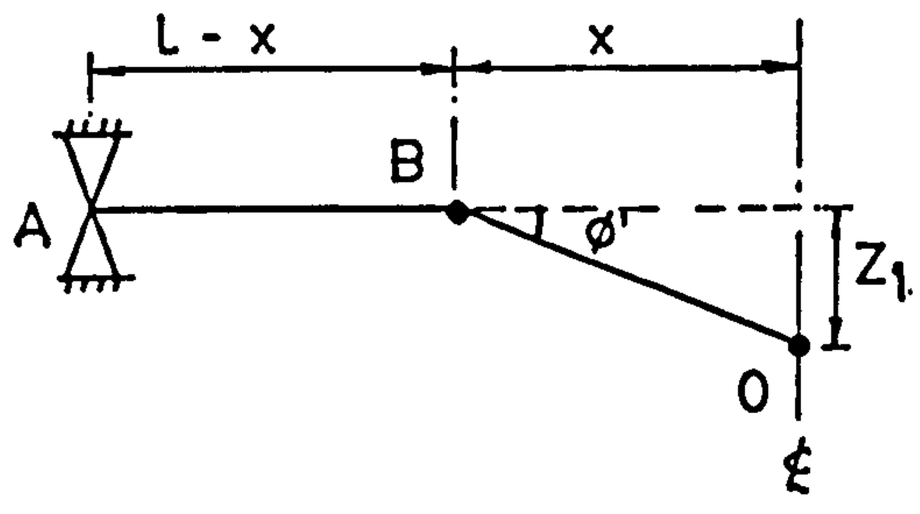

(a) Early stage

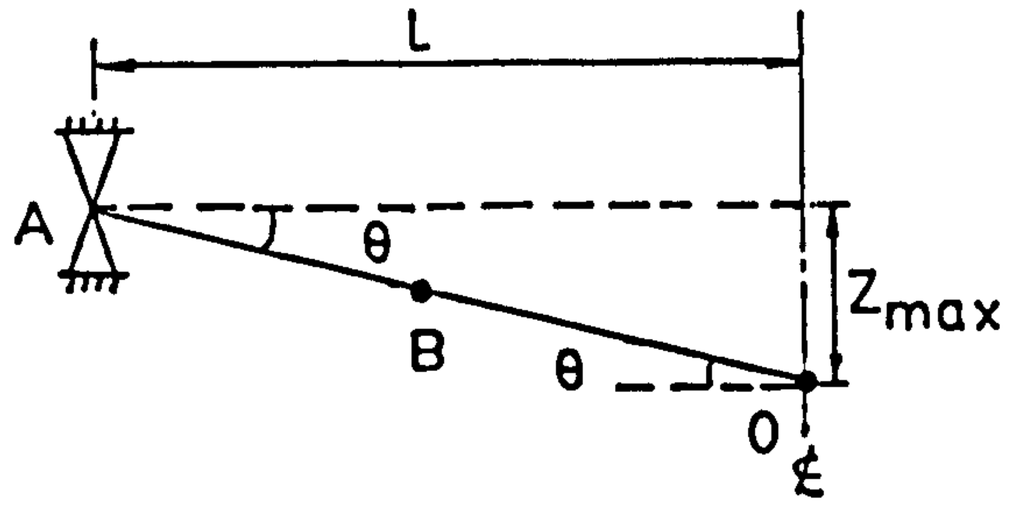

(b) Later stage

FIG. 5.8 BEAM DEFORMATION DIAGRAM

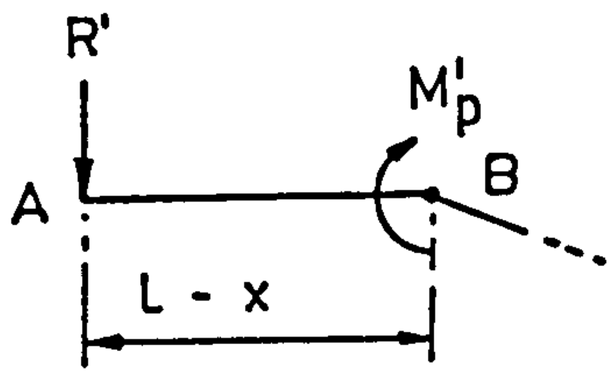

(a) Uplift

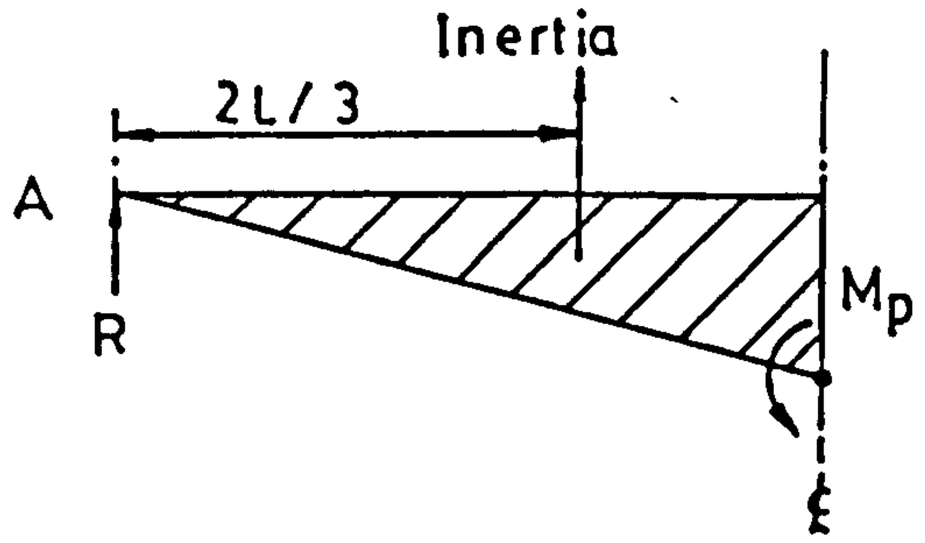

(b) Normal

FIG. 5.9 REACTION DIAGRAM

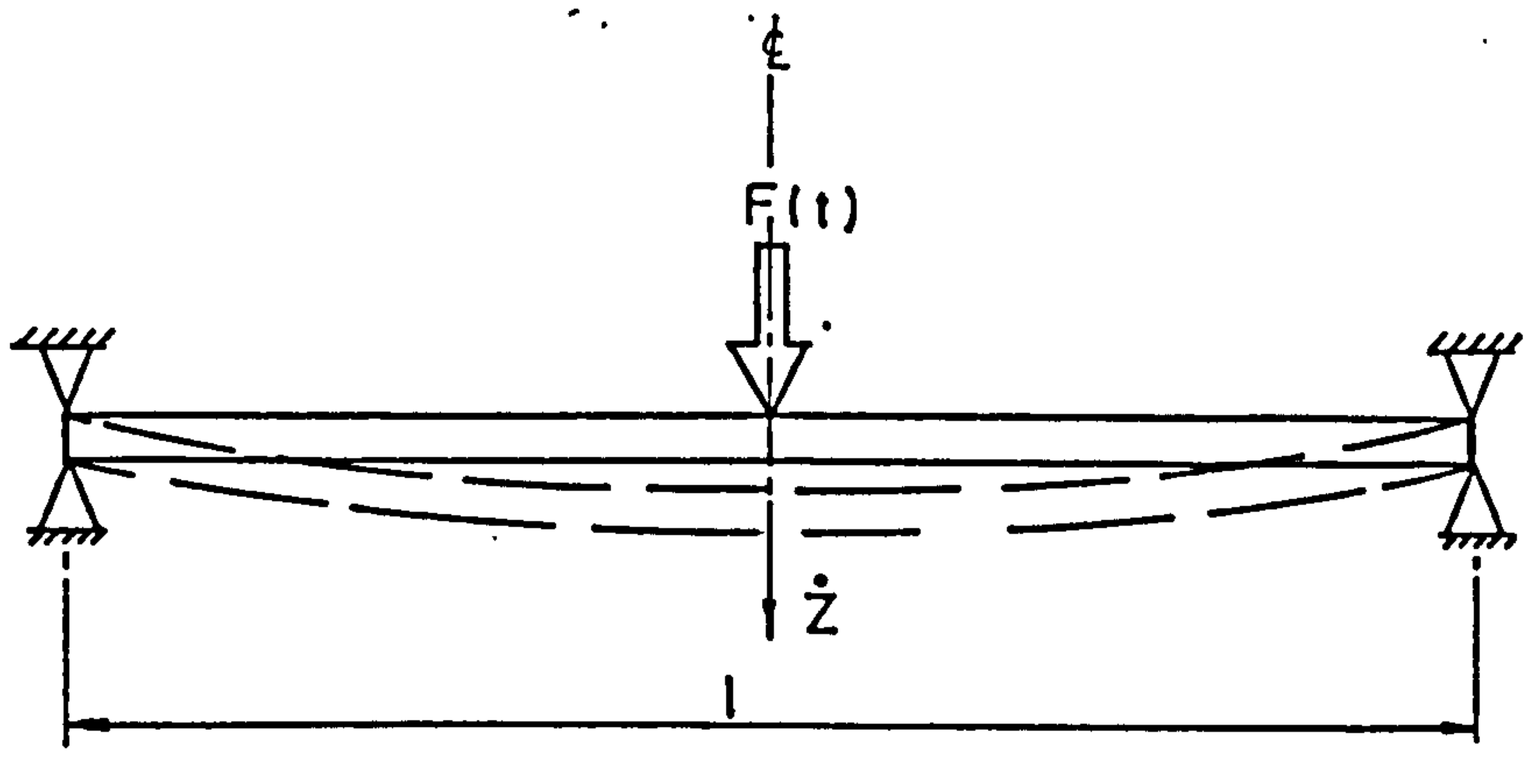

(a) Original system

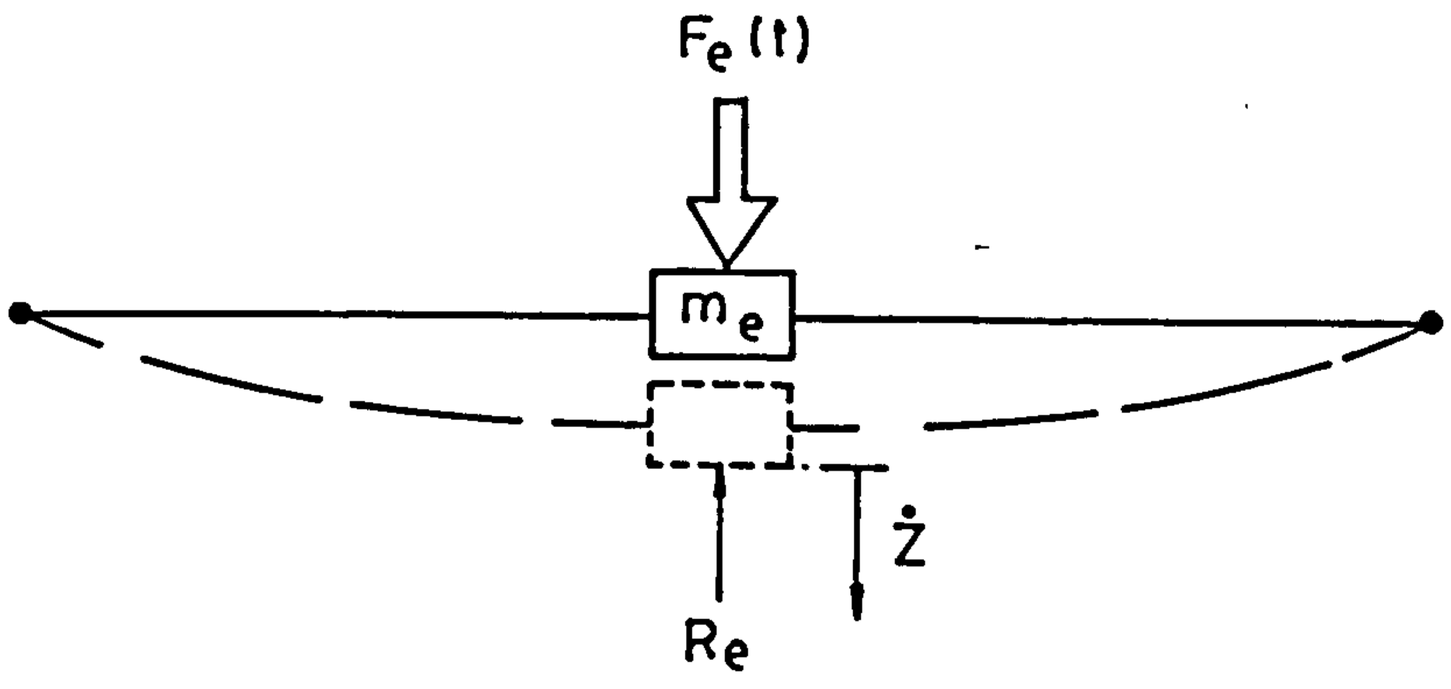

(b) Equivalent system

Notations: see section 5.5

FIG. 5.10 EQUIVALENT ONE DEGREE OF FREEDOM SYSTEM

Dynamic Increase Factor	Ultimate Moment of Resistance (kNm)			Load Carrying Capacity (kN)		
	P_e = 9.5 kN		Carrier bars only Normal	P_e = 9.5 kN		Carrier bars only Normal
	Normal	Reverse		Normal	Reverse	
1.000	0.81	0.23	0.13	5.40	1.33	0.87
*1.125	0.91	0.26	0.15	6.07	1.49	0.97

* section 5.2.1

Notation P_e = effective prestressing force

TABLE 5.1 ULTIMATE MOMENT OF RESISTANCE
AND
LOAD CARRYING CAPACITY (FOR ALL BEAMS)

Piano wire	Fully Bonded P_e = 9.5 kN		All Bond Loss	
Section	Uncracked	Cracked	Uncracked	Cracked
Second Moment of Area I (mm^4)	1.10×10^6	2.38×10^5	1.08×10^6	1.47×10^5
Beam* Stiffness K (kN/mm)	5.44	1.18	5.35	0.73

* Eqn. 5.1

TABLE 5.2 BEAM STIFFNESS

Force at Bullet/Pressure Bar Interface F_I	Time after Impact μs
1.000	0
0.098	134
0.010	268
-0.674	383

TABLE 5.3 FORCE AT BULLET/PRESSURE BAR INTERFACE

Time (μs)	F_{RM} x -1 (kN)	F_I' x -1 (kN)	A_2 (mm^2)	F_T (kN)	I_T (kNμs)	Notations see section 5.3
0	80.6		0	0	0	A_2 linearly interpolated
1	55.2		506.7	25.4	12.7	
5	55.0		509.0	25.6	102.2	
10	54.9		513.7	25.8	128.5	
15	54.7		516.1	25.9	129.2	
20	54.5		520.8	26.1	130.0	A_2 eqn. 5.9
25	54.5		523.2	26.2	130.7	
30	52.5		571.6	28.2	136.0	
35	50.5		621.5	30.2	146.0	
40	44.4		783.5	36.3	166.2	
45	38.2	25.6	2123.7	71.1	268.4	
50	34.2	25.8	2300.9	74.3	363.3	
55	28.2	25.9	2581.1	78.9	382.8	
60	26.2	26.1	2694.9	80.6	398.7	
65	24.2	26.2	2803.0	82.2	407.2	
70	20.2	28.2	3128.1	86.2	422.1	
75	20.2	30.2	3235.2	88.0	436.5	
80	16.1	36.3	3826.8	94.6	456.5	
85	16.1	71.1	5765.5	109.9	511.4	A_2 eqn. 5.11
90	16.1	74.3	5944.0	111.0	552.2	
95	20.2	78.9	5840.2	110.4	553.4	
100	20.2	80.6	5933.4	110.9	553.2	
105	22.2	82.2	5848.8	110.4	533.3	Beam 2.1
110	24.2	86.2	5913.3	110.8	533.0	Total I_T = 10.19 Ns
115	26.2	88.0	5820.3	110.2	552.6	
120	28.2	94.6	5993.8	111.2	533.8	
125	30.2	109.9	6581.6	114.4	564.3	
130	33.2	111.0	6468.0	113.9	570.8	
134	33.7	110.5	6316.8	113.1	453.8	

TABLE 5.4 IMPULSE TRANSMITTED CALCULATION SHEET

Reference	Series		1	2	3	4
Table 3.2	Mass Per Unit Length, m (kg)		6.717	6.662	6.822	7.032
Table 5.1	Dynamic ultimate moment of resistance (kNm)	Normal Mp	0.91			
		Reverse Mp'	0.26			
Section 3.7.6	Mass of Bullet, M (kg)		1.687			
Section 3.2.1	Half span L (m)		0.3			
Eqn. 5.2.2	Effective span le (m)		0.4284	0.4284	0.4287	0.4290
Eqn. 5.30	Dynamic Deflection constants x 10^{-3} (s^2/m)	k_1	0.015			
Eqn. 5.37		k_2	0.134			
Eqn. 5.38	Dynamic Reactions (kN)	Uplift R'	3.03	3.03	3.04	3.04
Eqn. 5.39		Normal R	4.55			

TABLE 5.5 THEORETICAL RESULTS DERIVED FROM DYNAMIC PLASTIC MODEL

Series	Beam Number	Impulse Transmitted (Section 5.3.3) I_T (Ns)	Equivalent Mass m_e (kg) (Eqn. 5.40)			Energy Absorbed by Beam $W_e(I)(J)$ (Eqn. 5.46)			Equivalent Mass ** M_e (Eqn. 5.50) (kg)	Initial Beam Velocity $\dot{Z}_o$ (Eqn. 5.50) (m/s)
			Pin-ended (Elastic)	Fix-ended (Elastic)	Plastic	Pin-ended (Elastic)	Fix-ended (Elastic)	Plastic		
1	1	7.24*	1.410	1.065	0.950	18.6	24.6	27.6	5.100	3.60
	4	5.44				10.5	13.9	15.6		2.23
	5	16.86				100.8	133.5	149.6		22.53
	6	16.98*				102.2	135.4	151.7		21.70
	7	20.58				150.2	198.8	222.9		31.33
	8	19.94*				141,0	186.7	209.3		31.42
	9	22.24				175.4	232.2	260.3		38.52
	10	20.82				153.7	203.5	228.1		38.50
2	1	10.19	1.398	1.056	0.942	36.5	48.3	54.1	5.095	7.15
	3	7.00				17.5	23.2	26.0		3.00
	5	15.02				80.7	106.8	119.8		13.89
	6	15.37				84.5	111.8	125.4		15.90
	7	19.79				140.1	185.4	207.9		30.20
	8	19.35				133.9	177.3	198.7		28.65
	9	20.99				157.6	208.6	233.8		36.59
	10	19.02				129.4	171.3	192.0		36.42
3	1	7.23	1.433	1.082	0.965	18.2	24.1	27.1	5.117	4.28
	4	8.43				24.8	32.8	36.8		4.34
	5	16.29				92.6	122.6	137.5		21.87
	6	15.21				80.7	106.9	119.8		18.26
	7	18.67				121.6	161.1	180.6		20.35
	8	20.04				140.1	185.6	208.1		29.87
	9	21.95				167.6	222.0	248.9		38.52
	10	21.39				159.6	211.4	237.1		37.21
4	1	15.46	1.478	1.116	0.996	80.8	107.1	120.0	5.151	12.92
	4	15.13				77.4	102.6	114.9		13.56
	5	14.86				74.7	98.9	110.8		19.53
	6	17.60				104.8	138.8	155.5		19.95
	7	20.70				144.9	192.0	215.1		31.20
	8	19.84				133.2	176.4	197.6		30.20
	9	21.95				163.0	215.9	241.9		38.37
	10	22.42				170.1	225.2	252.3		38.92

* Estimation

** Mass of pressure bar + fix-ended equivalent mass

TABLE 5.6 THEORETICAL RESULTS DERIVED FROM ONE-DEGREE OF FREEDOM SYSTEM

CHAPTER SIX

DISCUSSION AND COMPARISON OF EXPERIMENTAL AND THEORETICAL RESULTS

6.1 Introduction

This chapter discusses and compares the experimental results of this present work with the theoretical results as predicted by the analysis done in chapter 5. Since most static model beams failed by tendons slipping, some experimental results obtained by Hughes and Speirs[22] are also compared with the predictions on deflection using the plastic model as proposed in chapter 5.

6.2 Static Test

6.2.1 Beam Stiffness

The average initial beam stiffness of all intact beams is 2.38 kN/mm with a maximum of 3.9 kN/mm and a minimum of 1.6 kN/mm (table 4.1 and table 4.3). Since the theoretical boundaries for the prestressed beams (cracked and uncracked sections) are 1.18 and 5.44 kN/mm (table 5.2), this indicates all the beams are partially cracked.

6.2.2 Failure Mode

All the statically loaded beams showed the regular load-deflection characteristics of a prestressed concrete beam at the beginning until the first crack formed. More cracks were formed later. The bond stress increased suddenly at these cracks owing to the abrupt transfer of stress from concrete to steel at such points. If the bond stress is higher than the bond strength, it would lead to local bond failure. This was usually the case in the experimental programme. As a result, the tendons slipped and it must be concluded that a better model prestressing tendon is needed.

In beam 3.2, all the tendons fractured which is as assumed in the theoretical analysis, but the failure load is 11 % higher than the predicted value (table 4.1 and table 5.1). This is probably due to the confinement of the concrete and hence there is an apparent increase in its strength and ultimate

strain. This beam is therefore used as the upper bound in every aspect for all beams in the impact test.

6.3 Impact Force-time History

The measured peak force is 4.5 % higher than the predicted value (equation 4.1 and equation 5,6). Ang[34] suggested that the higher value was due to the magnetostrictive effect of the strain gauges, but in any event is remarkably accurate for impact work.

The experimental incident pulse also differs from the theoretical incident pulse by being more rounded, having oscillations at peak amplitude, a trapezoidal shape and a larger pulse duration (fig. 4.2b and fig. 5.5). These characteristics have already been reported by Ang[34]. The increase in the pulse duration can be attributed to the inherent response time of the instrumentation system. The oscillation at peak amplitude is most likely due to the frequency dependence of propagation velocity, signal noise or magnetostrictive effect on the strain gauges.

Figure 4.2b and figure 5.4 confirms that the bullet must have separated from the pressure bar 383 μs after impact or wave form C would shift by 134 μs away from wave form B. Since wave form D is similar to wave form B, the pressure bar must separate from the beam between 356 to 460 μs after impact.

The impulse transmitted is calculated in section 5.3.3 and is compared with the incident impulse in figure 6.1. For low energy impact i.e. below 100 J which is less than 2.5 times the static beam energy absorption capacity, all data points lie below the average experimental line. For impact with energy above 100 J then although the data are scattered, most of them lie above the average line, i.e. less energy is transmitted with the higher energy impact than with the lower energy impact. This may be due to the fact that the instantaneous damage at the point of impact had interrupted the transmission.

6.4 Impact Behaviour

6.4.1 Deflection at Midspan

The experimental deflections for different impact energy are compared

with the predicted values in figure 6.2. The predicted line, plotted by using equation 5.36 and table 5.5 and assuming all the bullet energy is absorbed by the hinges, marks the upper boundary since the energy absorbed by the hinges cannot be greater than the bullet energy. The experimental line is the average energy absorbed by the hinges calculated for all the experimental results by rewriting equation 5.36, using the same notations as before, by including the term η which is the proportion of the bullet energy absorbed by the hinges, i.e.

$$Z_{max} = \frac{L}{4}\left(\eta \frac{M}{M_p} - \frac{4k_1}{\alpha x}\right) v^2 \qquad \text{equ. 6.1}$$

The average η of all data is 0.667. i.e. a total of 33.3 % of the bullet energy is not absorbed by the hinges. This 33.3 % is made up by the energy retained in the bullet and the pressure bar, crack formation, local damage at the impact point, noise and vibrations, etc.

6.4.2 Reactions at Supports

The experimental dynamic reactions show a good agreement in magnitude with the theoretical results (section 4.3.4 and table 5.5).

The maximum uplift reaction is overestimated by 13.3 % and this may be due to the fact that the response time of the instrumentation system is not fast enough to record the maximum. Alternatively, it could indicate that the extreme portions, which are assumed to be stationary, do in fact rotate (section 5.4.1). The peak normal reaction is underestimated by 3.3 %

The reaction drops at a rate of 2.5 kN/ms approximately after the peak (section 4.3.4. and fig. 4.9) because the lever arm (2L/3) in equation 5.39 becomes equal to half the span (L) as the inertia effect is diminishing when the beam is coming to rest at its maximum deflection position. At this point, the reaction, using same notations as before, is given by

$$R = M_p/L \qquad \text{equ. 6.2}$$
$$= 0.81/0.3$$
$$= 2.7 \text{ kN}$$

The measured value is 85.0 % (2.3 kN) of this theoretical value. This discrepancy is perhaps due to the residual resistance of the 'moving' plastic hinge, the inertia effect or the instrumentation system response.

Beyond this time, the resistance of the hinges starts to drop and the reaction is reduced to zero. The oscillation about the time axis is then in accord with the beam oscillation as recorded in figure 4.5b.

Compared with the static reaction of 3.0 kN (beam 3.2), the peak dynamic reaction is 4.7 kN, which indicates an increase in dynamic compared with static shear.

6.4.3 Impact Energy Absorbed by the Beam

Equation 5.46 calculates the amount of the impact energy absorbed for all the experimental results. Using table 5.6 and assuming fix-ended supports, the average energy absorbed is 99.6 % (fig. 6.3a) of the bullet energy. This value is high. If it is assumed to be pin-ended, the average decreases to 75.2 % (fig. 6.3b). Since the beam is neither truly pin or fix-ended, the average of these two would give a better estimation. i.e. 87.4 %. The energy distribution can now be estimated. If

bullet energy = U_I, then

total energy absorbed by beam = $0.874\,U_I$, and

energy absorbed by hinges = $0.667\,U_I$.

The calculated equivalent mass used in equation 5.46 is expected to be slightly underestimated because only the effective span deduced from the plastic model (section 5.4) is taken into consideration. The calculated total energy absorbed is therefore slightly overestimated, but is expected to be closer than that given by Simms' approach (section 2.4.2), probably because Simms neglected the higher mode (reverse bending) of vibration.

Figure 6.3b also shows that under low impact intensity, i.e. bullet energy less than about 120 J, which is less than three times the static beam energy absorption capacity, the data points are mainly above the average line. For the experiments with bullet energy above 120 J, the energy absorbed is below the average line. This suggests the amount of energy absorbed is

affected by the instantaneous local damage at the impact point which was much greater for the high impact intensity experiments.

6.4.4 Initial Beam Velocity

The theoretical initial beam velocity for each series is added onto figure 4.7 using equation 5.50 and table 5.6. It shows a better agreement than the predictions for deflection, reaction and energy absorption because at this initial stage, plastic hinges and cracking had not had time to develop. The slight discrepancy is probably due to instrumentation error.

6.4.5 Crack Patterns

The main differences in the crack patterns under static and impact loadings, is that there is a punching shear plug, and shear and inverted flexural cracks in the impacted beam.

Under a static load, punching shear failure or extensive shear cracks are only expected in shallow members with heavy tension reinforcement, but with inadequate shear or compression reinforcement. The beams used in the present test programme showed no shear cracks when tested statically. This confirms that the shear effect is more pronounced in a beam under impact load than it is under a static load as stated in section 6.4.2.

Table 4.2 indicates that if the impact exceeded more than 80 J, i.e. twice the static beam energy absorption capacity, then formation of the punching shear plug could not be prevented even with four times the normal shear reinforcement for static condition (series 4).

The presence of inverted flexural cracks indicates that there is a reverse bending region with higher odd numbered modes (3rd, 5th, etc) of vibration in the beam, contrary to Simms'[16] assumptions.

6.4.6 Other Comments

Since there was no beam failed in shear and the shear force was increased, the strength of the shear reinforcement must be enhanced.

In sections 6.4.1 to 6.4.5, the extended Ezra's plastic model and the equivalent one-degree of freedom system, successfully predict the behaviour of the beam under impact loading with very acceptable accuracy, even though the bond strength was obviously low because it would not resist the bond stress in the corresponding static tests (section 6.2.2). This indicated that the theoretical ultimate moment of resistance is preserved under impact loading. In this case, either the impact bond strength is increased or the tendons are trapped and locked into position, due to the geometry of the deformed shape, and have no time to slip.

To give a further assessment of this method of analysis, the dynamic deflections for those beams with a symmetric cross section (area of compression steel = area of tension steel, same concrete cover) used by Hughes and Speirs[22] in their experiment were predicted using the method developed in chapter five. In total, 14 beams are compared (appendix I). It is found that the measured value, on average, is 78.7 % of the predicted despite the fact that a padding was used on these beams. Again, the plastic model gives a conservative upper boundary with an acceptable tolerance.

6.5 Post-Impact-Static Test

6.5.1 Beam Stiffness

The post-impact stiffness of the impacted beams varies from 9.6 % to 88.5 % of the initial beam stiffness, depending on the impact intensity (table 4.3 and figure 4.11). The major difference between the beams in the impact test is the amount of shear reinforcement. With larger amounts of shear reinforcement, the post-impact beam stiffness is higher. This indicated that shear contributes greatly to the overall damage and the enhancing effect of shear reinforcement in impact is again confirmed (sections 6.4.2 and 6.4.5).

6.5.2 Load Carrying Capacity

Figure 4.12 shows there is a significant loss in load carrying capacity if the impact intensity is higher than the static beam energy absorption capacity. This decrease is predominantly due to the fact that the impact had caused the tendons to fracture or slip, and part of the concrete in the compressive zone was heavily damaged and even dislodged.

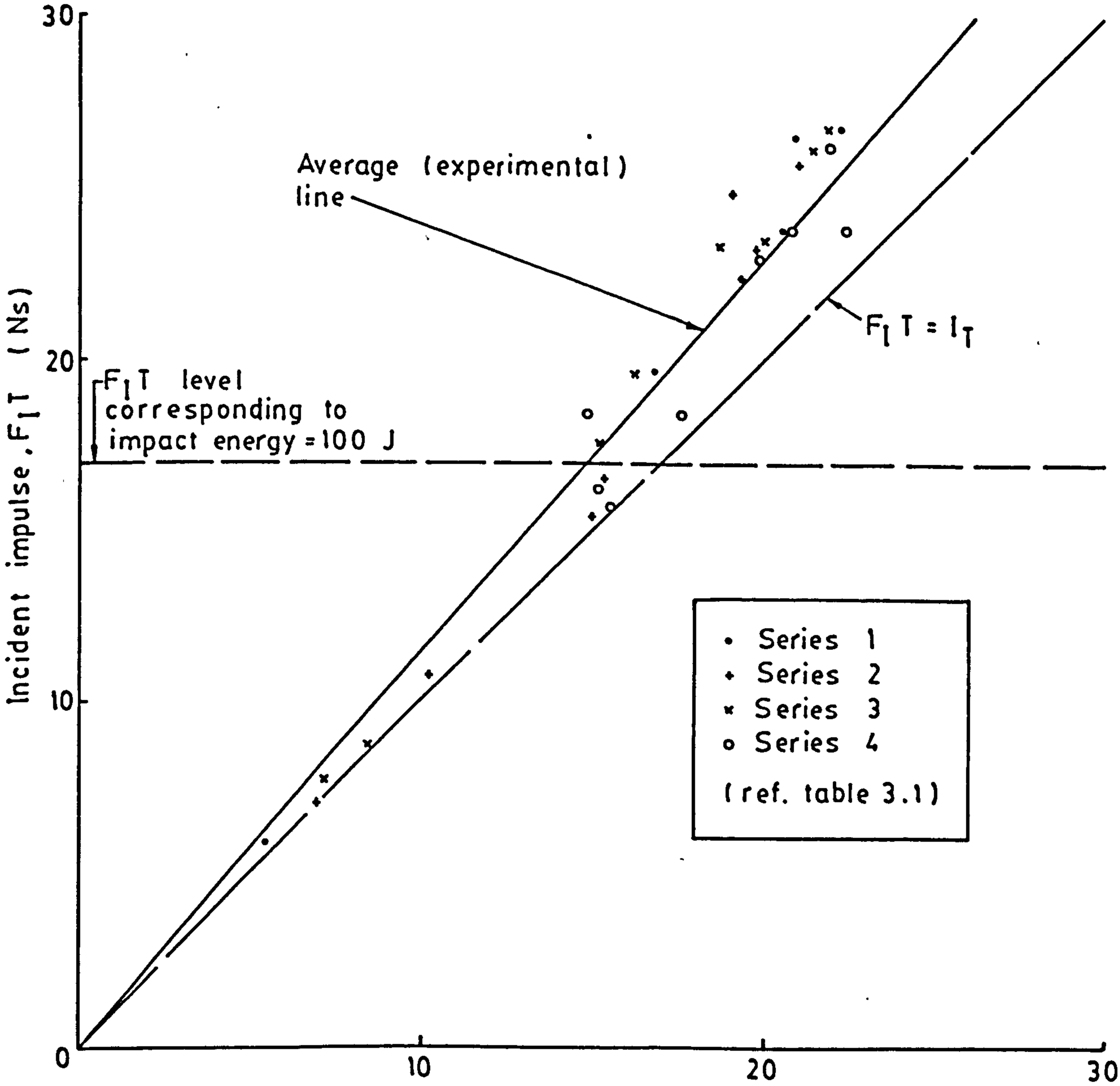

FIG. 6.1 INCIDENT IMPULSE AND IMPULSE TRANSMITTED RELATIONSHIP

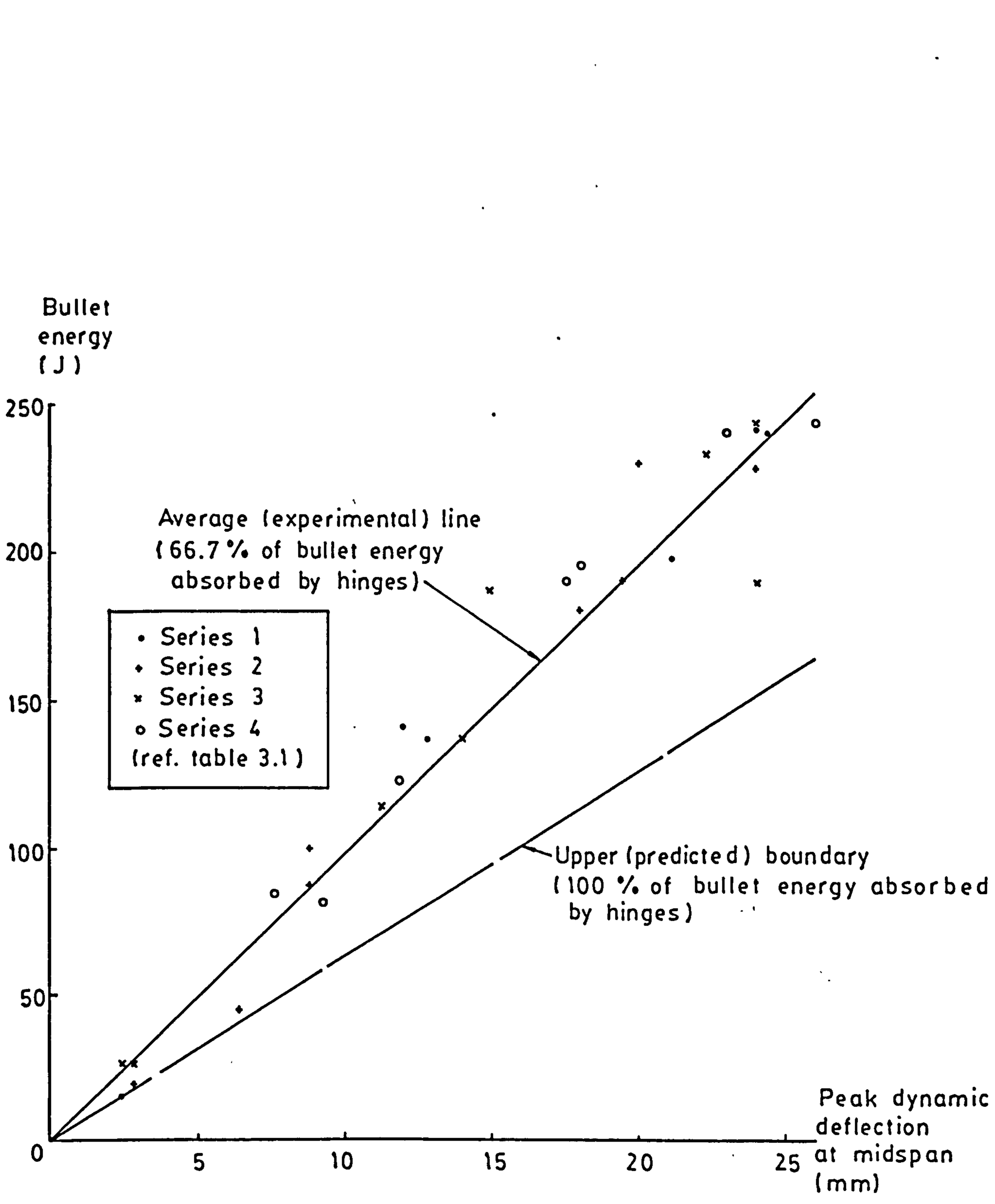

FIG. 6.2 BULLET ENERGY AND PEAK DYNAMIC DEFLECTION AT MIDSPAN RELATIONSHIP

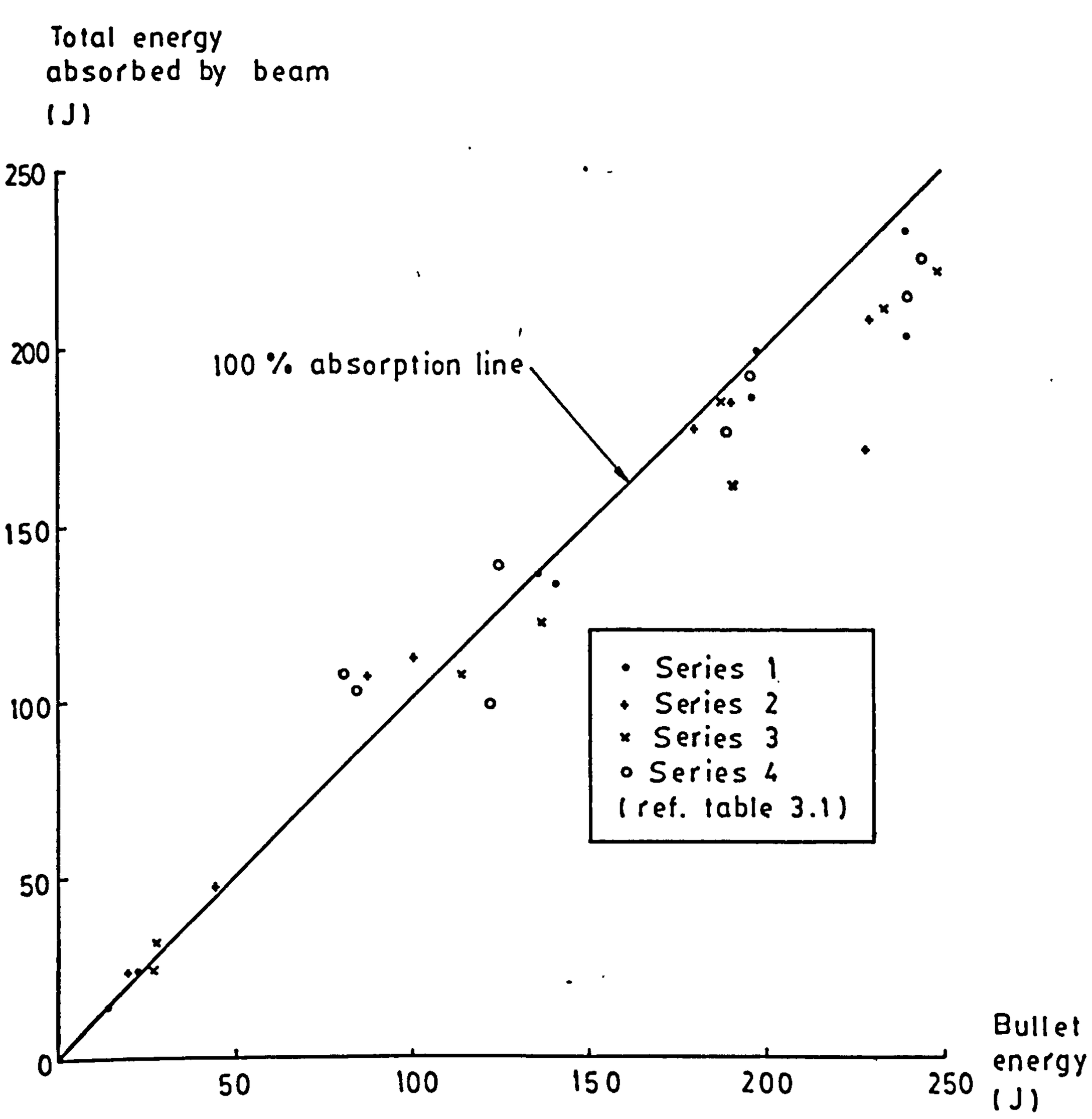

(a) Fixed end - elastic

FIG. 6.3 TOTAL ENERGY ABSORBED BY BEAM AND BULLET ENERGY RELATIONSHIP

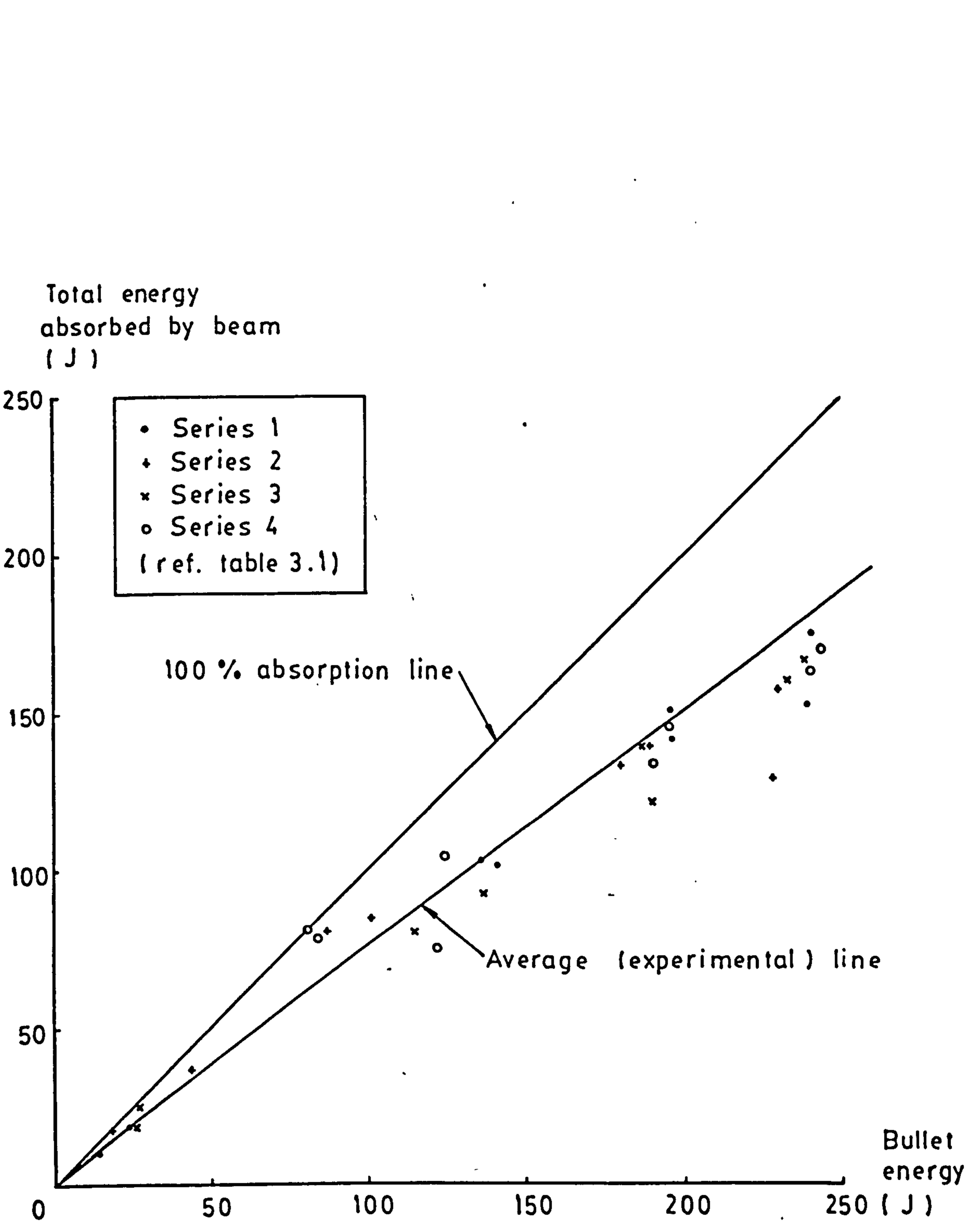

(b) Pinned end - elastic

FIG. 6.3 TOTAL ENERGY ABSORBED BY BEAM AND BULLET ENERGY RELATIONSHIP

CHAPTER SEVEN

CONCLUSIONS AND SUGGESTIONS FOR FUTURE WORK

7.1 Conclusions

From the experimental and theoretical studies carried out on pin-ended supported pretensioned prestressed concrete beams subjected to impact loading and static loading. the following conclusions can be drawn.

7.1.1 Static Tests

(1) Beams which failed in flexure (i.e. the tendons fractured), had a predicted failure load, determined by the method described in section 5.2.1, which was found to be in good agreement with the corresponding experimental failure load. Beams which failed by tendon slip, had an experimental failure much lower than the predicted failure load.

(2) From the experimental results, the initial beam stiffness for all beams was within the theoretical boundaries as calculated by the method described in section 5.2.2 using cracked and uncracked sections. This indicated that the beams must have been partially cracked.

(3) In both failure modes (i.e. tendon fracture or slip), all the beams showed the regular load-deflection characteristics for a prestressed concrete beam up to the formation of the first crack.

(4) The first crack was always a flexural crack under the loading point and was the widest.

(5) Only flexural cracks and flexural-shear cracks were found on the beams.

7.1.2 Impact Tests

(1) Theoretically (section 5.3.2), the impact force is directly proportional to the impact velocity and this was confirmed experimentally (section 4.3.1)

(2) The incident force-time history measured in the pressure bar was in good agreement with the prediction described in section 5.3.

(3) Higher percentage of the impact (bullet) energy was transmitted to the beam in low energy (i.e. below about three times the static beam energy absorption capacity) impact than in high energy impact.

(4) The deflection at midspan predicted by the plastic model, equation 5.36, (section 5.4), marked the upper boundary of all the experimental results.

(5) Theoretically (section 5.4.3), the deflection at midspan is directly proportional to the square of the impact velocity and this was confirmed experimentally (section 4.3.3).

(6) The average energy absorbed by the hinges in the plastic model (section 5.4) was found to be 66.7 % of the impact energy using equation 6.1 in section 6.4.1.

(7) The average total energy absorbed by the beam was found to be 87.4 % of the impact energy.

(8) The predicted magnitude of the reactions at the support based on the plastic model were in good agreement with the experimental results.

(9) The magnitude of the reactions was shown to be independent of the impact force but dependent on the span and the normal and reverse moment of resistance (section 5.4.4).

(10) Theoretically (section 5.5.4), the initial beam velocity is directly proportional to the impact velocity and this was confirmed experimentally (section 4.3.3).

(11) The crack pattern was very different from the one found in the static tests. In addition to the flexural and flexural-shear cracks, shear and inverted flexural cracks were present.

(12) The presence of the inverted flexural crack indicated that a higher odd number mode of vibration must be excited.

(13) The punching shear plug appeared whenever the impact energy was higher than about twice the static beam energy absorption capacity even with four times the required shear reinforcement for the static tests.

(14) Even when the tendons slipped, the predicted ultimate moment, assuming a flexural failure mode, was achieved.

(15) The magnitude of the shear force was greater than in the static tests.

(16) The effect of the shear reinforcement was enhanced.

(17) The effective span as defined in the plastic model, depended on the ratio of the bullet to beam mass (β) and ratio of the normal to reverse moment of resistance (α) as defined in section 5.4.2.

(18) The equivalent mass of the beam in the one-degree of freedom system, based on the concept of the effective span, was an underestimate and the transmitted energy was therefore overestimated, but was of acceptable accuracy.

(19) The method to predict the behaviour of the beams under impact loading, proposed in section 5.4 and section 5.5, appears to be satisfactory.

7.1.3 Post-Impact-Static Tests

(1) For similar bullet energy, the closer the shear stirrups, the higher was the percentage of the initial stiffness preserved.

(2) The higher the bullet energy, the lower was the peak strength and beam stiffness.

7.2 Suggestions for Future Work

(1) High speed cine photography which is not employed in this investigation may be used to record the beam response and the development of cracks during the period of impact.

(2) More conventional beam section for prestressed concrete beams, i.e. I-section, may be used so that the impact effect on the web or flange can be studied.

(3) The following parameters may be included in future work.

a. percentage of prestressing steel,

b. position of the prestressing steel,

c. prestressing force,

d. different concrete mix,

e. span/ depth ratio of the beam,

f. type of support condition,

g. different scales for comparison.

(4) The existing air gun may be modified by varying

a. the length of the bullet,

b. shape of the bullet nose,

so that the shape of the incident pulse can be varied.

References

(1) Allen A H, "An Introduction to Prestressed Concrete", C & C A, 1978.

(2) Lin T Y and Burns N H, "Design of Prestressed Concrete Structures", John Wily & Sons, 1982.

(3) Bernardnes C, "Effects of Impact on Reinforced Concrete Beams", MEng Thesis, University of Sheffield, 1979.

(4) Struck W and Voggenretier W, "Examples of Impact and Impulsive Loading in the Field of Civil Engineering", of 'The Effect of Impact Loading on Building, State-of-the-Art Report', Materials and Structures, RILEM, Vol. 8, No. 44, March/ April, 1975.

(5) Al-Azawi T K, "Impact Resistance of Reinforced Concrete Slabs", PhD Thesis, University of Sheffield, 1984.

(6) Lai K N, "Impact Capacity of Prestressed Beams Built with Plain, Polypropylene and Steel Fibre Concretes", PhD Thesis, University of Birmingham, 1980.

(7) Hughes G and Beeby A W, "Investigation of the Effect of Impact Loading on Concrete Beams", The Structural Engineer, Vol. 60B, No. 3, Sept., 1982.

(8) Burns N H, "Moment Curvature Relationships for Partially Prestressed Concrete Beams", Journal of PCI, Vol. 9, No. 1, Feb., 1964.

(9) Lin T Y, "Load Balancing Method for Design and Analysis of Prestressed Concrete Structures", Journal of ACI Proceedings, Vol. 60, No. 6, June,1963.

(10) Bate S C C, "The Effect of Impact Loading on Prestressed and Ordinary Reinforced Concrete Beams", National Building Studies Research Paper 35, Department of Scientific and Industrial Research, Building Research Station, 1961.

(11) ACI, "Nuclear Concrete Structures", ACI 349-76, Appendix C, JACI, Vol. 74, Feb., 1977.

(12) Mainstone R J, "Properties of Materials at High Rates of Straining or Loading", of 'The Effect of Impact Loading on Building, State-of-the-Art Report', Material and Structures, RILEM, Vol. 8, No. 44, March/ April, 1975.

(13) McHenry D and Shideler J J, "Review of Data on Effect of Speed in Mechanical Testing of Concrete", Symposium on Speed of Testing, ASTM, STP 185, 1956.

(14) Hughes B P and Watson A J. "Compressive Strength and Ultimate Strain of Concrete under Impact Loading", Magazine of Concrete Research, Vol. 30, No. 105, Dec., 1978.

(15) Mylrea T D, "Effect of Impact on Reinforced Concrete Beams", JACI, Vol. 36, June, 1940.

(16) Simms L G, "Actural and Estimated Impact Resistance of Some Reinforced Concrete Units Failing in Bending", JICE, No. 4, 1945.

(17) Cracknell C J and Jarman D A, "Effect of Heavy Impact Loads on Structural Member", Concrete, Sept., 1973.

(18) Norris C H et al, "Structural Design for Dynamic Loads", McGraw Hill, 1959 edition.

(19) Goldsmith W, "Impact - The Theory and Physical Behaviour of Colliding Solids", Edward Arnold, 1960 edition.

(20) Biggs J M, "Introduction to Structural Dynamics", McGraw Hill, 1964 edition.

(21) Van der Veen C and Blaauwendraad J, "Dynamic Elasto-Plastic Model for Reinforced Concrete Members", Heron, Vol. 28, No. 1, 1983.

(22) Hughes G and Speirs D M, "An Investigation of the Beam Impact Problem", Technical Report 546, C & C A, April, 1982.

(23) Home Office, "Domestic Nuclear Shelters - Technical Guidance", Home Office, 1982.

(24) BSI, "The Structural Use of Concrete", CP 110, part 1, BSI, 1972.

(25) Mavis F T and Greaves M J, "Destructive Impulse Loading of Reinforced Concrete Beams", JACI, Sept., 1957.

(26) Fey E H, Hansen R, Johnstone B, Newmark N and White M, "Discussion of Paper by Mavis and Greaces - Destructive Impulse Loading of Reinforced Concrete Beams", JACI, March, 1958.

(27) Seabold R H, "Dynamic in Shear Strengths of Reinforced Concrete", of 'Shear in Reinforced Concrete', ACI publication SP 42, Vol. 1, part 2, 1974.

(28) Karim M R, "Impact and Static Strengths of Prestressed Concrete Beams", PhD Thesis, University of Birmingham, 1977.

(29) Hughes B P, "Design of Prestressed Fibre Reinforced Concrete Beams for Impact", JACI, Vol. 78, No. 4, July-August, 1981.

(30) Watson A J and Ang T H, "Impact Resistance of Reinforced Concrete Structures", Joint Institution of Structural Engineers/ Building Research Establishment International Seminar of Dynamic Modelling of Structures, Nov., 1981.

(31) Watson A J and Ang T H. "Reinforced Microconcrete Beams under Impact Loading", RILEM, CEM, IABSE, IASS Interassociation Symposium Concrete Structures Under Impact and Impulsive Loading, Berlin, June, 1982.

(32) Mahmood A T, "Impact Behaviour of Model Prestressed Concrete Beams in Flexure", PhD Thesis, University of Birmingham, 1983.

(33) Hughes B P and Mahmood A T, "Impact Behaviour of Prestressed Concrete Beams in Flexure", Magazine of Concrete Research, Vol. 36, No. 128, Sept., 1984.

(34) Ang T H. "Impact Response and Post Impact Residual Capacity of Reinforced Concrete Structures", PhD Thesis, University of Sheffield, 1984.

(35) Mirza M S, "Reliability of Structural Concrete Models", of 'Reinforced and Prestressed Microconcrete Models', edited by Garas F K and Armer G S T, The Construction Press, 1980.

(36) Langhaar H L, "Dimensional Analysis and Theory of Models", Wiley, 1951 edition.

(37) Baker W E, Westine P S and Dodge F T. "Similarity Methods in Engineering Dynamics - Theory and Practice of Scale Modelling", Hayden Book Company, 1973 edition.

(38) Brideman P W, "Dimensional Analysis", Yale University Press, 1931.

(39) Inkester J E. "Dynamic Loading of a Reinforced Conccrete Model", PhD Thesis, University of Sheffield, 1980.

(40) Brock G, "Direct Models as an Aid to Reinforced Concrete Design", Engineering (London), Vol. 187, April, 1959.

(41) Harris H G et al, "Small Scale Direct Models of Reinforced and Prestressed Concrete Structures", School of Civil Engineering, Cornell Universty Report No. 326, Sept., 1966.

(42) Harris H G et al, "Reinforcement for Small Scale Direct Models of Concrete Structures", of 'Models for Concrete Structures', ACI SP 24, 1970.

(43) Clark L A, "Flexural Crack Similitude in Slabs Spanning One-Way", C & C A, Technical Report No. 496, Oct., 1974.

(44) Sabedi N K and Garas F K, "Bond Characteristics of Small Diameter Bars Used in Microcincrete Models", of 'Reinforced and Prestressed Microconcrete Models', edited by Garas F K and Armer G S T, The Construction Press, 1980.

(45) Evans D J and Clarke J L, "A Comparison Between the Flexural Behaviour of Small Scale Microconcrete Beams and that of Prototype Beams", C & C A Technical Report No. 542, March, 1981.

(46) Vos E. "Influence of Loading Rate and Radial Pressure on Bond in Reinforced Concrete - A Numerical and Experiment Approach", Delft University, 1983.

(47) White I G and Clark L A, "Bond Similitude in Reinforced Microconcrete Models", of 'Reinforced and Prestressed Microconcrete Models', edited by Garas F K and Armer G S T, The Construction Press, 1980.

(48) Clark L A, "Crack Similitude in Reinforced Microconcrete", of 'Reinforced and Prestressed Microconcrete Models', edited by Garas F K and Armer G S T, The Construction Press, 1980.

(49) Mirza M S, "Bond in Reinforced Concrete Models", of 'Reinforced and Prestressed Microconcrete Models', edited by Garas F K and Armer G S T, The Construction Press, 1980.

(50) Noor F A and Khalid M, "Deformed Wire Reinforcement for Microconcrete Models", of 'Reinforced and Prestressed Microconcrete Models', edited by Garas F K and Armer G S T, The Construction Press, 1980.

(51) Johnson R P, "Strength Tests on Small Scaled Down Concrete Suitable for Models, with a note on Mix Design", Magazine of Concrete Research, Vol. 14, No. 40, March, 1962.

(52) Litle W A and Paparoni M, "Size Effect in Small Scale Models of Reinforced Concrete Beams", Proc. ACI Journal, Vol. 63, No. 11, Nov., 1966.

(53) Syamal P K, "Direct Model in Combined Stress Investigations", MEng Thesis, Structural Concrete Series, No. 17, McGill University, July, 1971.

(54) Evans D J et al, "Some Size Effects in Reinforced Microconcrete Models", Structural Model Conference, Sydney, 1972.

(55) Sabnis G M and Mirza M S, "Size Effect in Model Concrete", ASCE Journal, Vol. 105, ST 6, June, 1979.

(56) Chowdhury A H and White R N, "Materials and Modelling Techniques for Reinforced Concrete Frames", JACI Proc., Vol. 74, No. 11, Nov., 1977.

(57) Mirza M S and McCutcheon J O, "Direct Models of Prestressed Concrete Beams in Bending and Shear", of 'Reinforced and Prestressed Microconcrete Models', edited by Garas F K and Armer G S T, The Construction Press, 1980.

(58) Alexander B F, "Use of Microconcrete Models to Predict Flexural Behaviour of Reinforced Concrete Structures under Static Loads", MIT, School of Engineering, March, 1965.

(59) Sabnis G M et al, "Structural Modelling and Experumental Techniques", Prentice-Hall, 1983.

(60) BSI. "Test Sieves". BS 410. BSI. 1962.

(61) BSI. "Concrete Aggregate from Natural Sources". BS 882. BSI. 1965.

(62) BSI. "Methods of Testing Concrete - Methods of Testing Hardened Concrete for Other Than Strength". BS 1881. part 5. BSI. 1970.

(63) BSI. "Recommendation for Non-destructive Methods of Test for Concrete : Measurement of the Velocity of Ultrasonic Pulses in Concrete". BS 4408. part 5. BSI. 1974.

(64) AASHTO. "Standard Specifications for Highway Bridges". article 1.6.15. American Assocition of State Highway and Transportation Officals. 12th edition. 1977.

(65) Marsall W T and Mattock A H. "Control of Horizontal Cracking in the Ends of Pretensioned Prestressed Concrete Girders". JPCI. Vol. 7. No. 5. Oct.. 1962.

(66) ACI. "Building Code Requirements for Reinforced Concrete". ACI std.. 318-77. ACI. 1977.

(67) Zia P and Mosatafa T. "Development Length of Prestressing Concrete". JPCI. Sept./ Oct.. 1977.

(68) ACI. "Models of Concrete Structures". Reprints of the Symposium of Models of Concrete Structures. ACI committee 444. 1972.

(69) Dally J W and Riley W F. "Experimental Stress Analysis". McGraw Hill. 1978 edition.

(70) Doebelin E O. "Measurement Systems - Application and Design". McGraw Hill. 1975 edition.

(71) Fylde Electronic Laboratories Ltd.. "Fylde Modular Instrumentation Handbook for FE-359-TA d.c. Bridge/ Transducer Amplifier". 1975.

(72) Solartron Instrumentation Group. "Dgital Multimeter 7045 Operating Manual",1981.

(73) Robinson T and Watson A J. "Manual for Operation of Commodore/ Bentham Data Logging System for Commodore 4032. Commodore 64. Bentham 266F A/D Convertor". Department of Civil and Structural Engineering. University of Sheffield. 1985.

(74) Tektronic Inc.. "T912 10 MHz Storage Oscilloscope Instruction Manual". 1975.

(75) BSI. "Wrought Steel for Mechanical and Applied Engineering Purposes". BS 970. BSI. 1970/ 72.

(76) Gould Instruments Ltd.. "Digital Storage Oscilloscope OS 4020 Instruction Manual".

(77) Robinson T. Private communication. Department of Civil and Structural Engineering, University of Sheffield.
(78) RDP Electronics Ltd., "Transducers for Research and Industry".
(79) Racal Thermionic Ltd., "Store 4 Provisional Technical Handbook", 1973.
(80) S E Laboratories (Engineering) Ltd., "Ultra-violet Recorders Types SE 3006 and SE 3006 DL Instruction Manual", 1968.
(81) Cass H. Private communication, Department of Civil and Structural Engineering, University of Sheffield.
(82) Racal-Dana Instruments Ltd., "Operators Handbook for Universal Counter Timer 9903", 1978.
(83) Johnson W. "Impact Strength of Materials", Edward Arnold, 1983 edition.
(84) Davies R M. "A Critical Study of the Hopkinson Pressure Bar", Philosophical Transactions of the Royal Society of London. Vol. 240, 1948.
(85) Hognestad E. "A Study of Combined Bending and Axial Load in Reinforced Concrete Members", Urbana, University of Illinois, Engineering Experiment Station Bulletin, No. 399, 1951.
(86) Pfrang E O, Siess C P and Sozen M A. "Load-Moment-Curvature Characteristics of Reinforced Concrete Cross Section", JACI, July, 1964.
(87) Corley W G. "Rotational Capacity of Reinforced Concrete Beam", JASCE, Structural Division, Vol. 92, No. ST 5, Oct., 1966.
(88) Bolton A. "Natural Frequencies of Structure for Designers", The Structural Engineer, Vol. 56 A, No. 9, Sept., 1978.
(89) Ripperger E A and Abramson H N. "Reflection and Transmission of Elastic Pulses in a Bar at a Discontinuity in Cross Section", Proc. 3rd Midwestern Conf. on Solid Mechanics, University of Michigan, 1957.
(90) Ezra A A. "The Plastic Response of a Simply Supported Beam to an Impact Load at the Centre", Proc. 3rd U. S. Nat. Congr. Appl. Mech. Am. Soc. Mech. Engrs., 1958.
(91) Parkes E W. "The Permanent Deformation of a Cantilever Struck Transversely at its Tip", Proc. Royal Soc., Series A, Vol. 228, 1955.
(92) Timoshenko S et al, "Vibrations Problems in Engineering", John Wiley and Sons, 1974 edition.

APPENDIX A

Load-Deflection Curves - Static Test

This appendix presents the load-deflection curves for the eight beams which were tested statically. These curves were obtained as described in section 3.7.5. The following notes apply to all 8 curves.

(a) The axis marked LC 1 is the load at midspan (section 3.7.4).

(b) The axis marked LVDT is the midspan deflection.

(c) The identification number of the beam is located at the top right-hand corner of the graph.

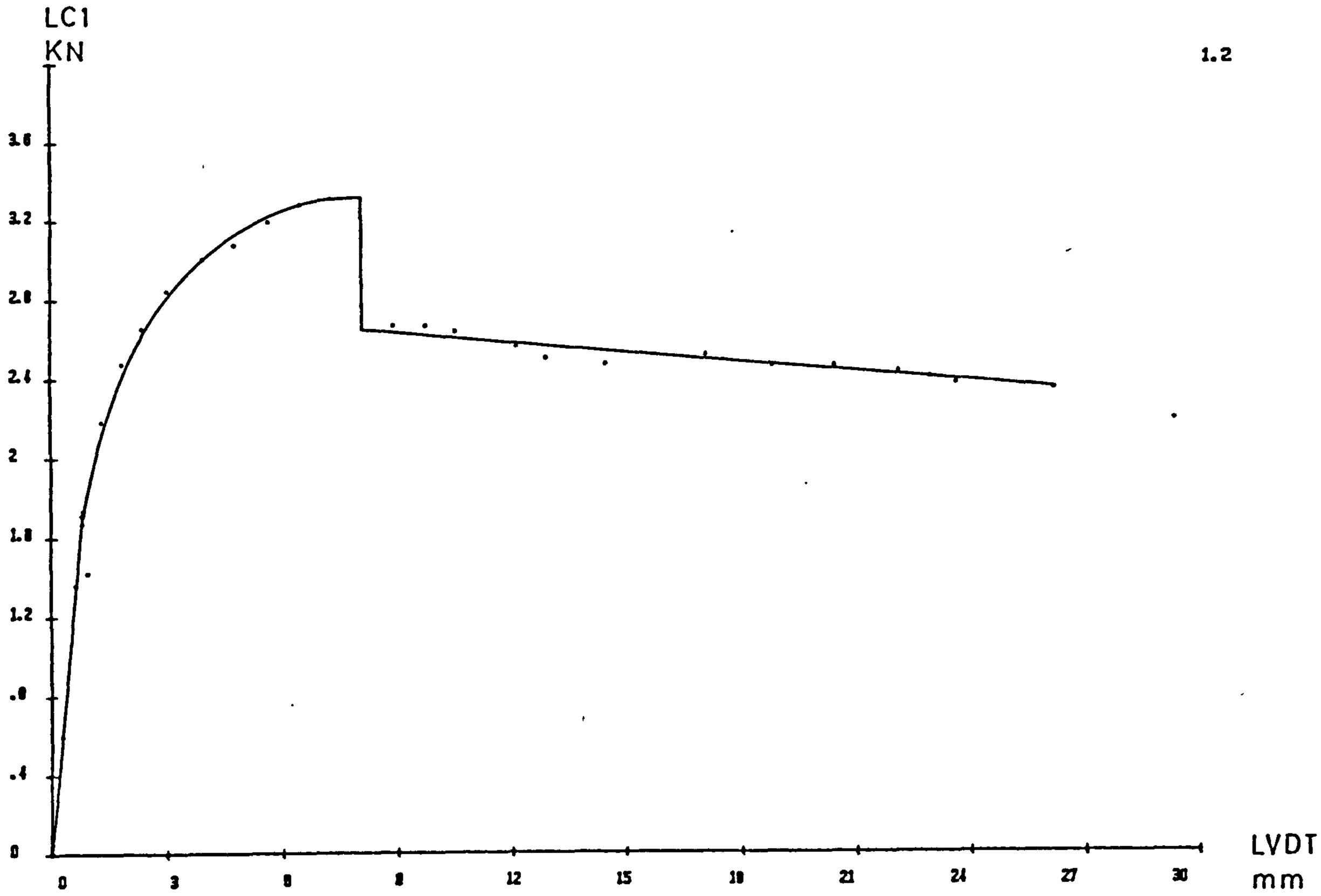

Notes : see page A1.

APPENDIX A LOAD - DEFLECTION CURVES - STATIC TEST

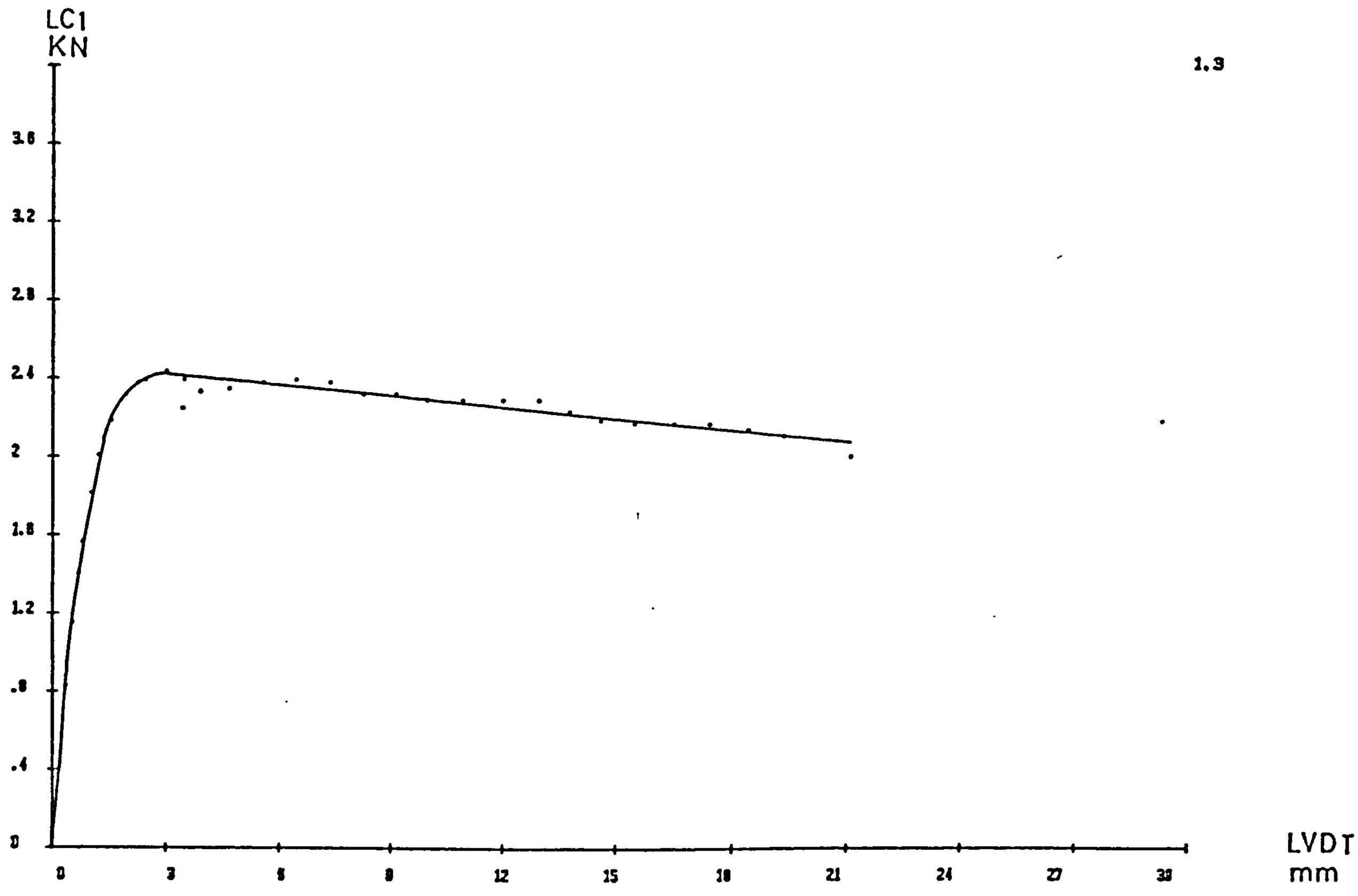

Notes : see page A1.

APPENDIX A LOAD - DEFLECTION CURVES - STATIC TEST

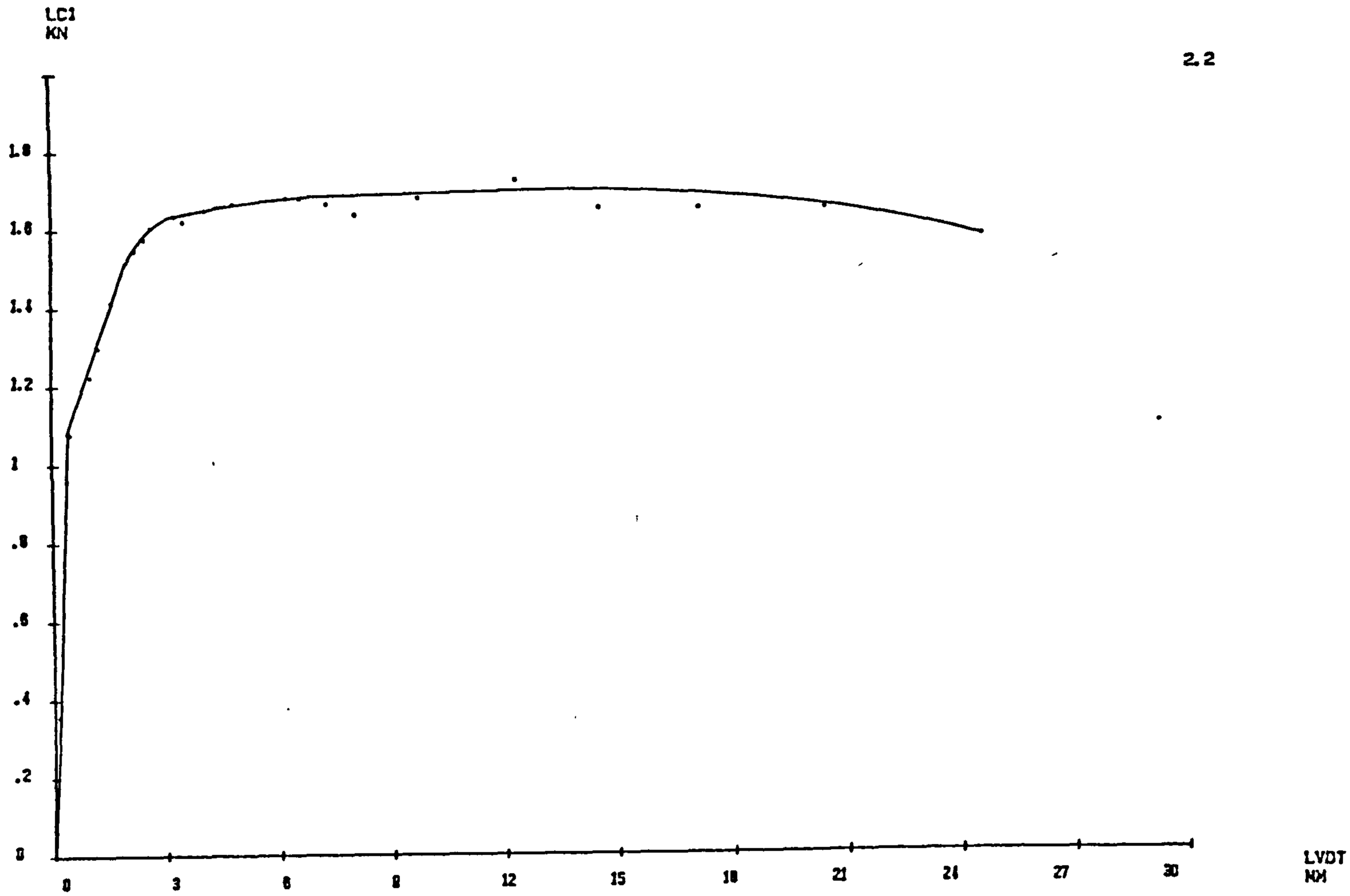

Notes : see page A1.

APPENDIX A LOAD – DEFLECTION CURVES – STATIC TEST

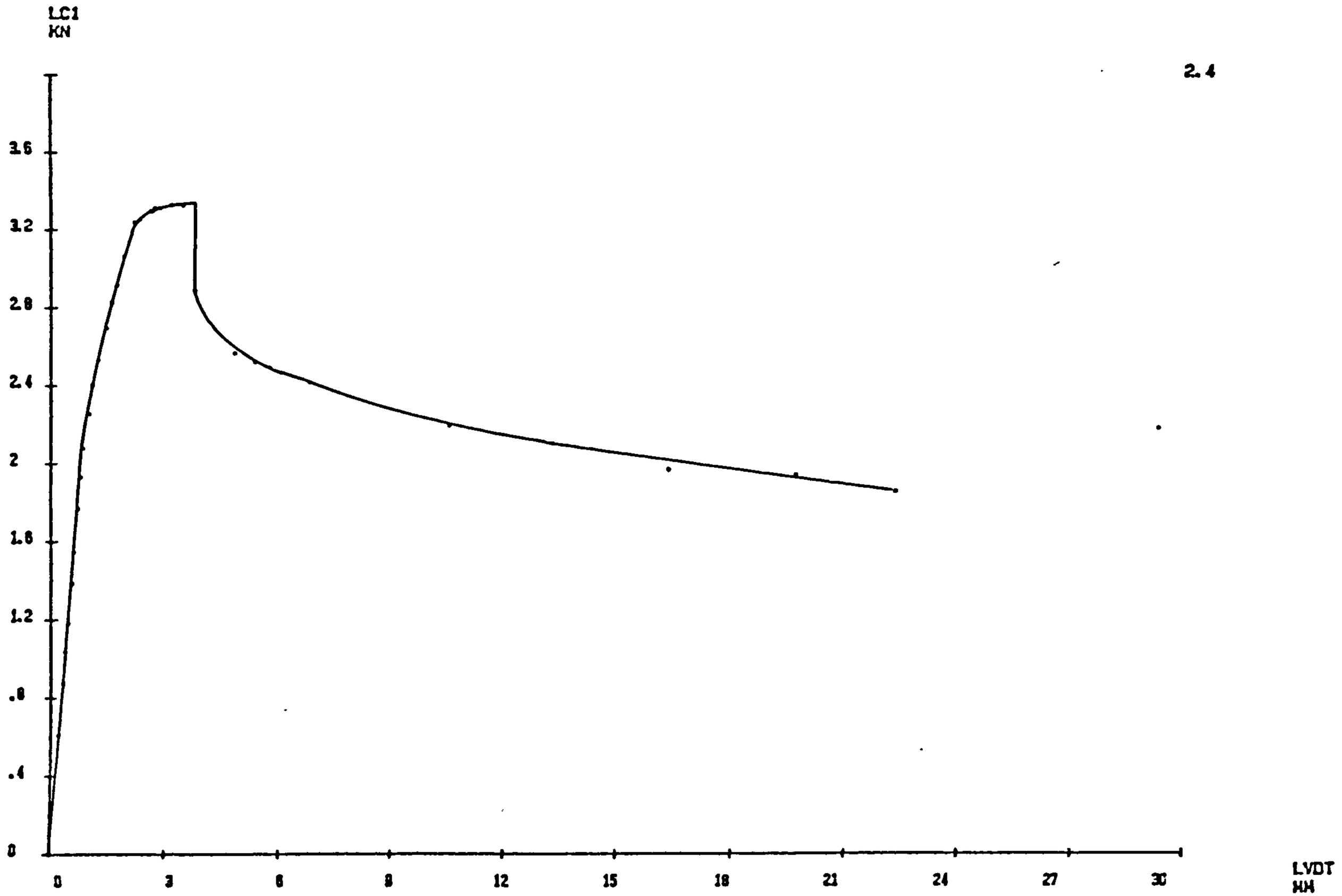

Notes : see page A1.

APPENDIX A LOAD - DEFLECTION CURVES - STATIC TEST

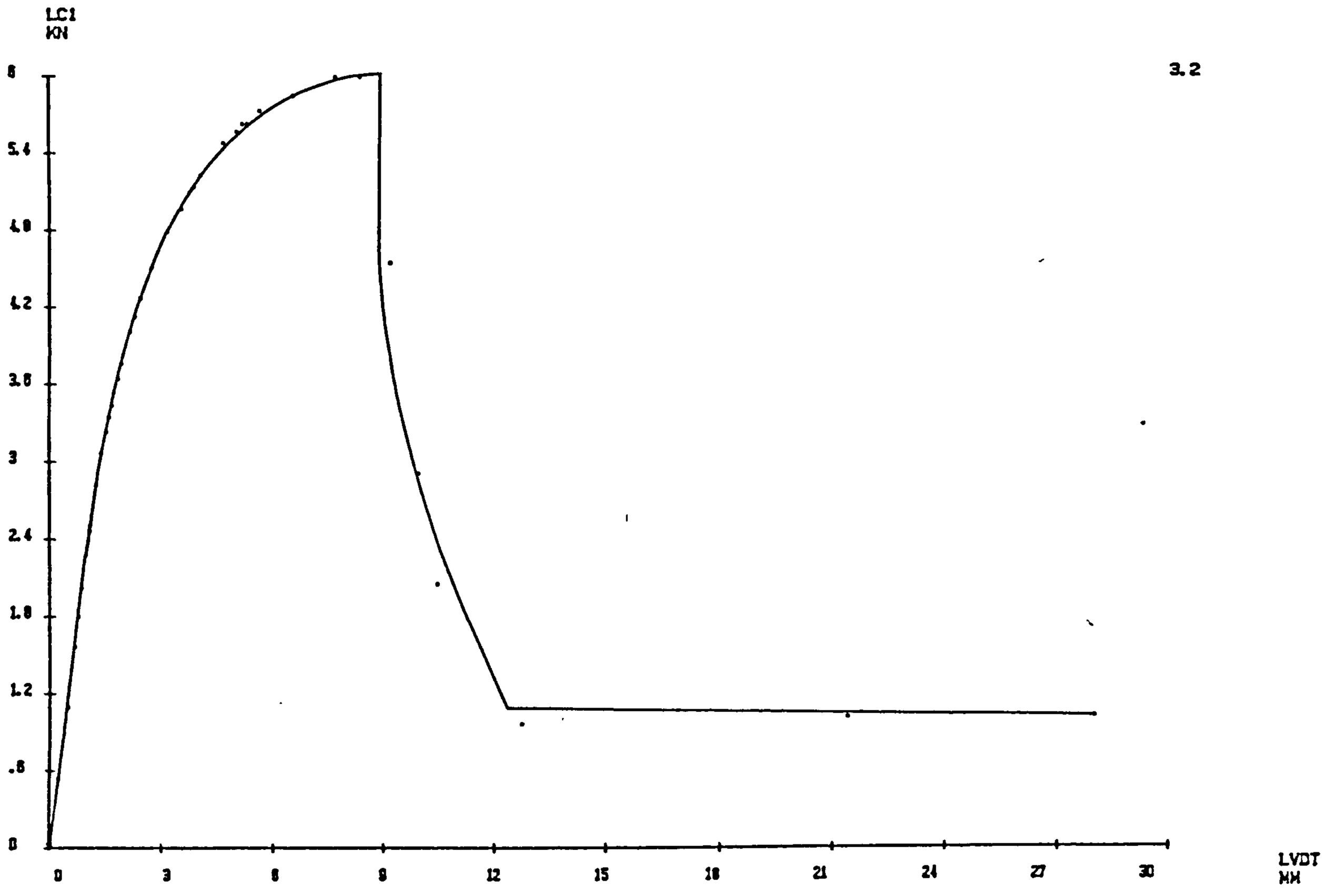

Notes : see page A1.

APPENDIX A LOAD - DEFLECTION CURVES - STATIC TEST

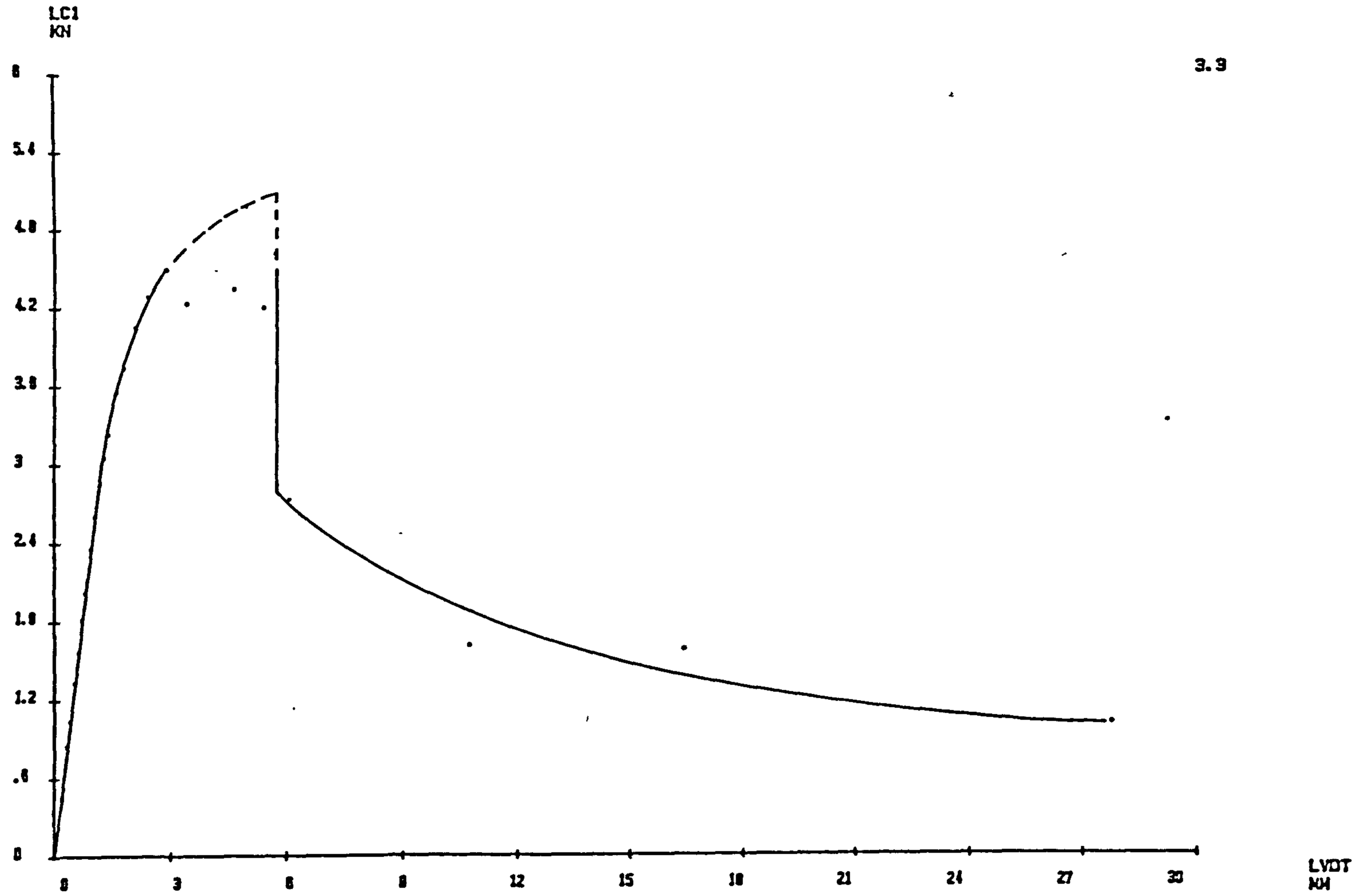

Notes : see page A1.

APPENDIX A LOAD - DEFLECTION CURVES - STATIC TEST

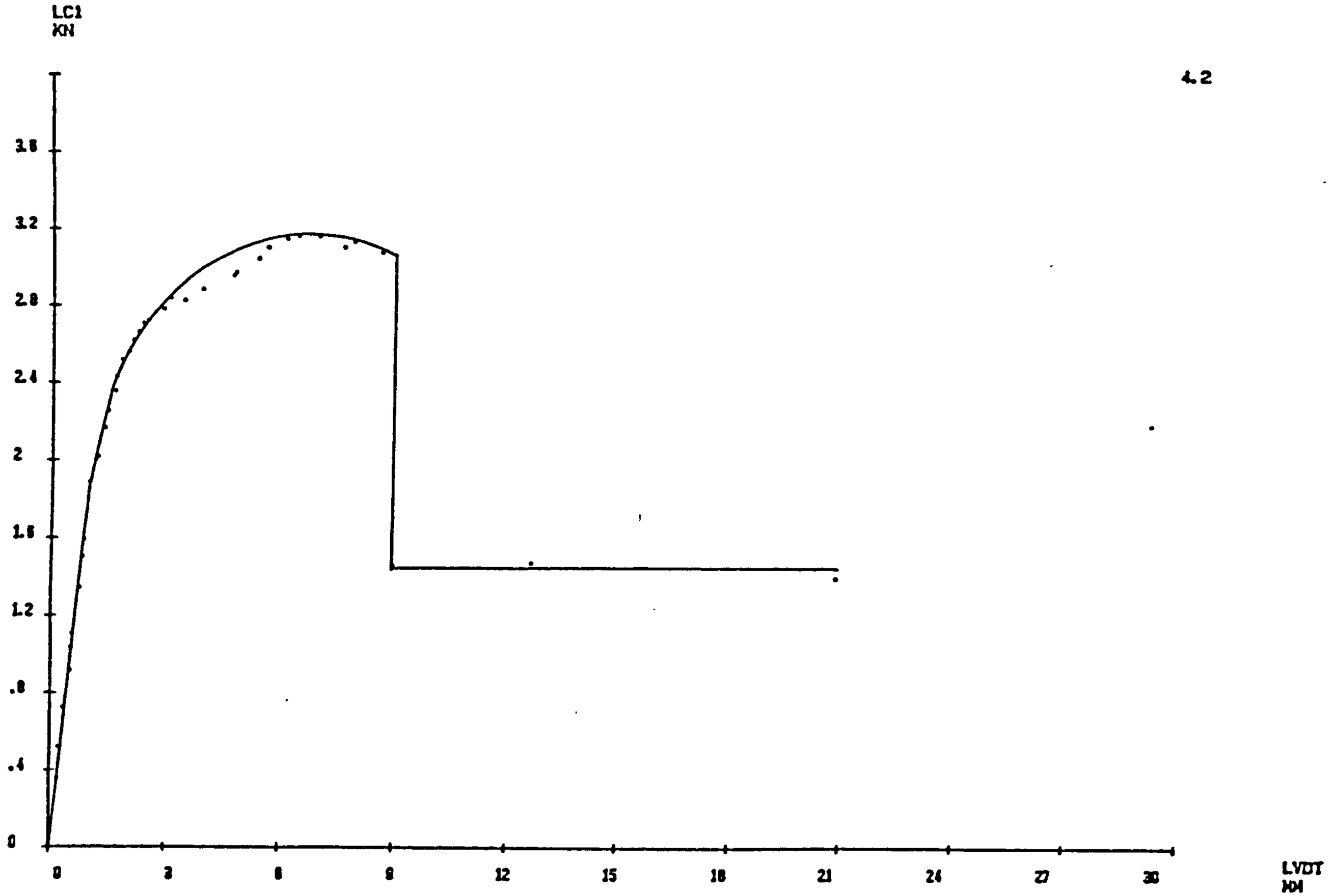

Notes : see page A1.

APPENDIX A LOAD - DEFLECTION CURVES - STATIC TEST

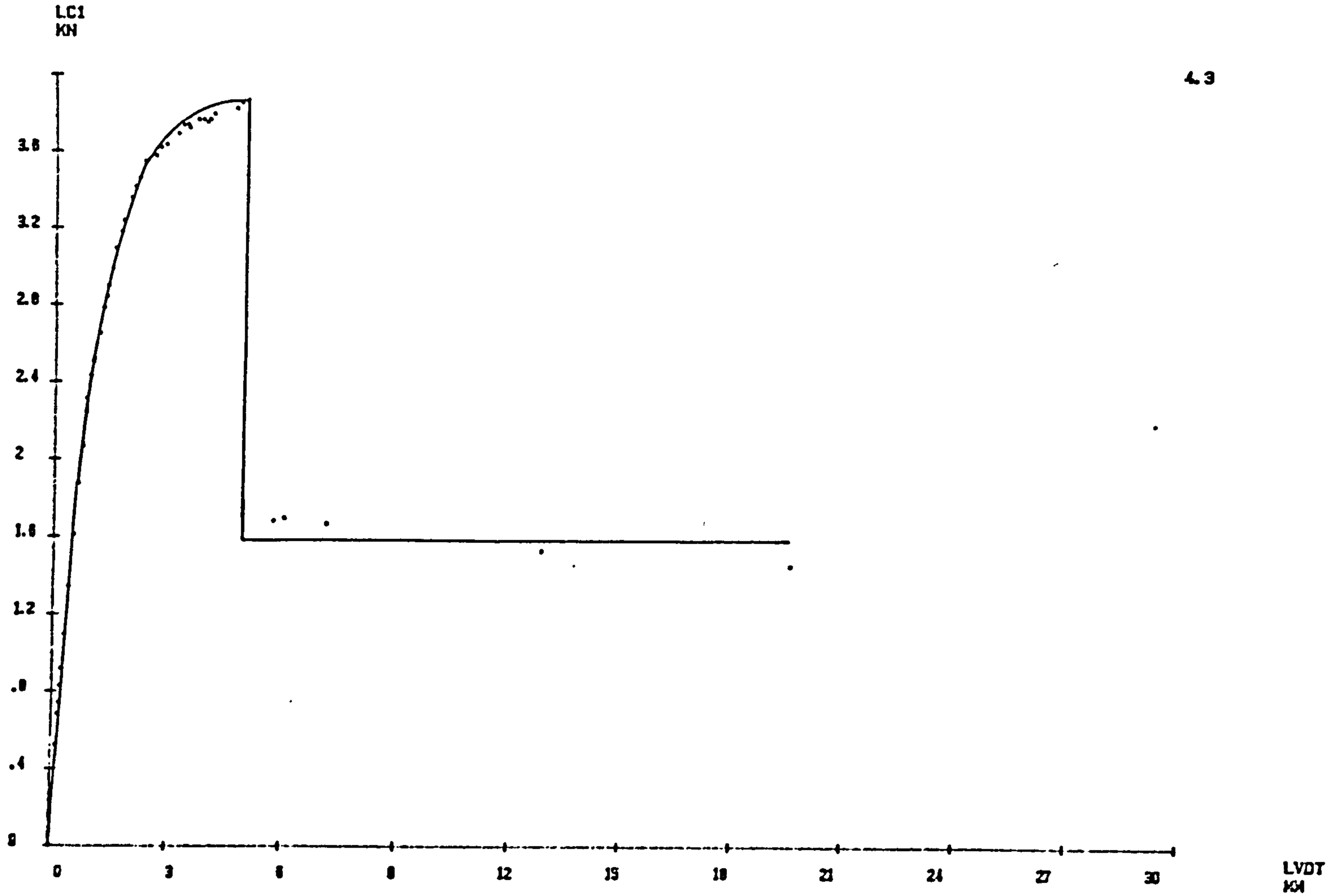

Notes : see page A1.

APPENDIX A LOAD - DEFLECTION CURVES - STATIC TEST

APPENDIX B

Impact Pulse Trace

This appendix contains the impact pulse traces which are obtained as described in section 3.7.5. The traces for beams 1.1, 1.6 and 1.8 were not recorded successfully. i.e. only 29 traces are presented. The following notes apply to all the 29 traces.

(a) The force axis has an abstract unit of volt and one volt is equivalent to 30 kN.

(b) The oscilloscope was triggered when the wavefront of the incident pulse reached the strain gauge station PB 2 (fig. 3.9) on the pressure bar.

(c) The trace which is marked CHANNEL 2 was connected to the strain gauge station PB 2.

(d) The trace which is marked CHANNEL 1 or unmarked was connected to the strain gauge station PB 1 (fig. 3.9) on the pressure bar.

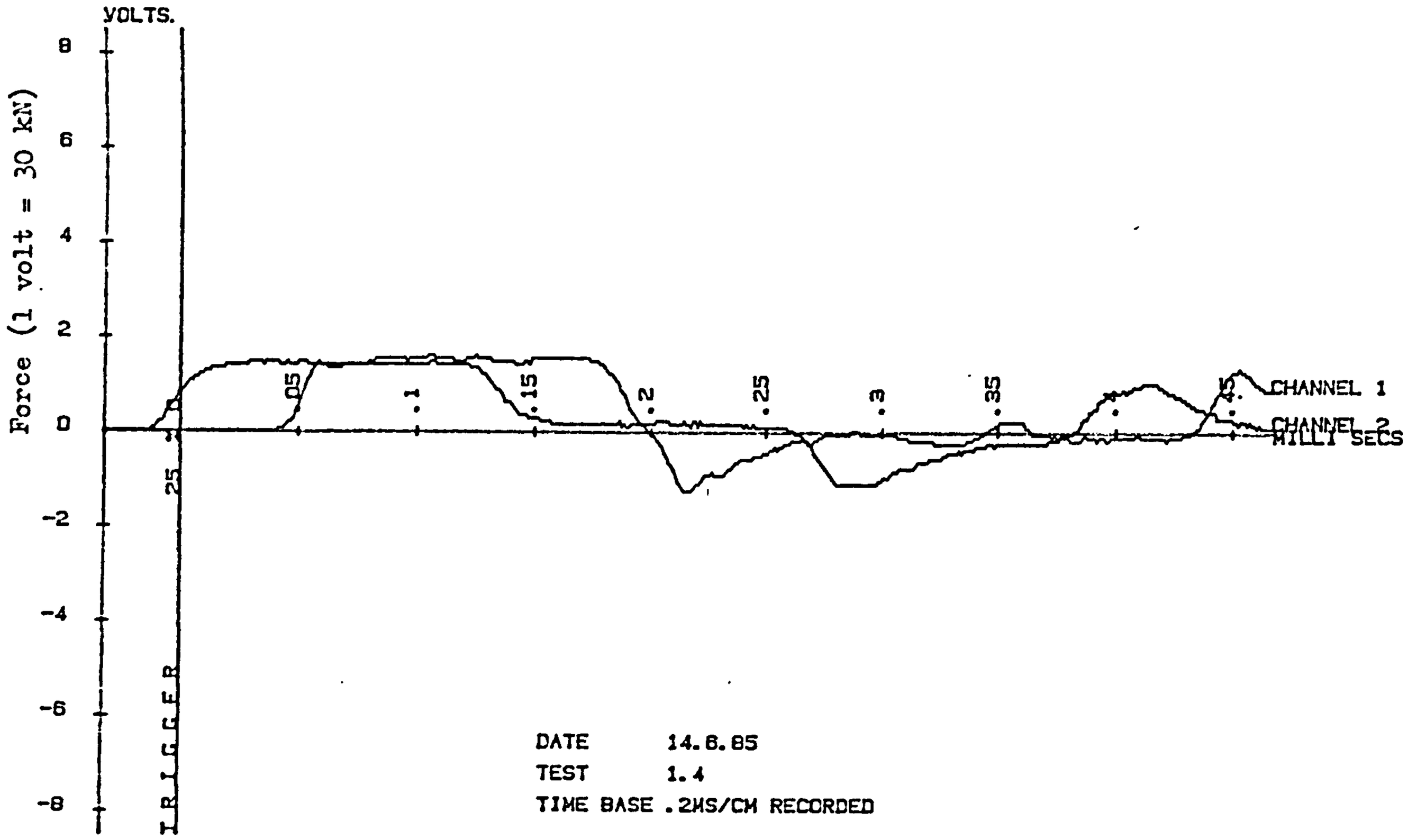

Notes : see page B1.

APPENDIX B IMPACT PULSE TRACE

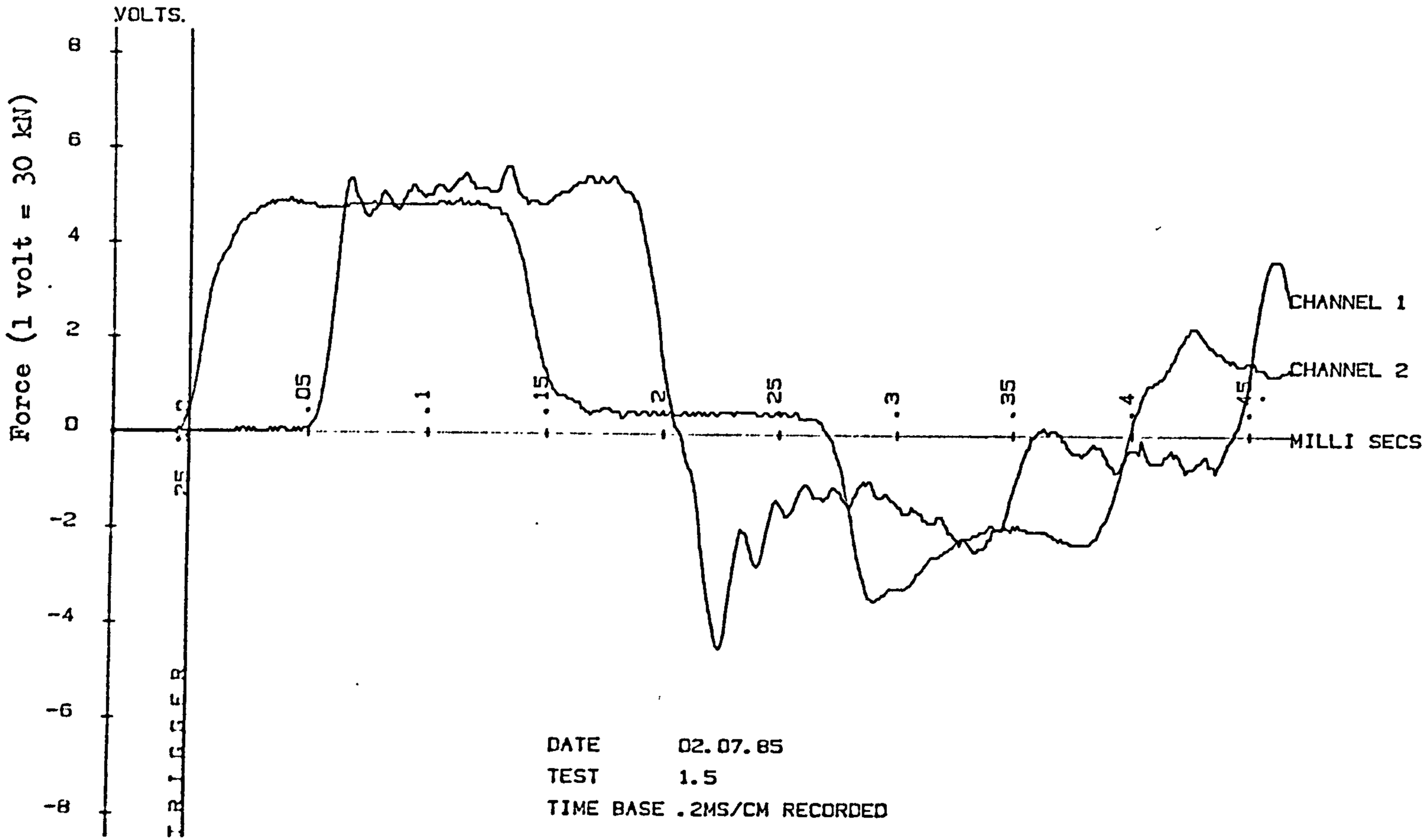

Notes : see page B1.

APPENDIX B IMPACT PULSE TRACE

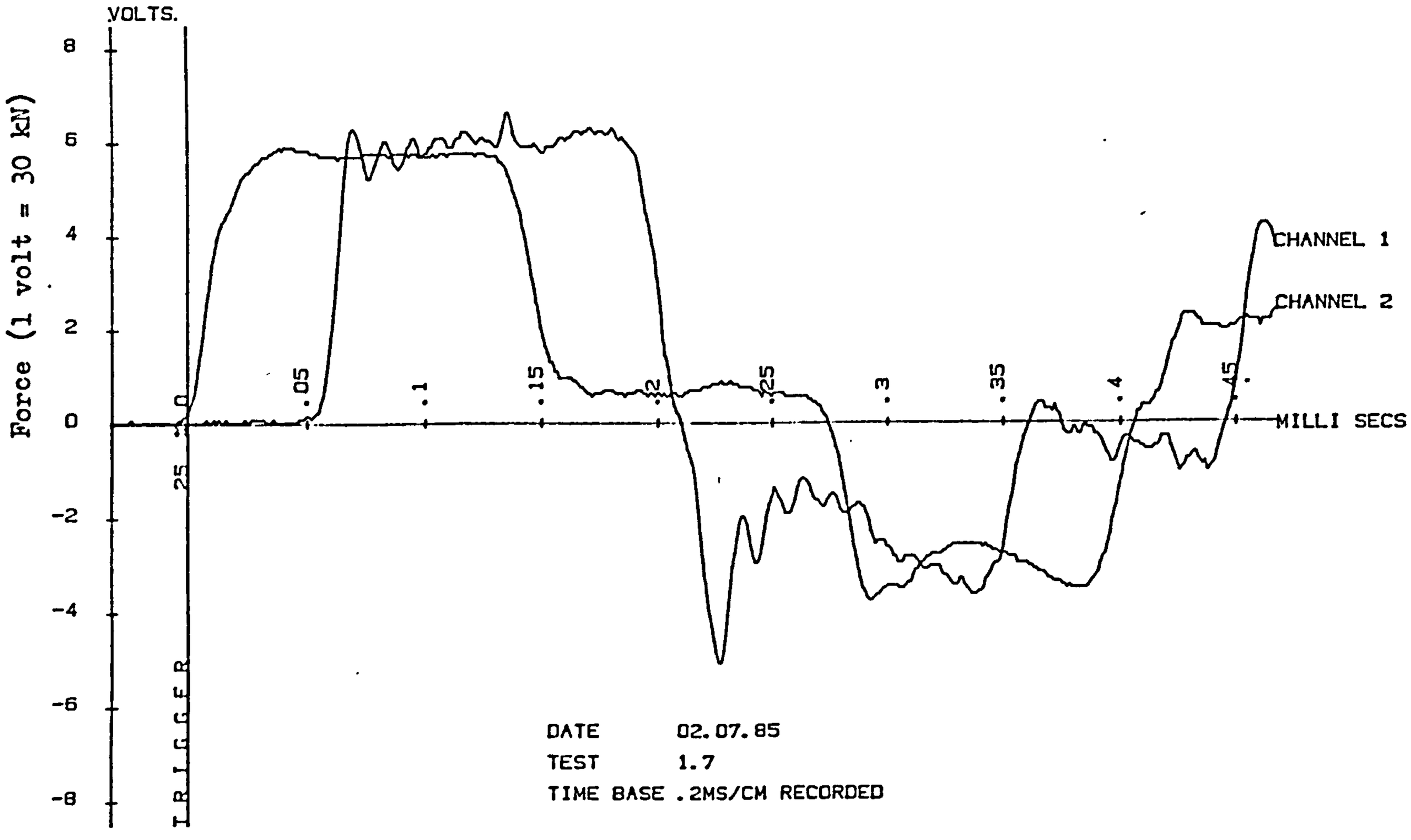

Notes : see page B1.

APPENDIX B. IMPACT PULSE TRACE

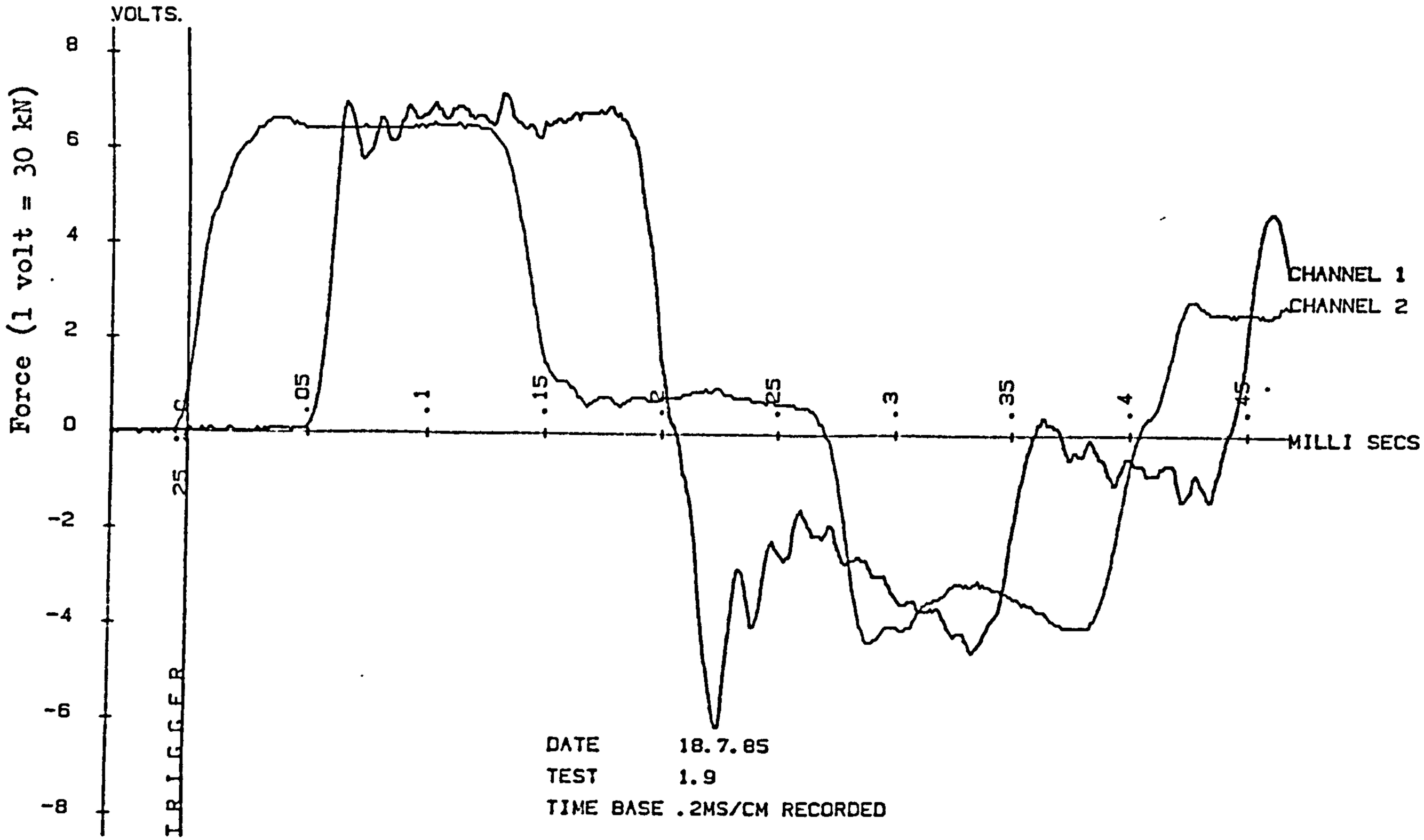

Notes : see page B1.

APPENDIX B IMPACT PULSE TRACE

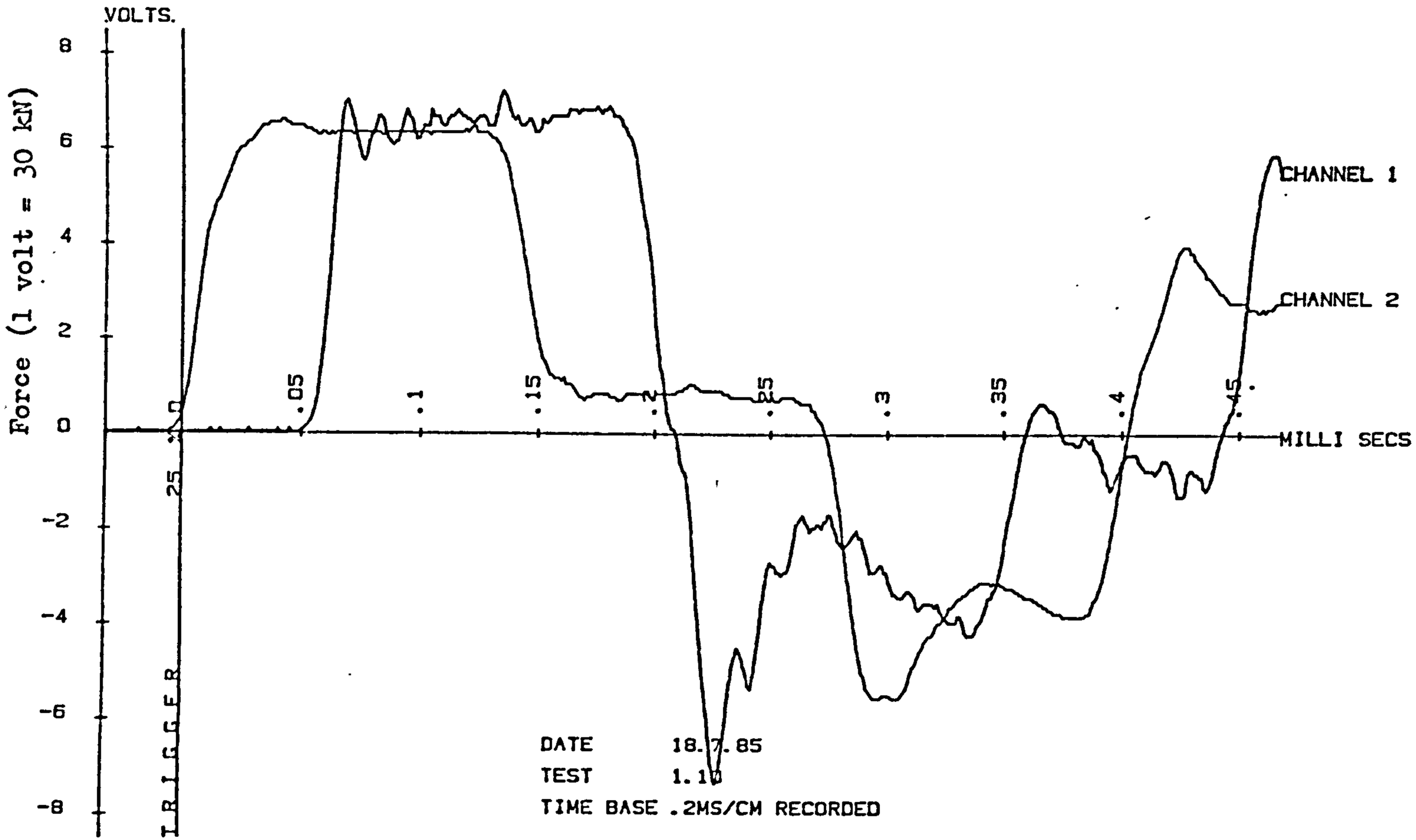

Notes : see page B1.

APPENDIX B IMPACT PULSE TRACE

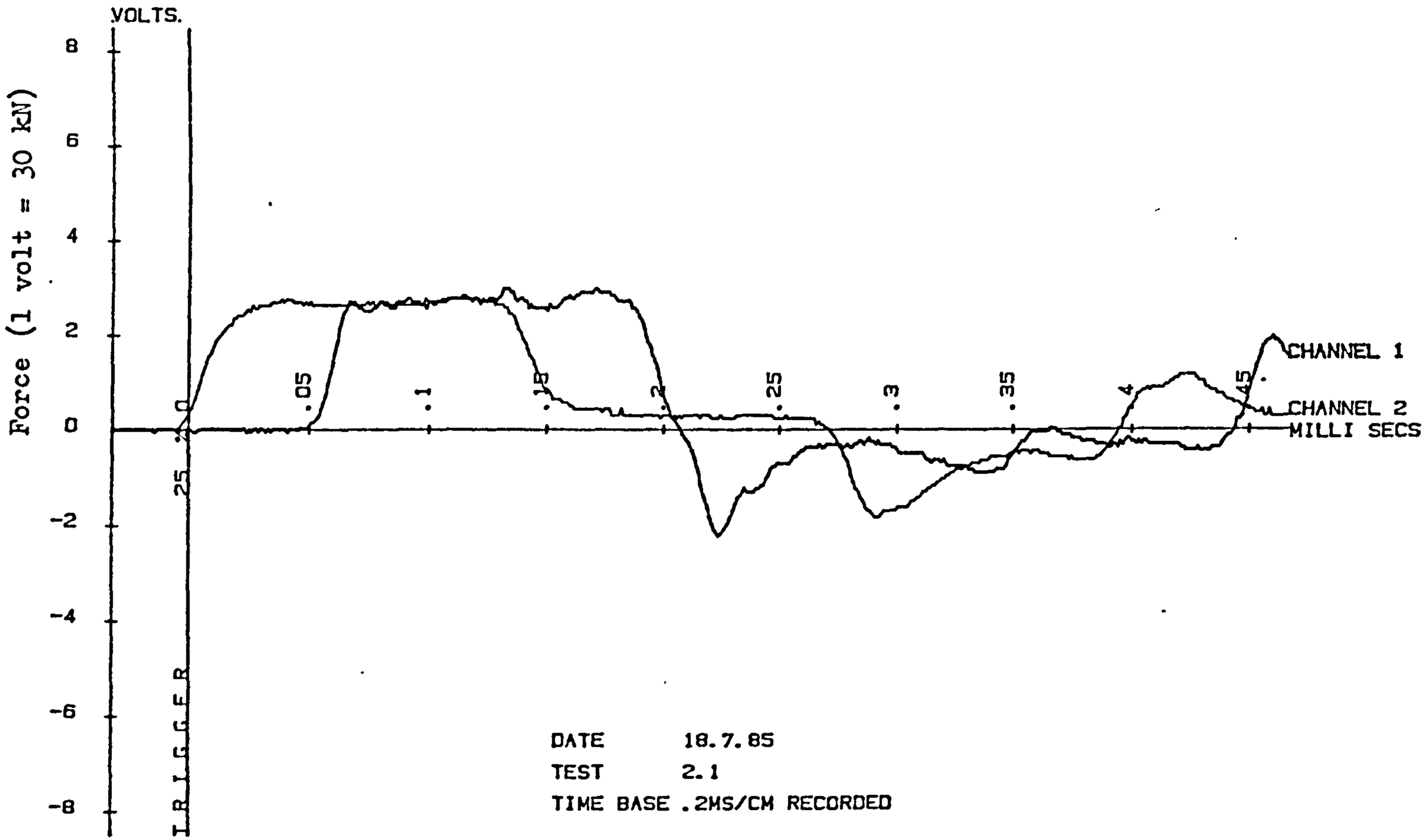

Notes : see page B1.

APPENDIX B IMPACT PULSE TRACE

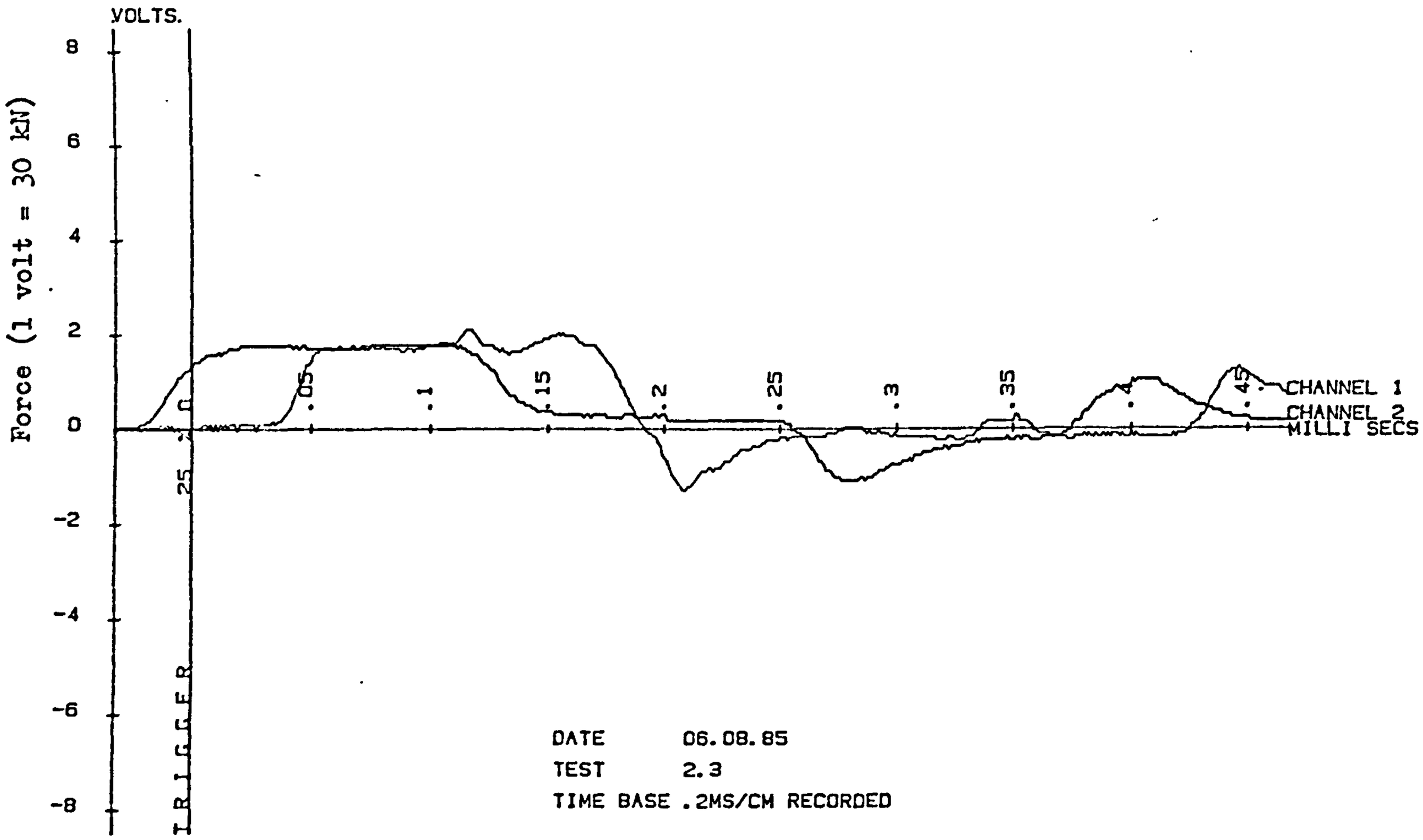

Notes : see page B1.

APPENDIX B IMPACT PULSE TRACE

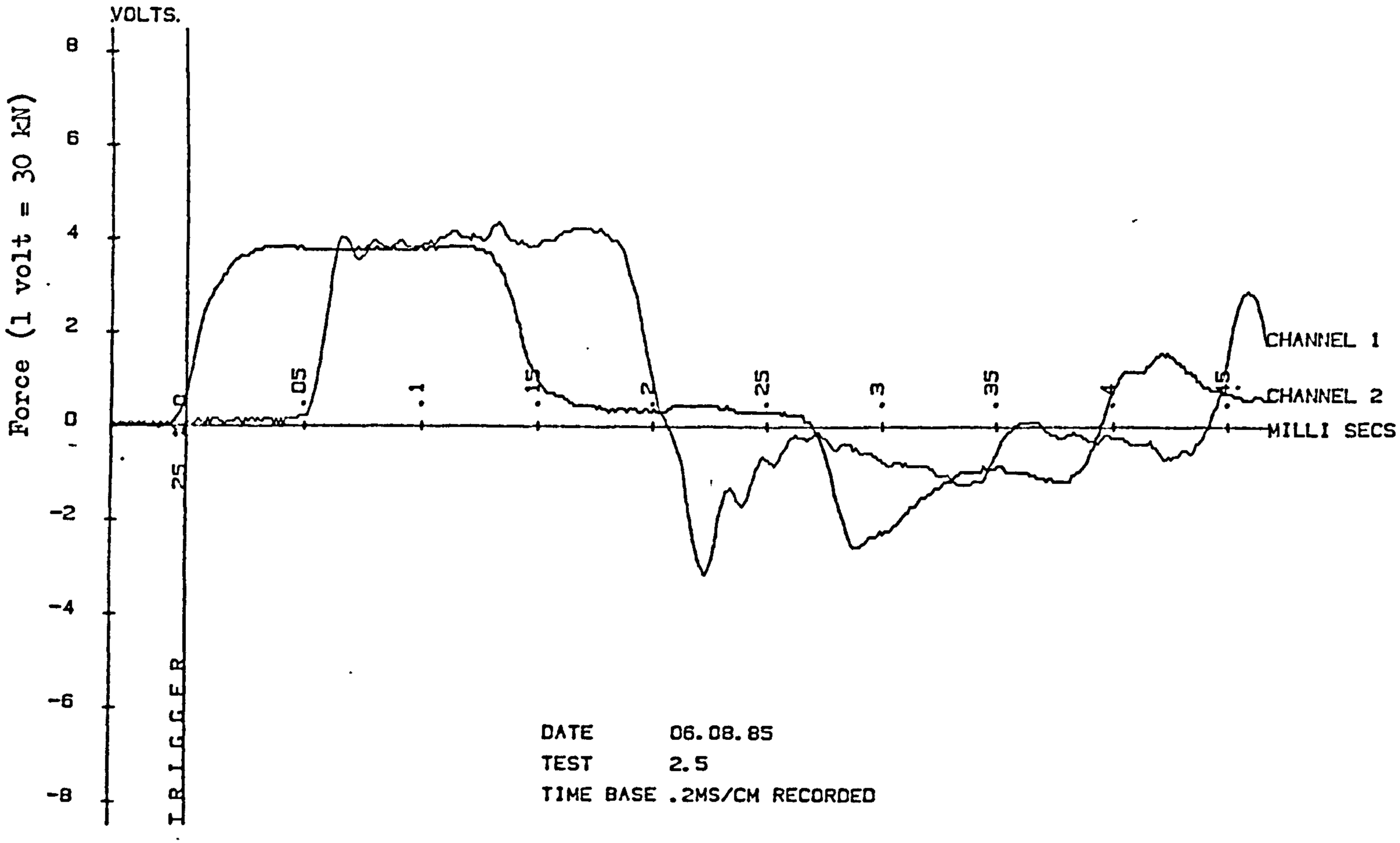

Notes : see page B1.

APPENDIX B IMPACT PULSE TRACE

APPENDIX B IMPACT PULSE TRACE

Notes : see page B1.

DATE 06.08.85

TEST 2.6

TIME BASE .2MS/CM RECORDED

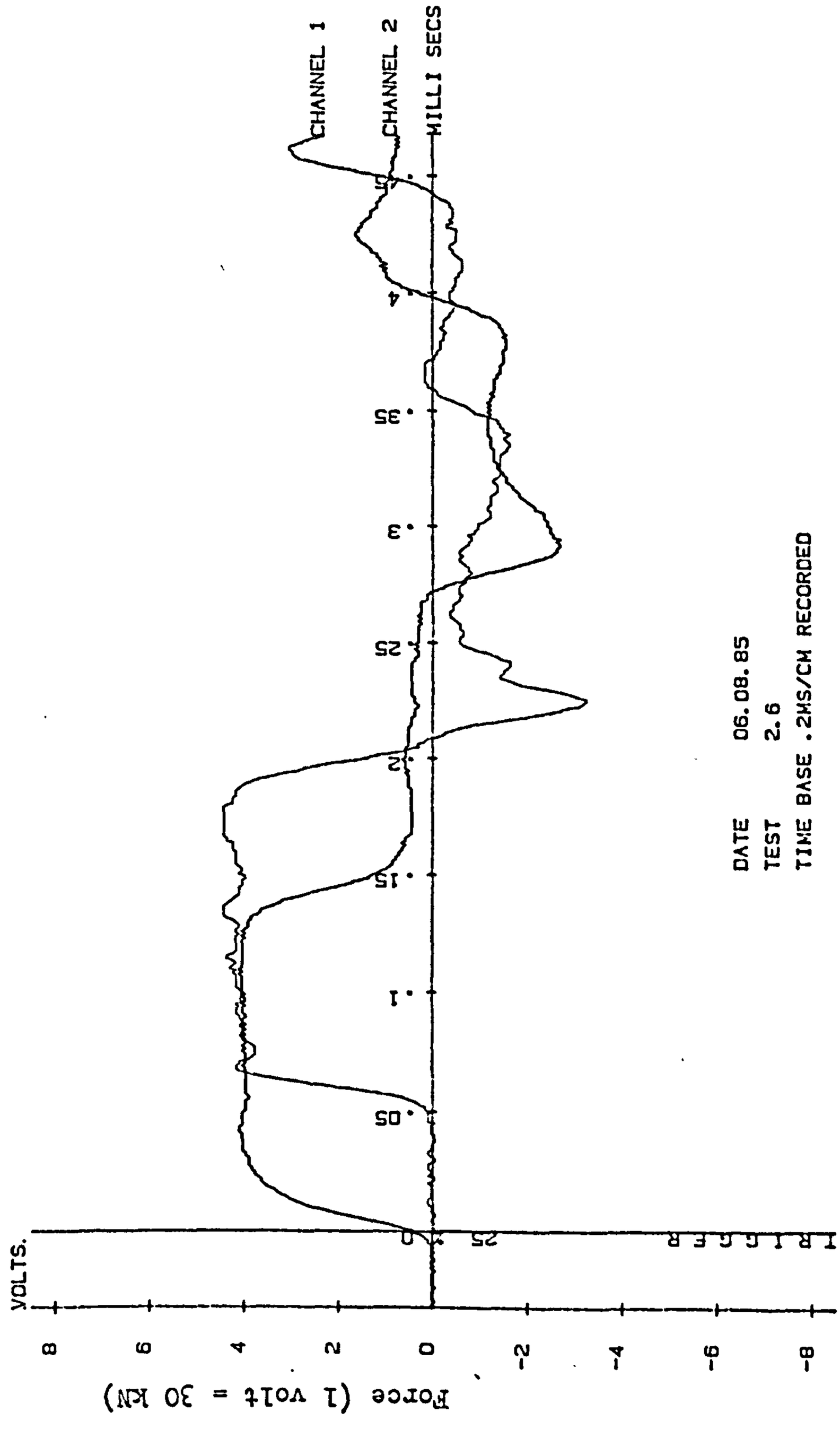

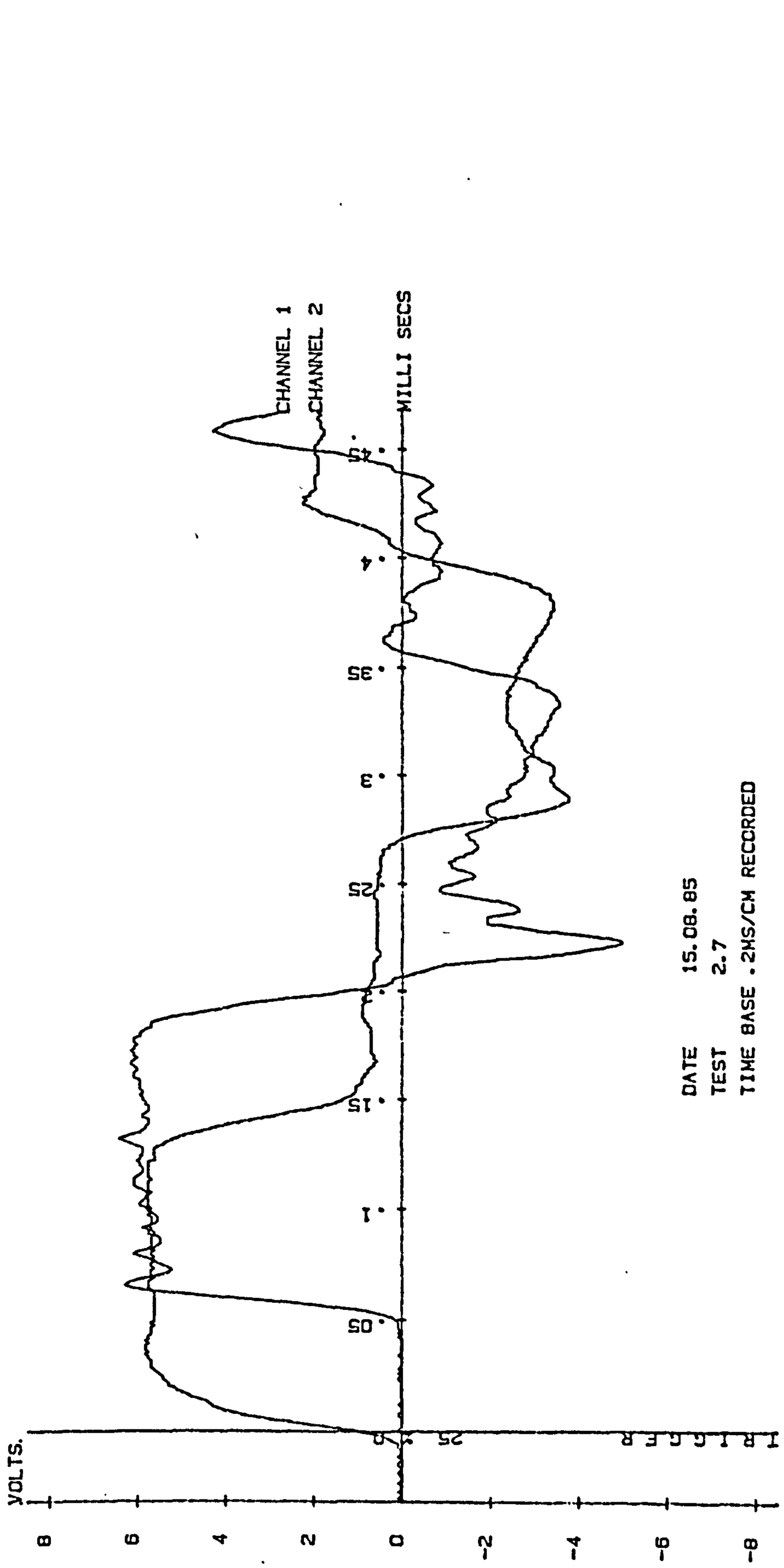

APPENDIX B IMPACT PULSE TRACE

Notes : see page B1.

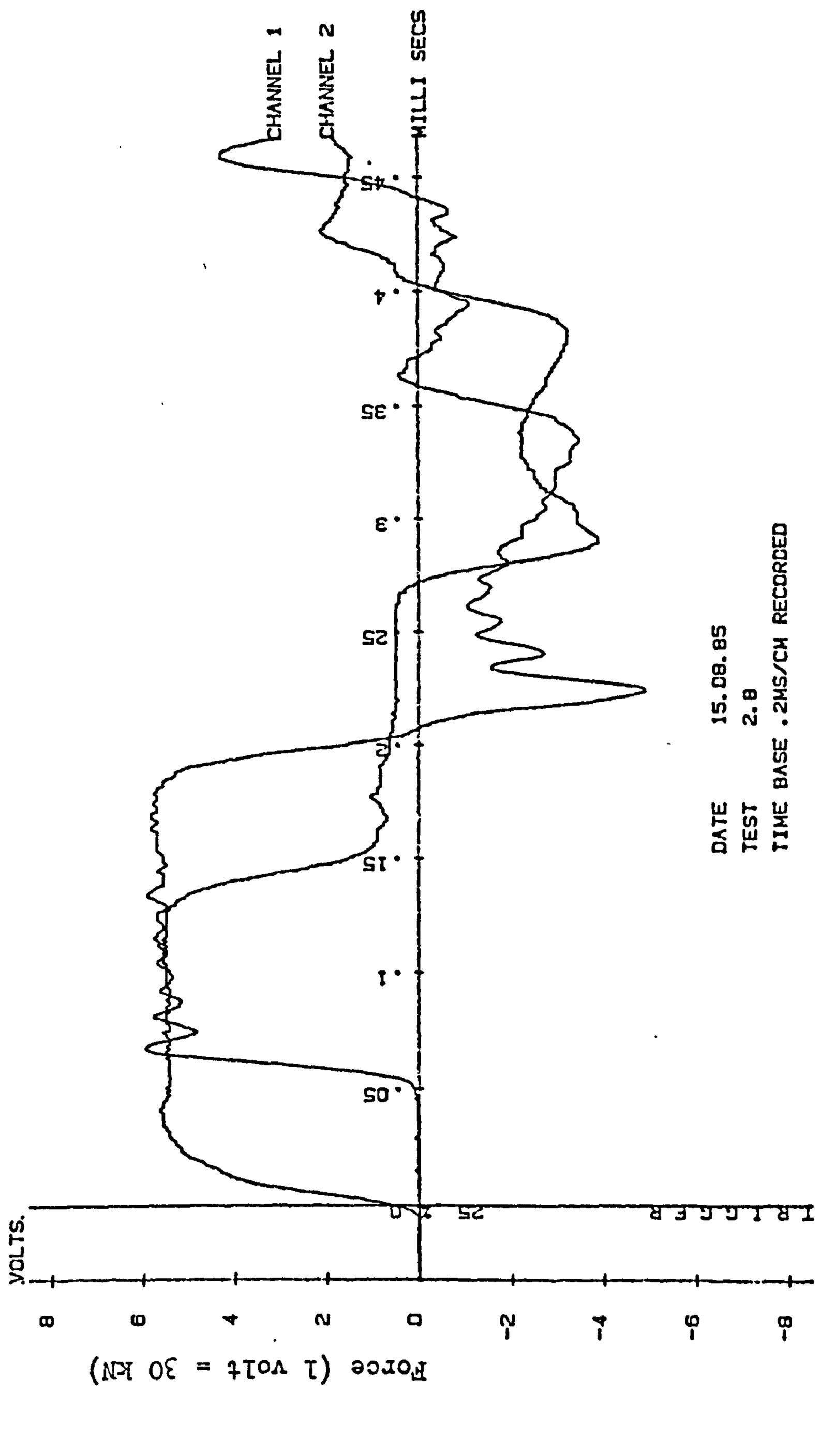

DATE 15.08.85
TEST 2.8
TIME BASE .2MS/CM RECORDED

Notes : see page B1.

APPENDIX B IMPACT PULSE TRACE

Notes : see page B1.

APPENDIX B IMPACT PULSE TRACE

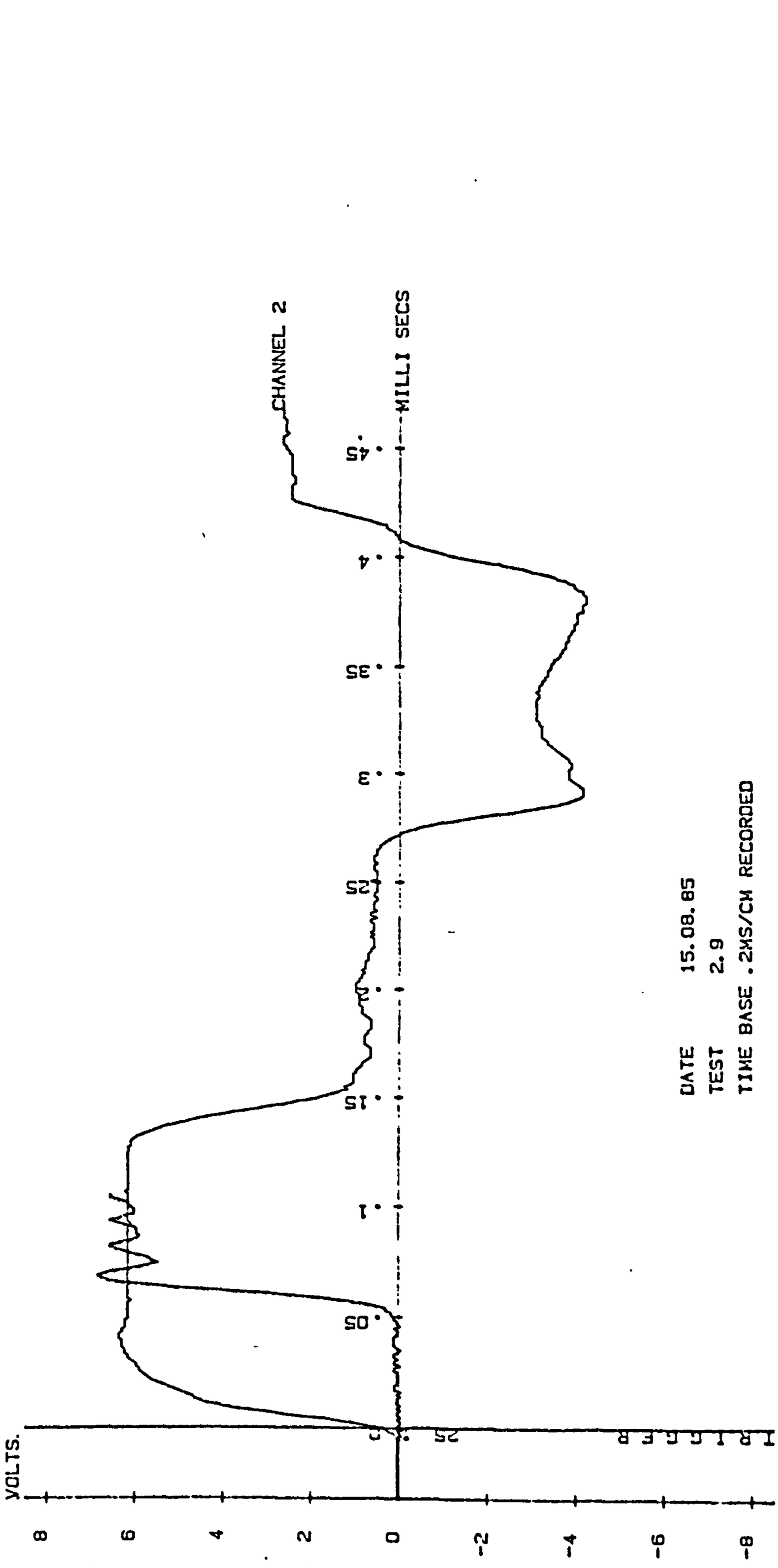

APPENDIX B IMPACT PULSE TRACE

Notes : see page B1.

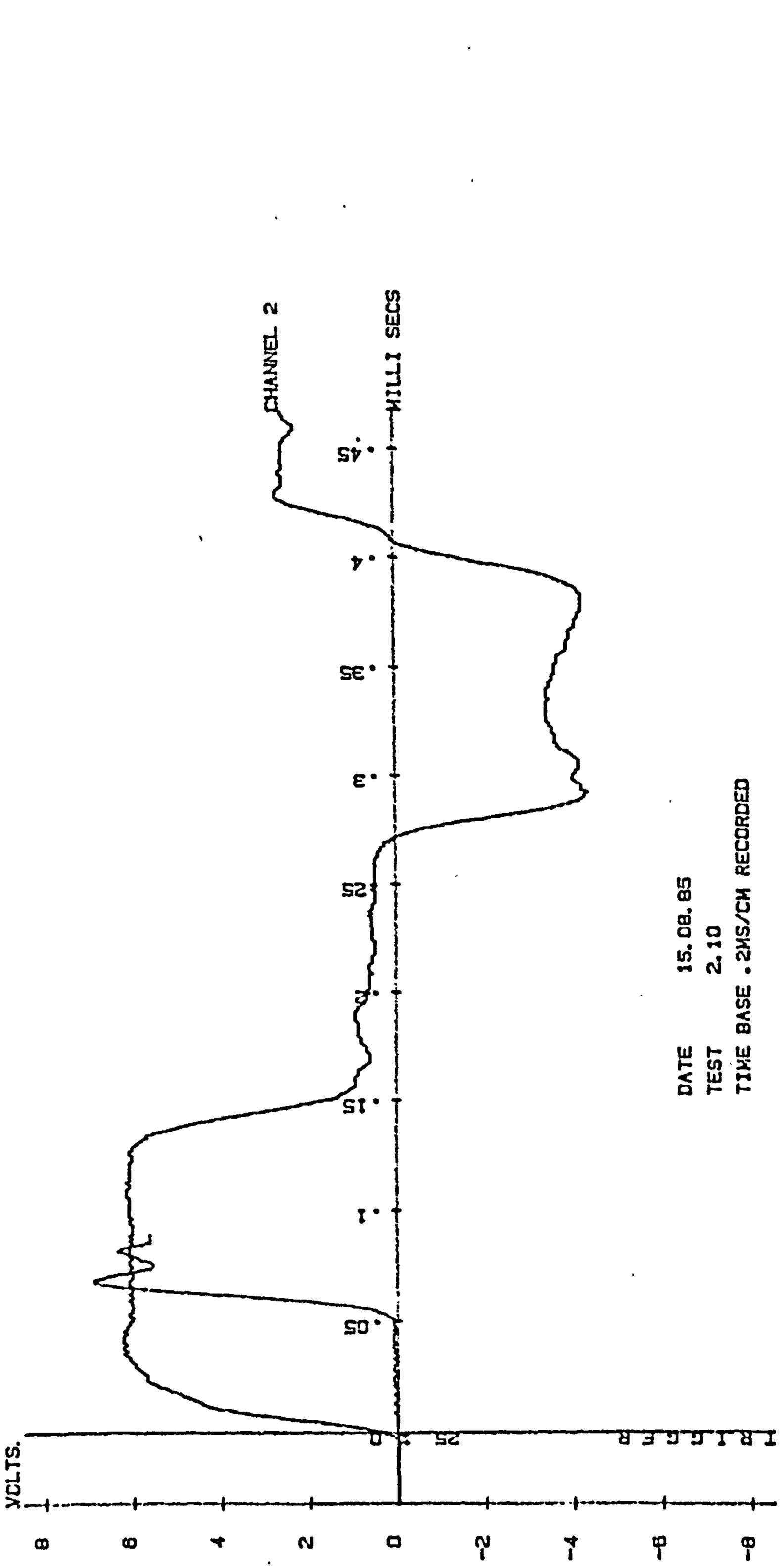

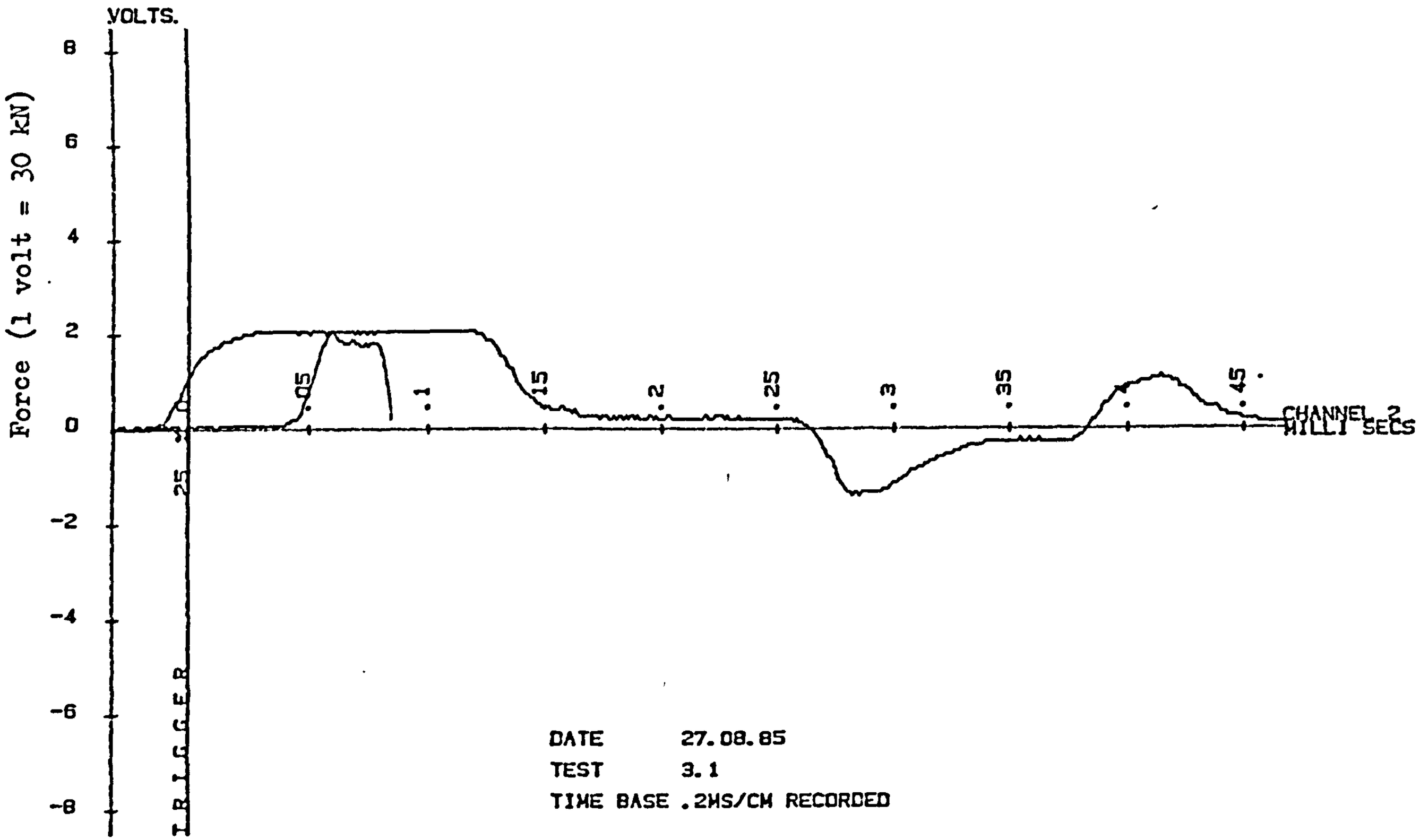

Notes : see page B1

APPENDIX B IMPACT PULSE TRACE

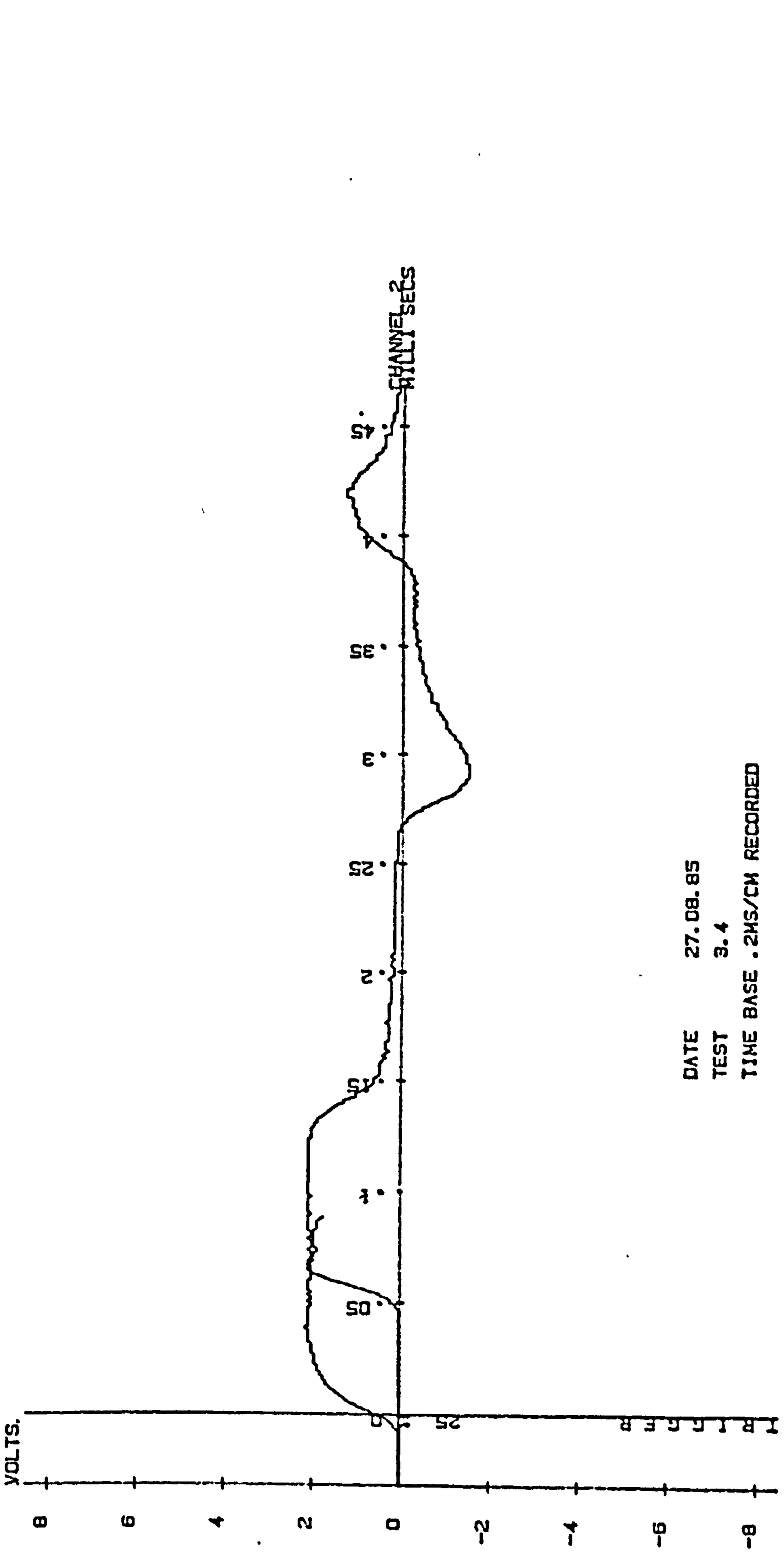
Notes : see page B1.
APPENDIX B IMPACT PULSE TRACE
DATE 27.08.85
TEST 3.4
TIME BASE .2MS/CM RECORDED
CHANNEL SECS
.45
.4
.35
.3
.25
.2
.15
.1
.05
0
FIRE
-2
-4
-6
-8
Force (1 volt = 30 kN)
VOLTS.
8
6
4
2
0

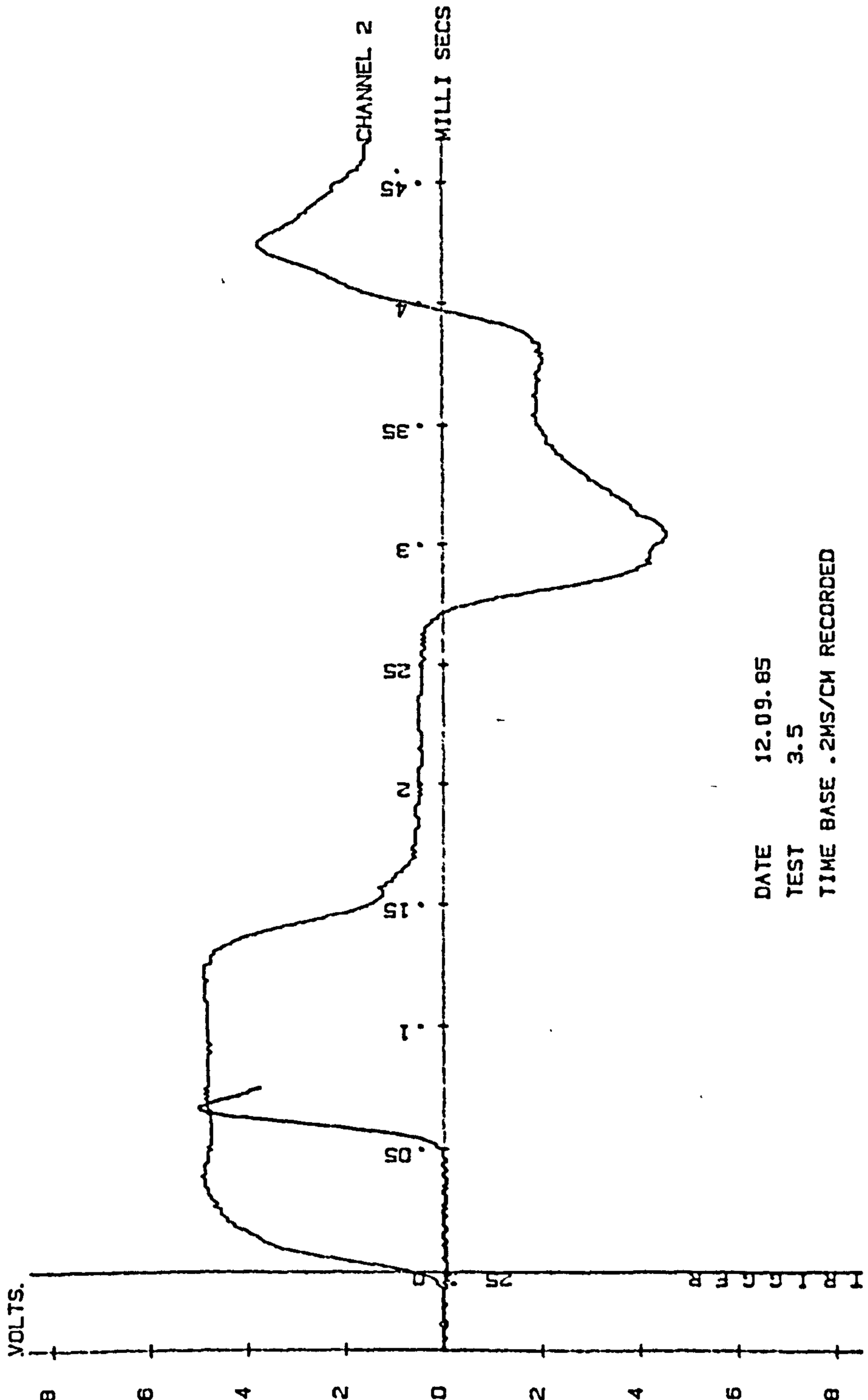

Notes : see page B1.

APPENDIX B IMPACT PULSE TRACE

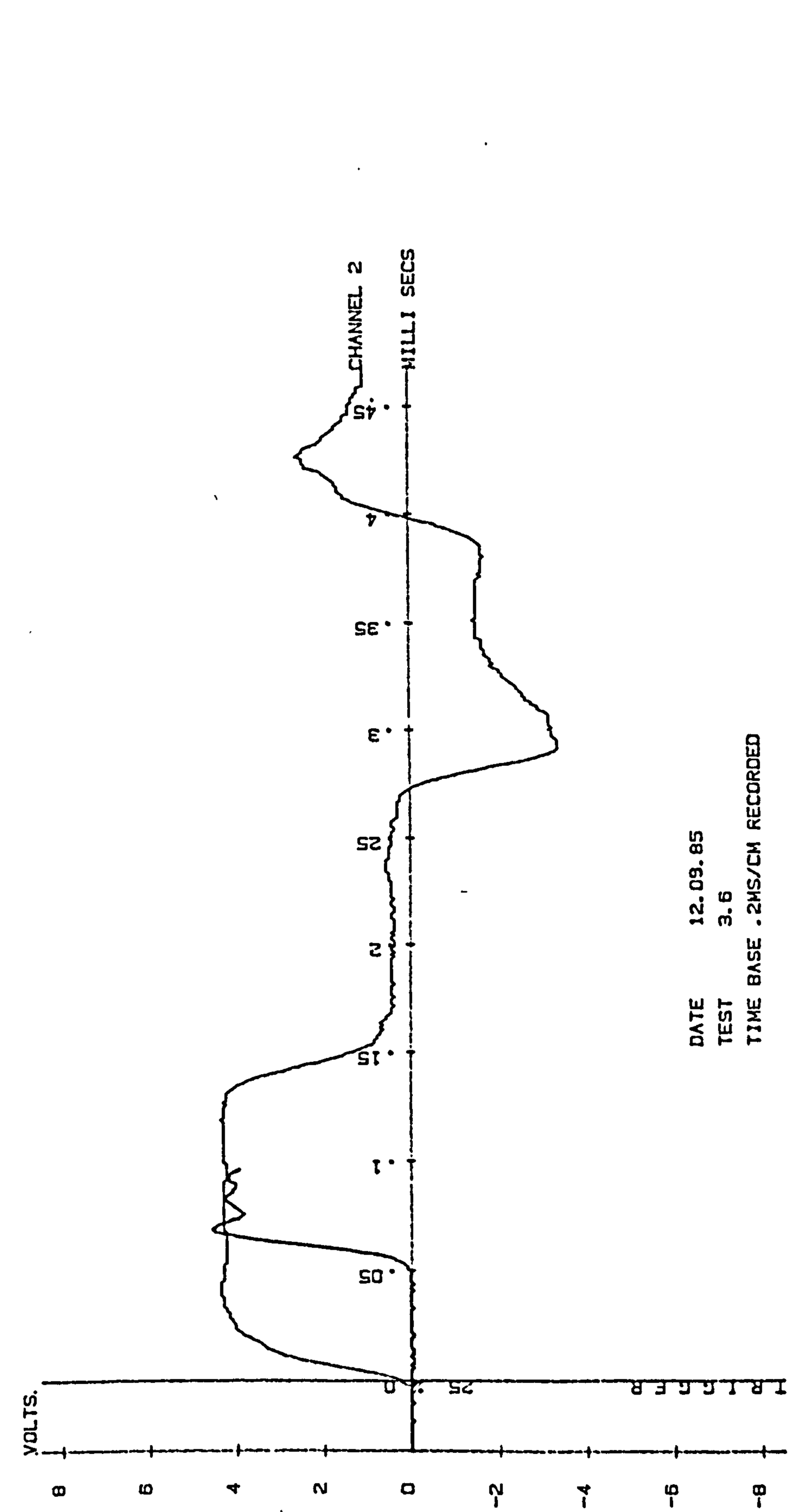

Notes : see page B1.

APPENDIX B IMPACT PULSE TRACE

APPENDIX B IMPACT PULSE TRACE

Notes : see page B1.

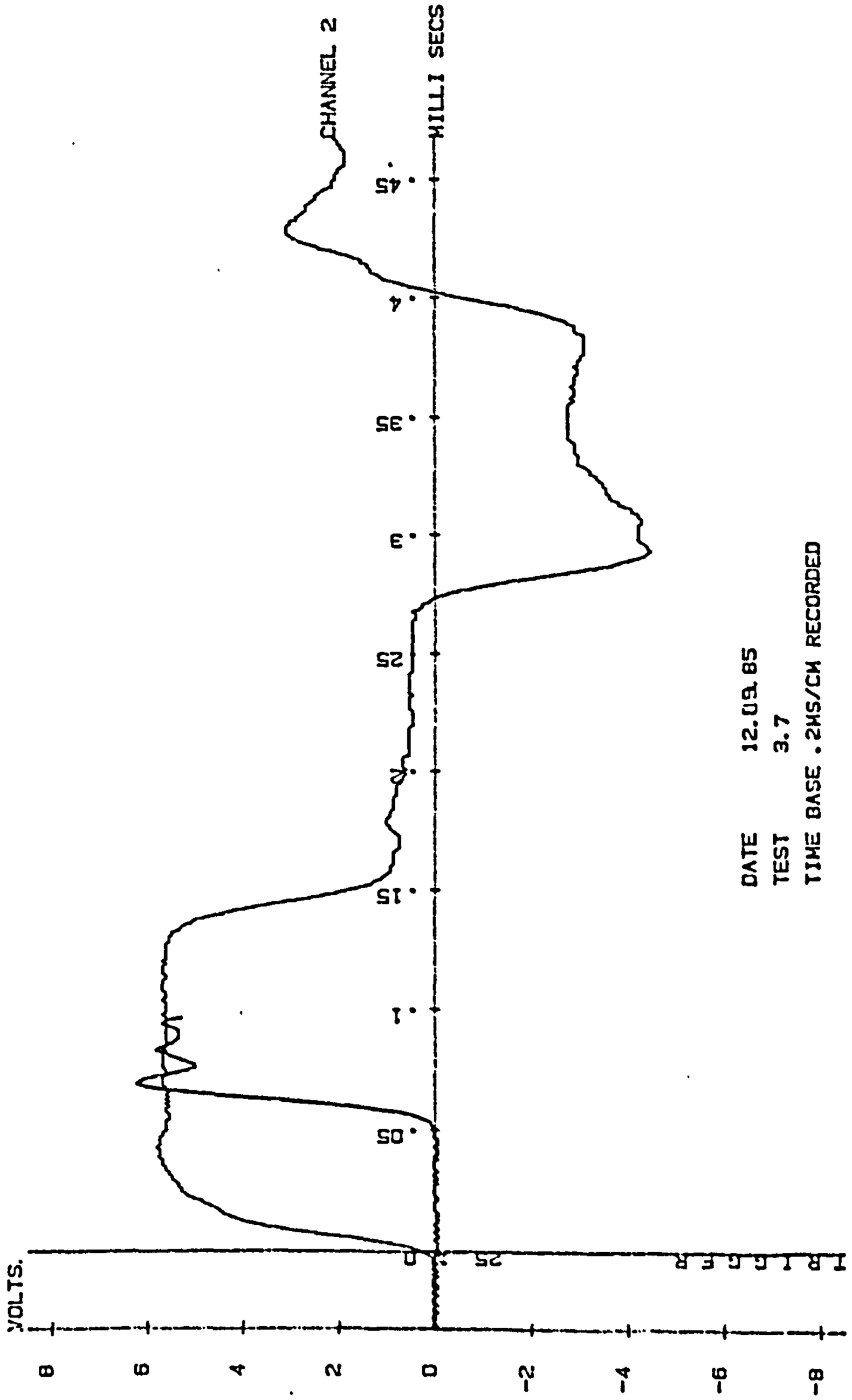

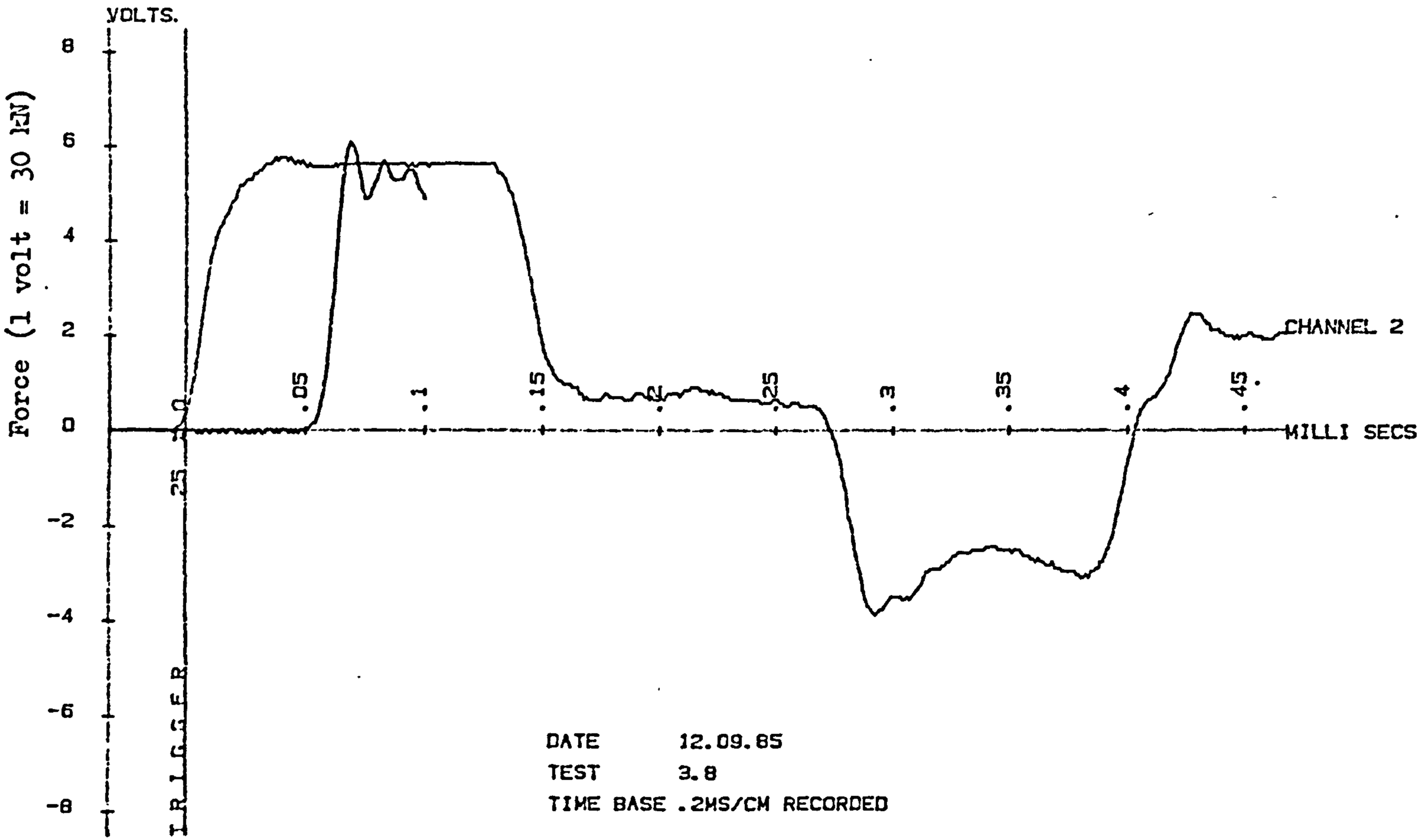

Notes : see page B1.

APPENDIX B IMPACT PULSE TRACE

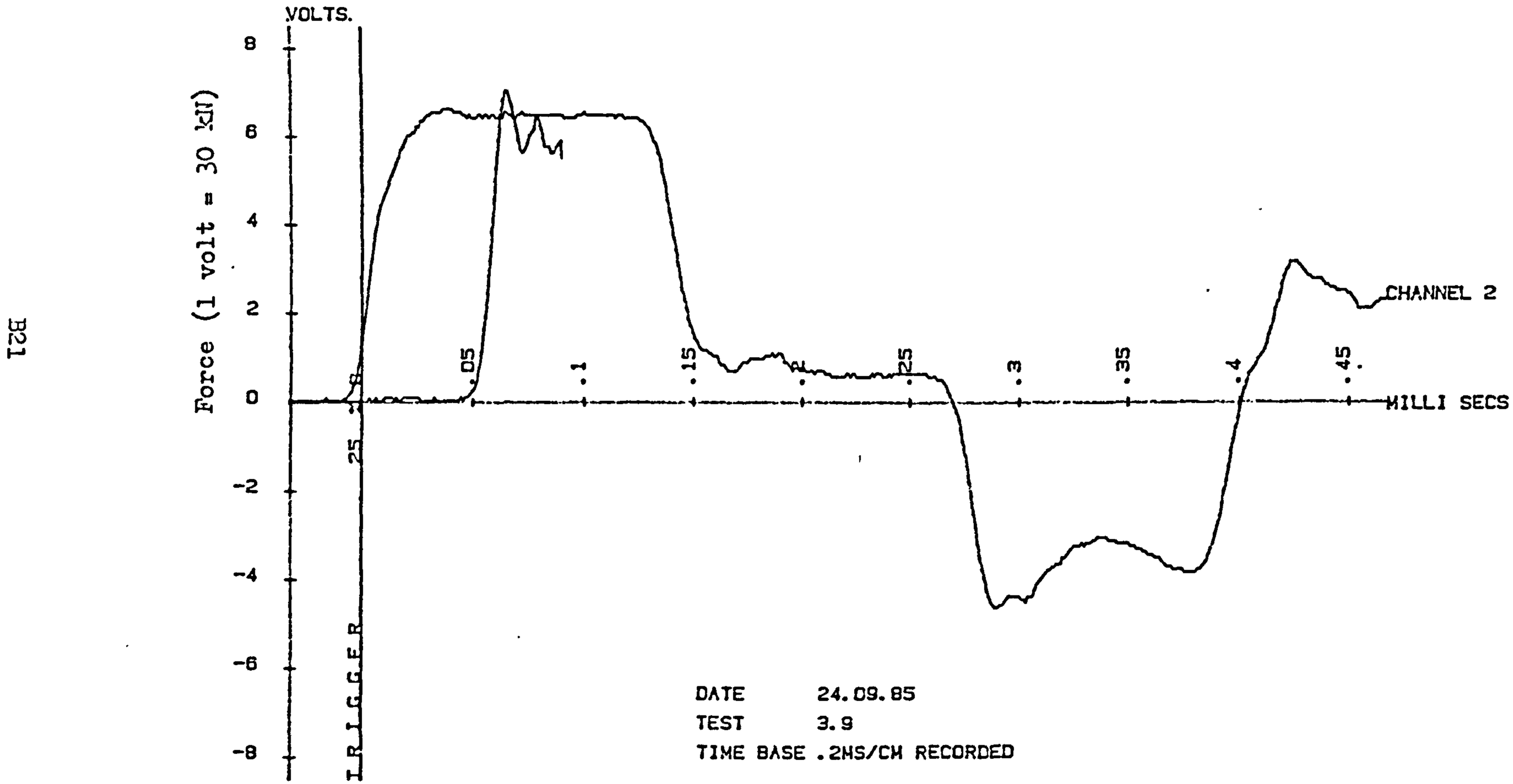

Notes : see page B1.

APPENDIX B IMPACT PULSE TRACE

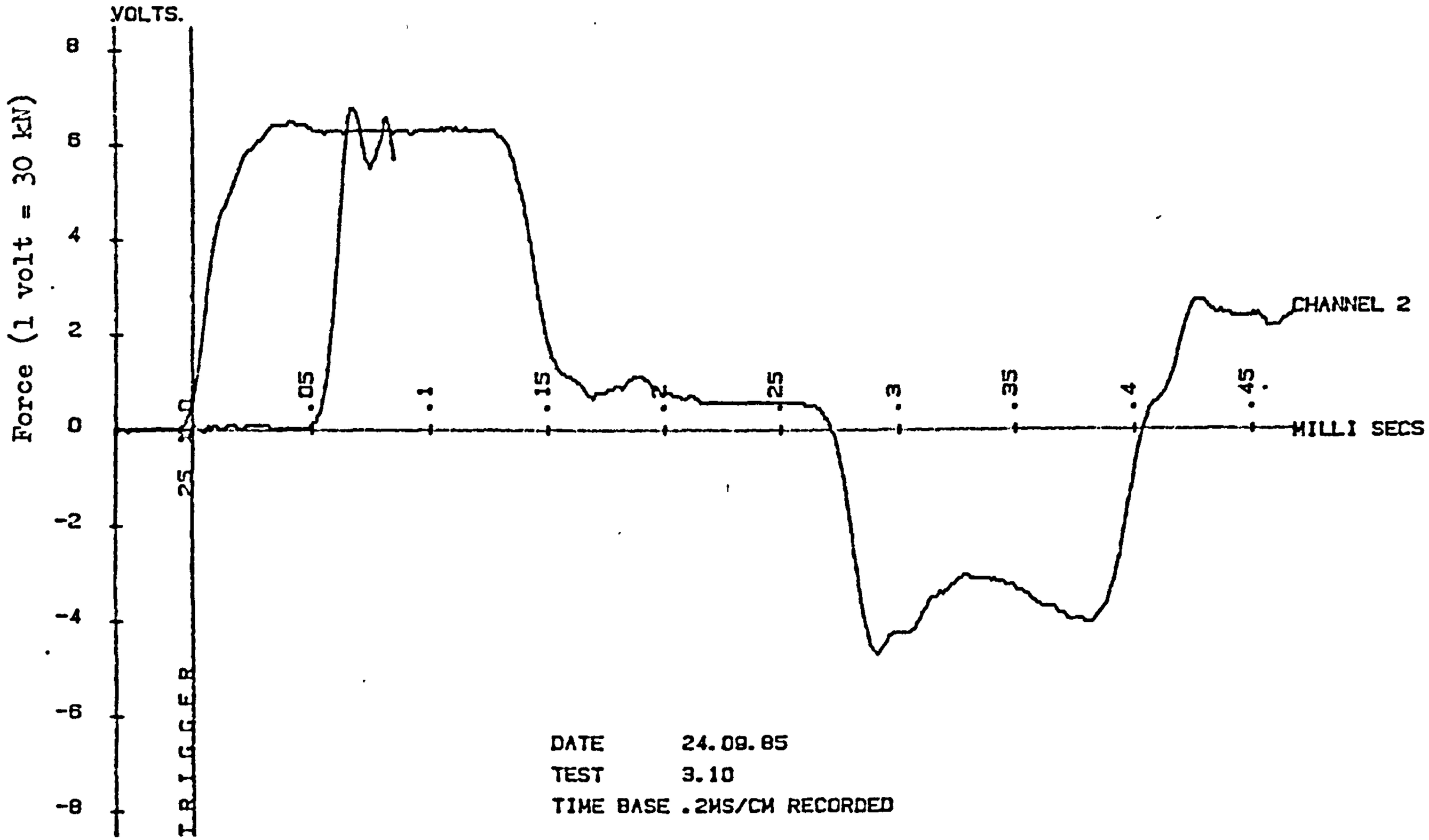

Notes : see page B1.

APPENDIX B IMPACT PULSE TRACE

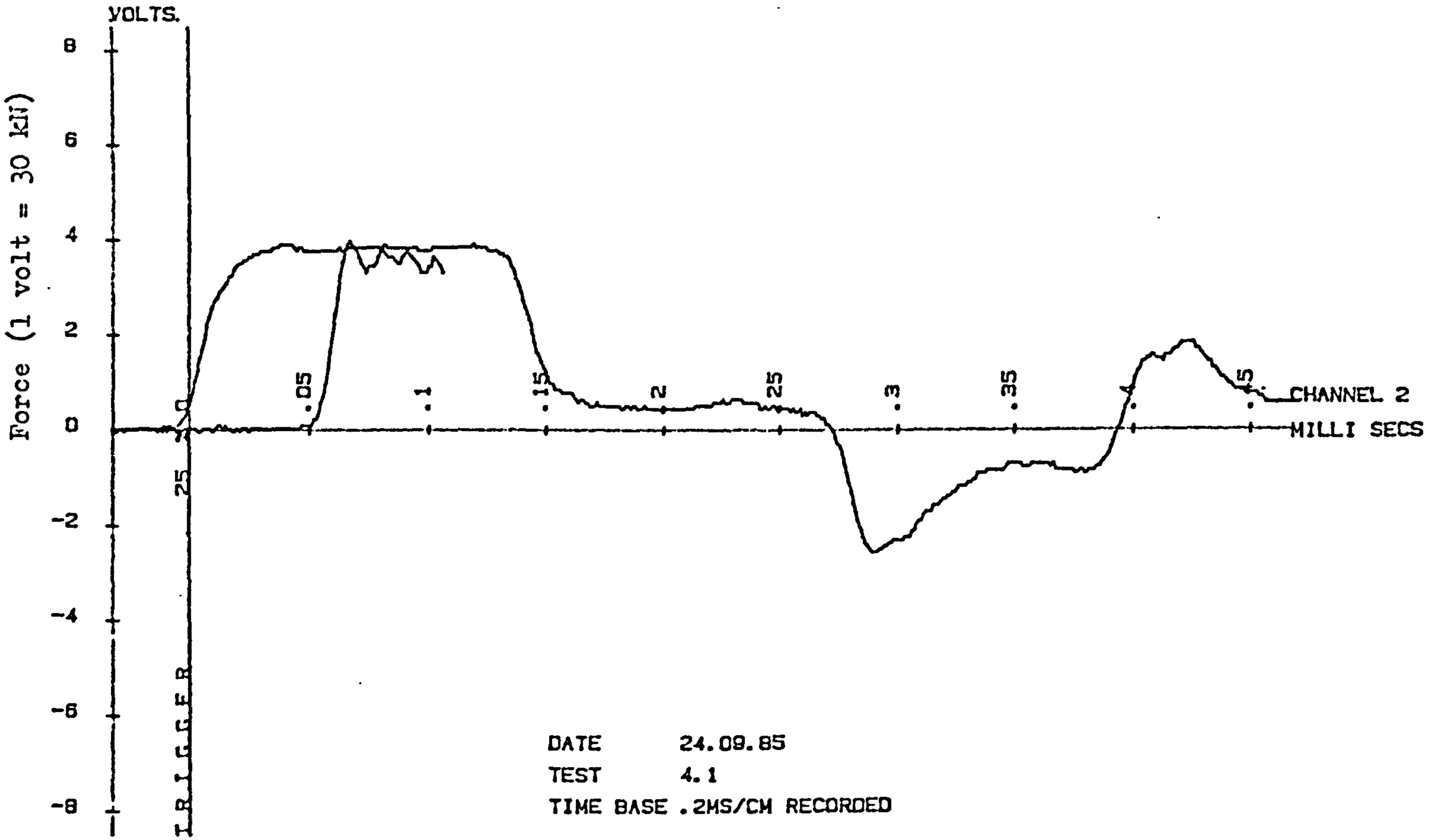

Notes : see page B1.

APPENDIX B IMPACT PULSE TRACE

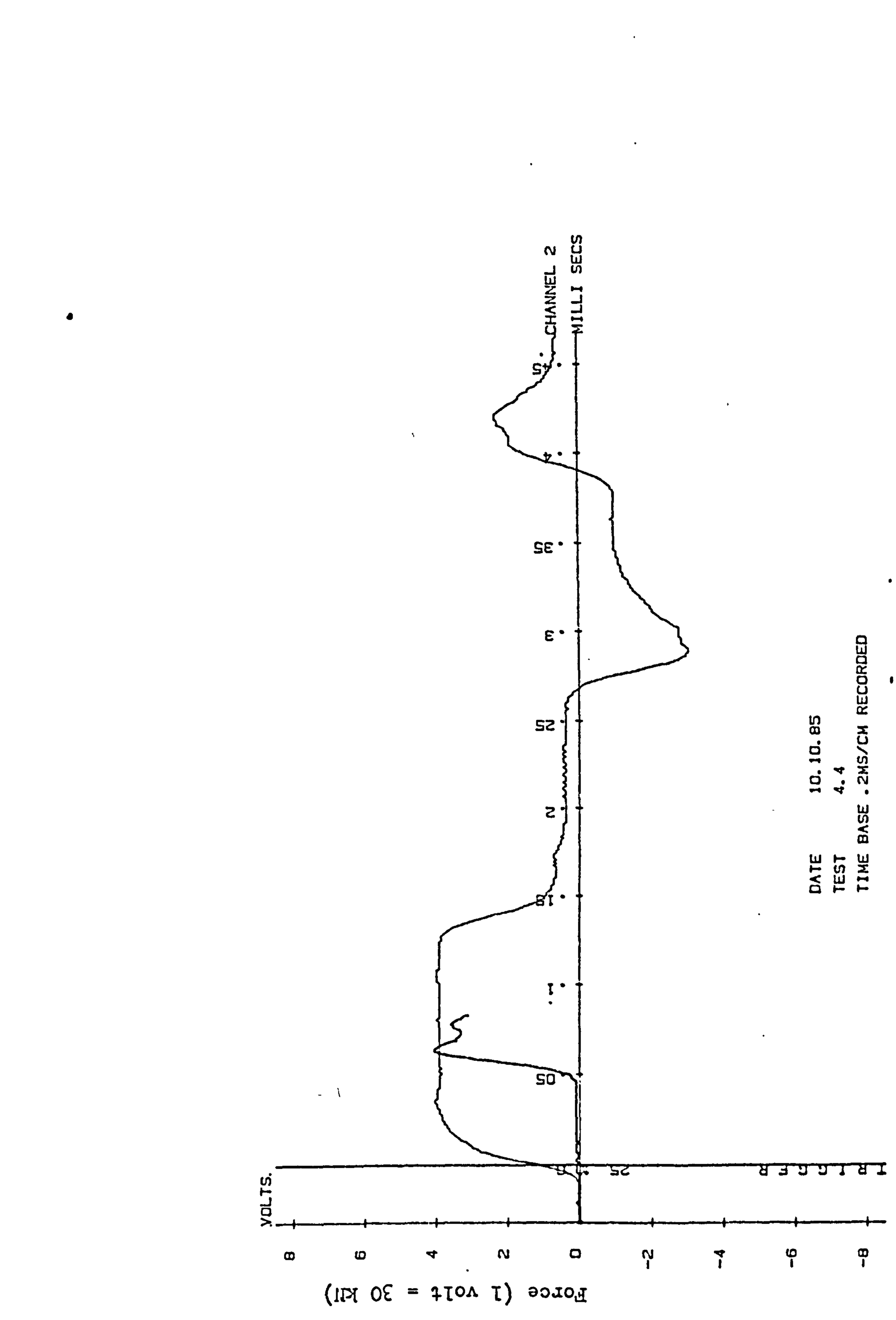
Notes : see page B1.
APPENDIX B IMPACT PULSE TRACE
TIME BASE . 2MS/CH RECORDED
TEST 4.4
DATE 10.10.85
CHANNEL 2
MILLI SECS
VOLTS.
8
6
4
2
0
-2
-4
-6
-8
Force (1 volt = 30 kN)

APPENDIX B IMPACT PULSE TRACE

Notes : see page B1.

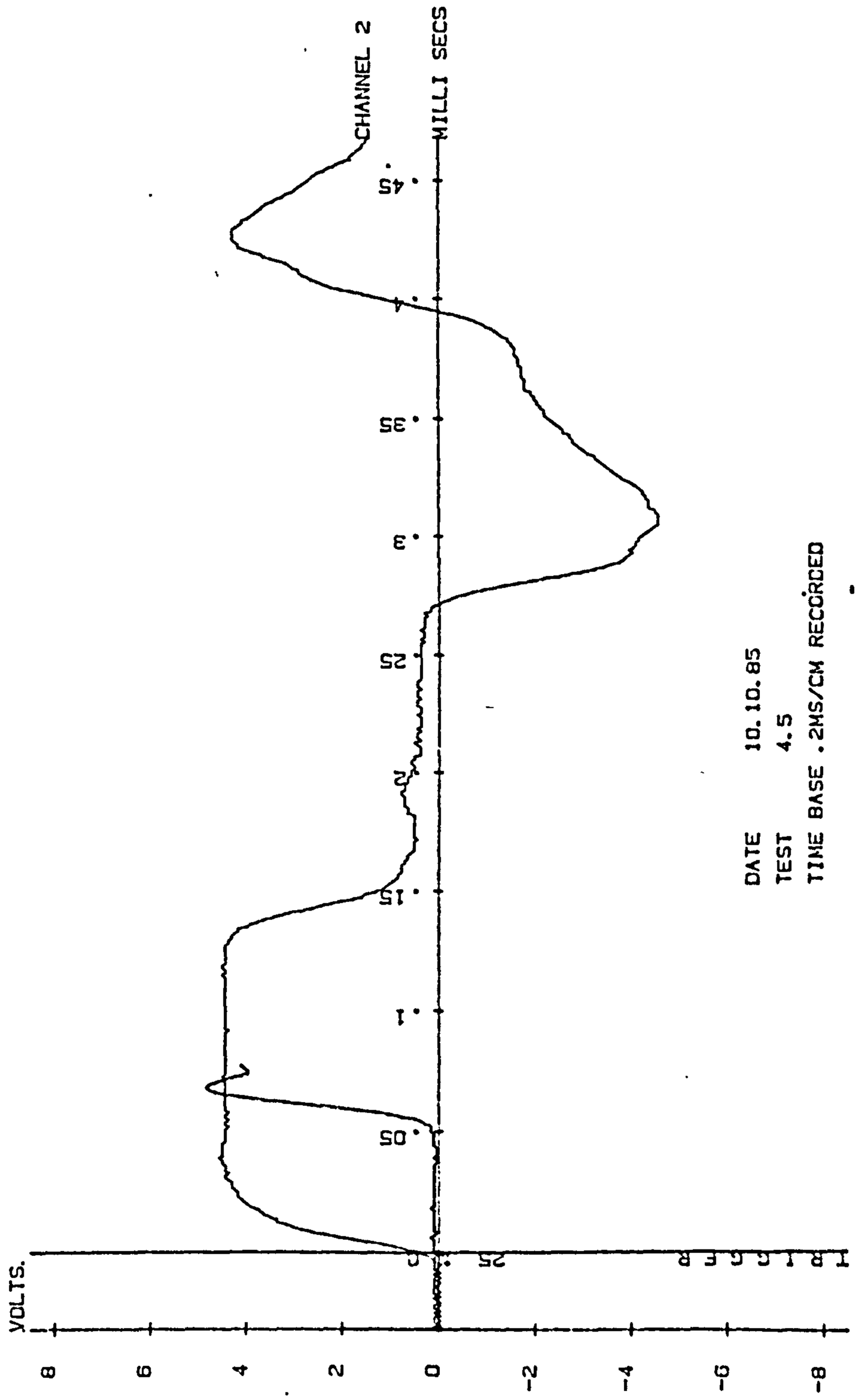

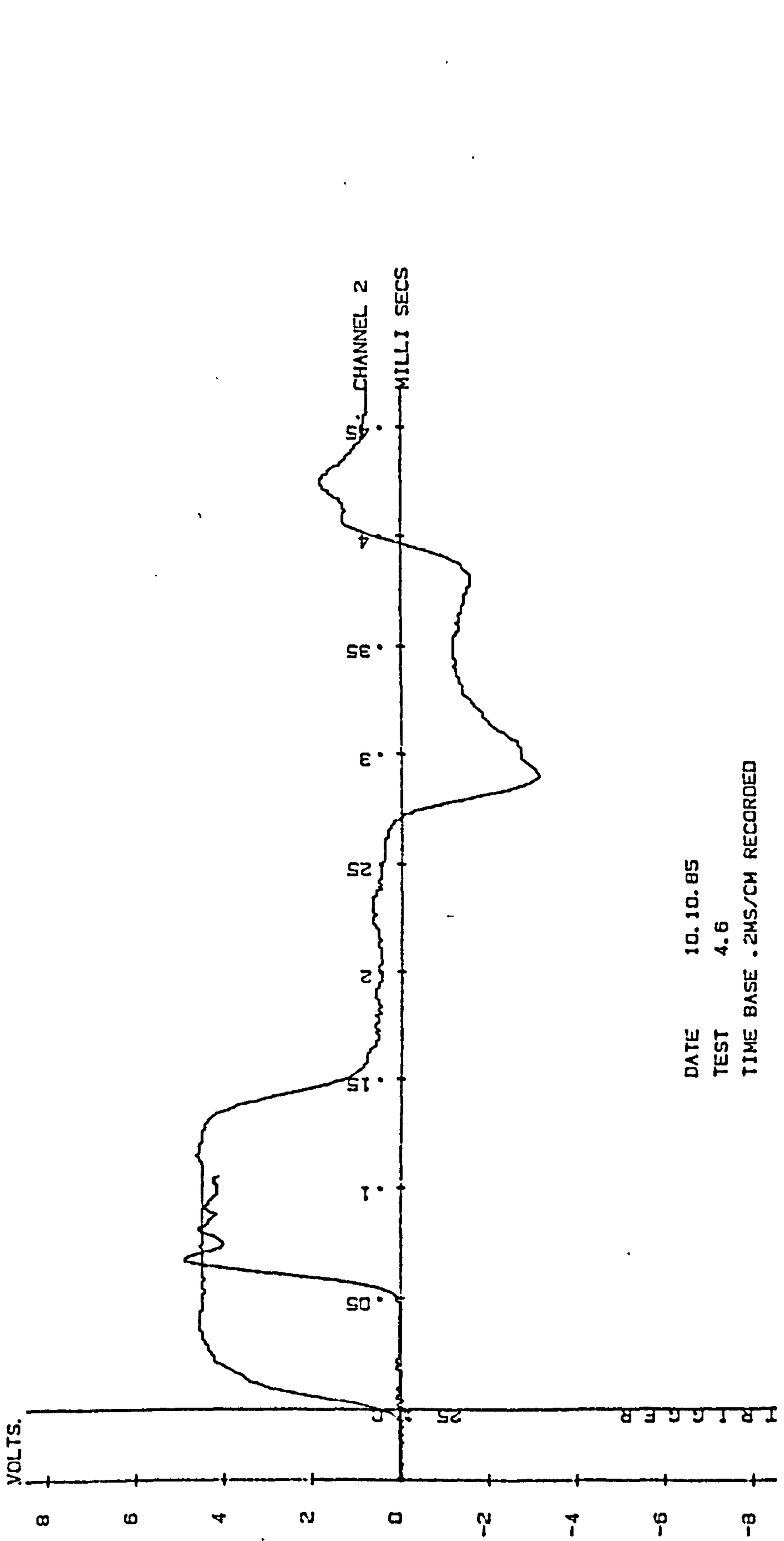

Notes : see page B1.

APPENDIX B IMPACT PULSE TRACE

APPENDIX B IMPACT PULSE TRACE

Notes : see page B1.

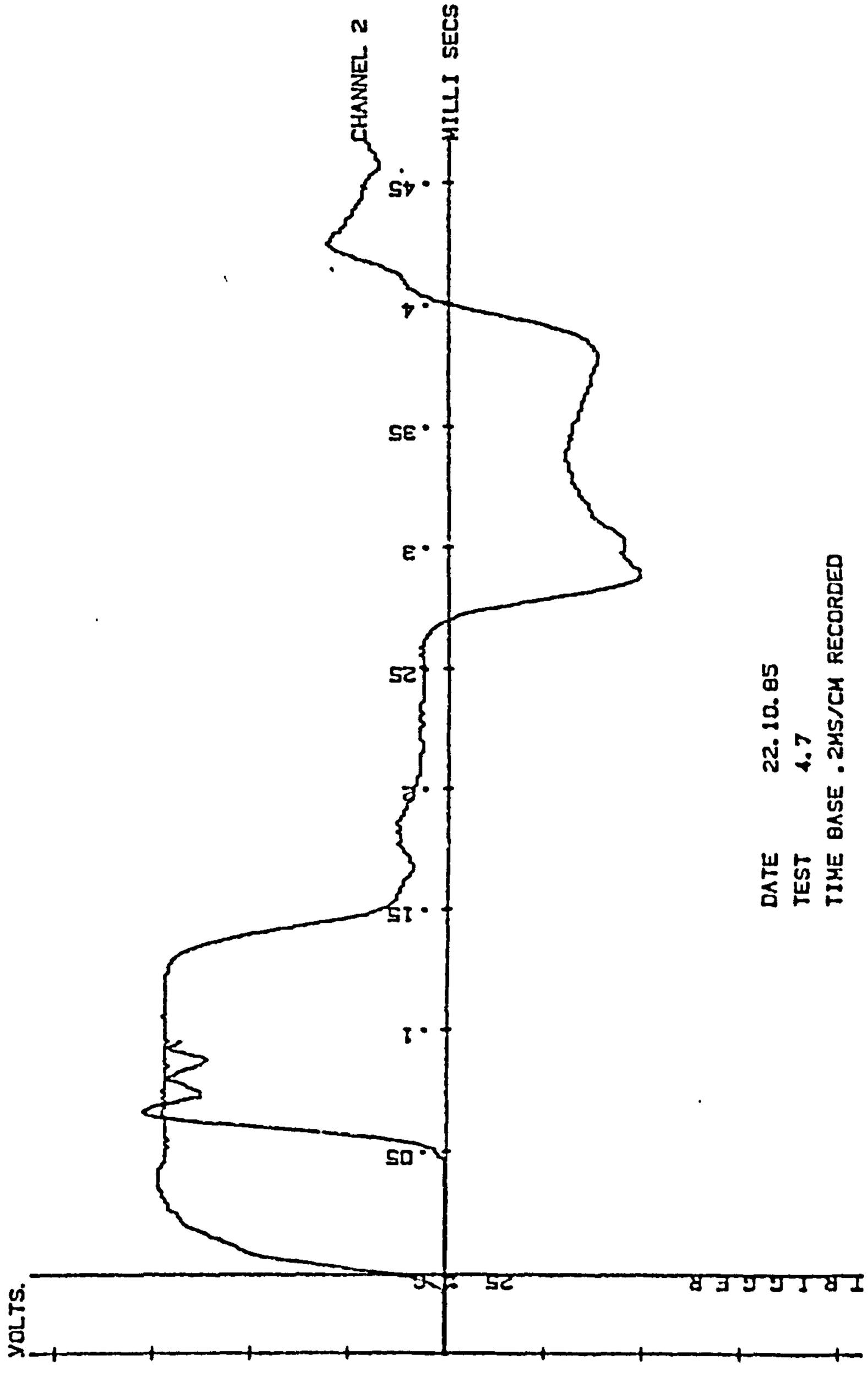

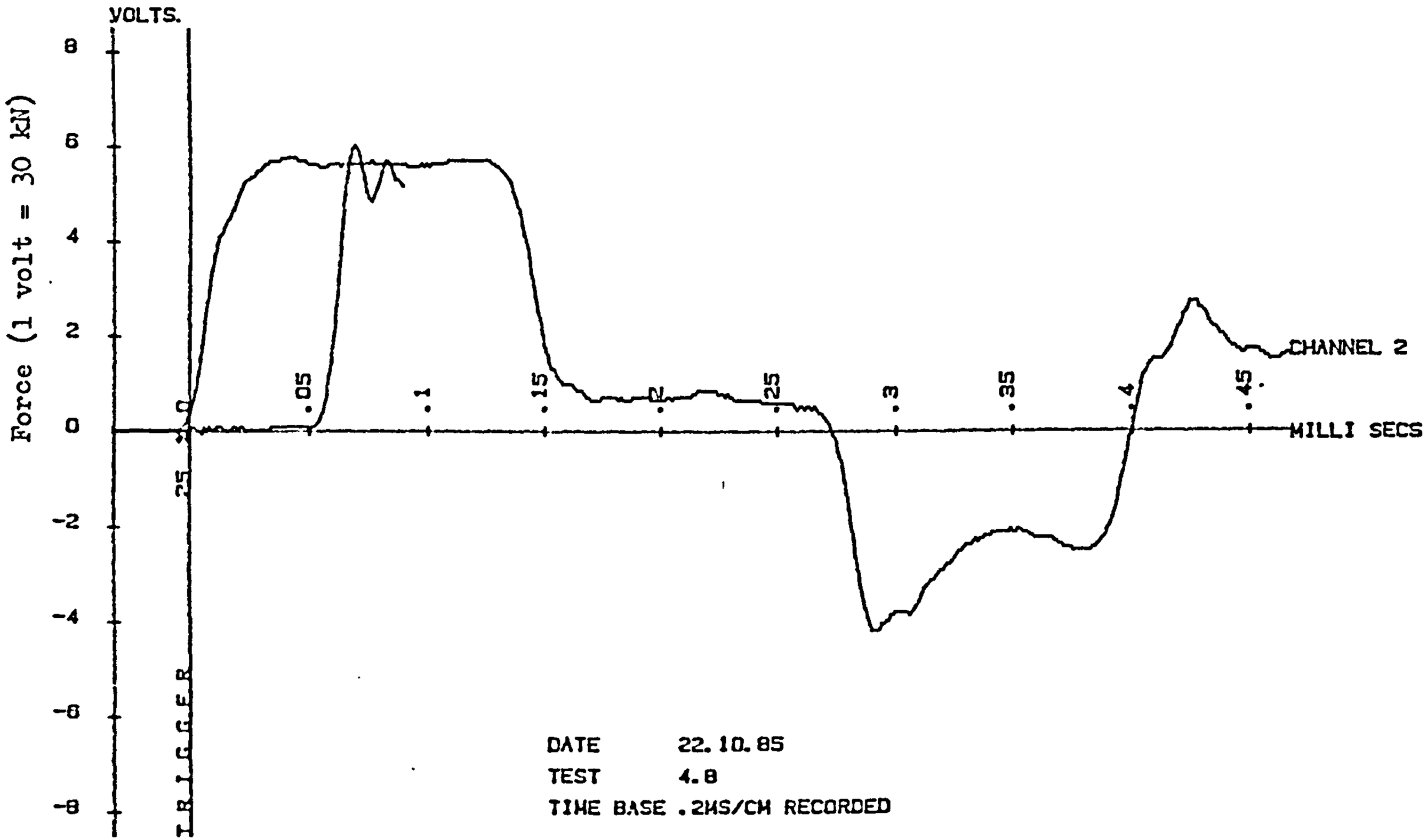

Notes : see page B1.

APPENDIX B IMPACT PULSE TRACE

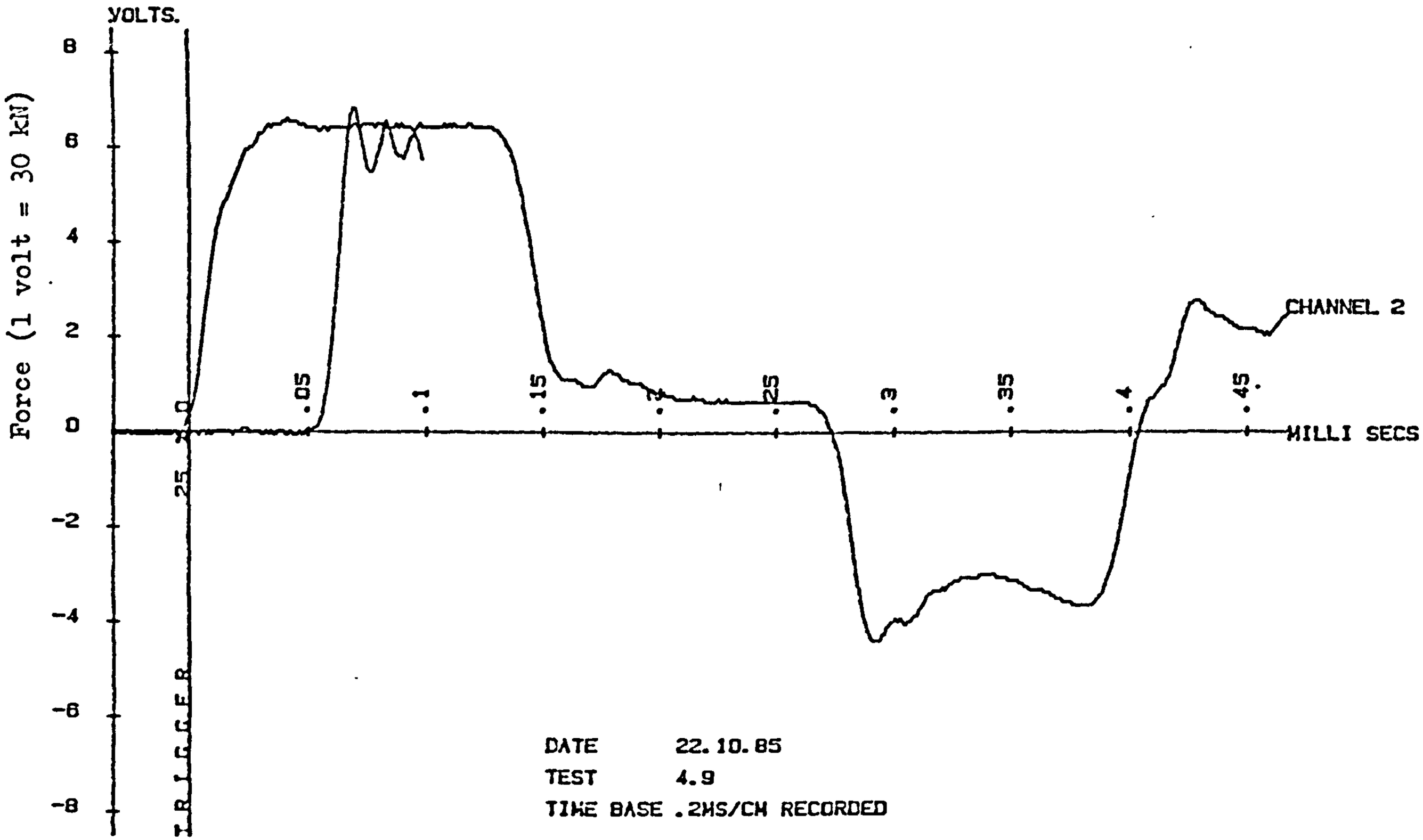

Notes : see page B1.

APPENDIX B IMPACT PULSE TRACE

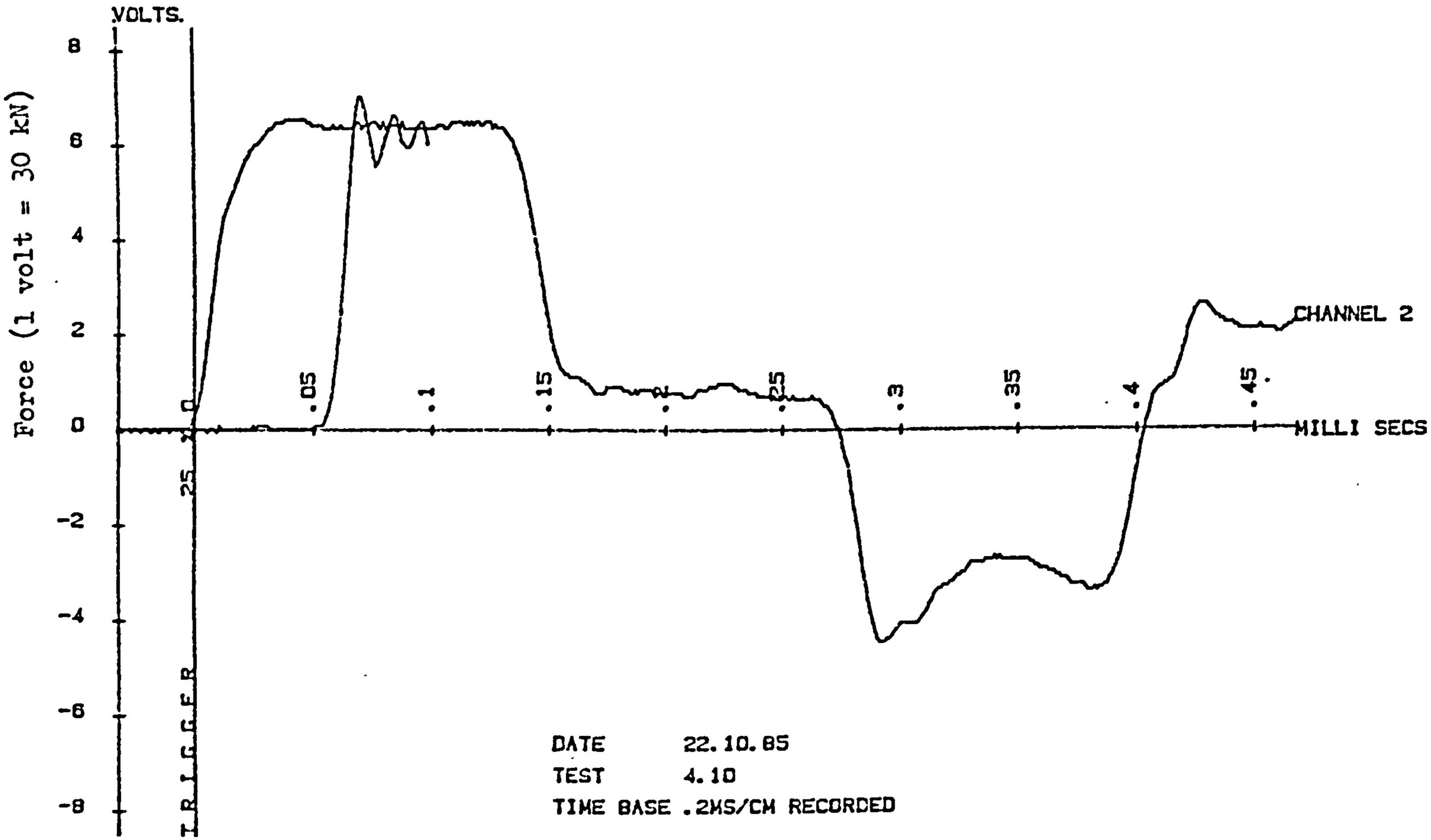

Notes : see page B1.

APPENDIX B IMPACT PULSE TRACE

APPENDIX C

Crack Pattern

This appendix shows the crack pattern of all the beams. Part (a) shows the statically tested beams while part (b) shows the impacted beams after the post-impact-static test.

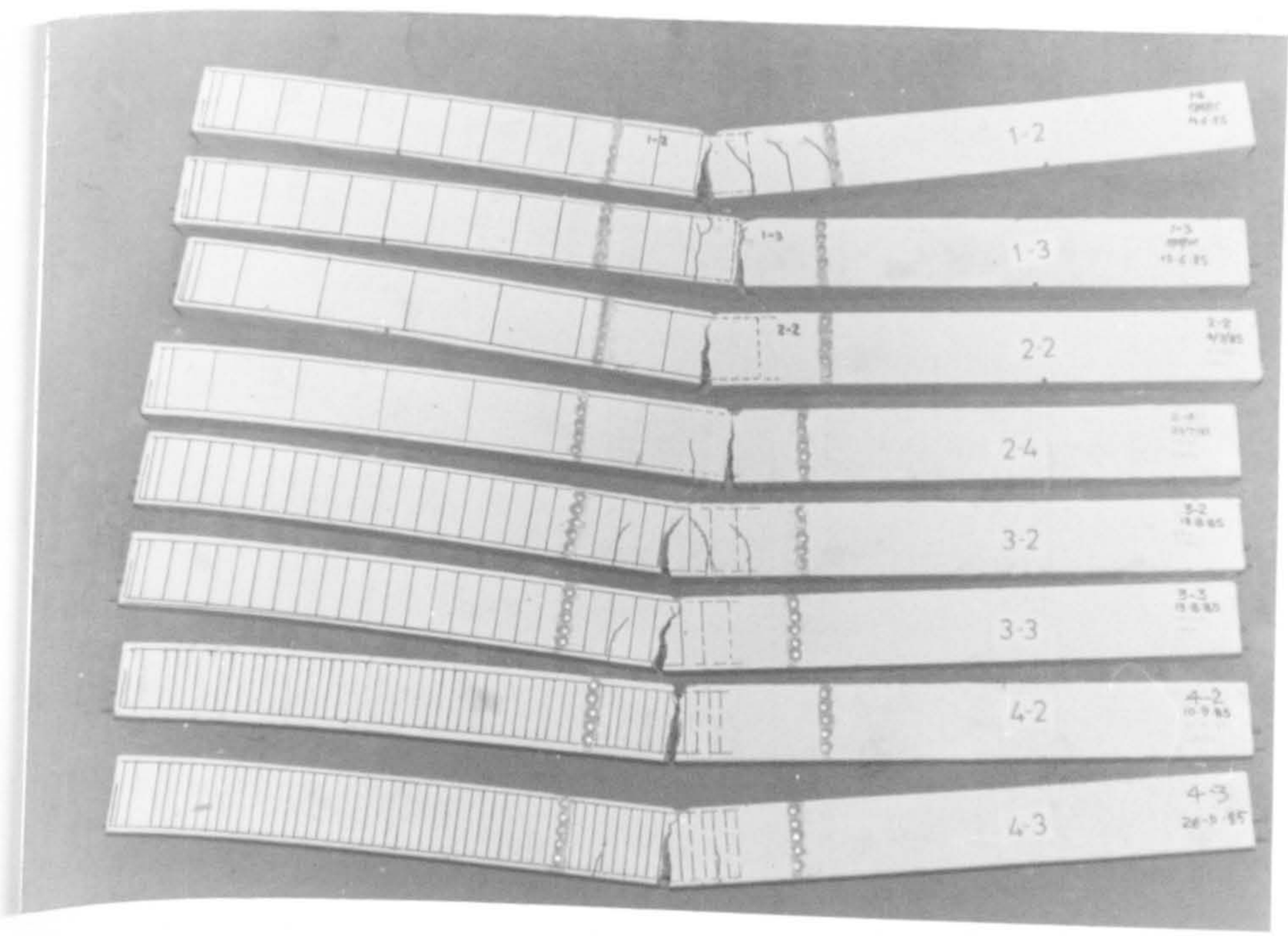

SERIES 1 TO 4

APPENDIX C CRACK PATTERN

(a) STATIC TEST

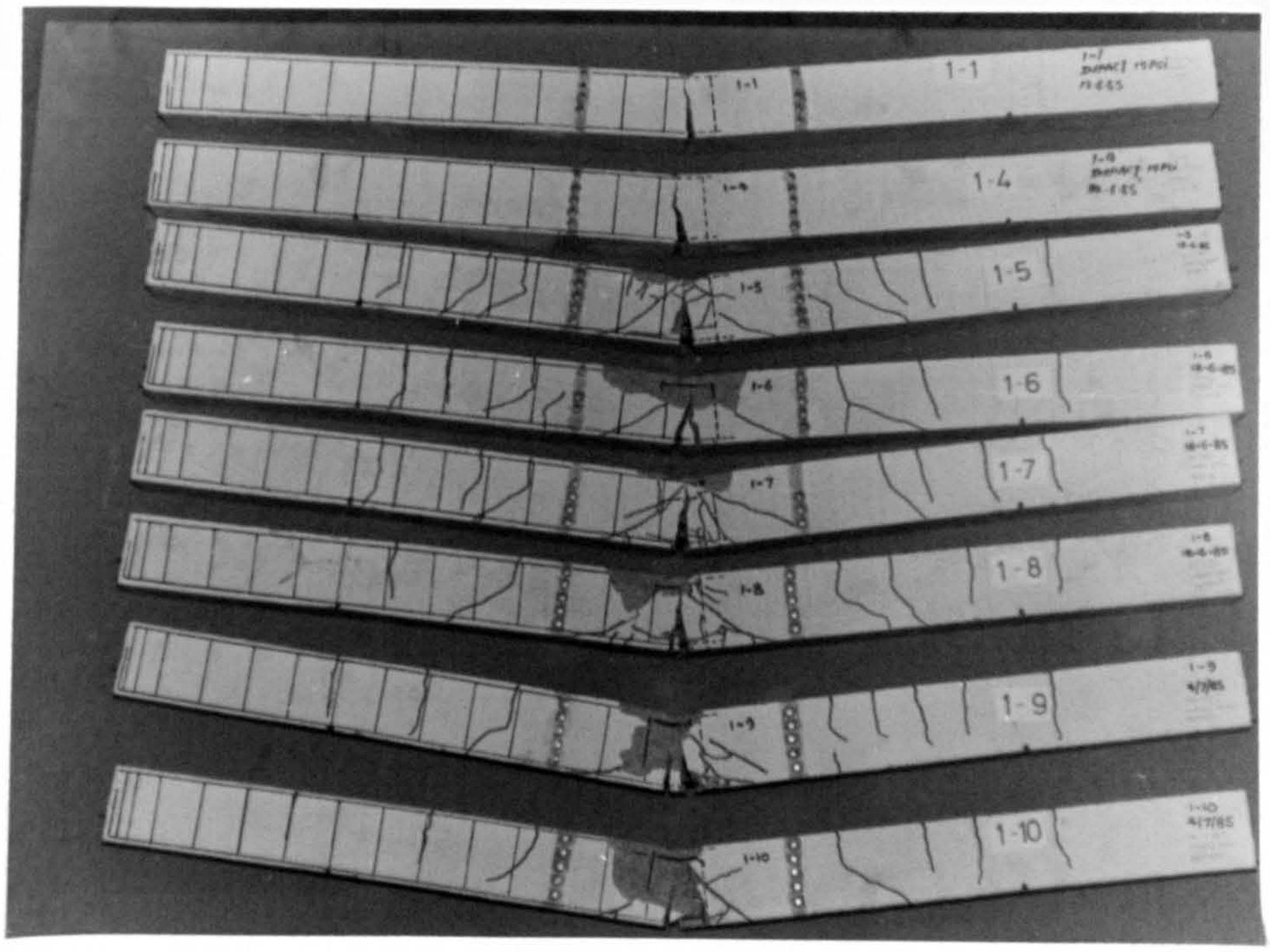

SERIES 1

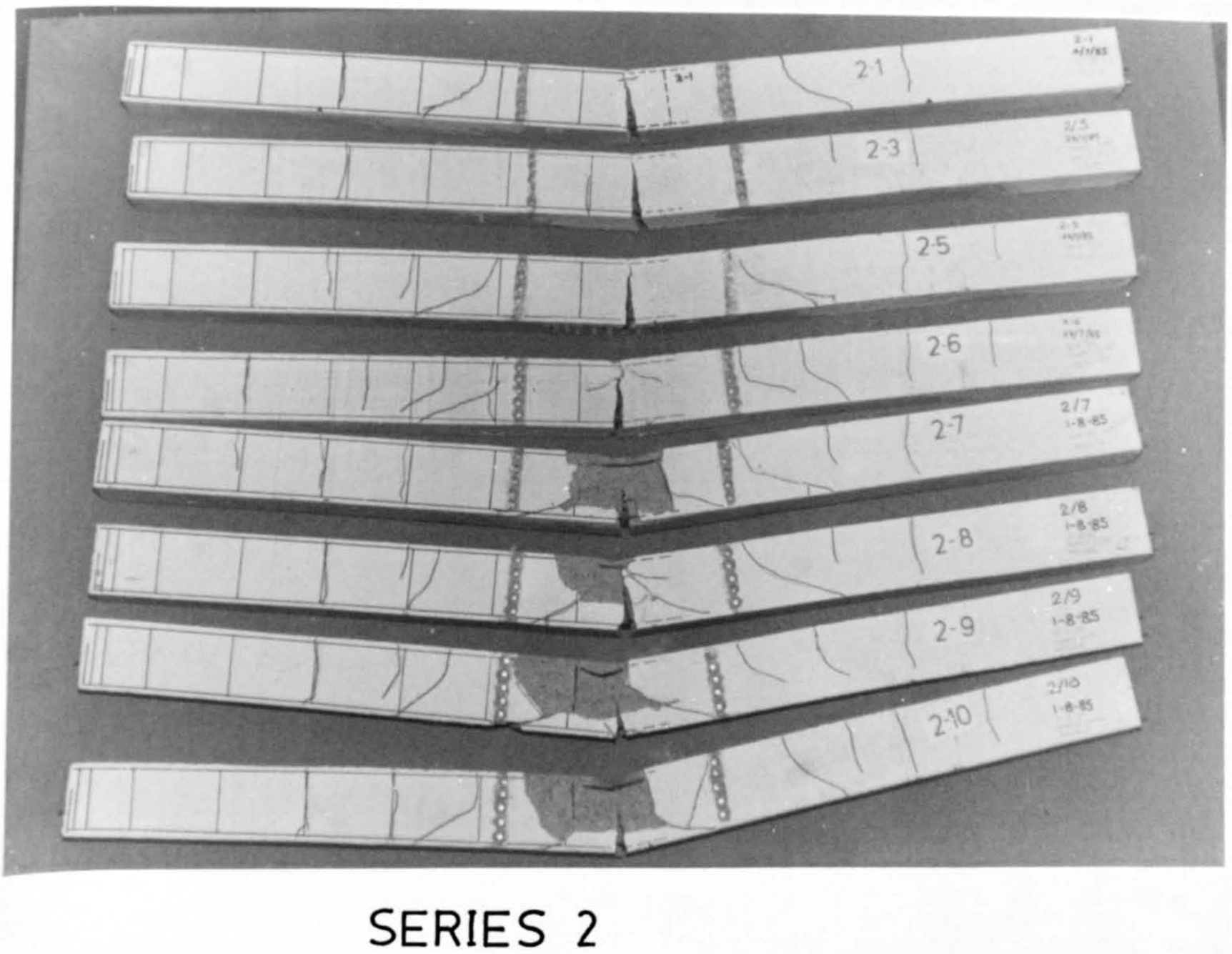

SERIES 2

APPENDIX C CRACK PATTERN
(b) IMPACTED BEAMS

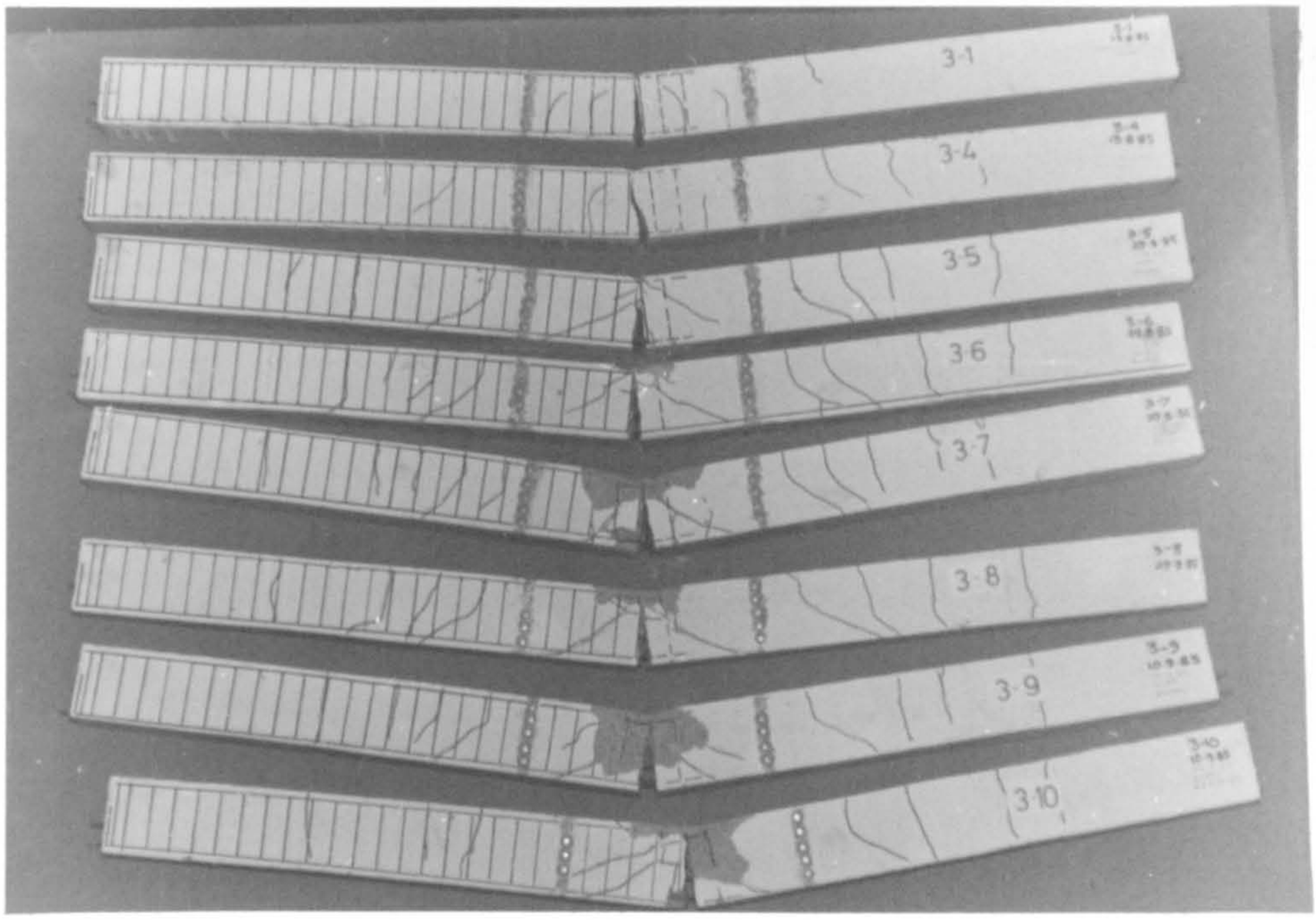

SERIES 3

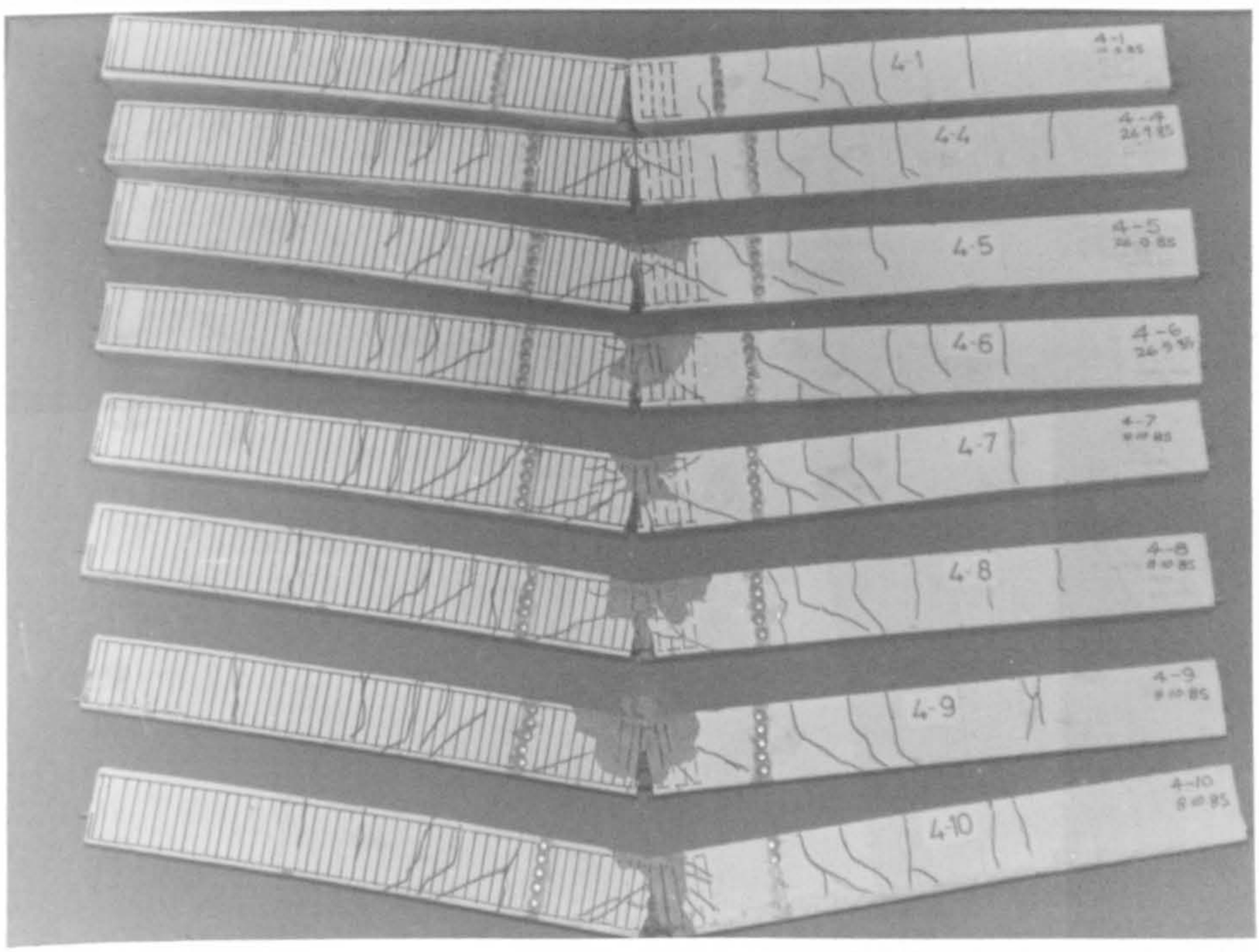

SERIES 4

APPENDIX C CRACK PATTERN
(b) IMPACTED BEAMS

APPENDIX D

LVDT Records and Deformation Profiles

The LVDT records were obtained as described in section 3.7.5 and are presented in part (a) of this appendix. The traces for beams 1.1, 1.7 and 4.6 failed to record.

The deformation profiles in part (b) are obtained from the LVDT records. i.e the deflections indicated by LVDTs at a certain time were joined by a curve to give the deformation profile at this particular time.

The following notes are applied to both part (a) and part (b) in this appendix.

(a) ∂ = dynamic deflection, and t = time.

(b) Time = 0 at trigger (section 4.3.4).

(c) LVDT 1 is at 1/2 span (fig. 3.9).

(d) LVDT 2 is at 1/3 span (fig. 3.9).

(e) LVDT 3 is at 1/6 span (fig. 3.9).

Beam 1.1

unsuccessful
in
recording

Beam 1.7

unsuccessful
in
recording

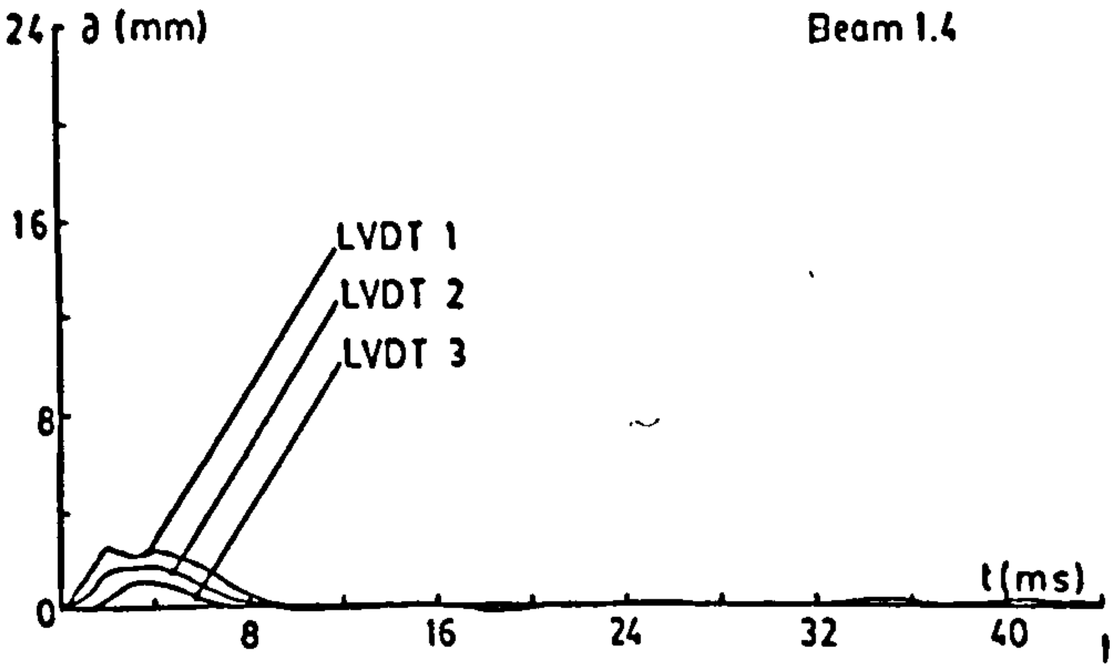

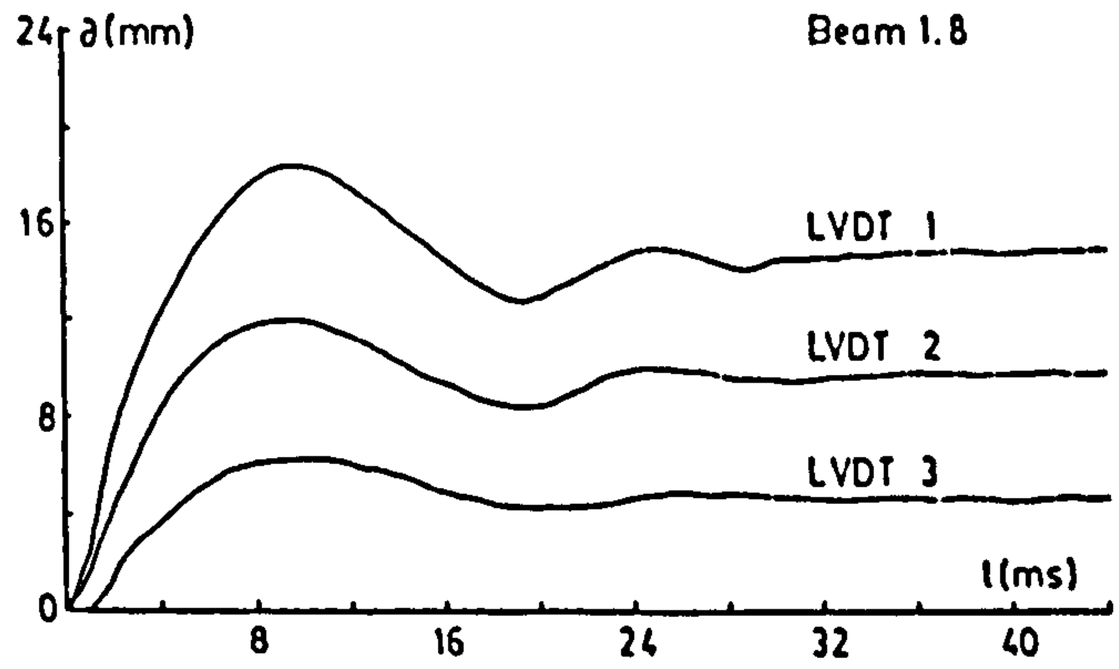

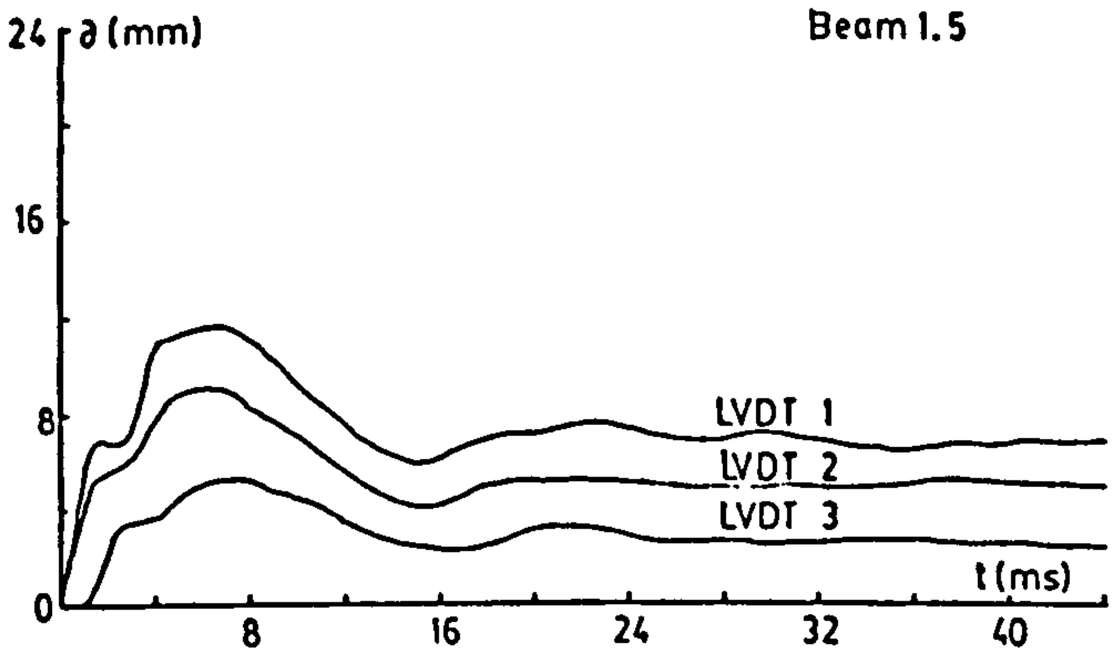

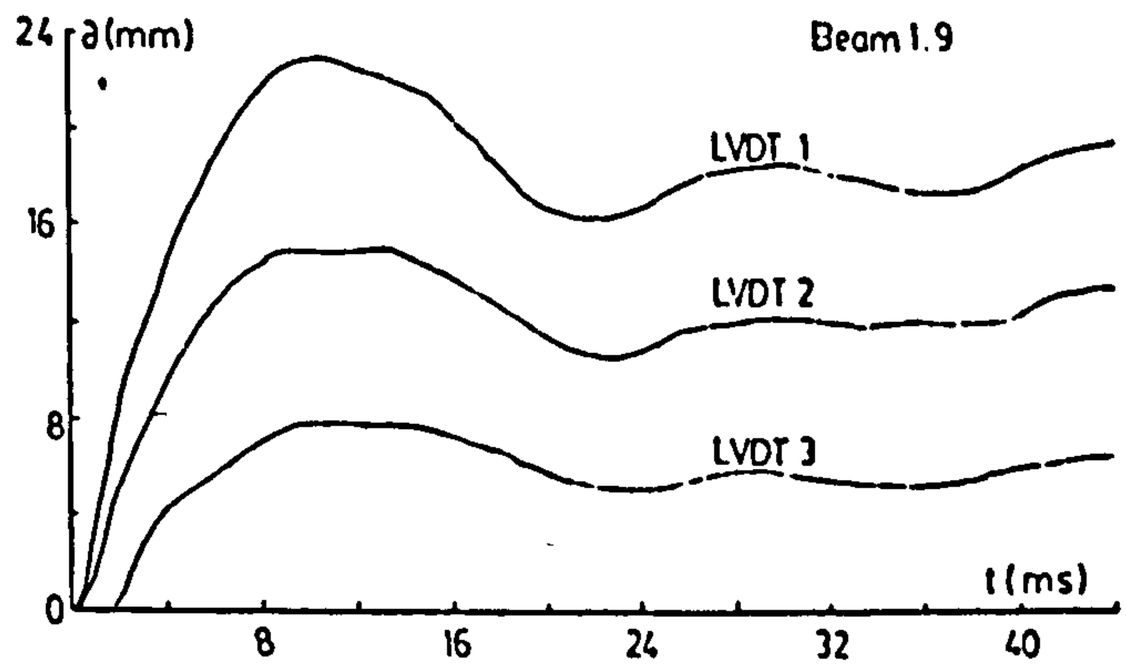

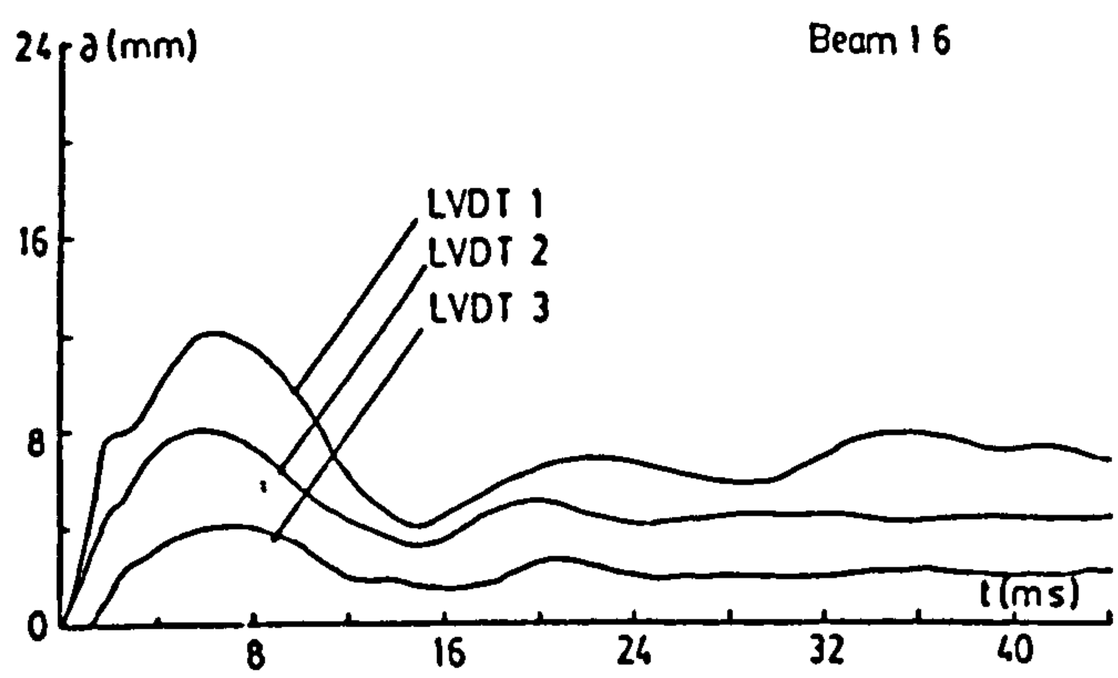

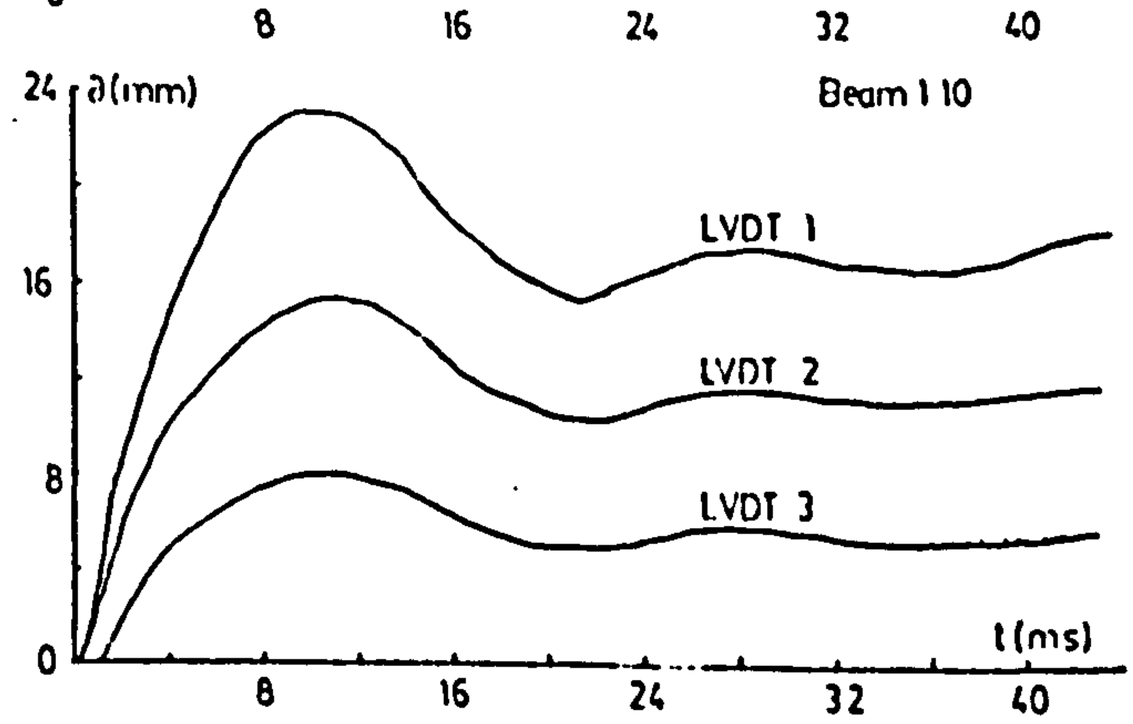

Notes : see page D1.

APPENDIX D (a) LVDT RECORDS

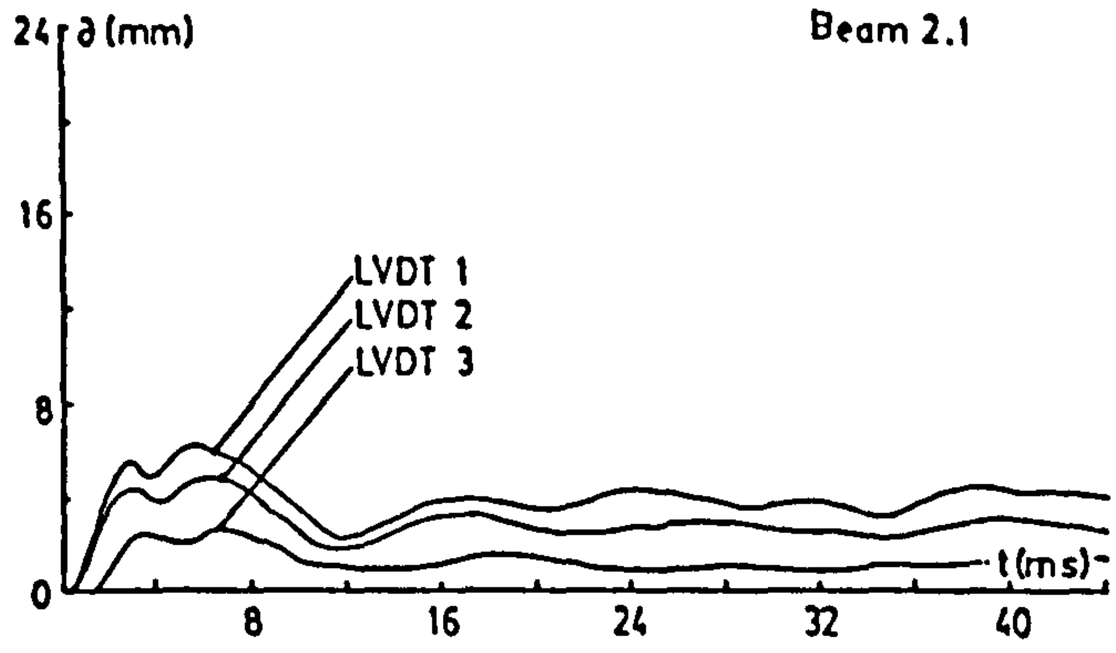

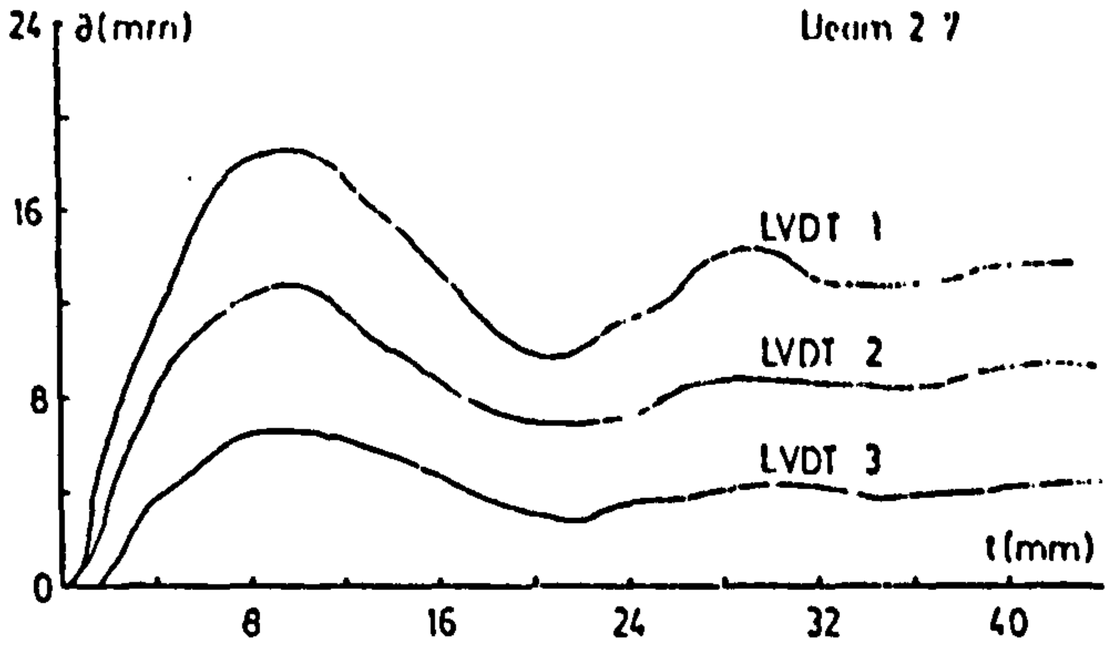

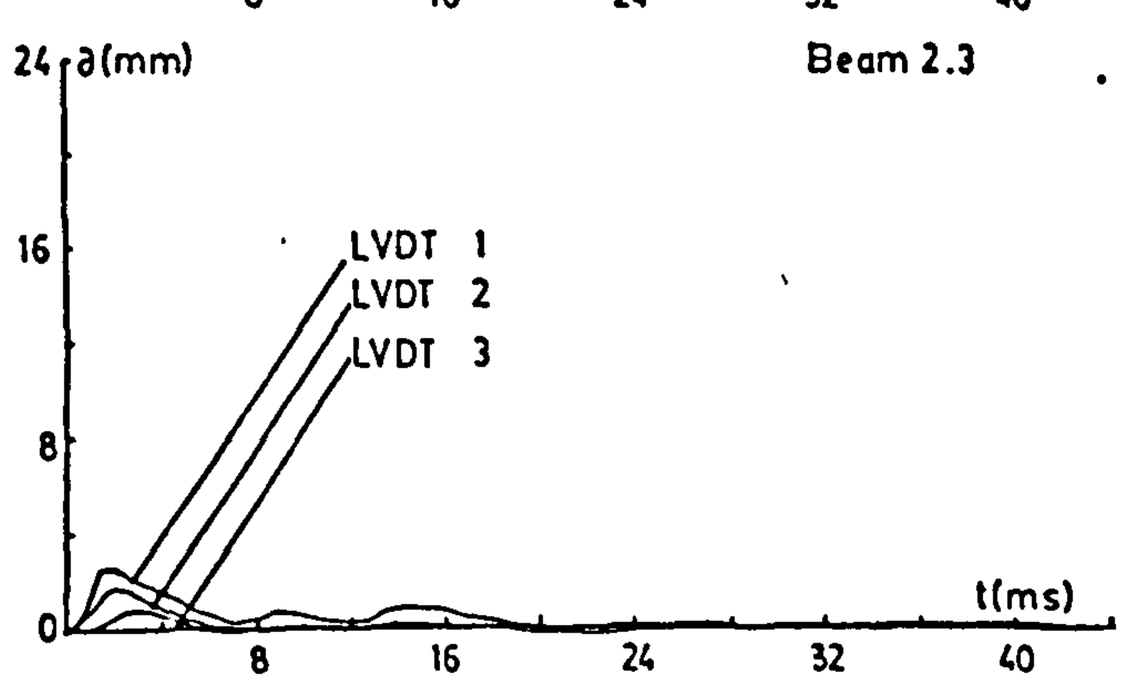

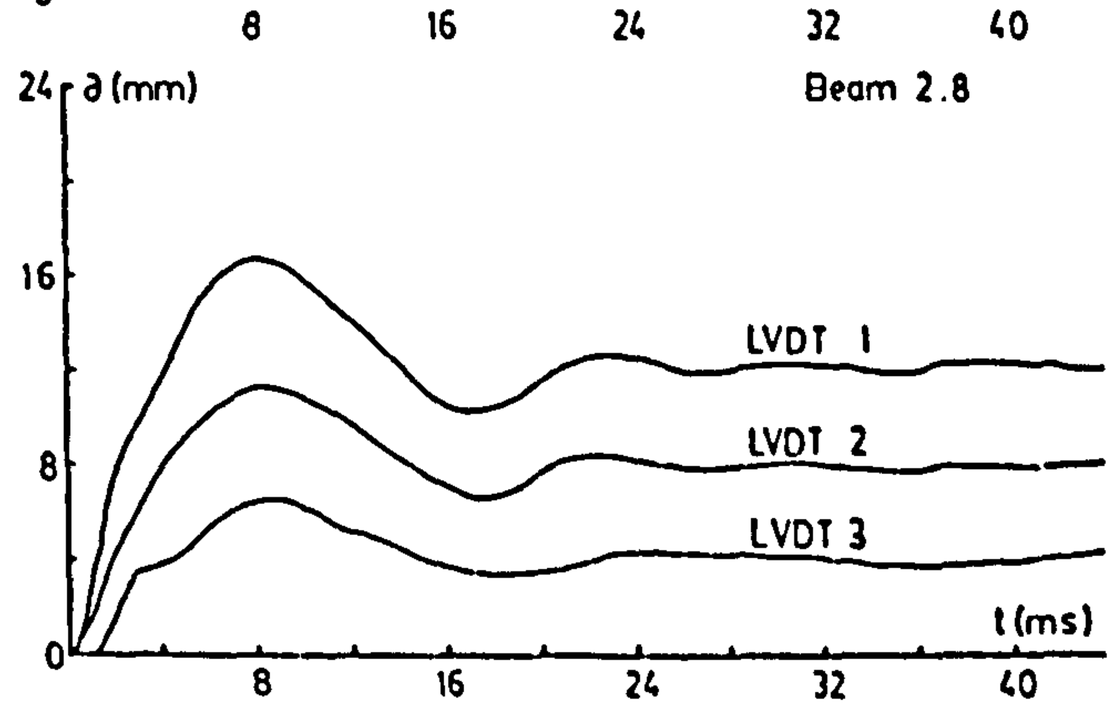

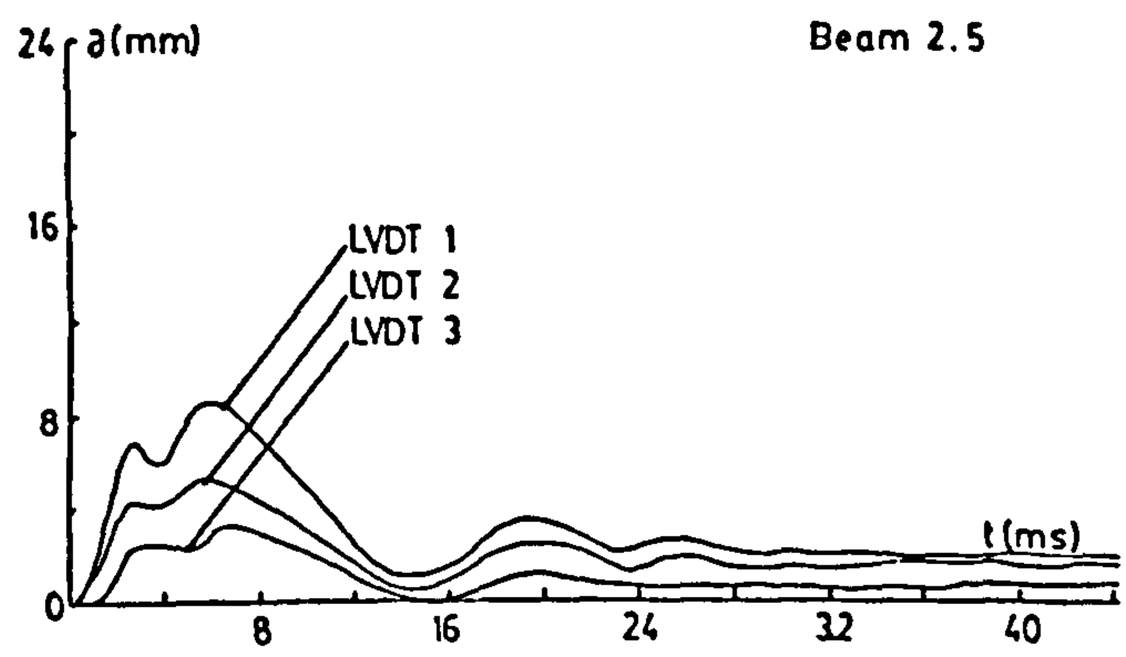

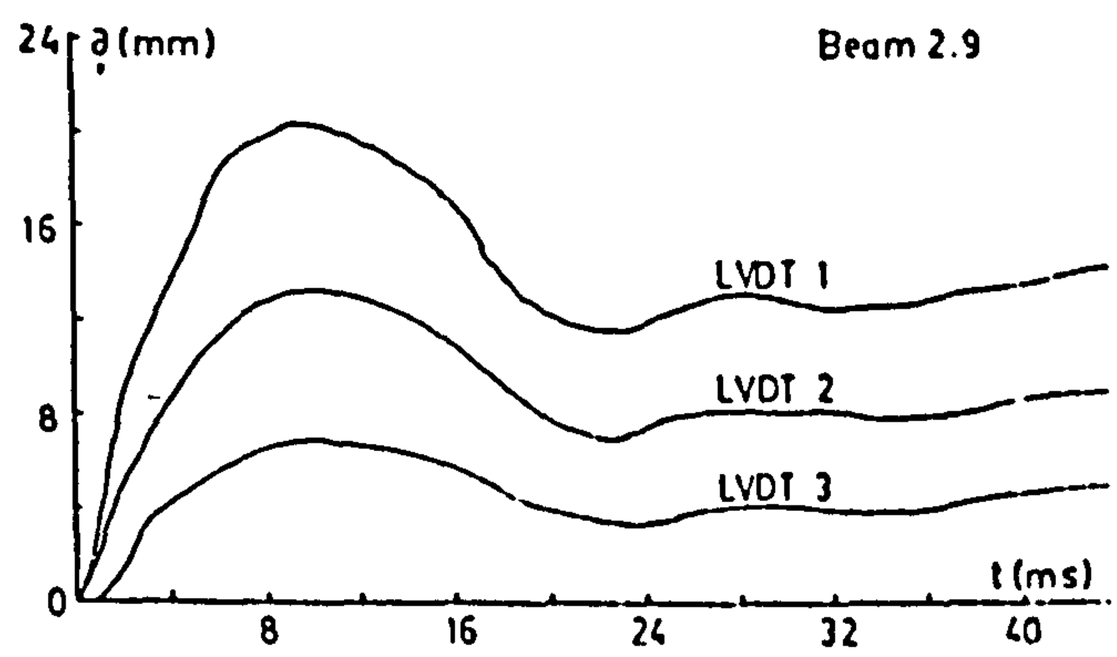

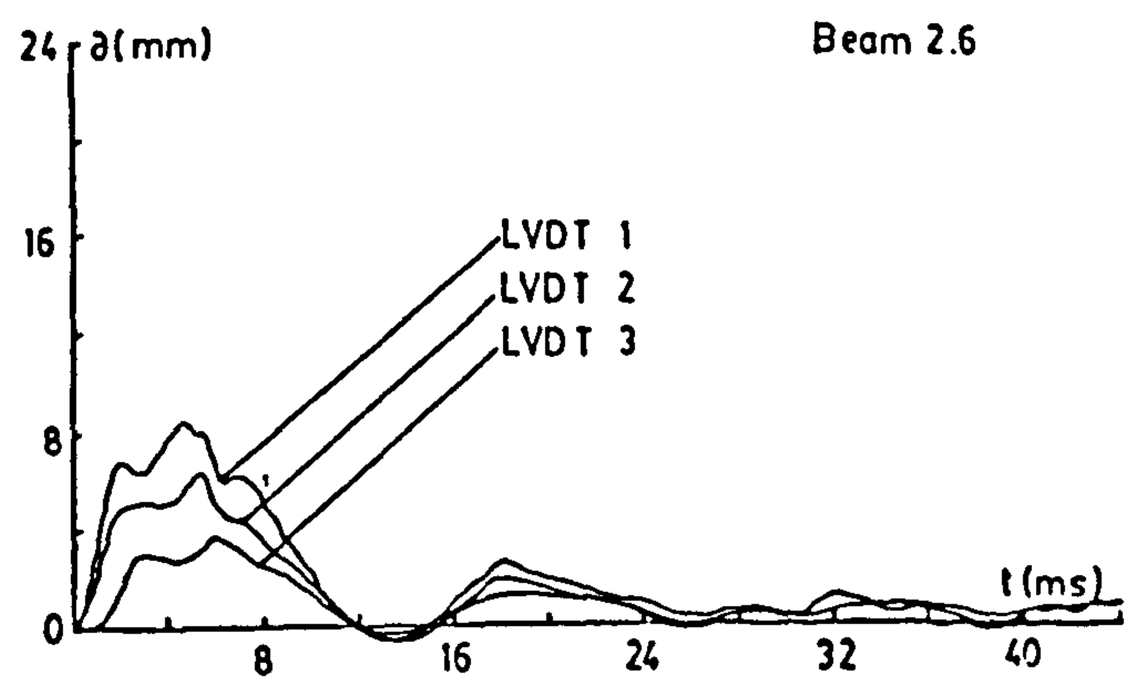

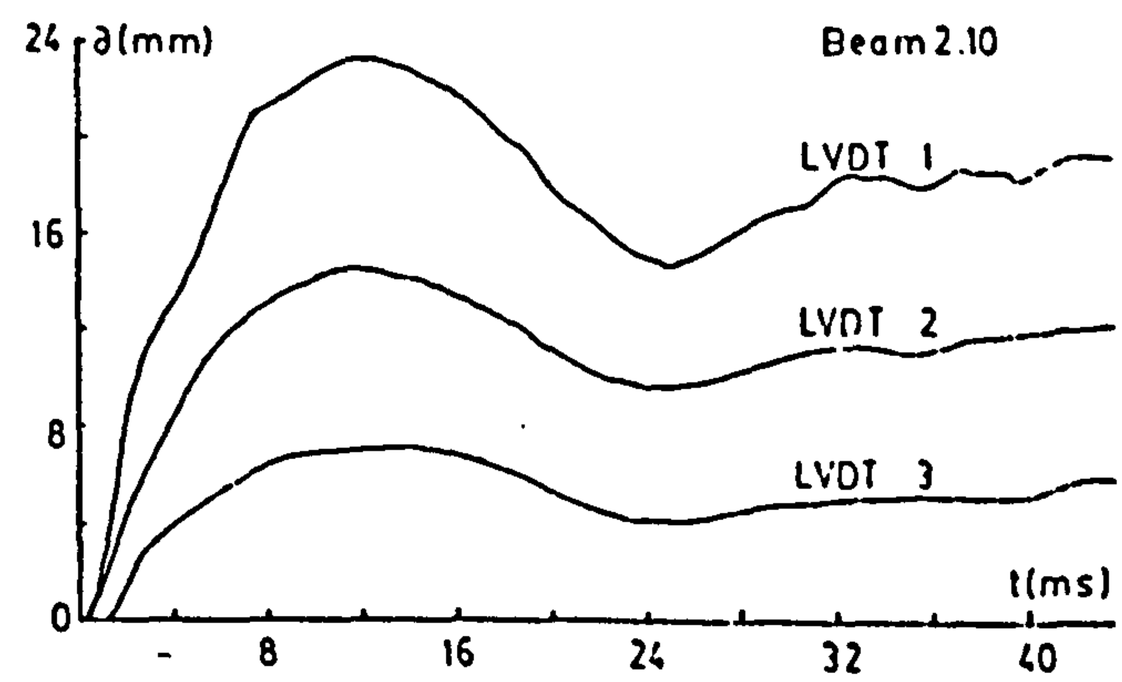

Notes : see page D1.

APPENDIX D (a) LVDT RECORDS

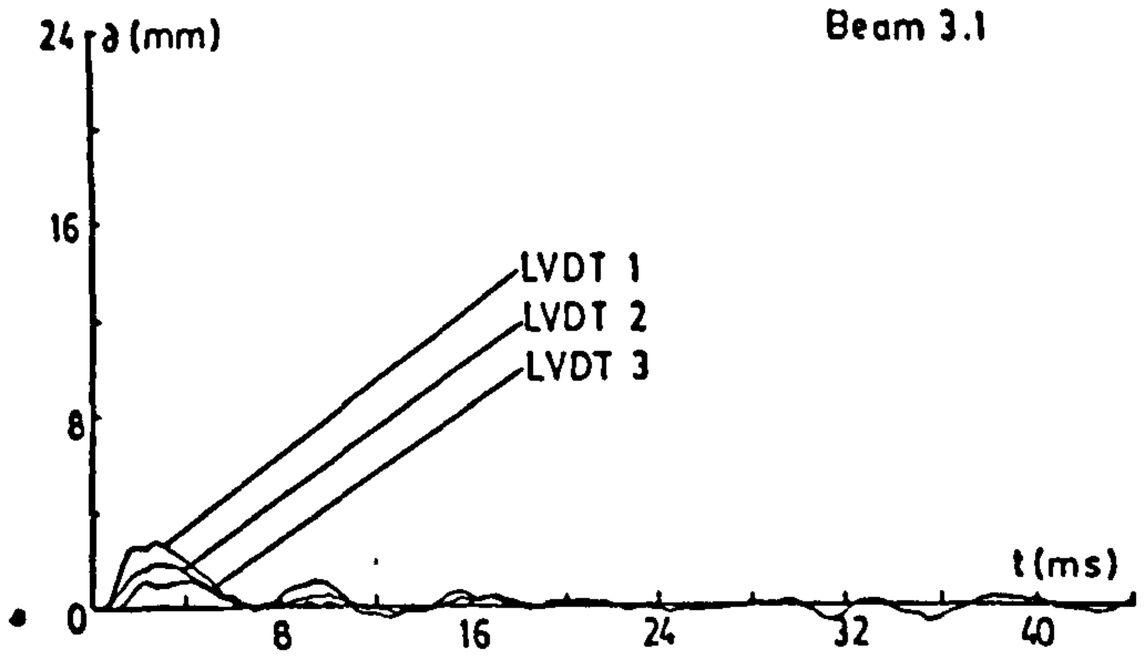

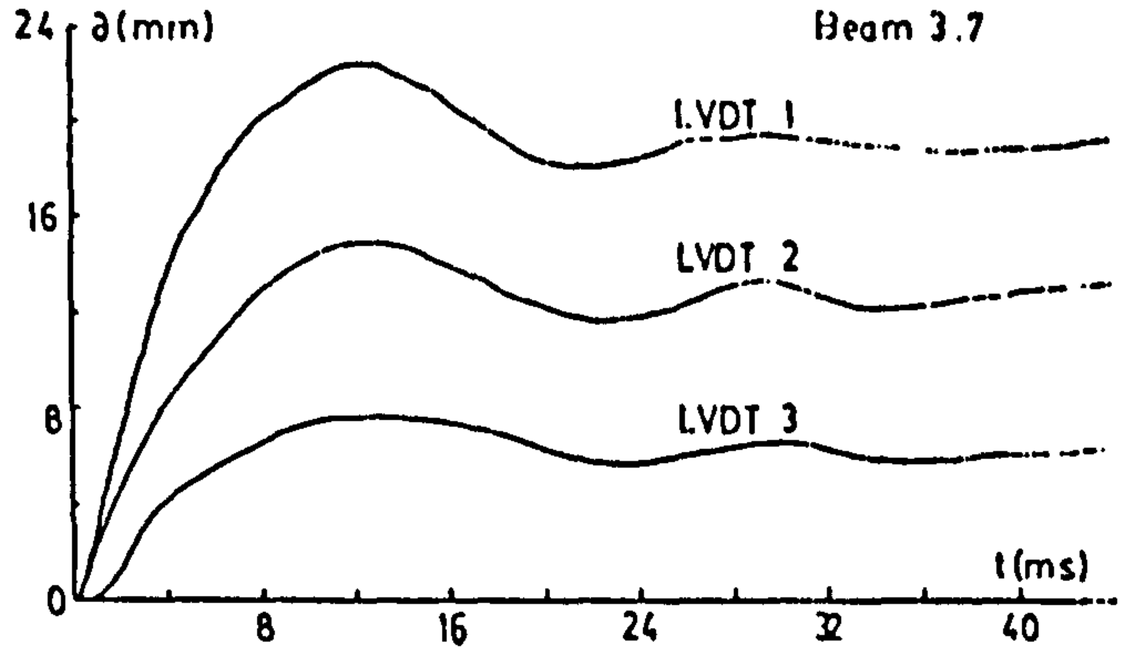

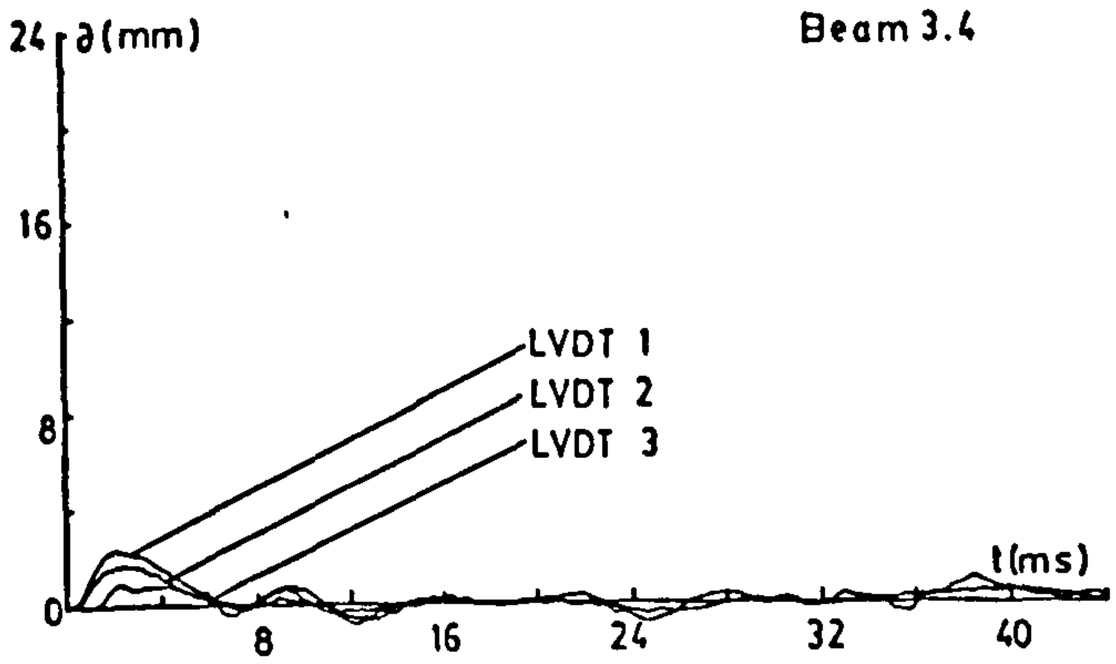

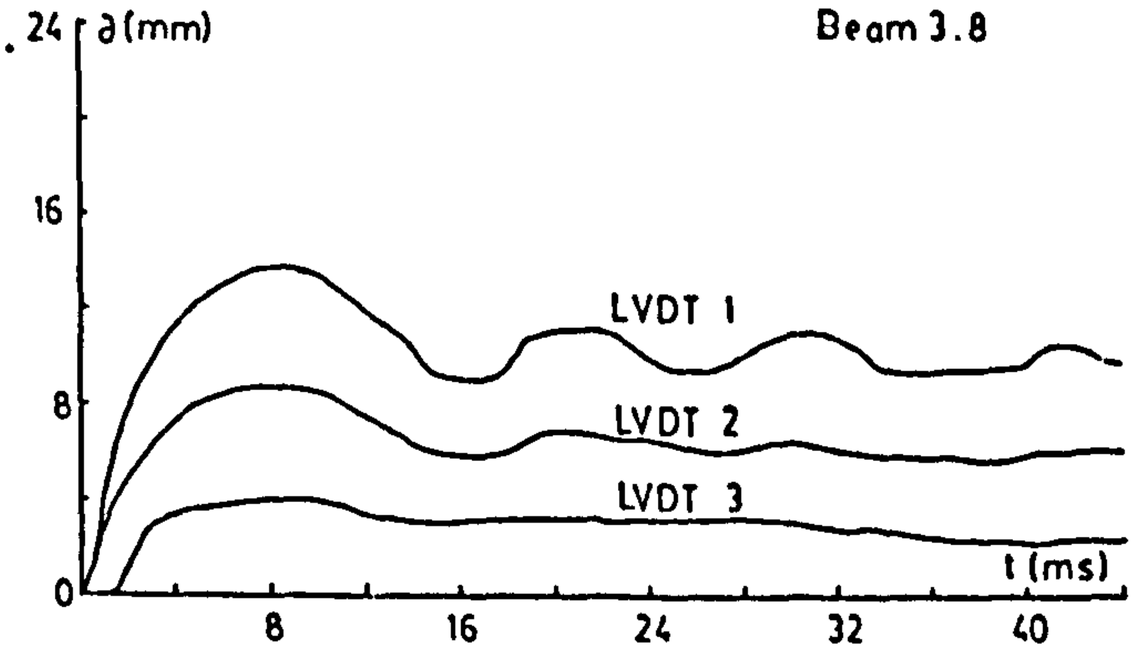

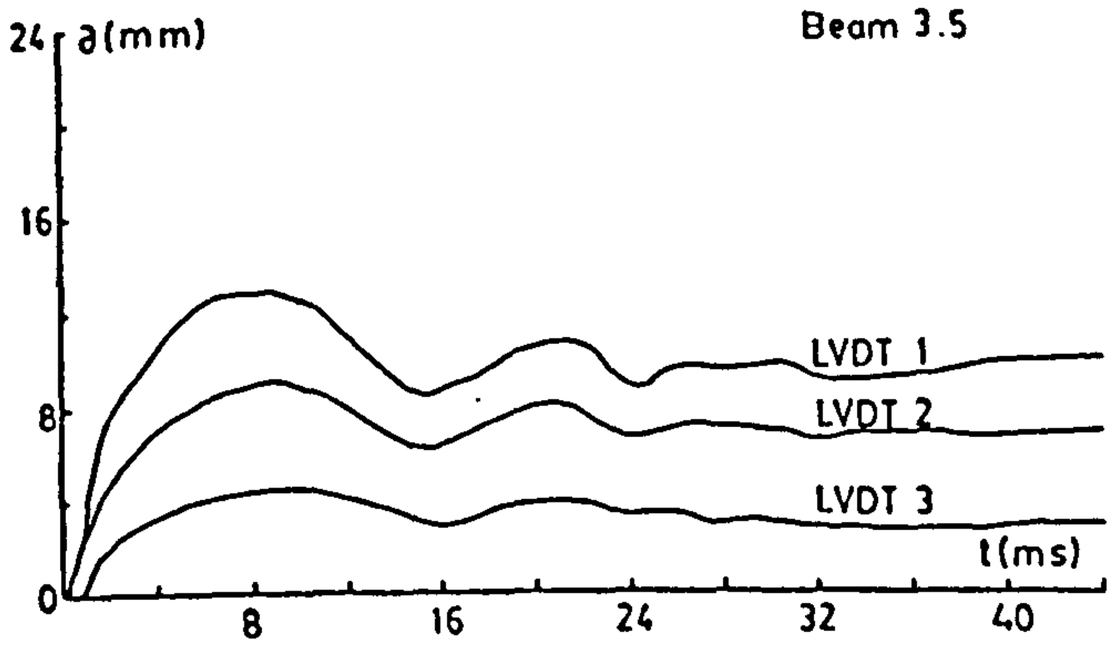

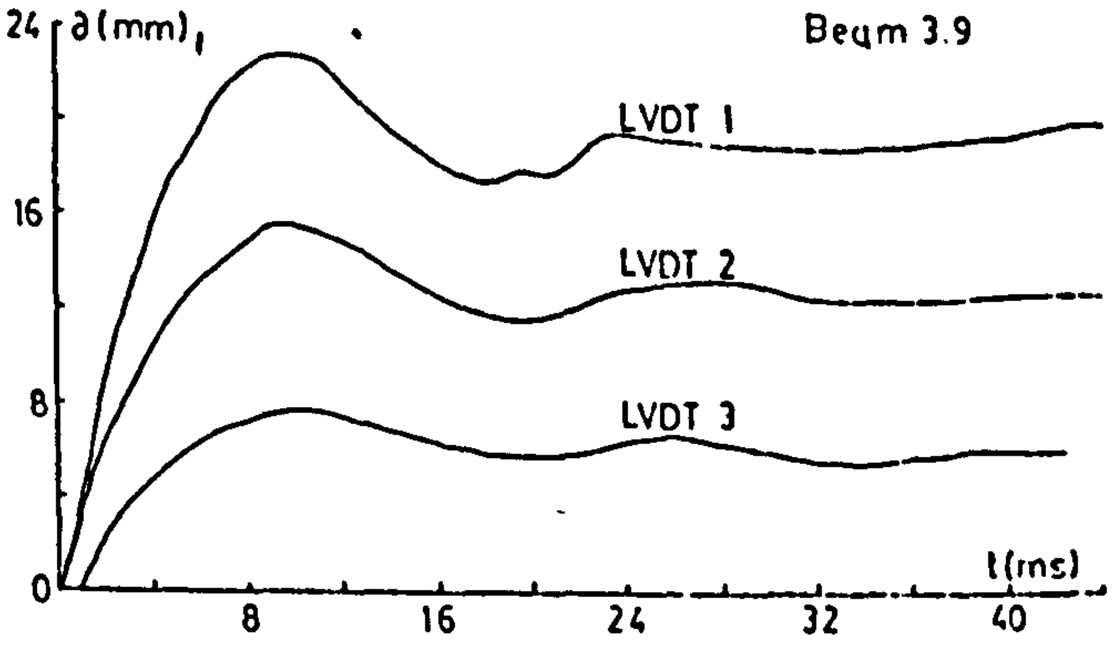

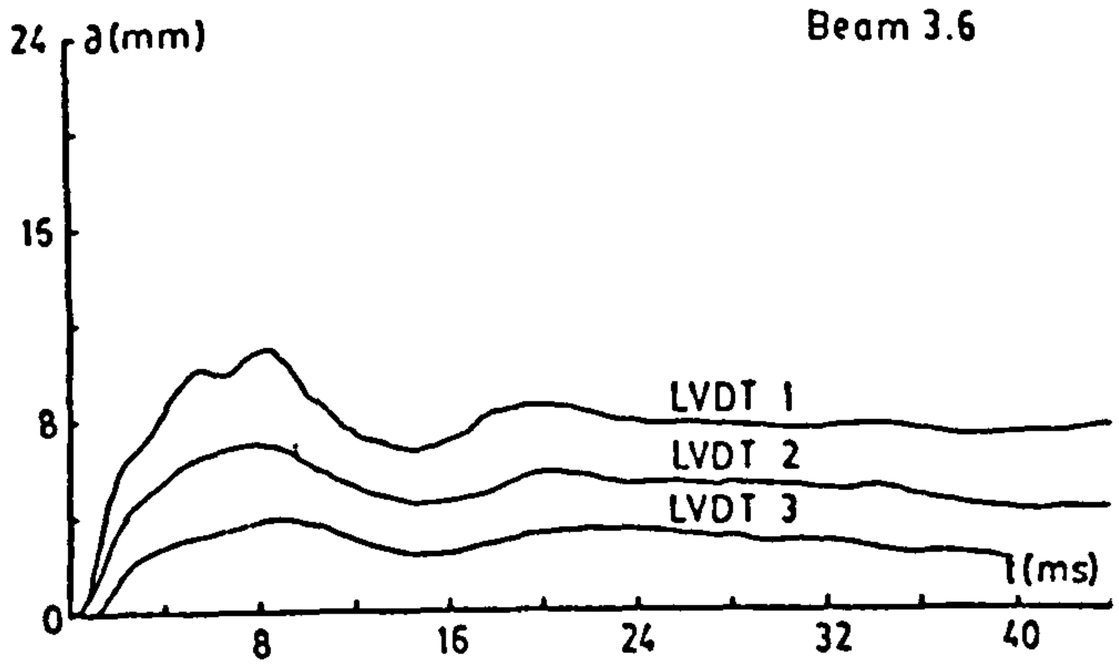

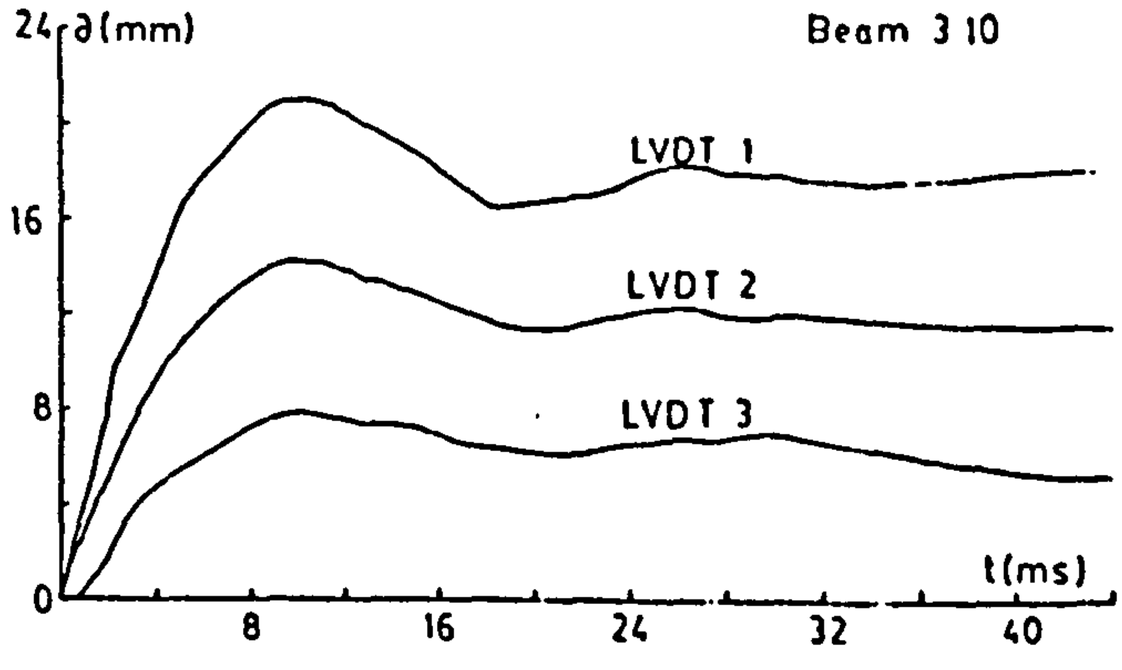

Notes : see page D1.

APPENDIX D (a) LVDT RECORDS

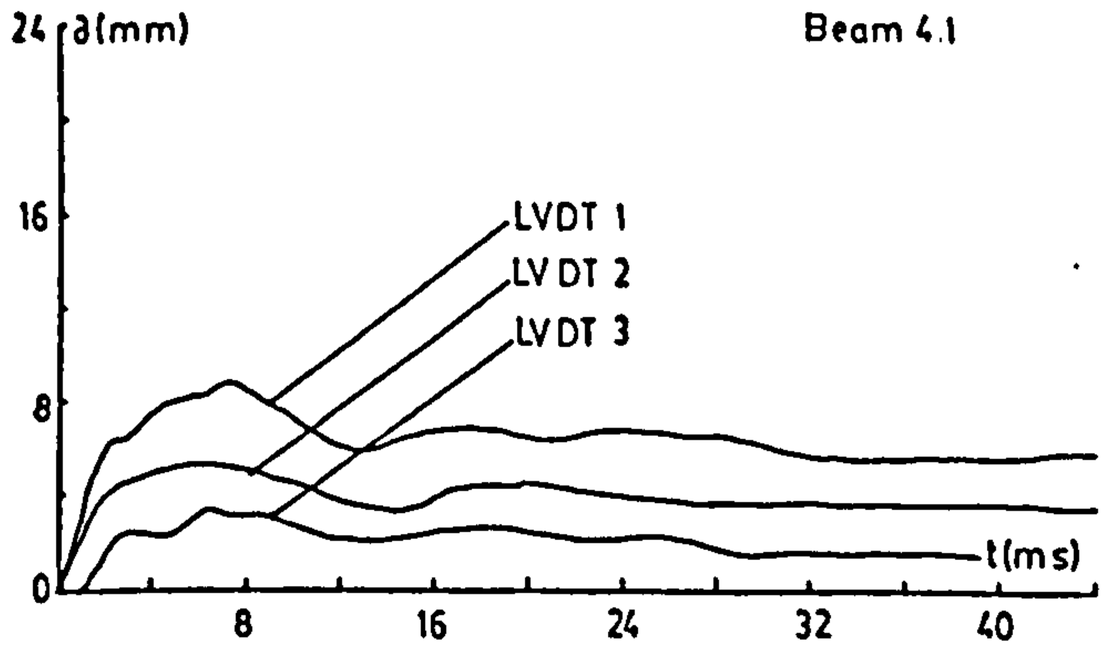

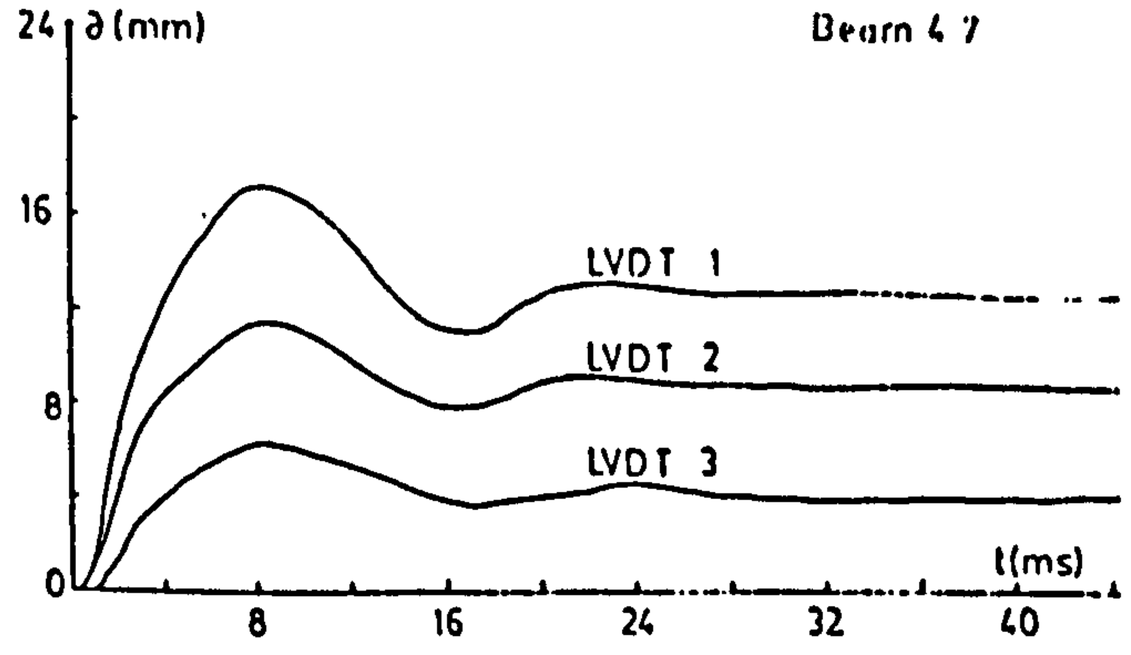

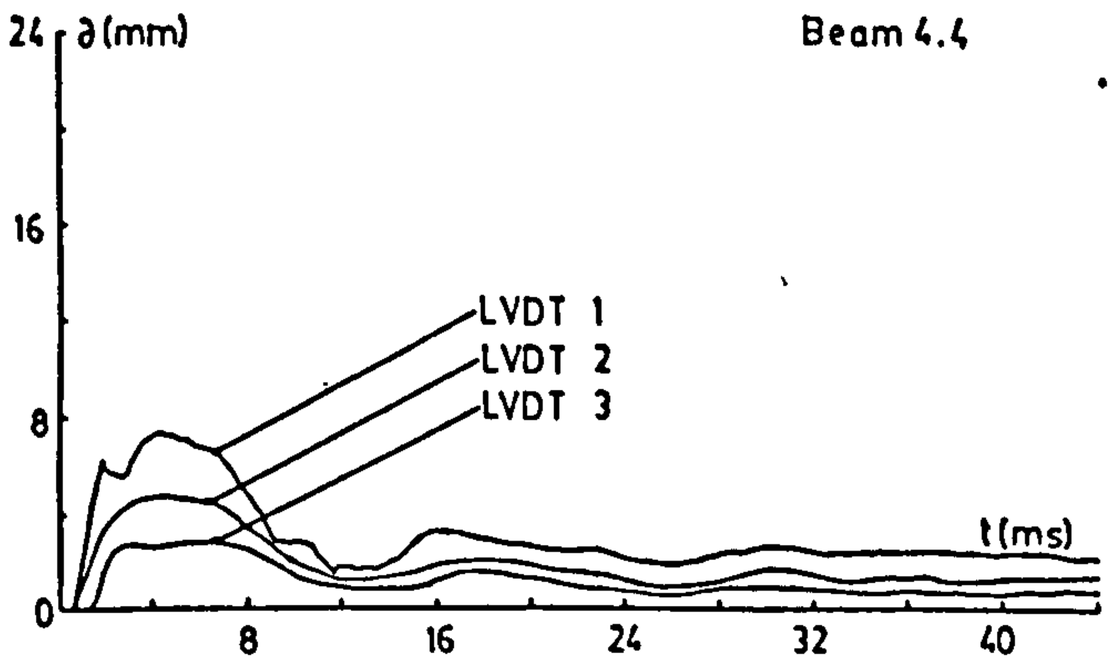

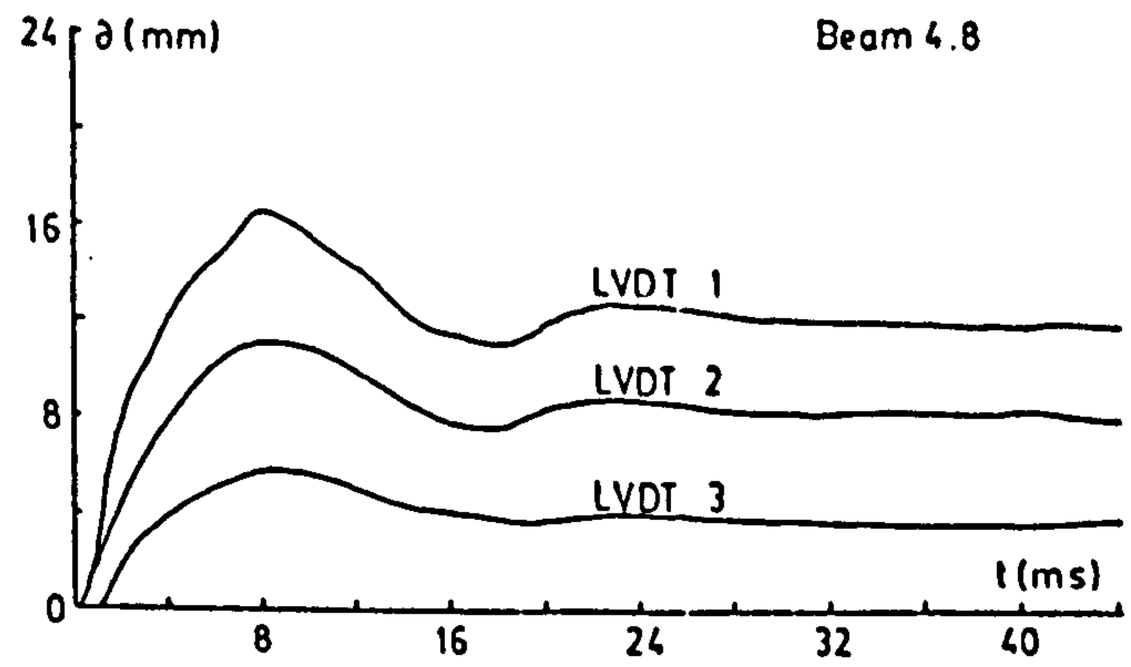

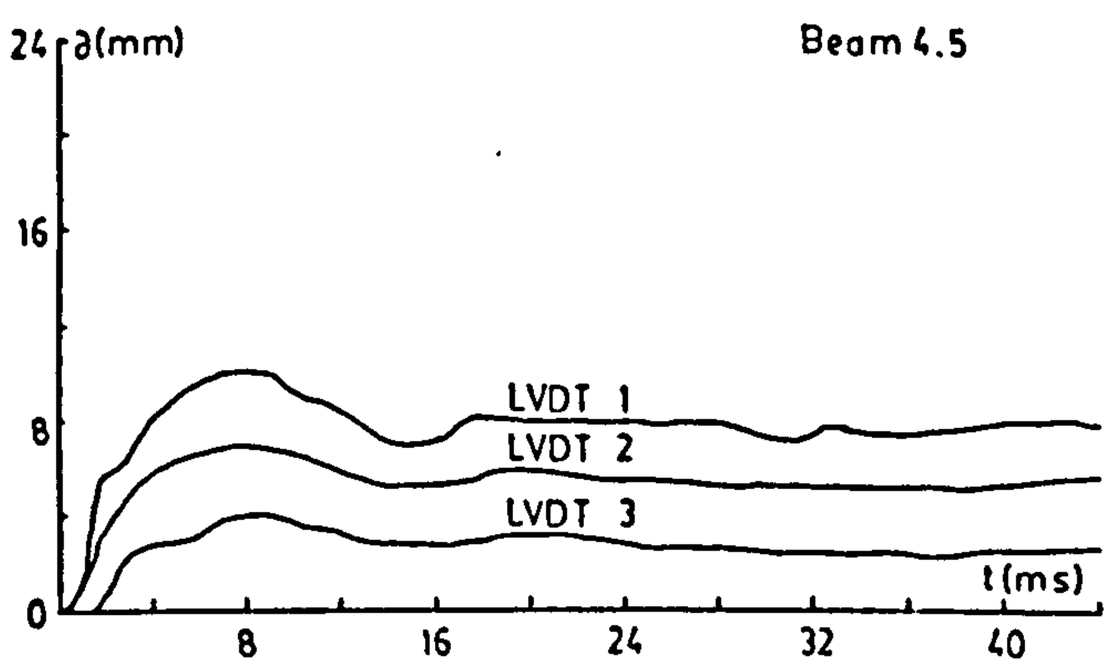

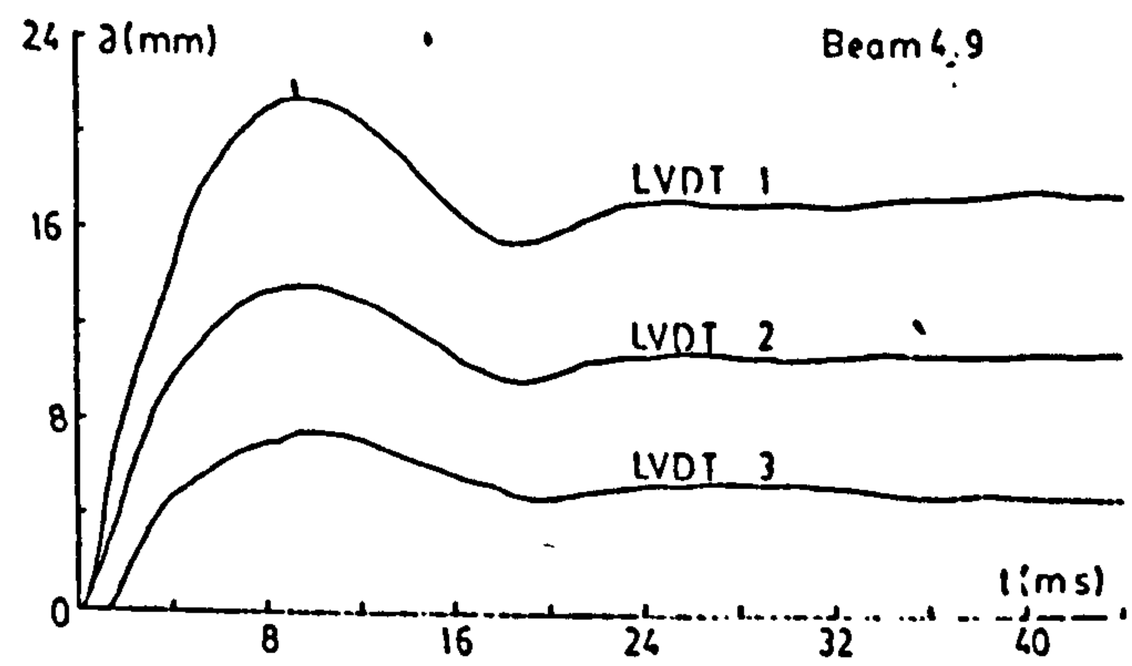

Beam 4.6

unsuccessful

in

recording

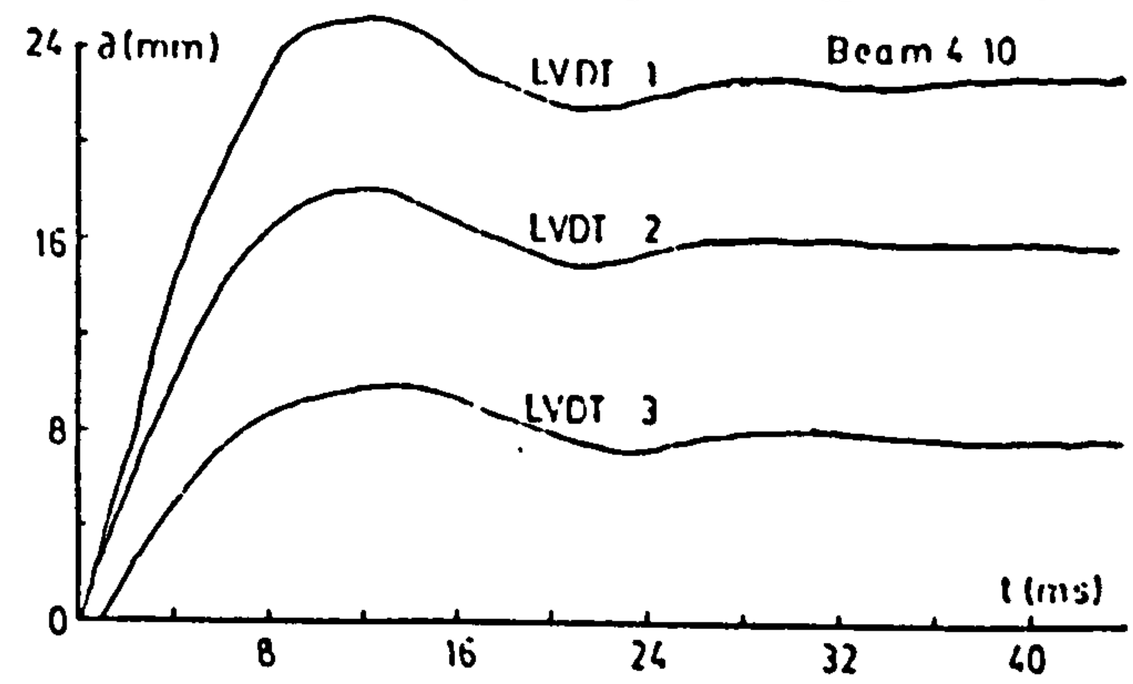

Notes : see page D1.

APPENDIX D (a) LVDT RECORDS

Beam 1.1

see page D2

Beam 1.7

see page D2

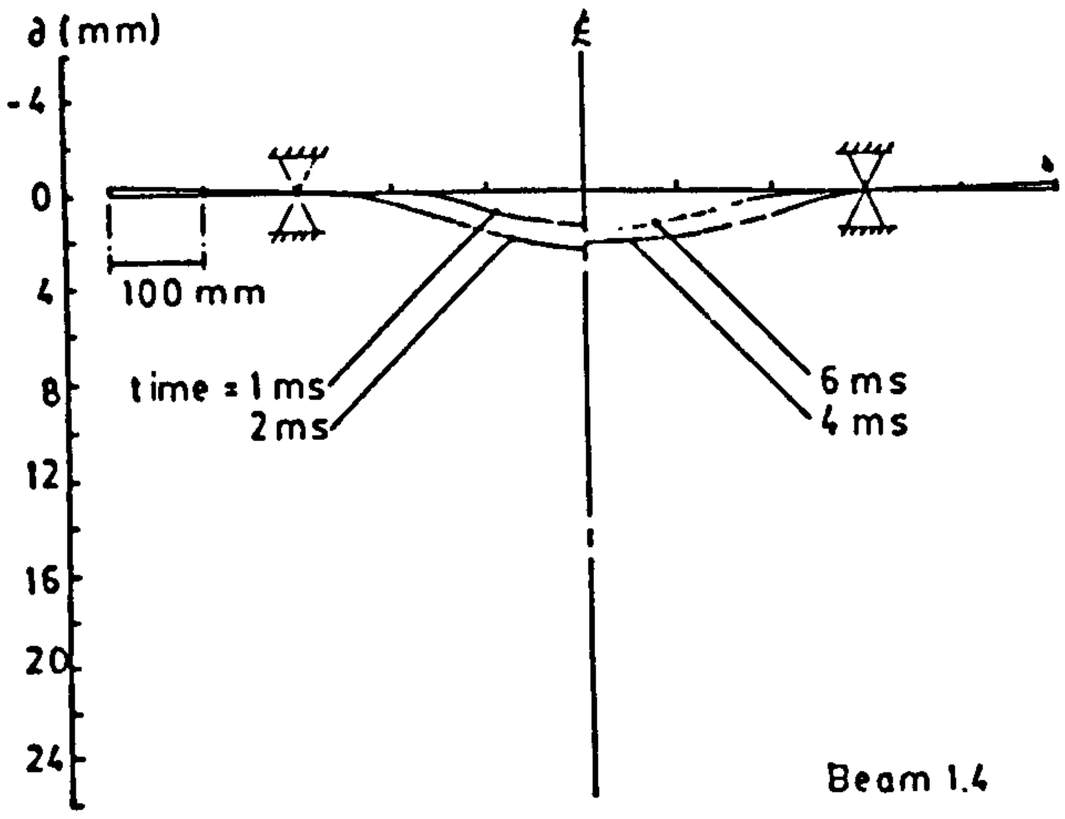

Beam 1.4

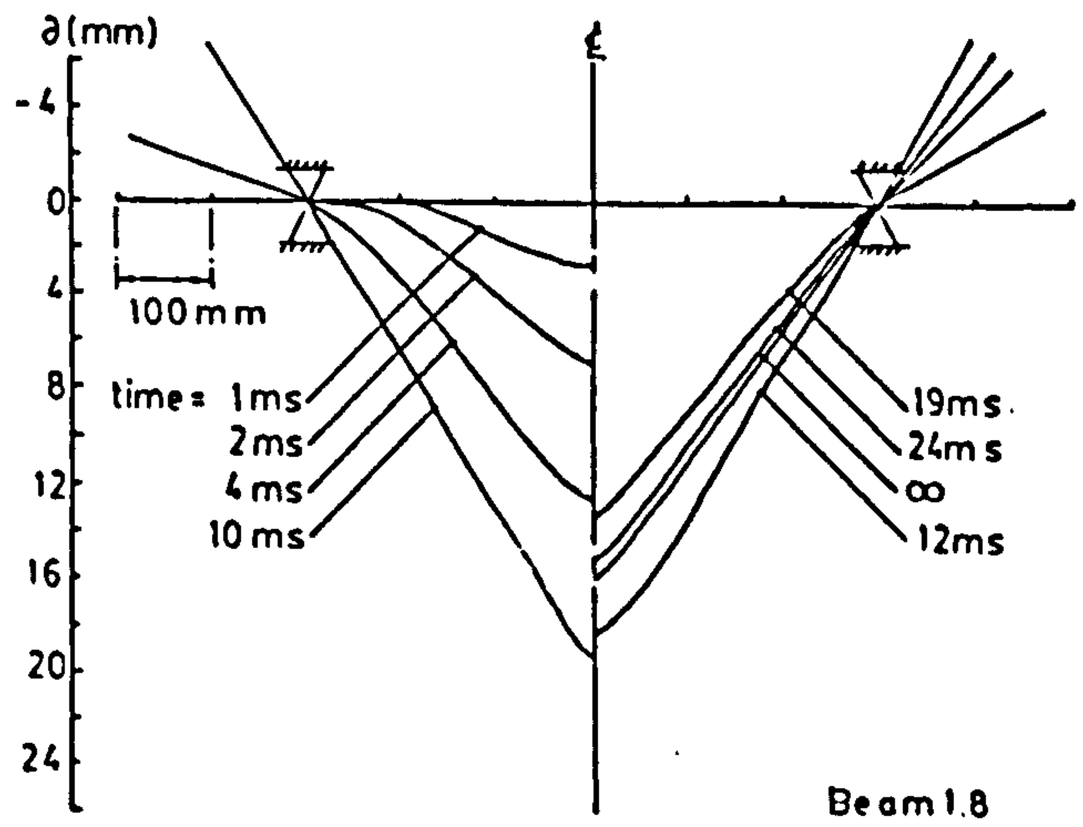

Beam 1.8

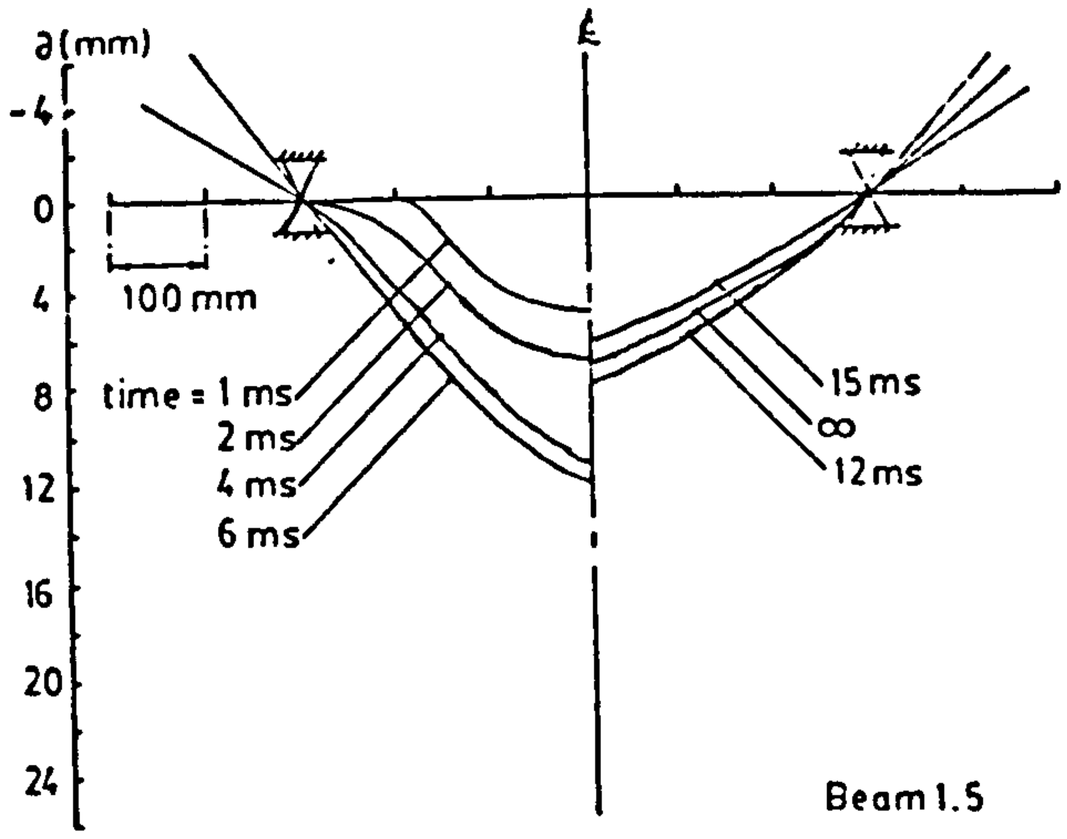

Beam 1.5

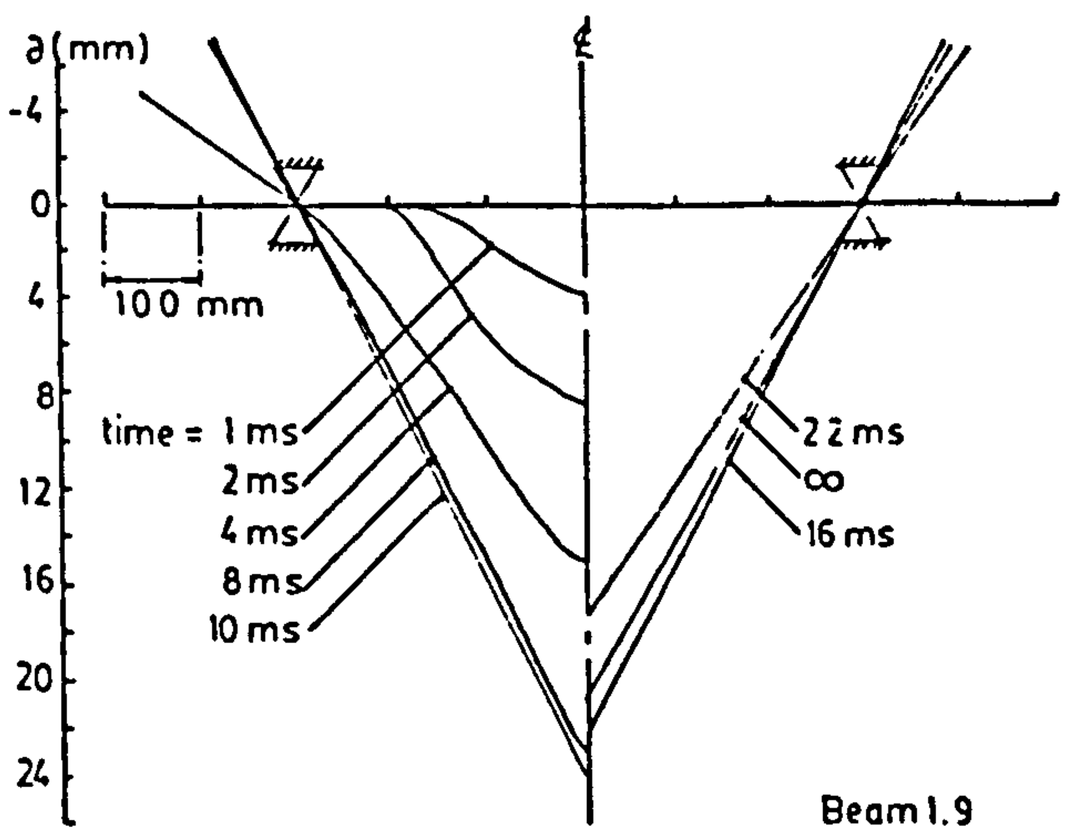

Beam 1.9

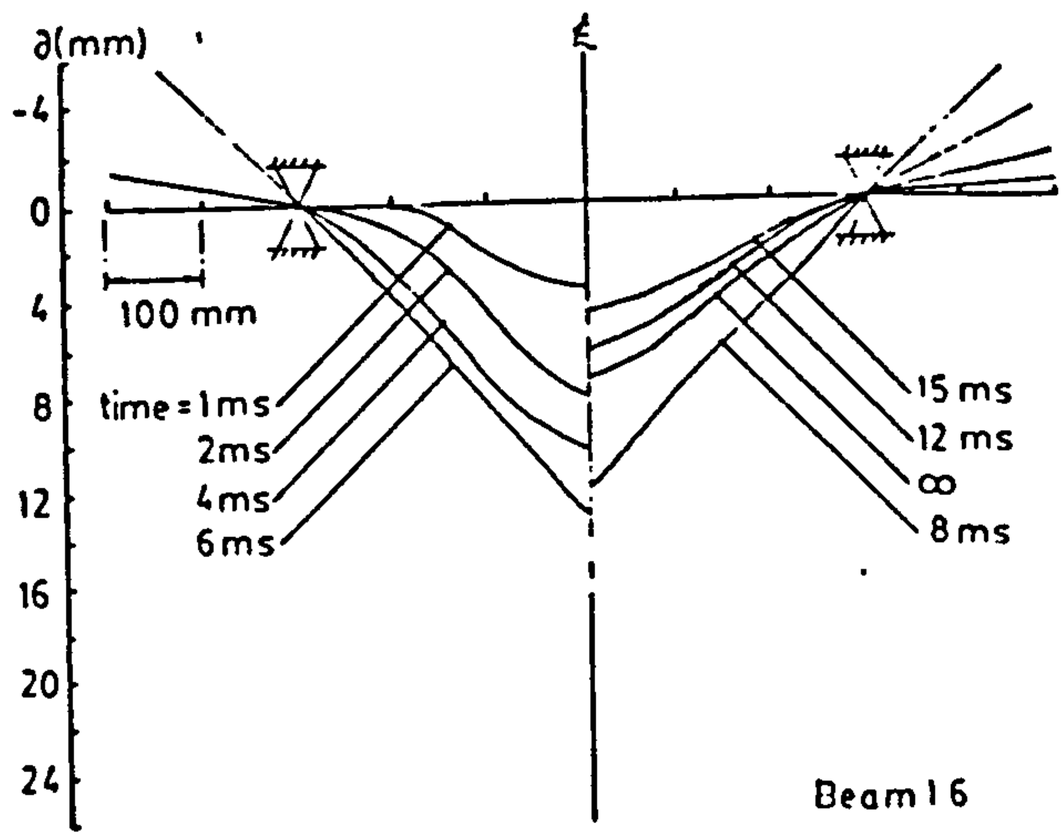

Beam 1 6

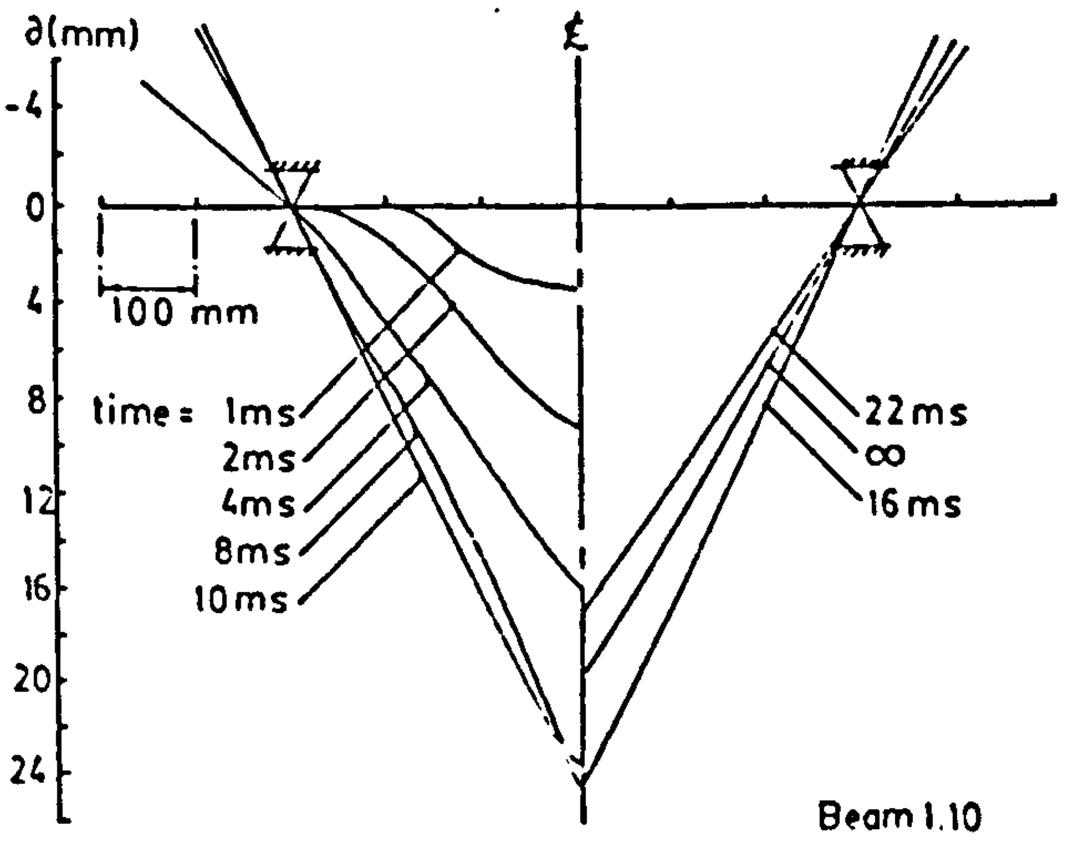

Beam 1.10

Notes : see page D1.

APPENDIX D (b) DEFORMATION PROFILES

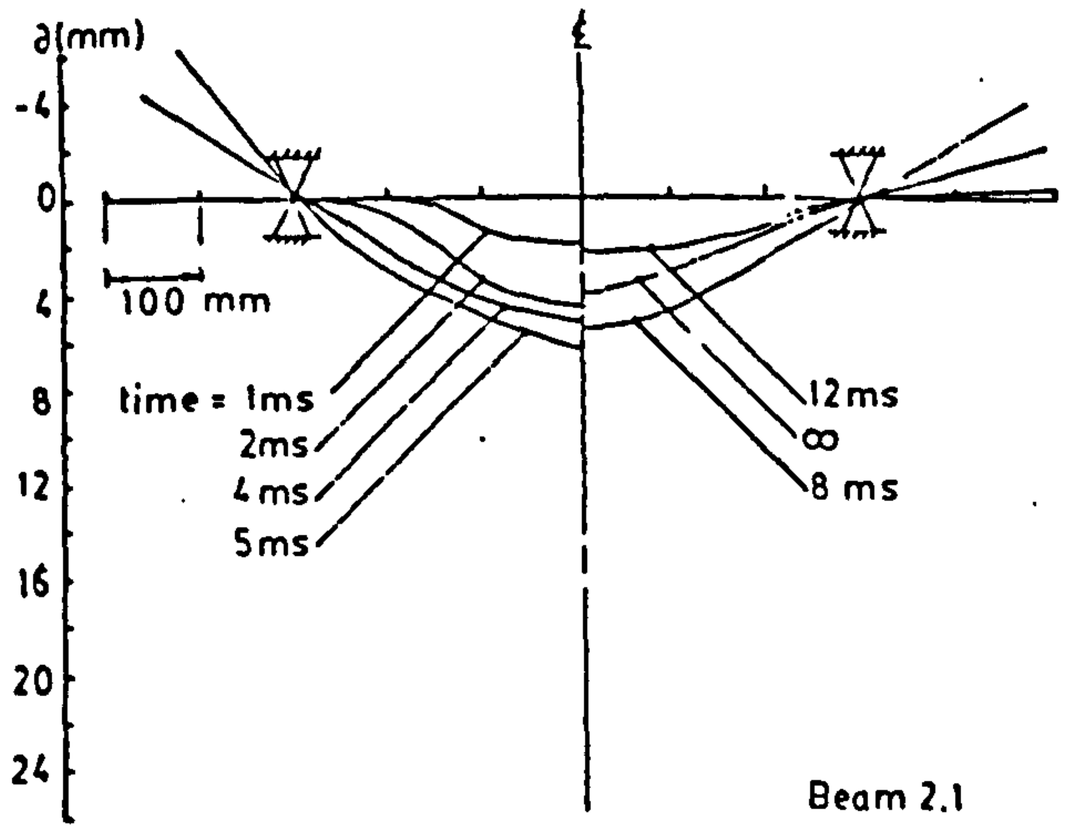

Beam 2.1

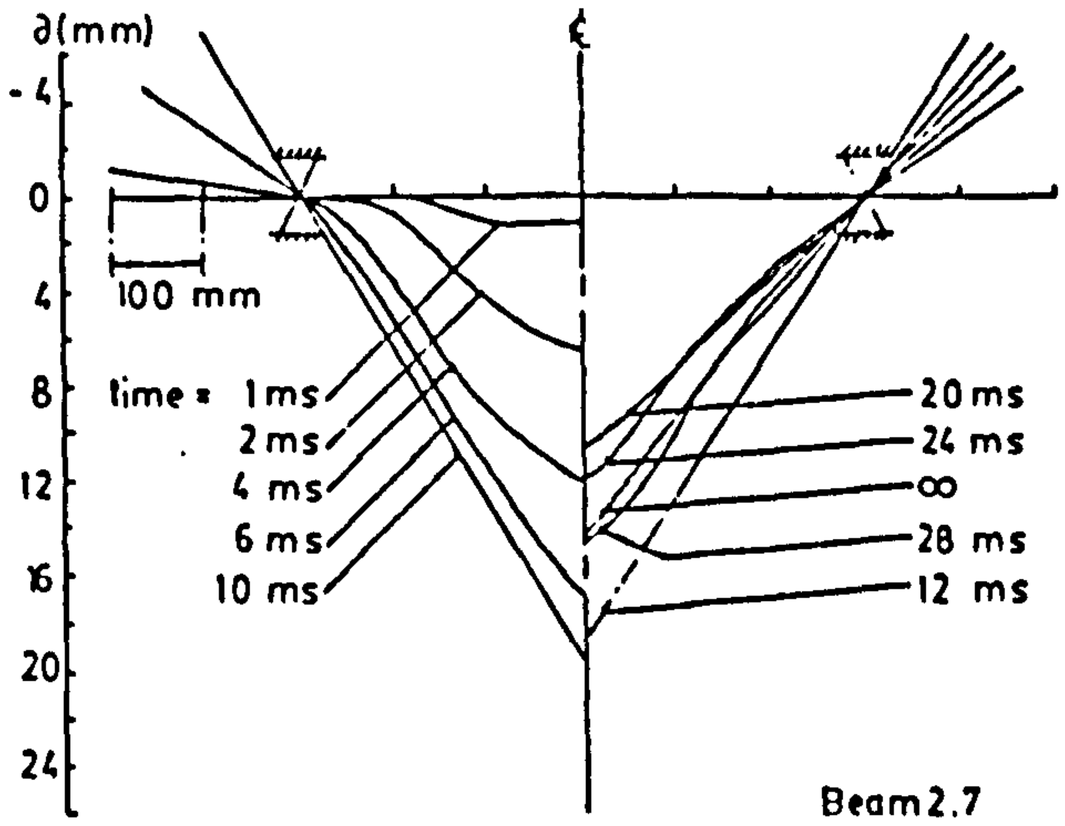

Beam 2.7

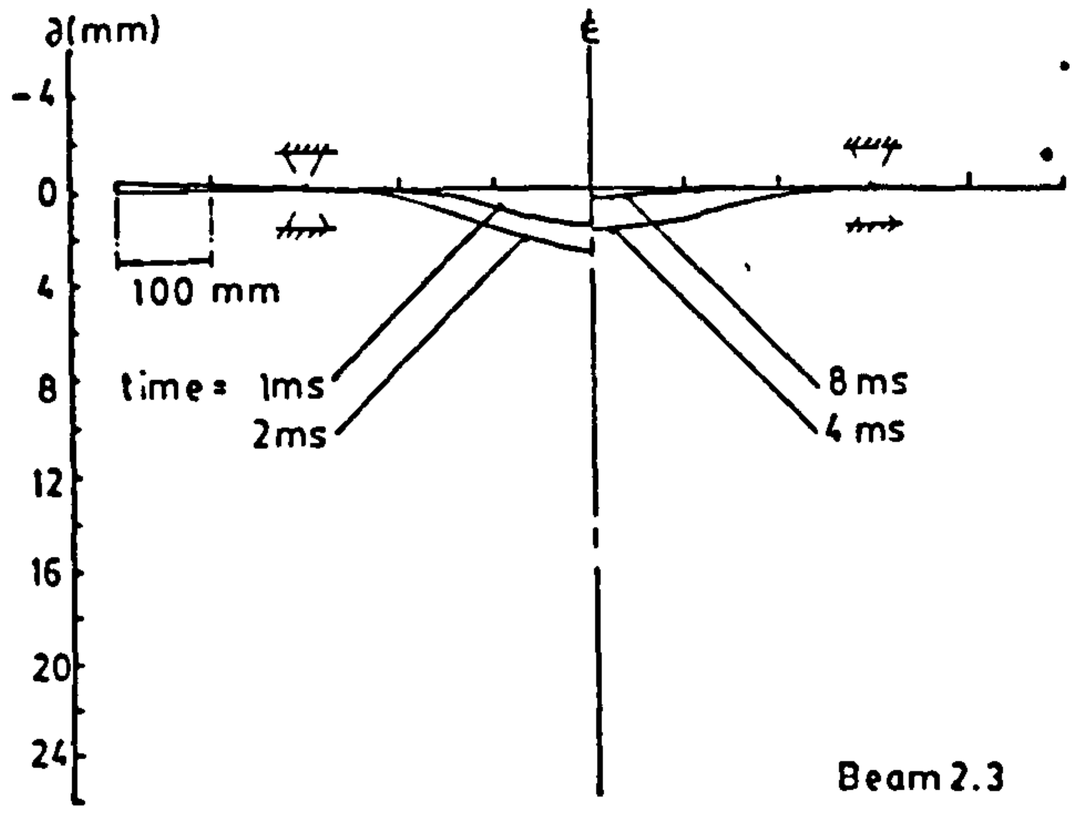

Beam 2.3

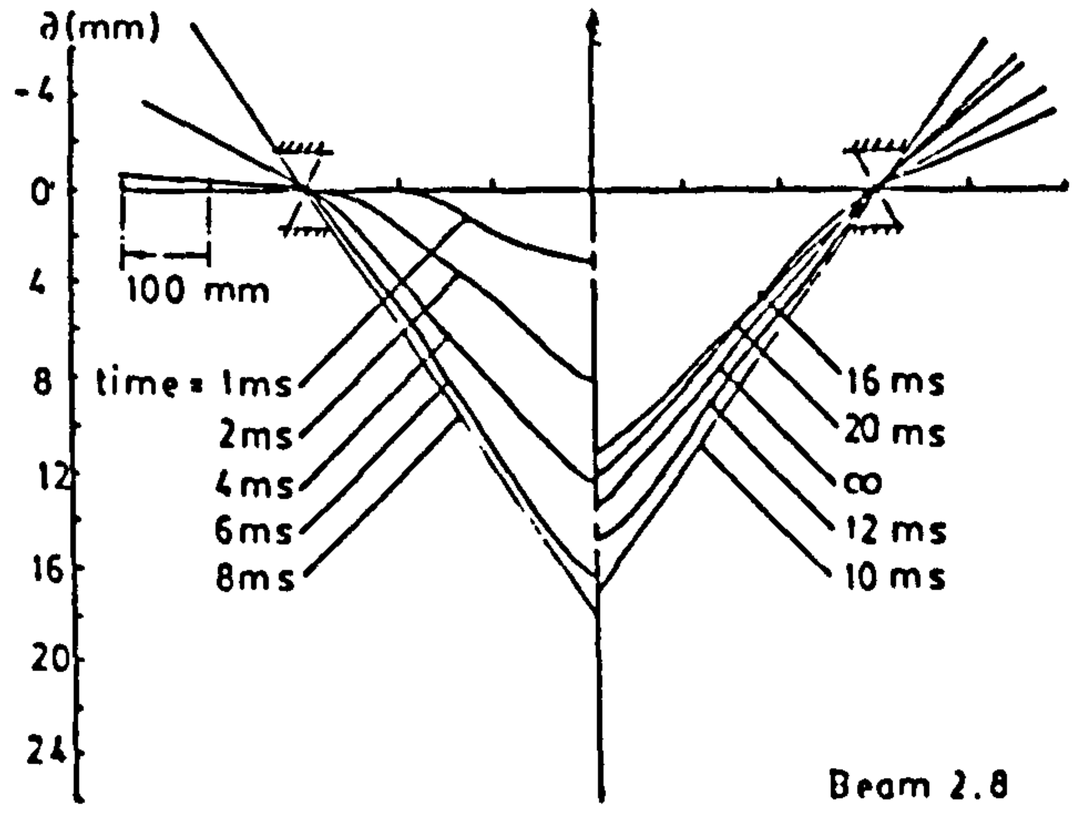

Beam 2.8

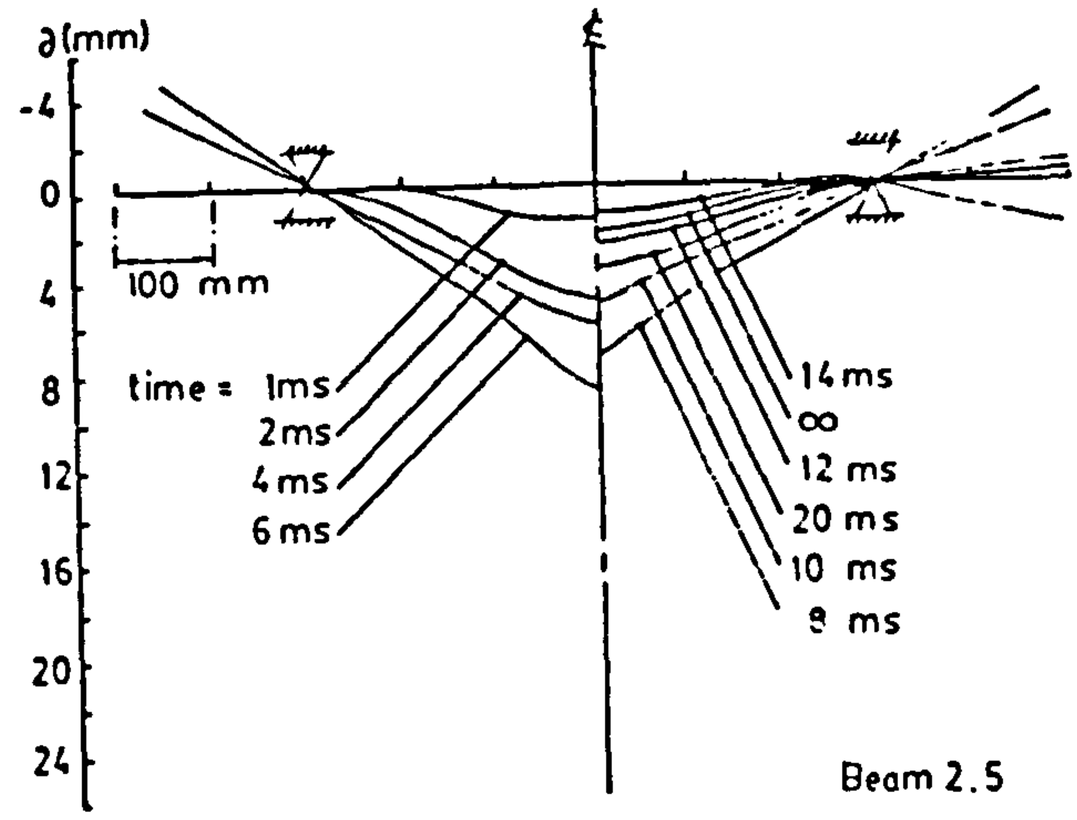

Beam 2.5

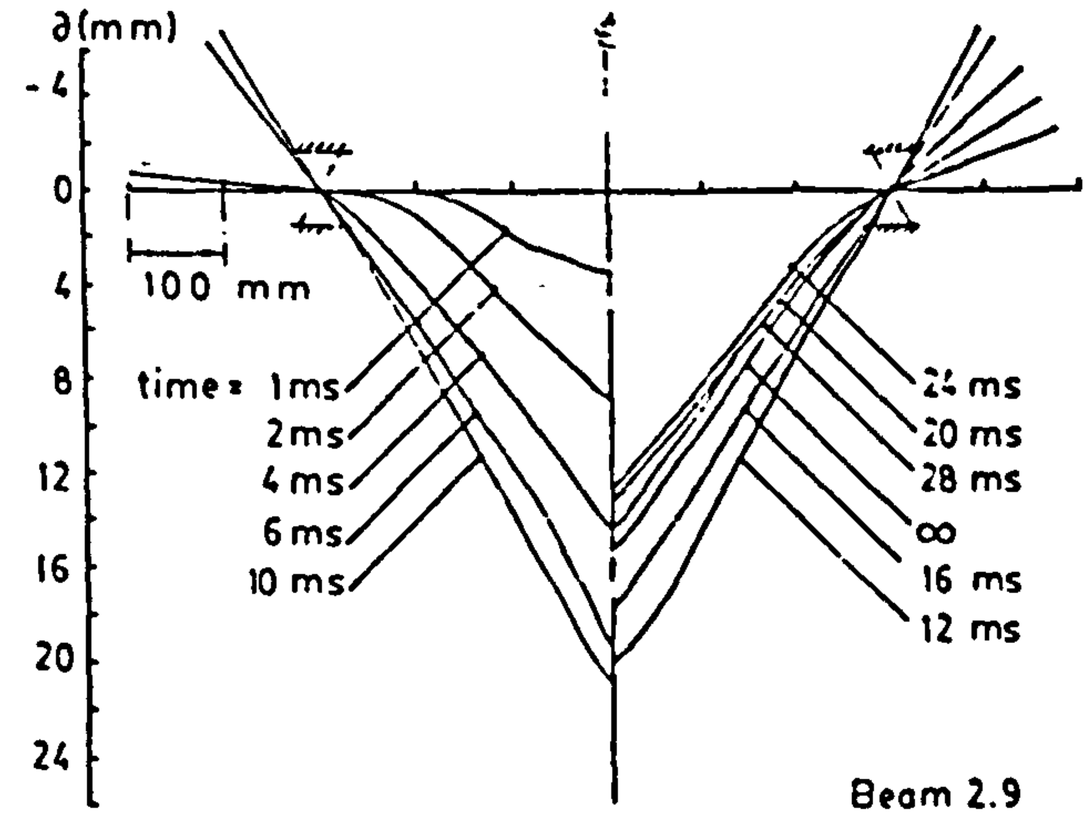

Beam 2.9

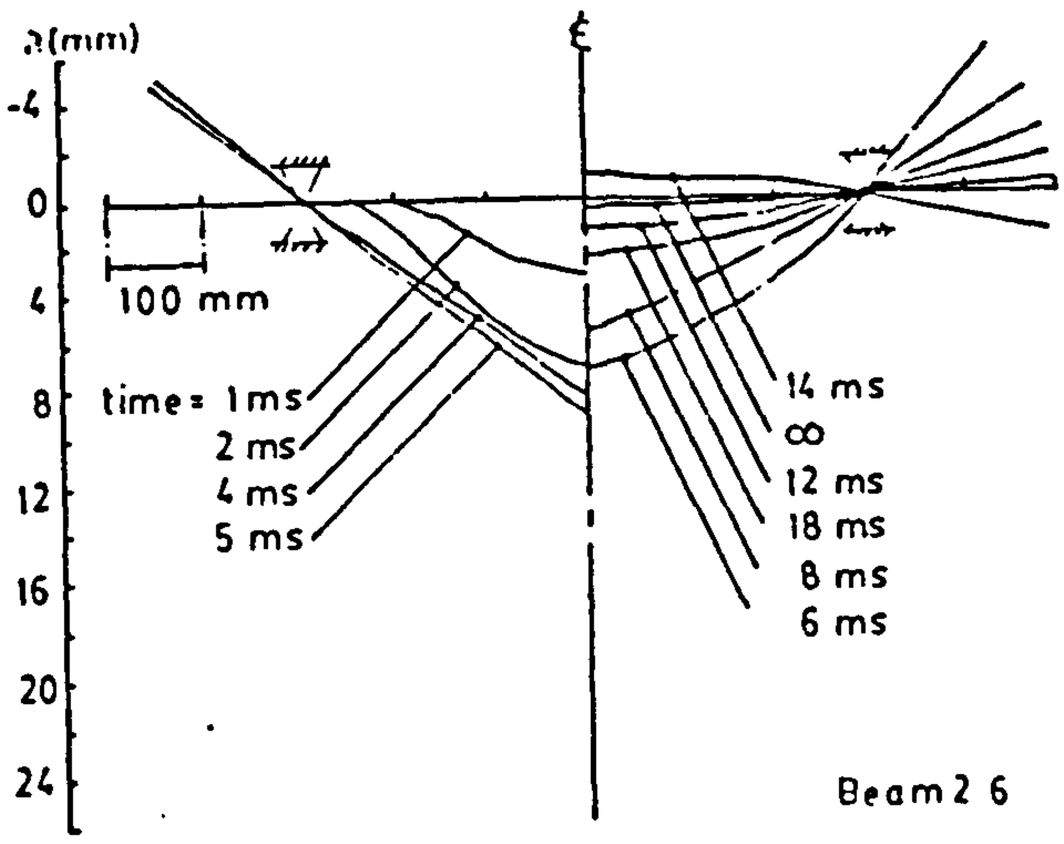

Beam 2 6

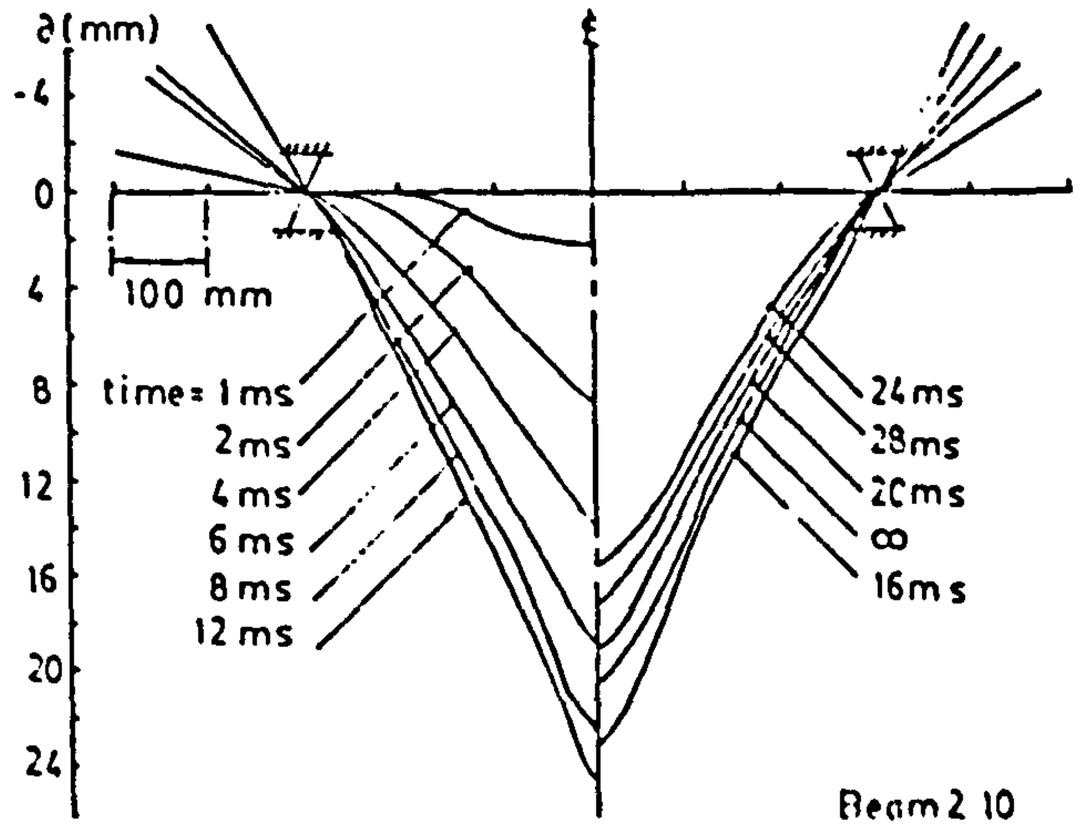

Beam 2 10

Notes : see page D1.

APPENDIX D (b) DEFORMATION PROFILES

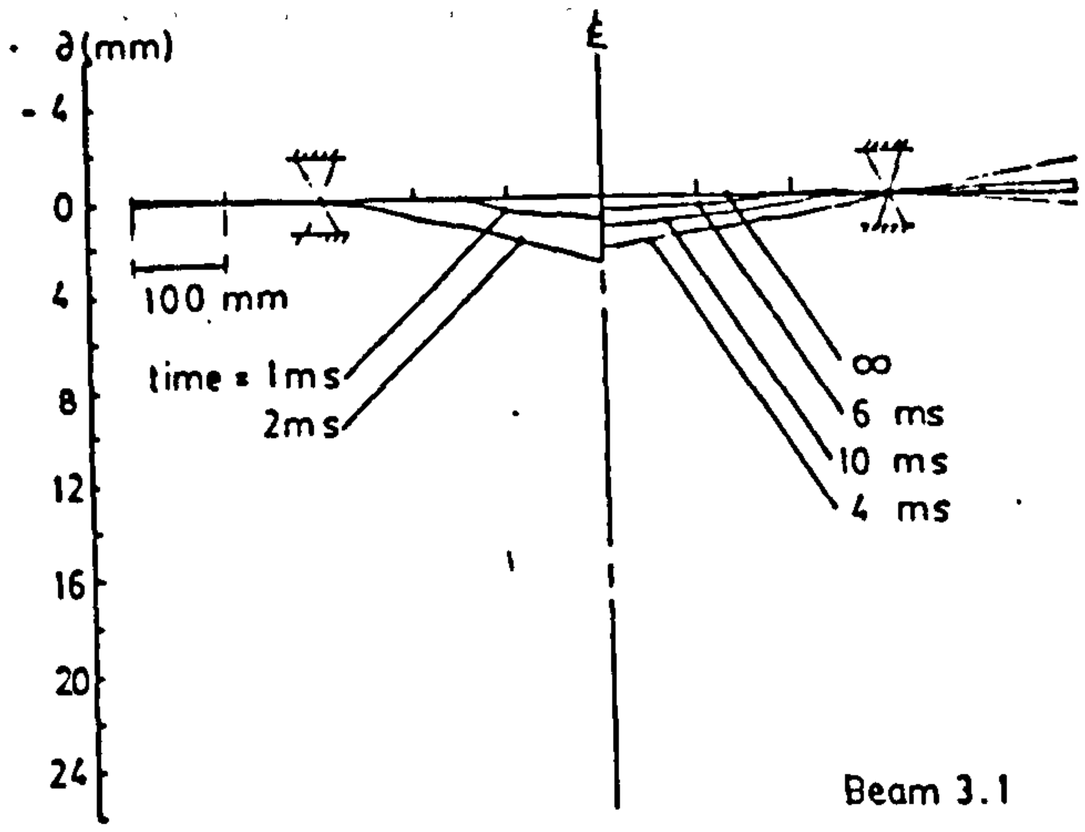

Beam 3.1

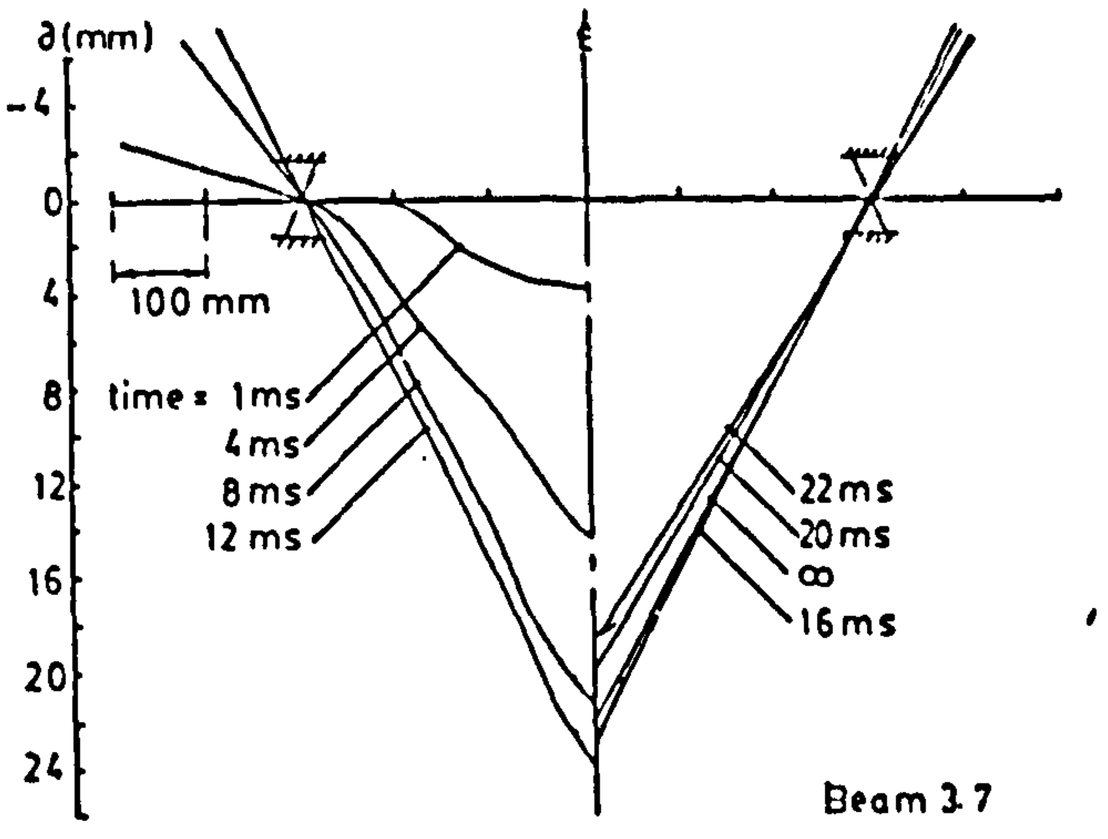

Beam 3.7

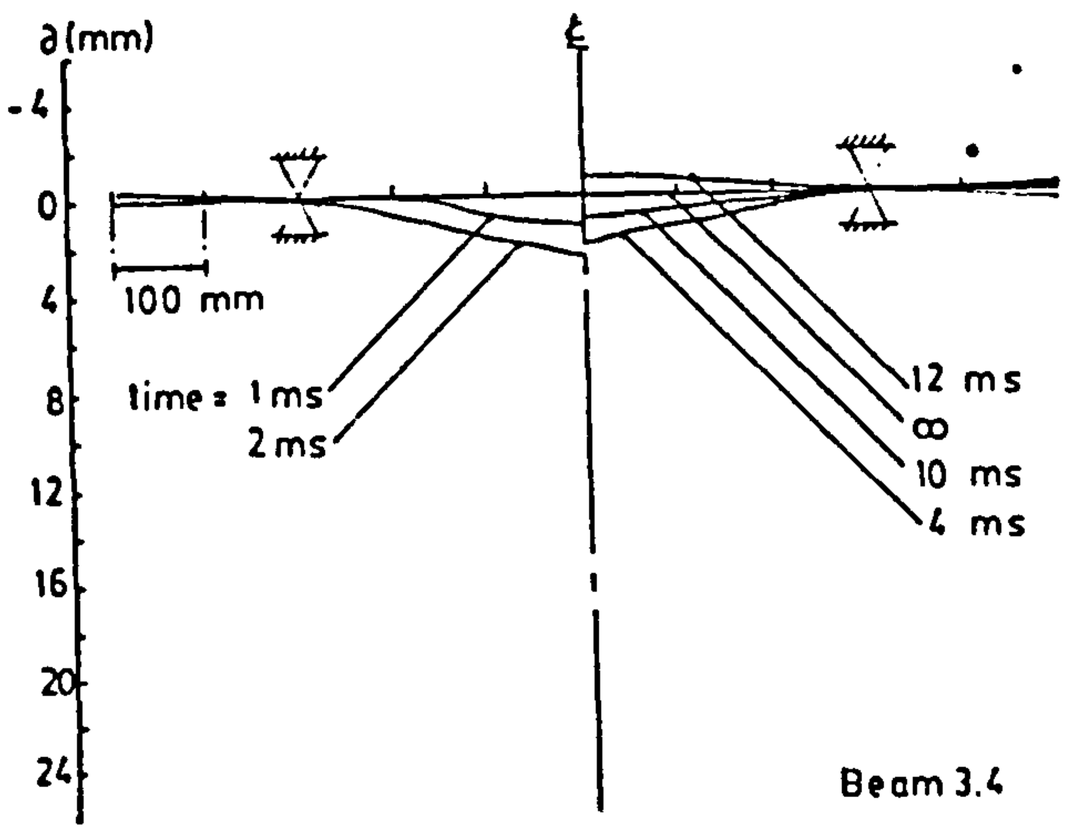

Beam 3.4

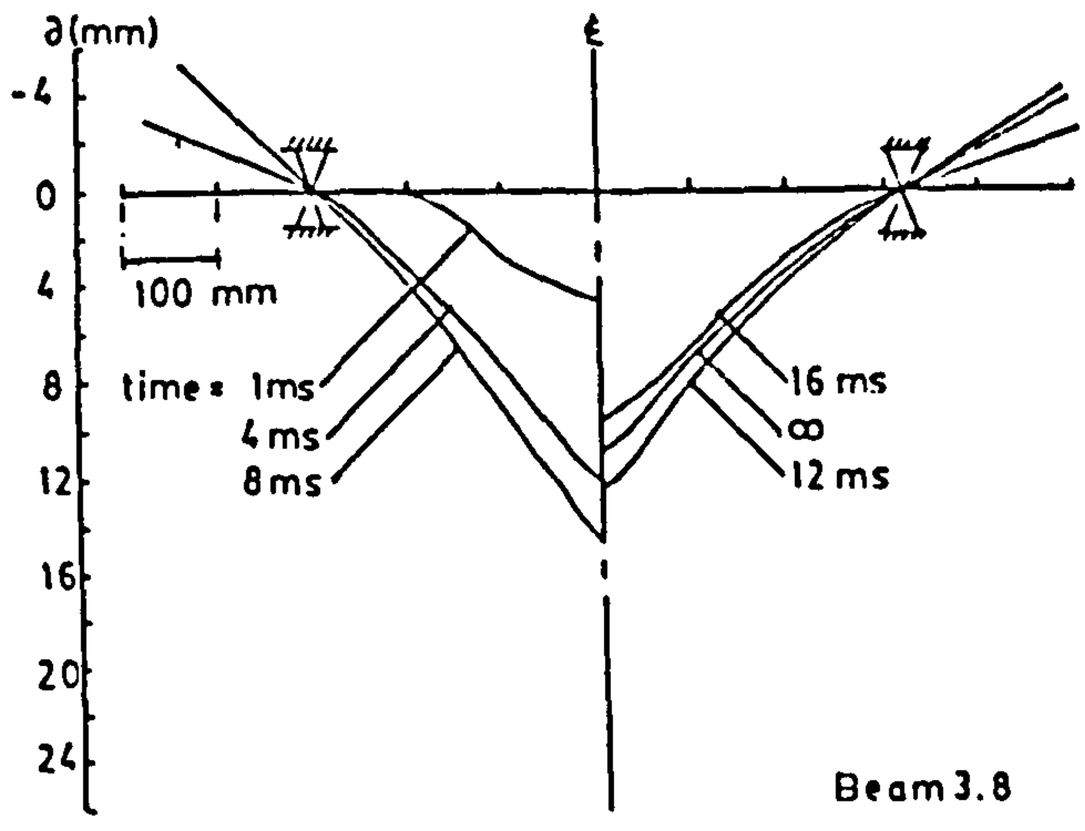

Beam 3.8

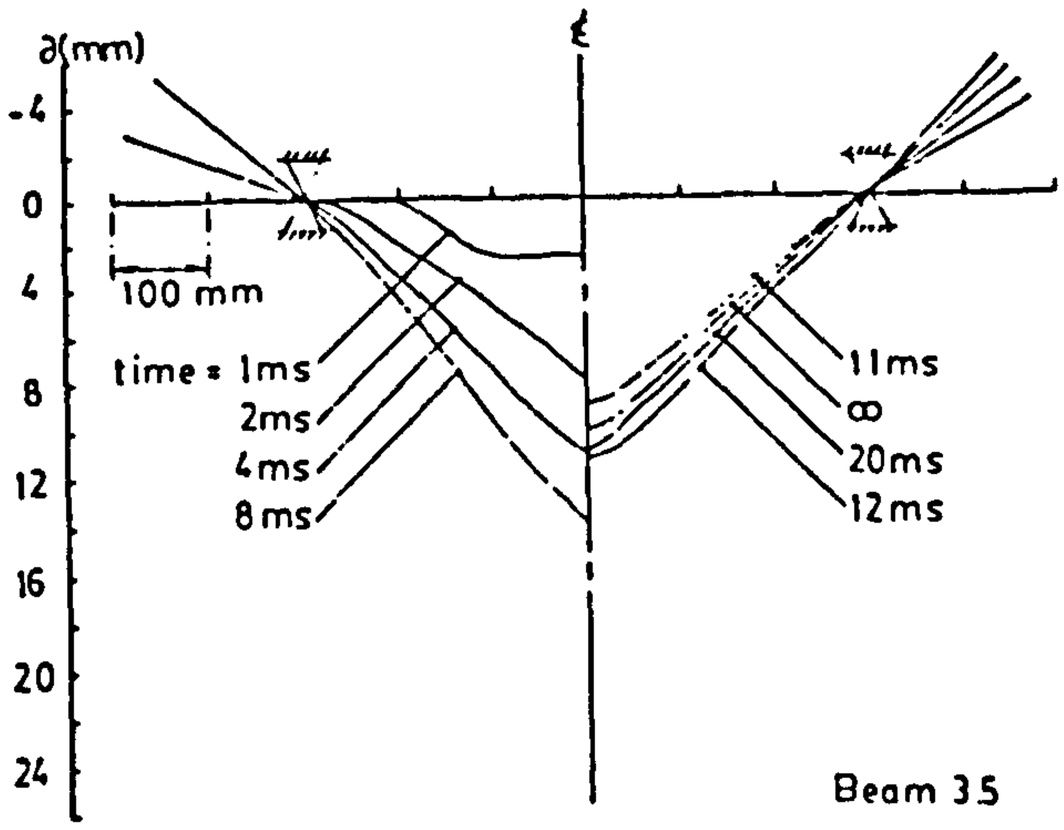

Beam 3.5

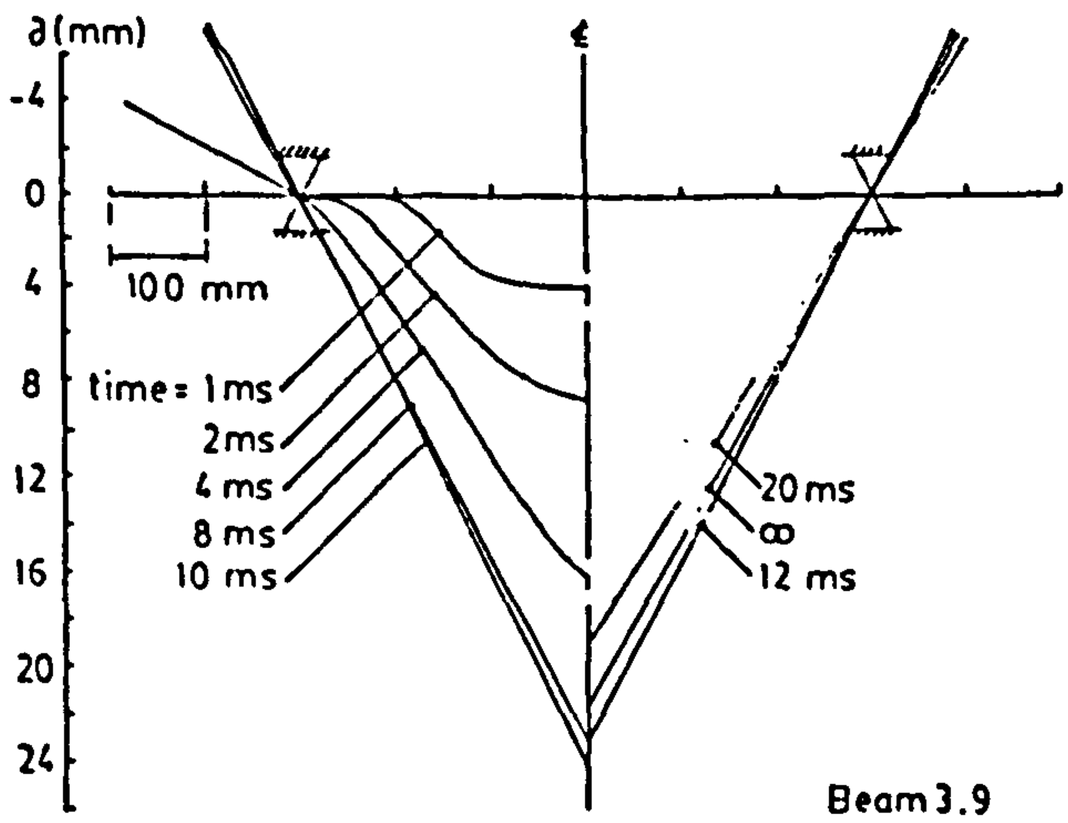

Beam 3.9

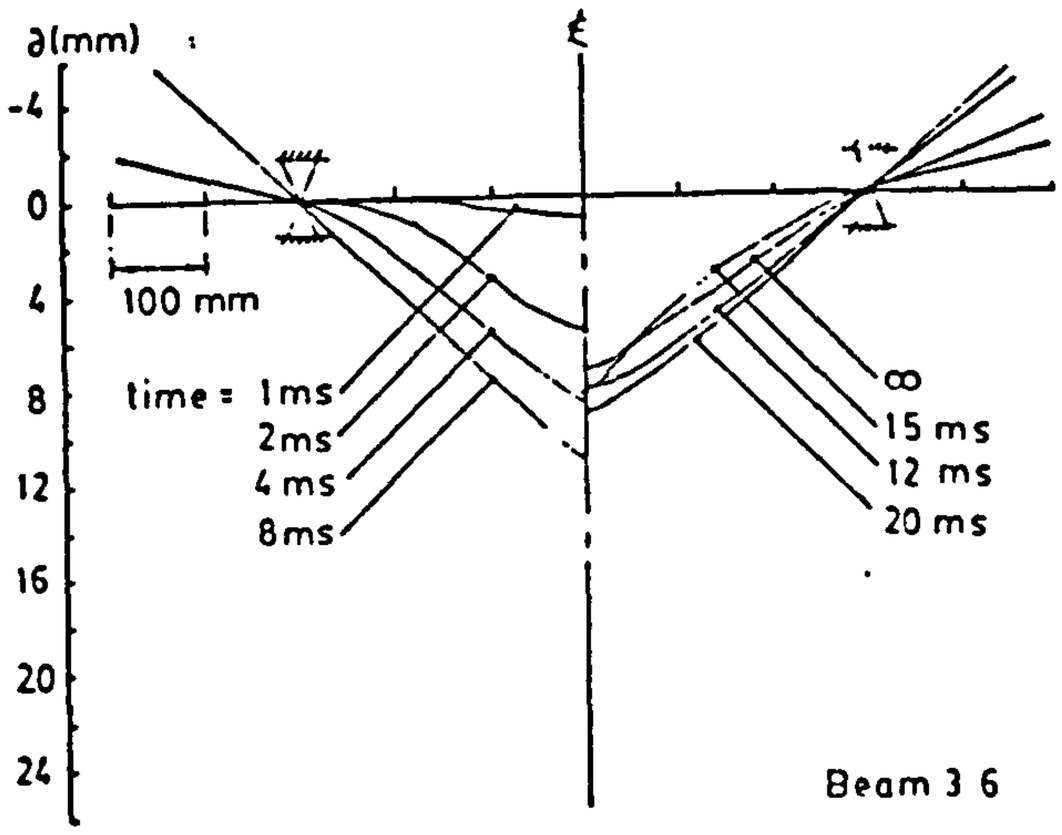

Beam 3 6

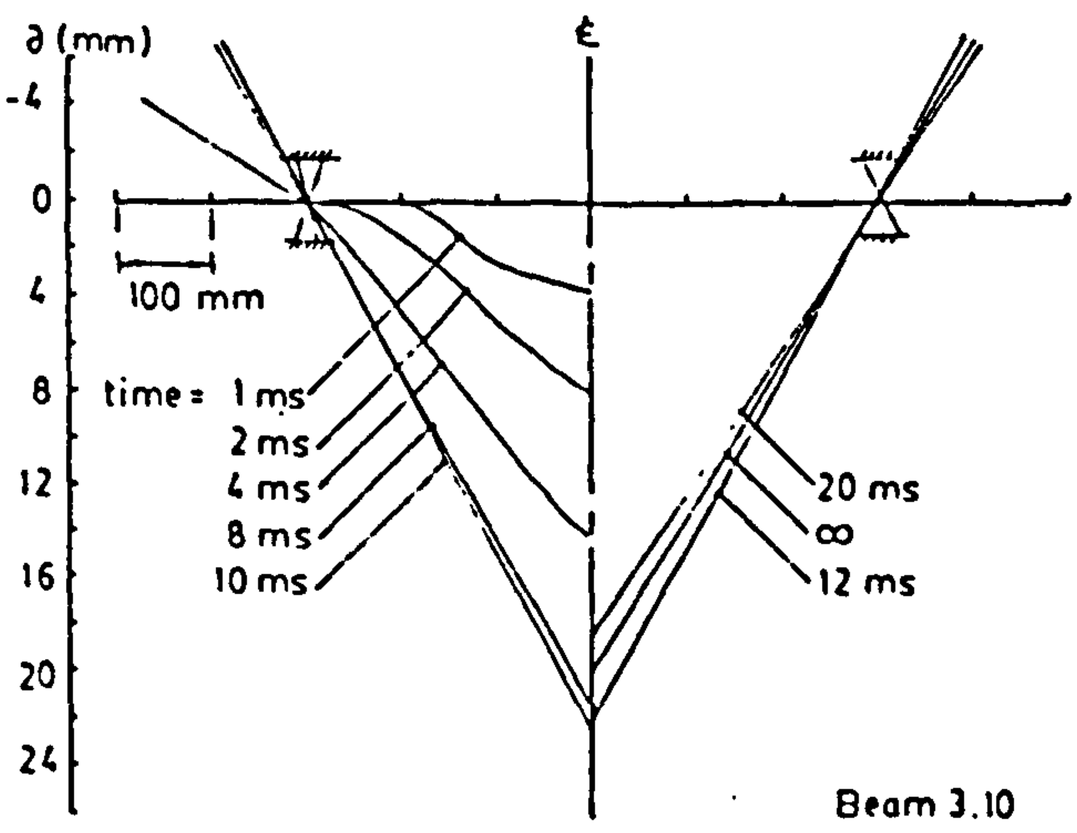

Beam 3.10

Notes : see page D1.

APPENDIX D (b) DEFORMATION PROFILES

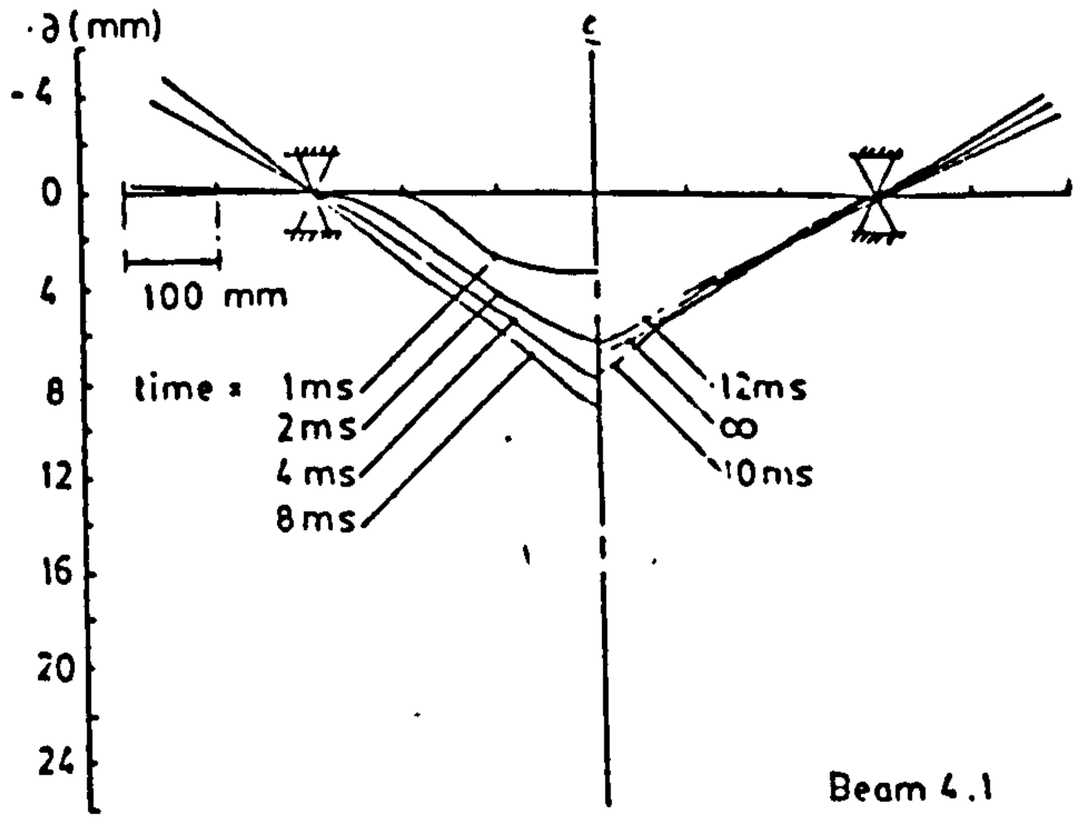

Beam 4.1

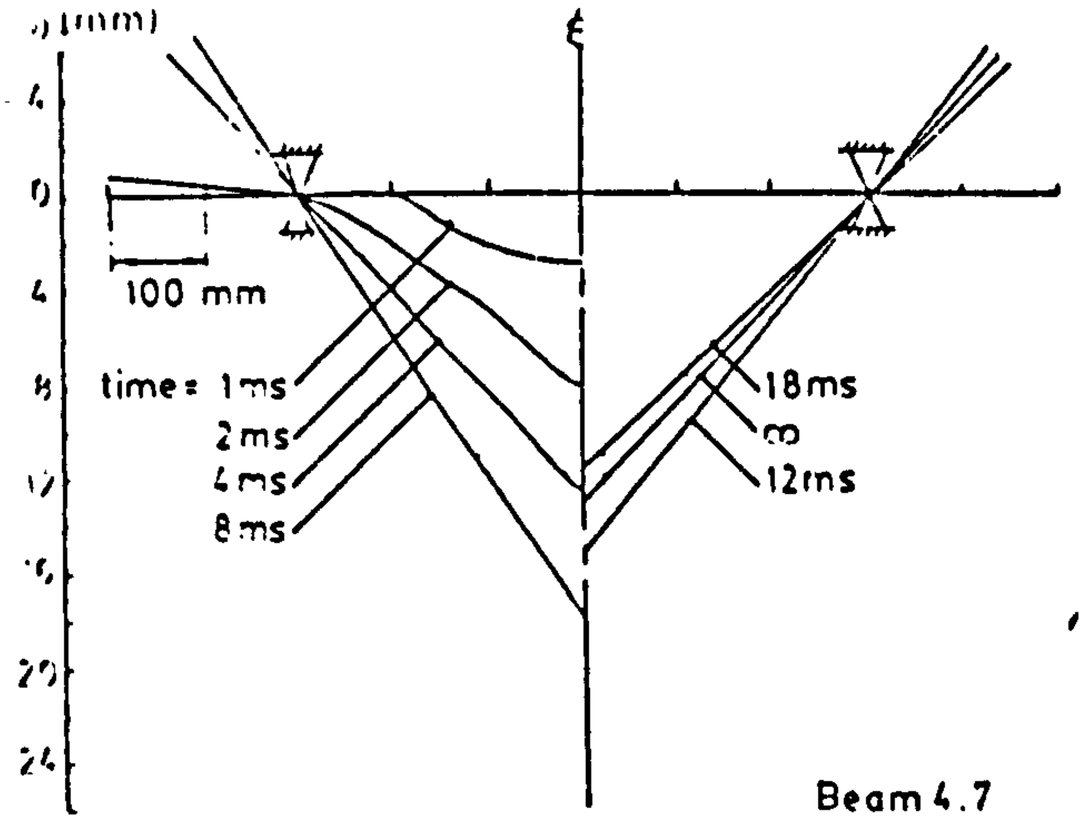

Beam 4.7

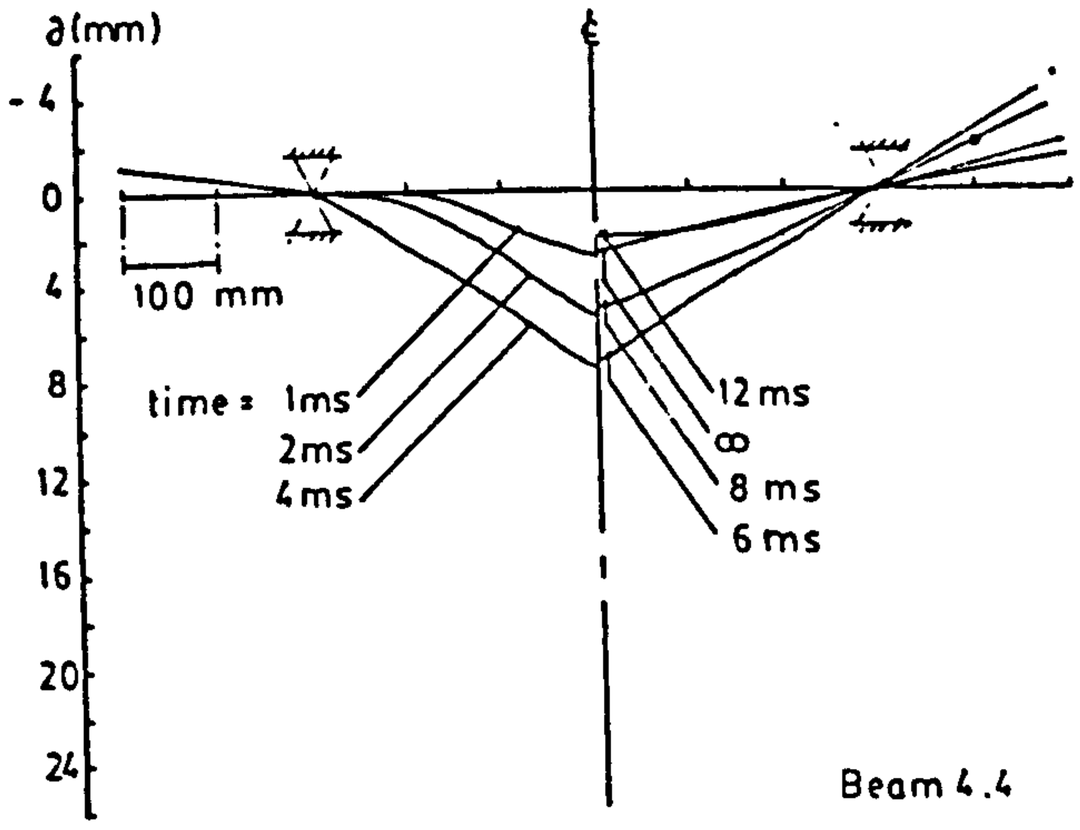

Beam 4.4

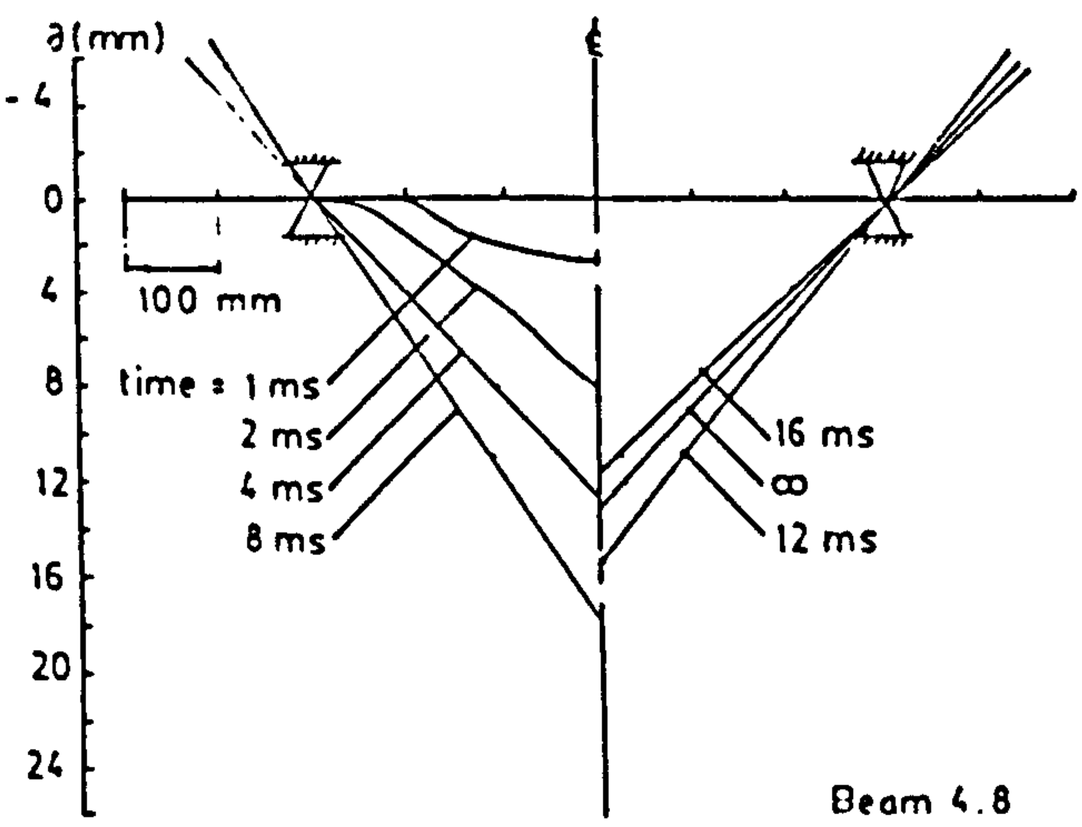

Beam 4.8

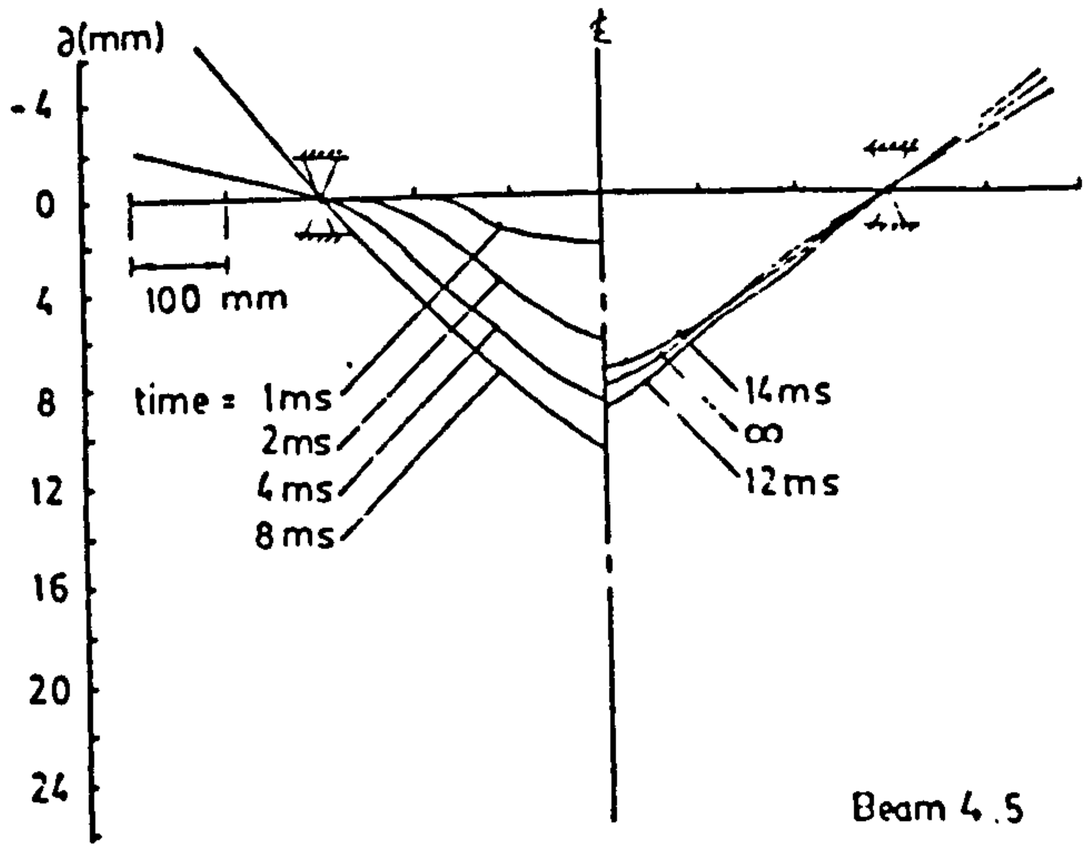

Beam 4.5

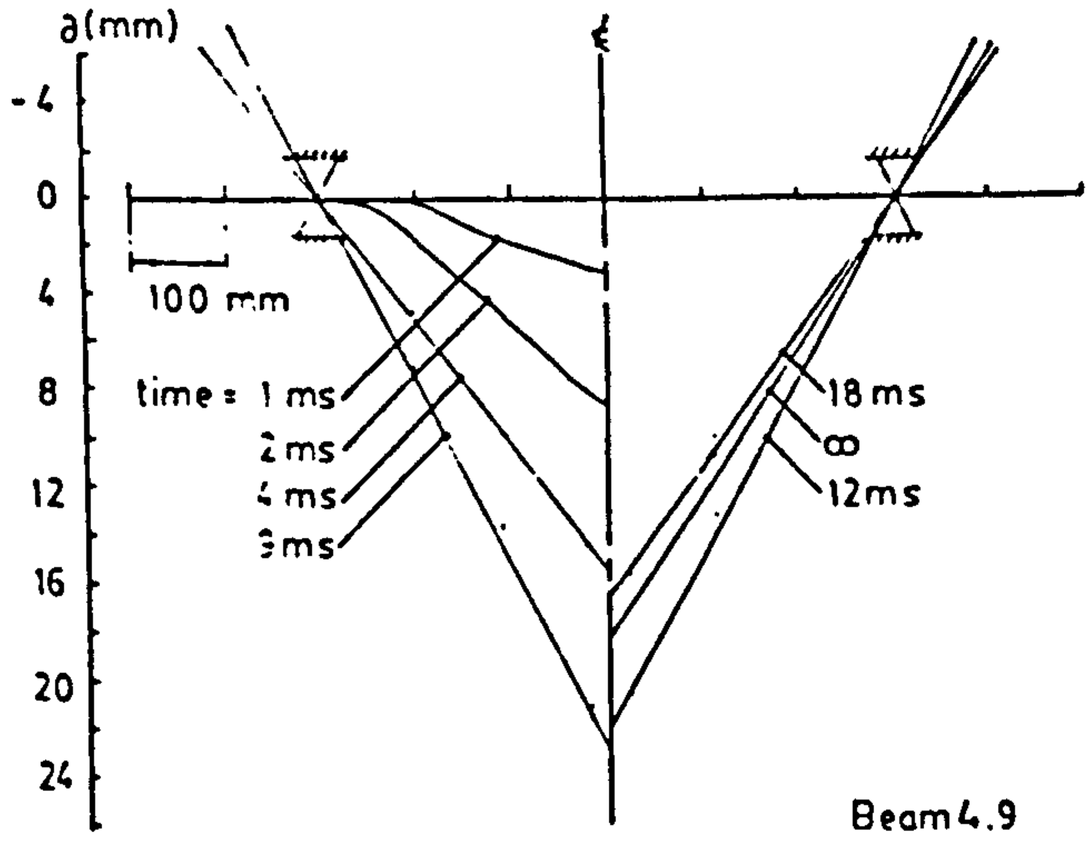

Beam 4.9

Beam 4.6

see page D5

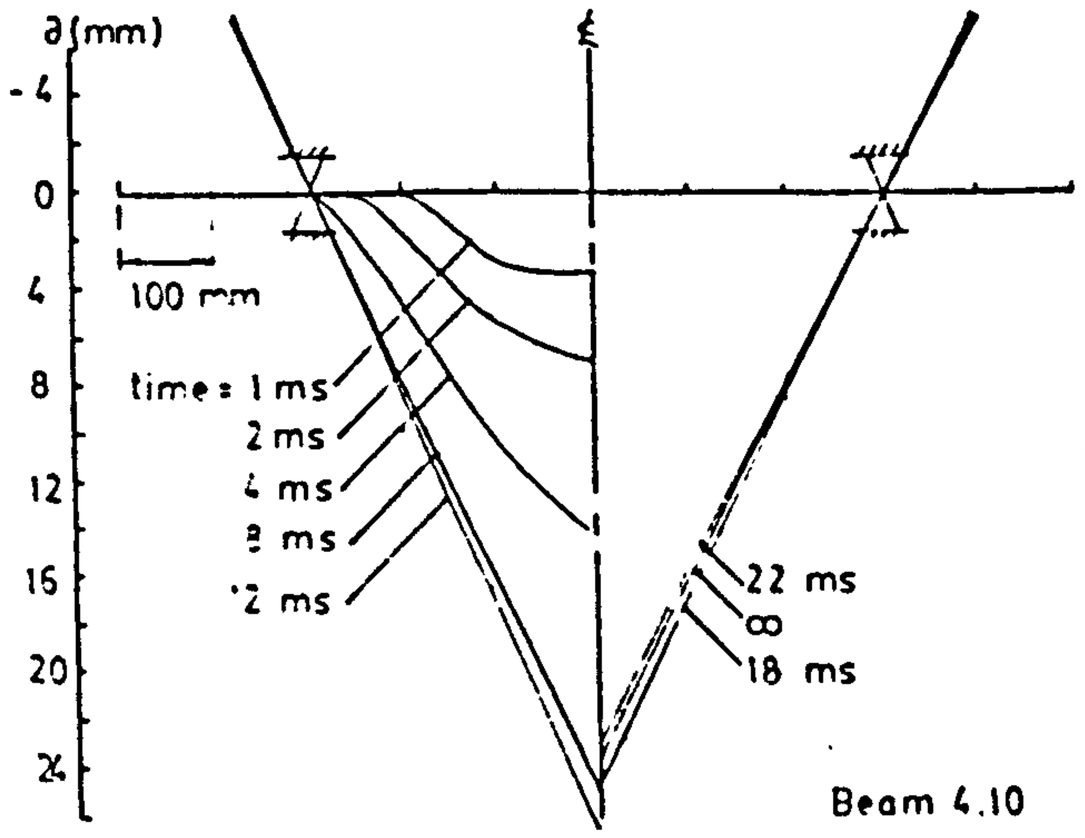

Beam 4.10

Notes : see page D1.

APPENDIX D (b) DEFORMATION PROFILES

APPENDIX E

Reaction Traces

This appendix contains the reaction traces obtained as described in section 3.7.3. Normal reaction is positive and is above the zero reaction line which is the horizontal line bisecting the screen of the oscilloscope.

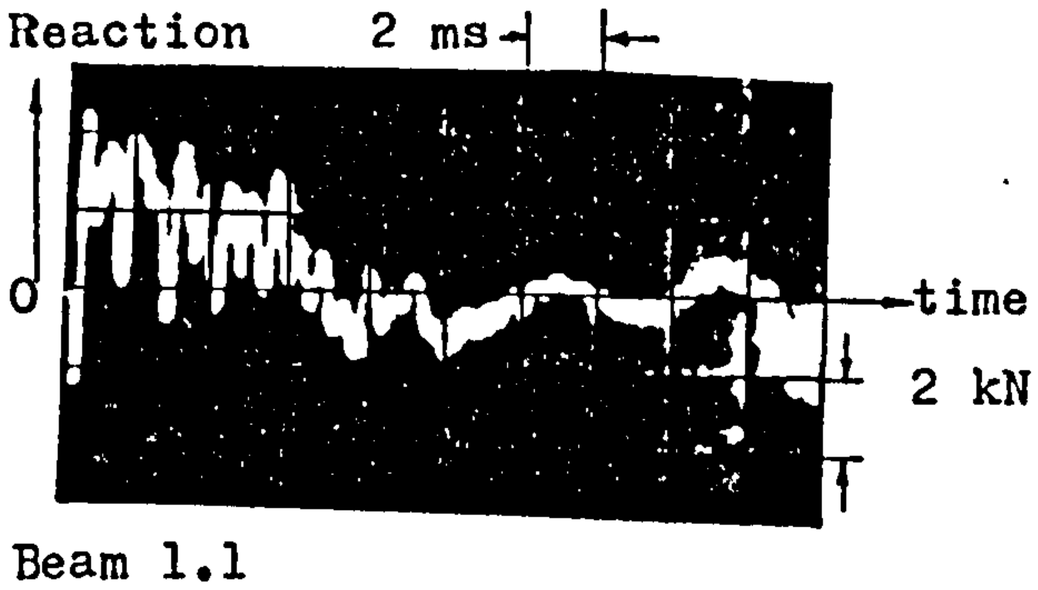

Beam 1.1

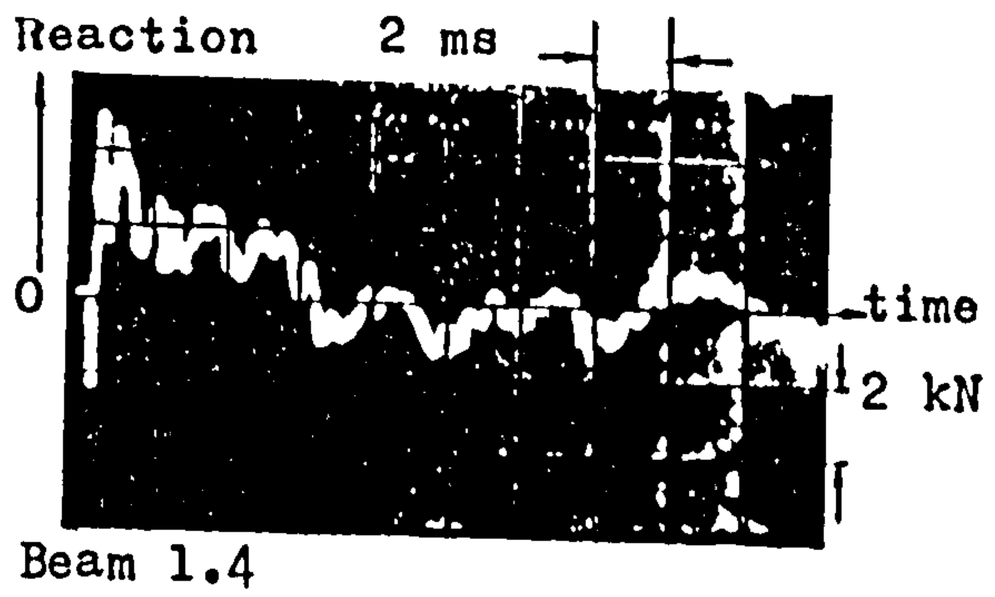

Beam 1.4

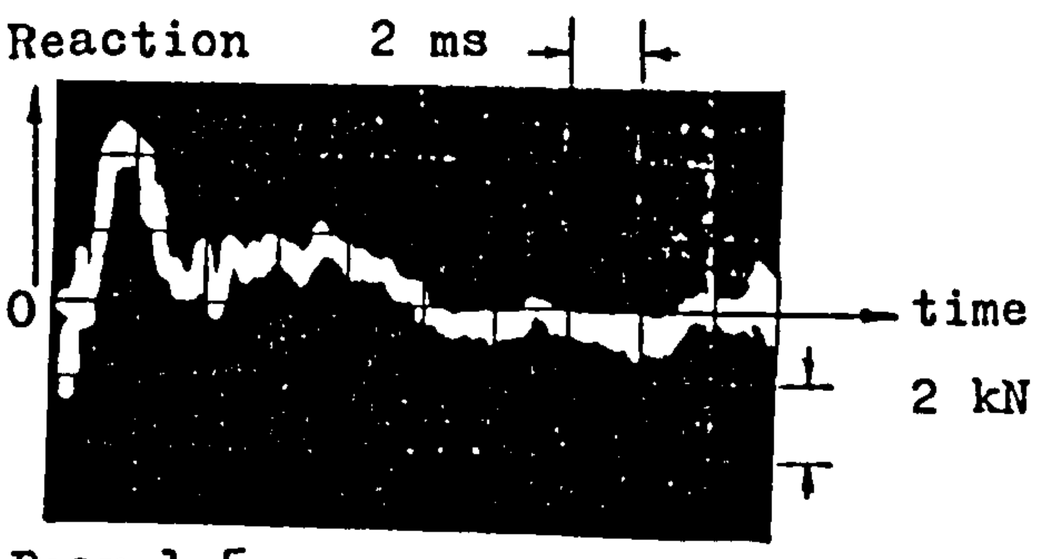

Beam 1.5

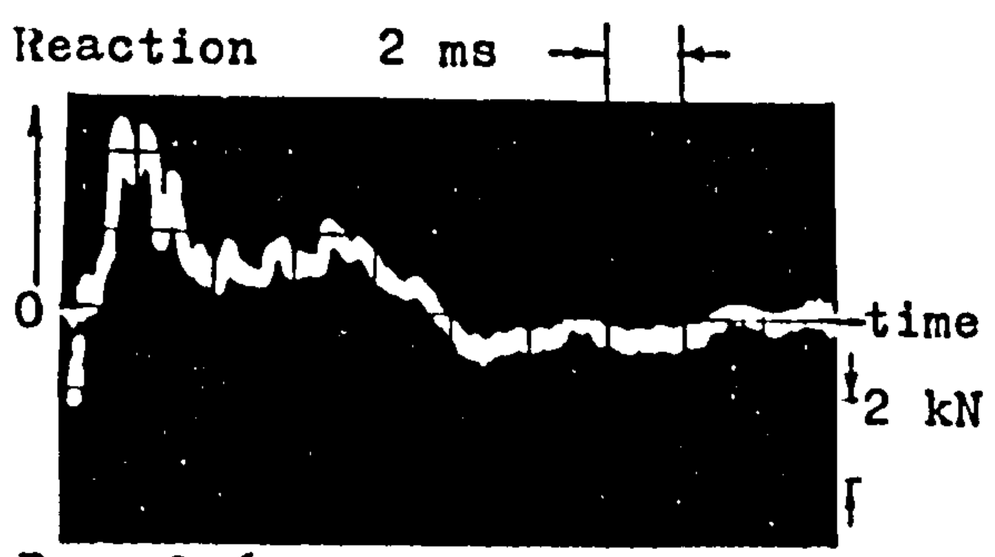

Beam 1.6

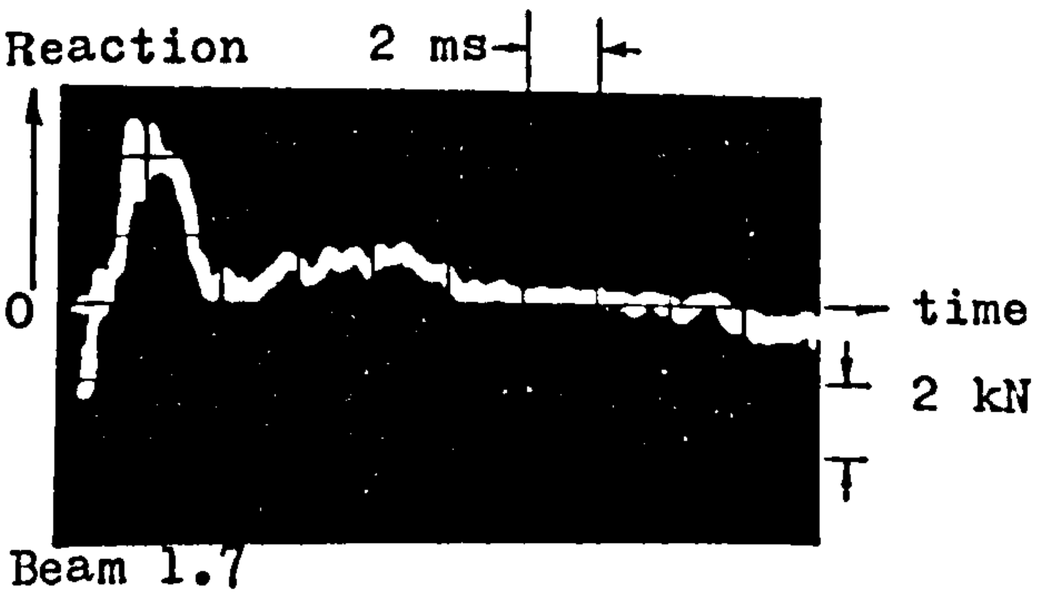

Beam 1.7

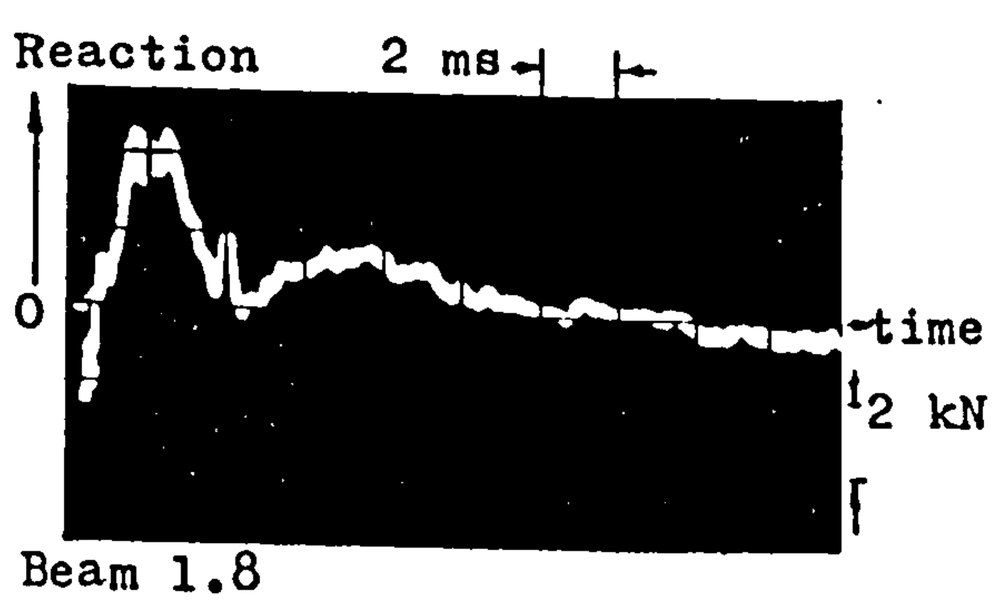

Beam 1.8

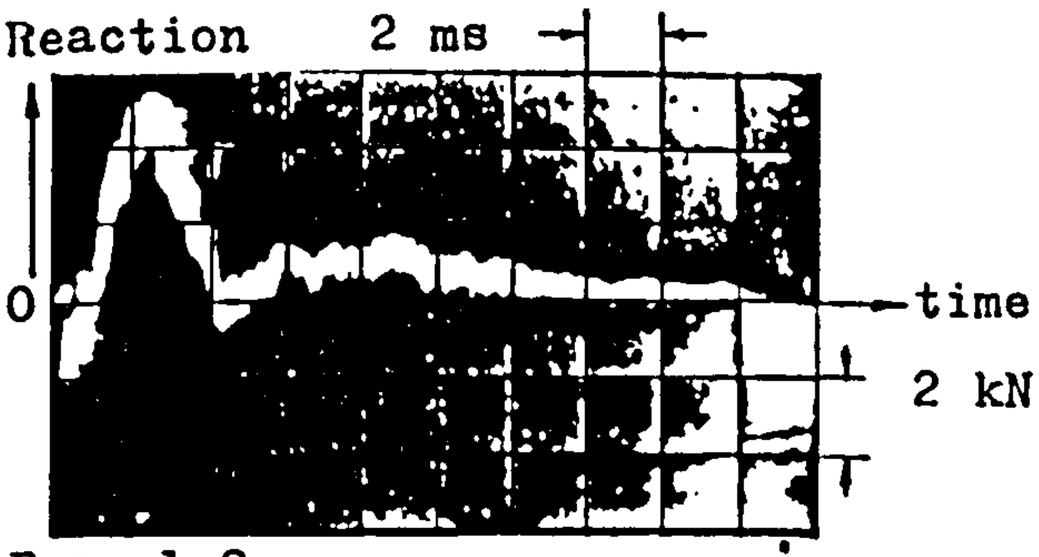

Beam 1.9

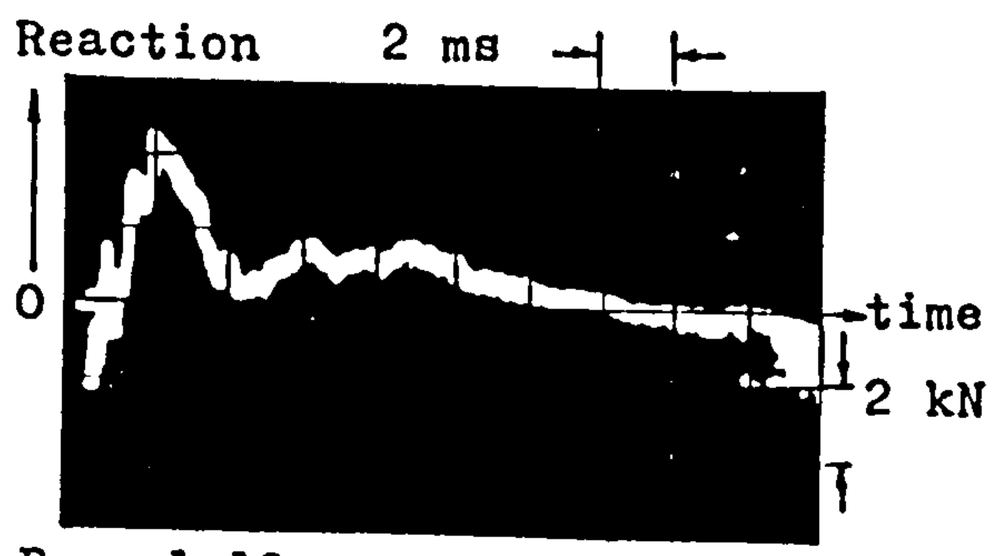

Beam 1.10

Note : Time = 0 at trigger (section 4.3.4).

APPENDIX E REACTION TRACE

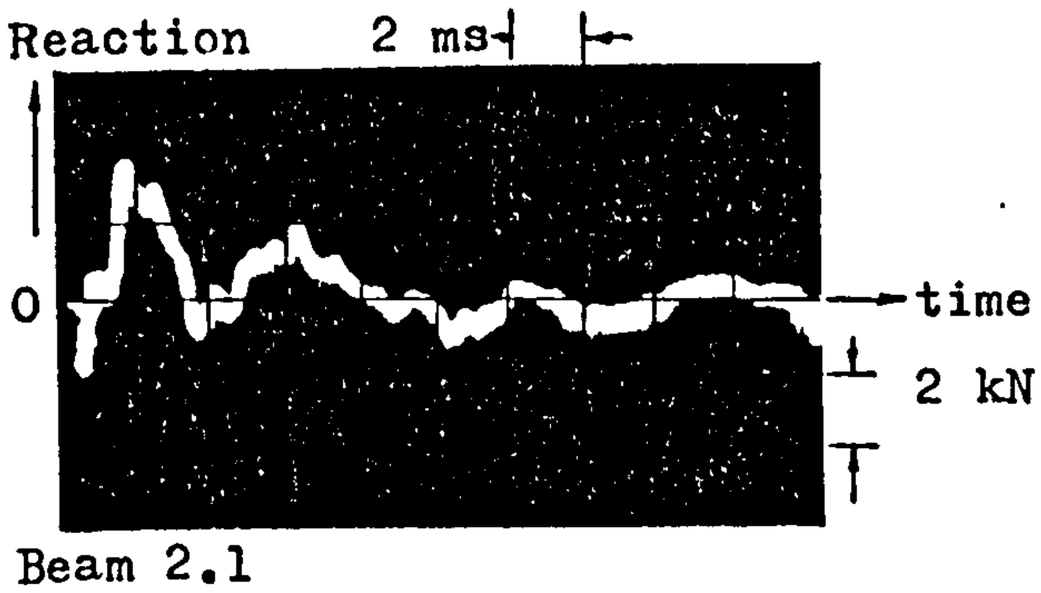

Beam 2.1

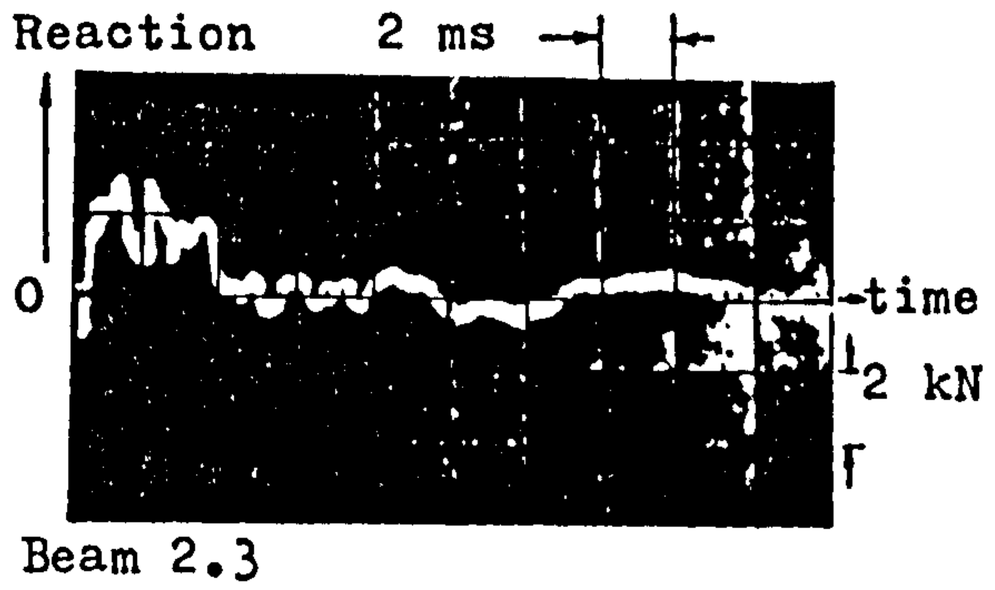

Beam 2.3

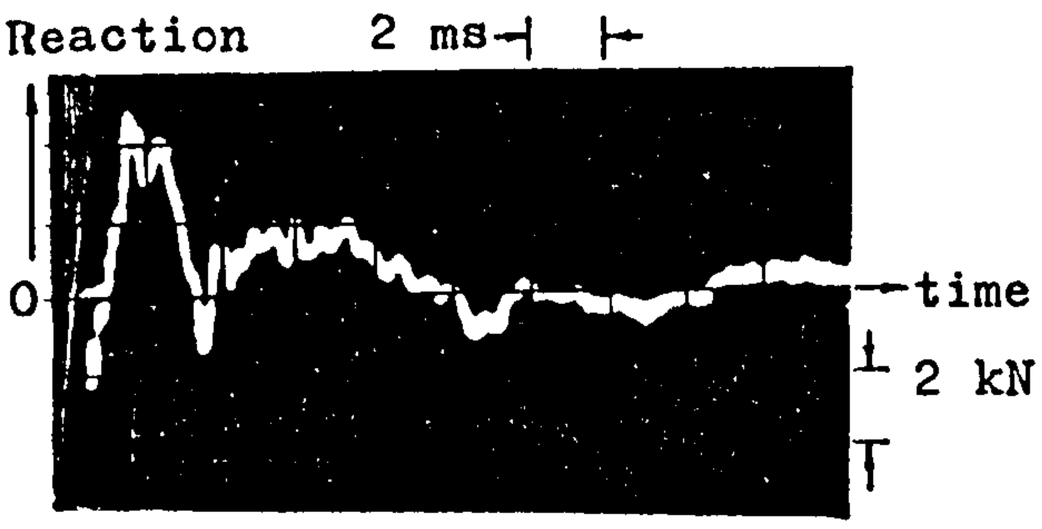

Beam 2.5

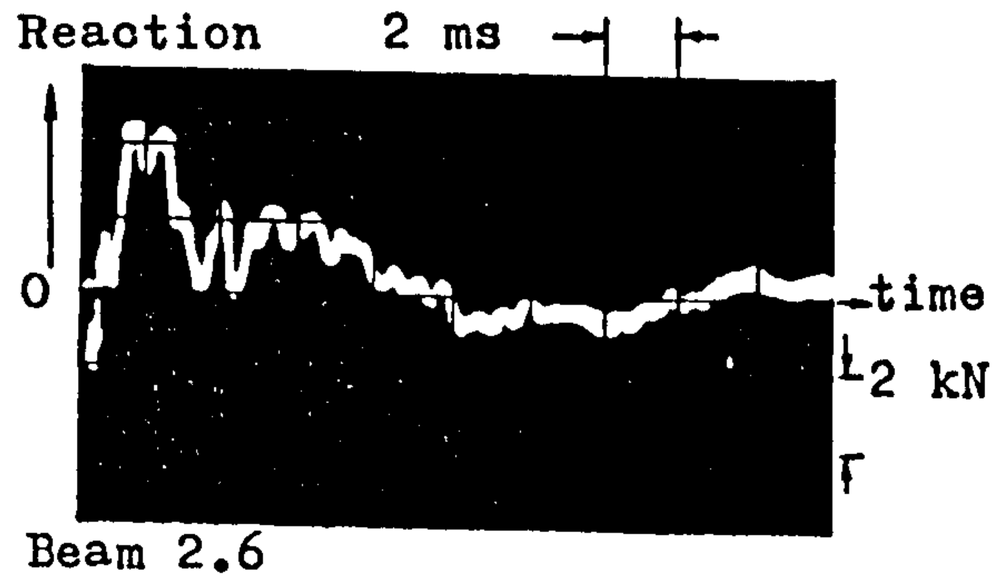

Beam 2.6

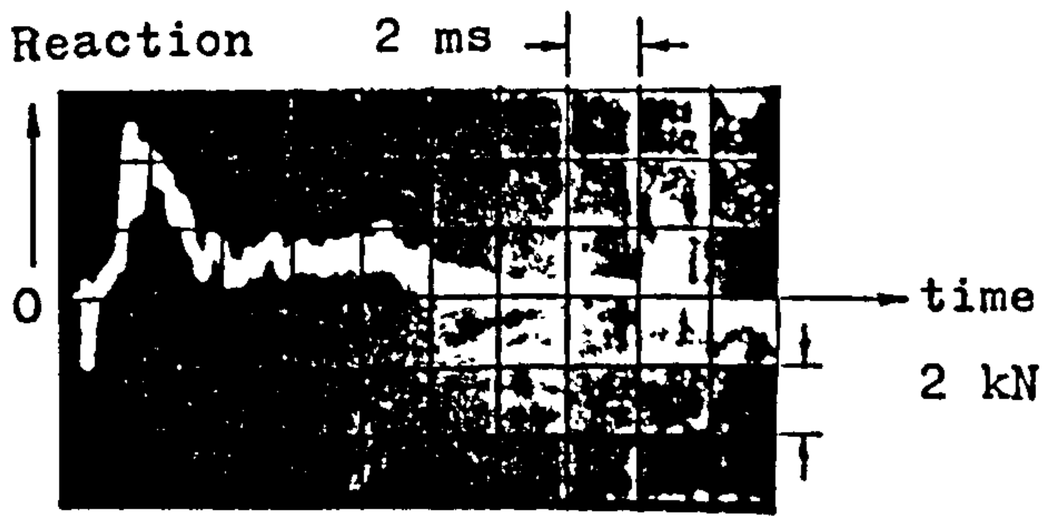

Beam 2.7

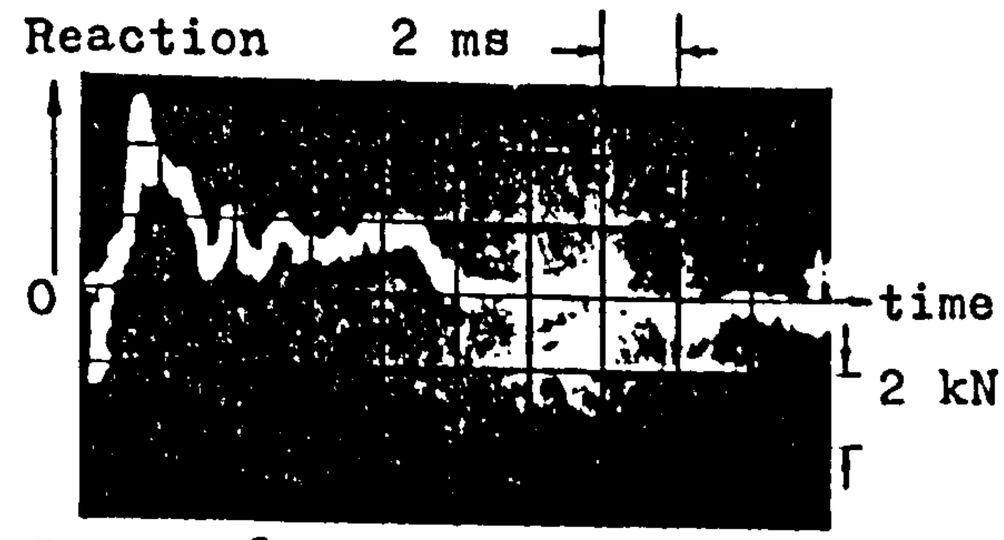

Beam 2.8

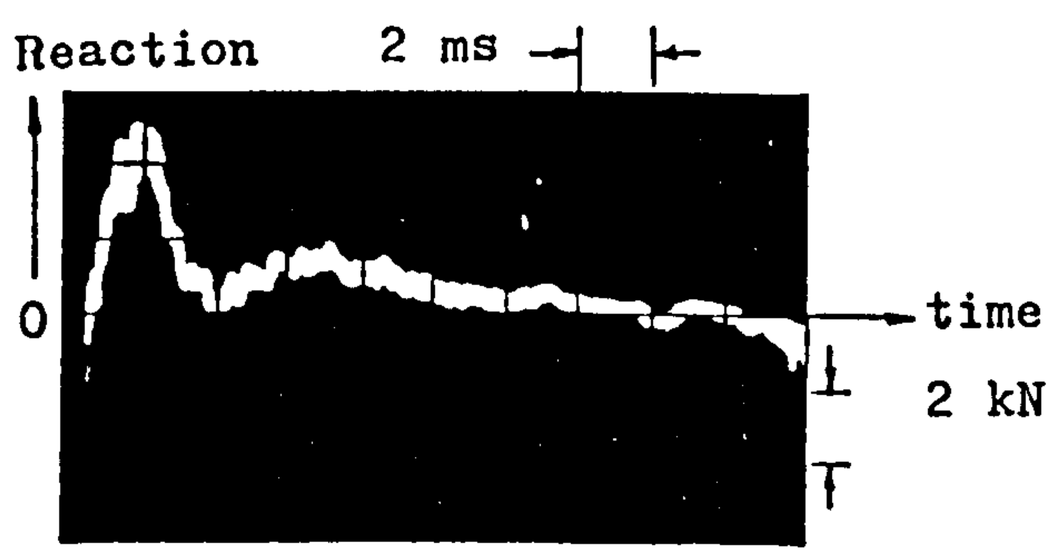

Beam 2.9

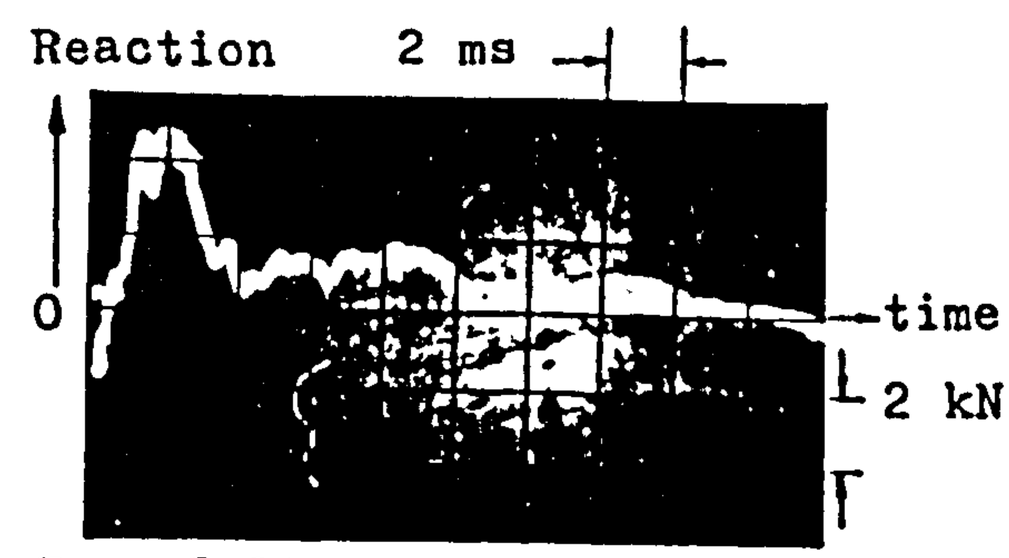

Beam 2.10

Note : Time = 0 at trigger (section 4.3.4).

APPENDIX E REACTION TRACE

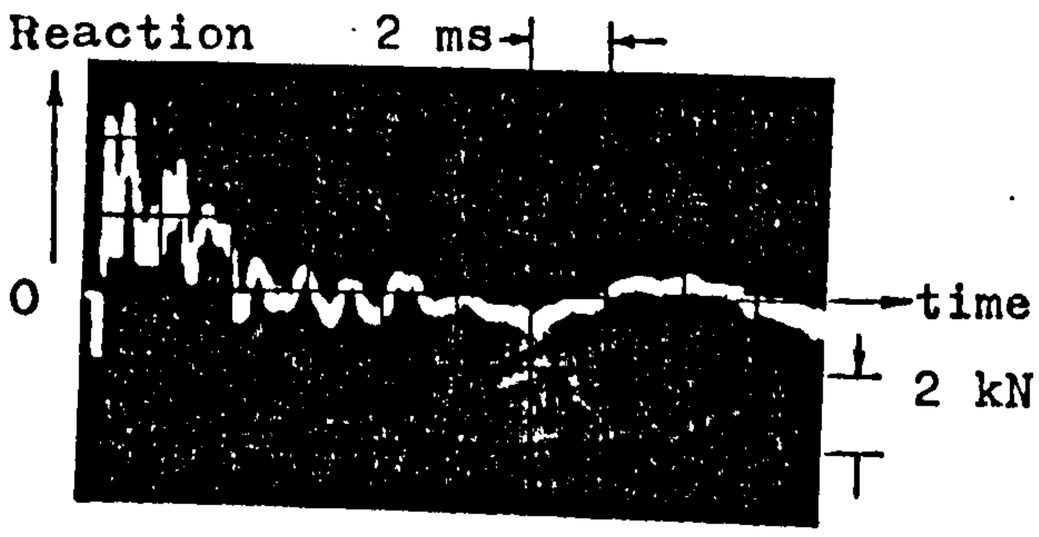

Beam 3.1

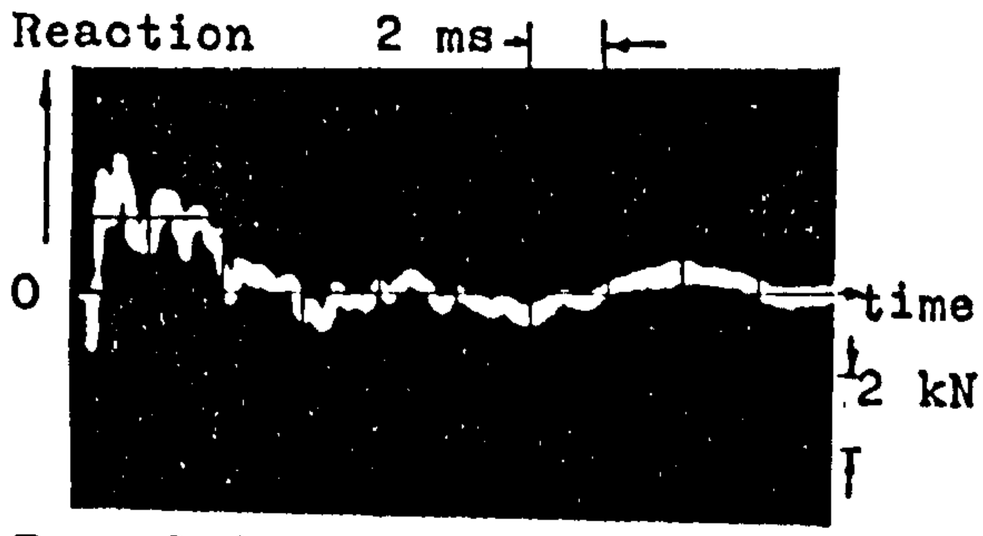

Beam 3.4

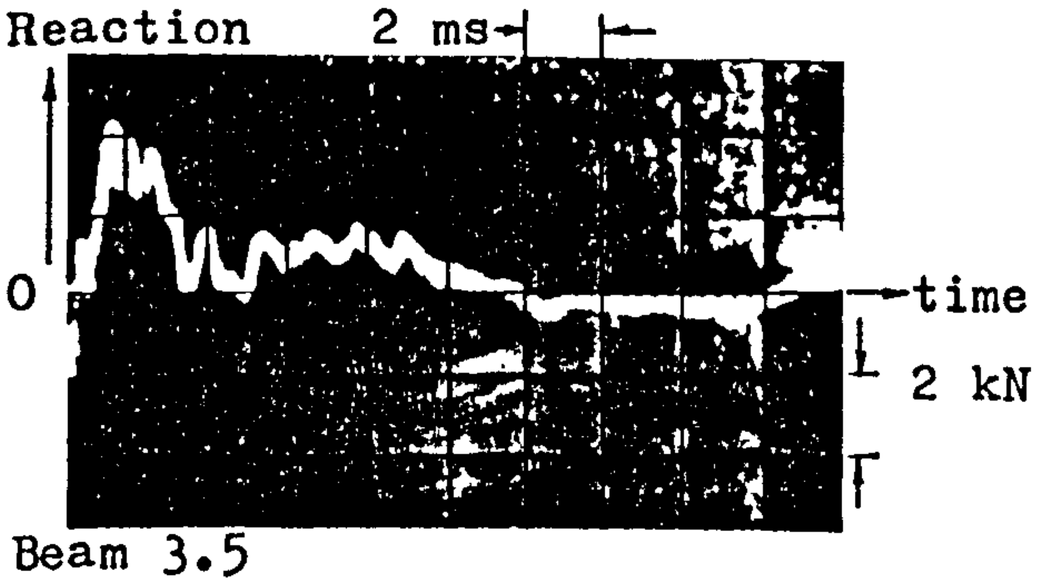

Beam 3.5

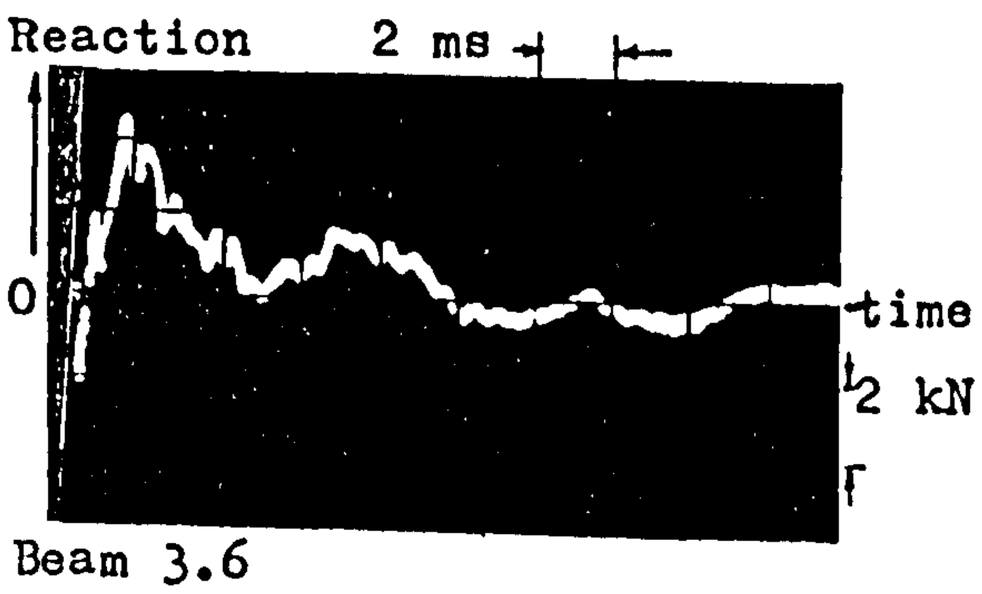

Beam 3.6

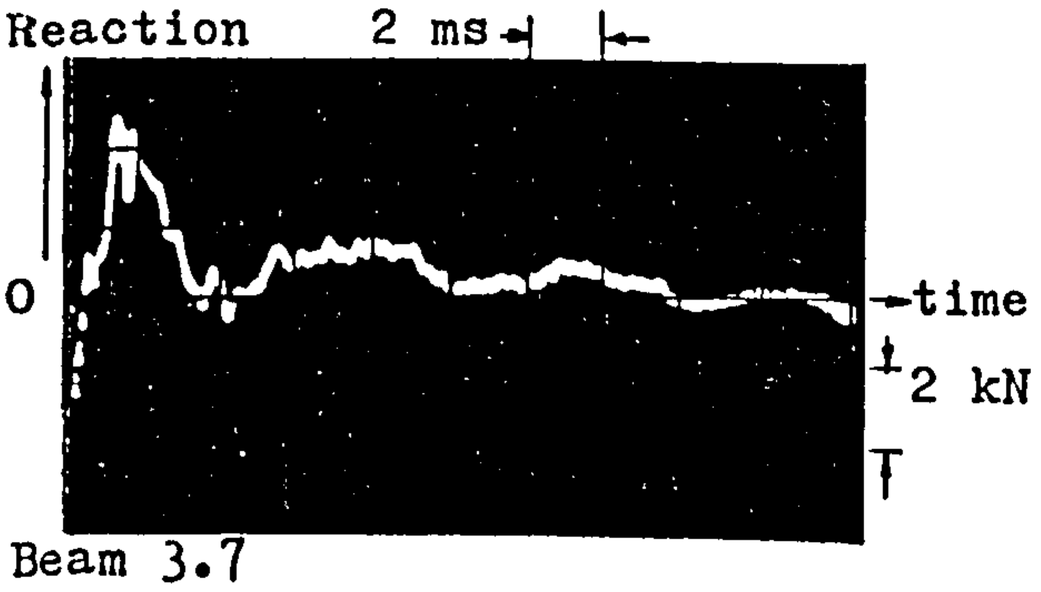

Beam 3.7

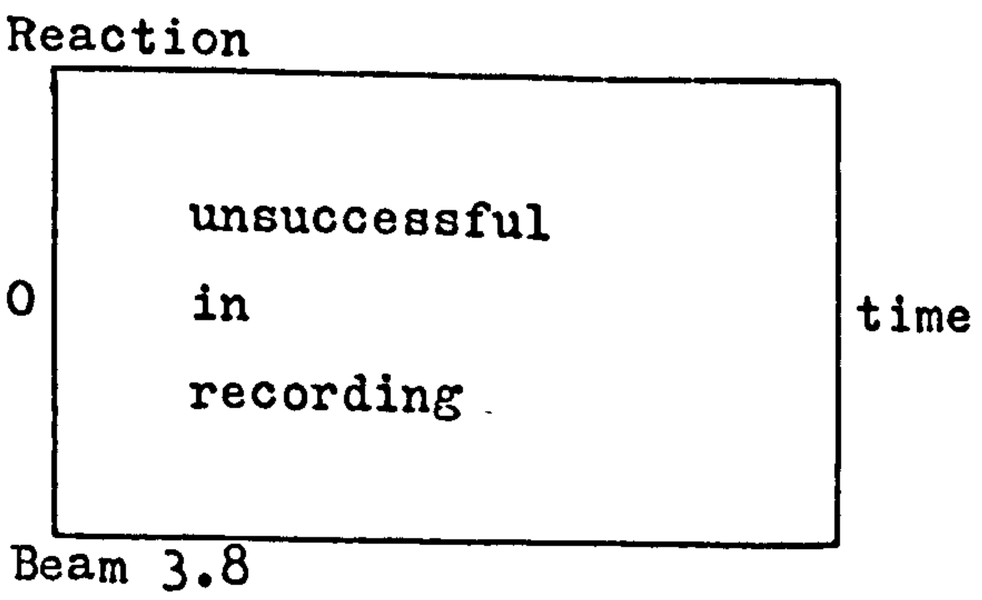

Beam 3.8

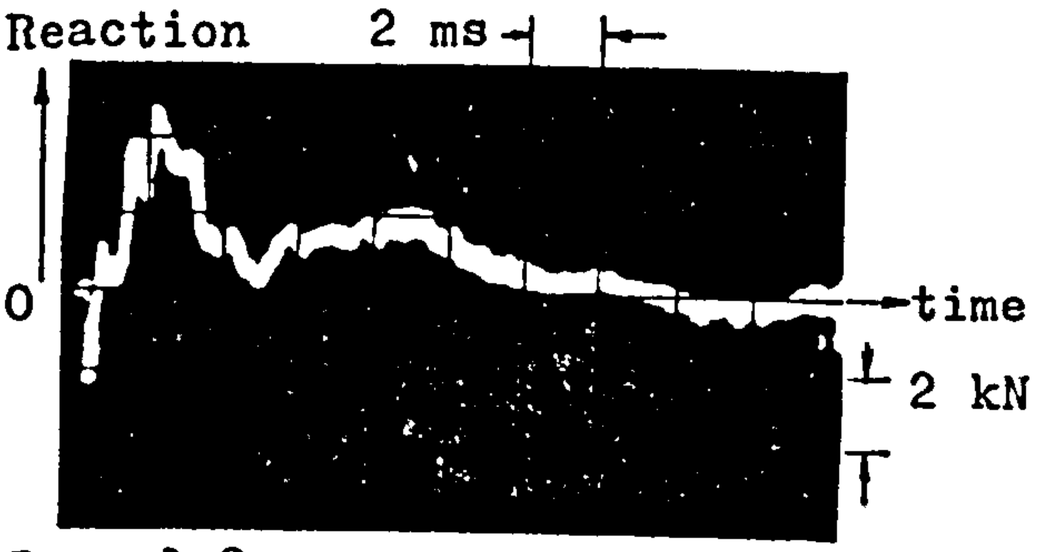

Beam 3.9

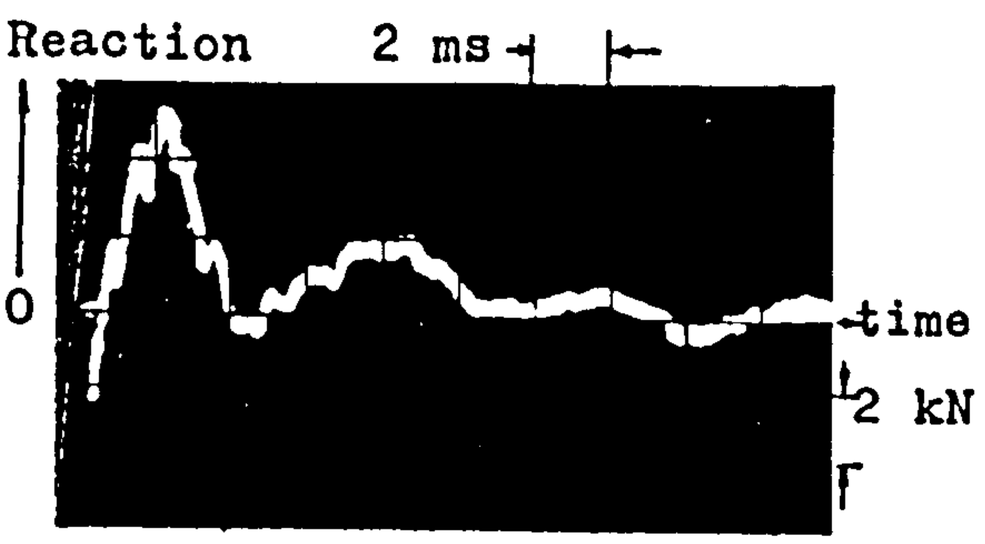

Beam 3.10

Note : Time = 0 at trigger (section 4.3.4).

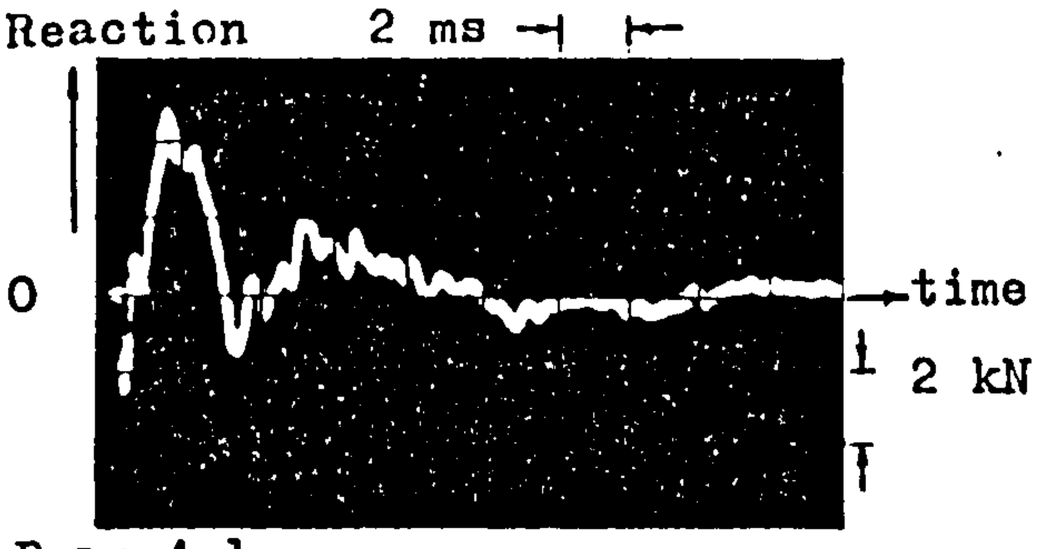

Beam 4.1

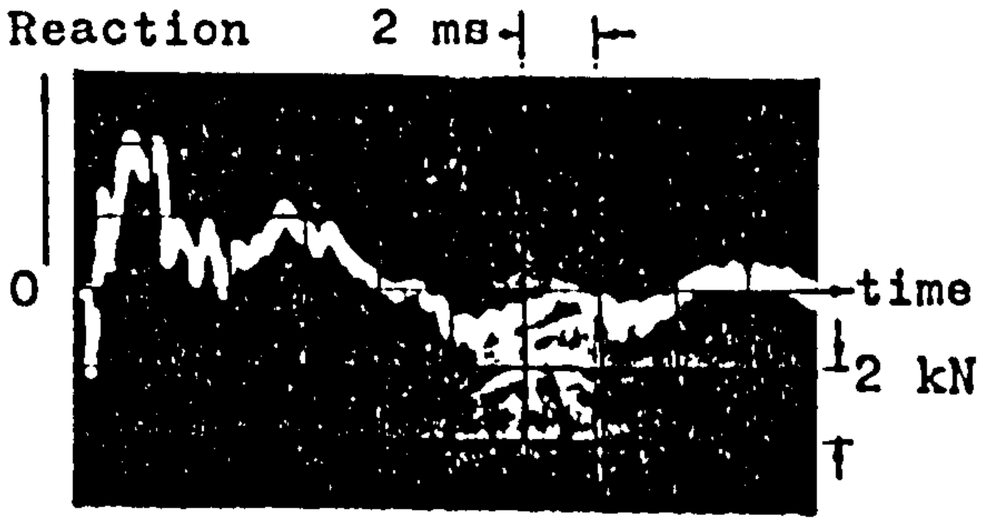

Beam 4.4

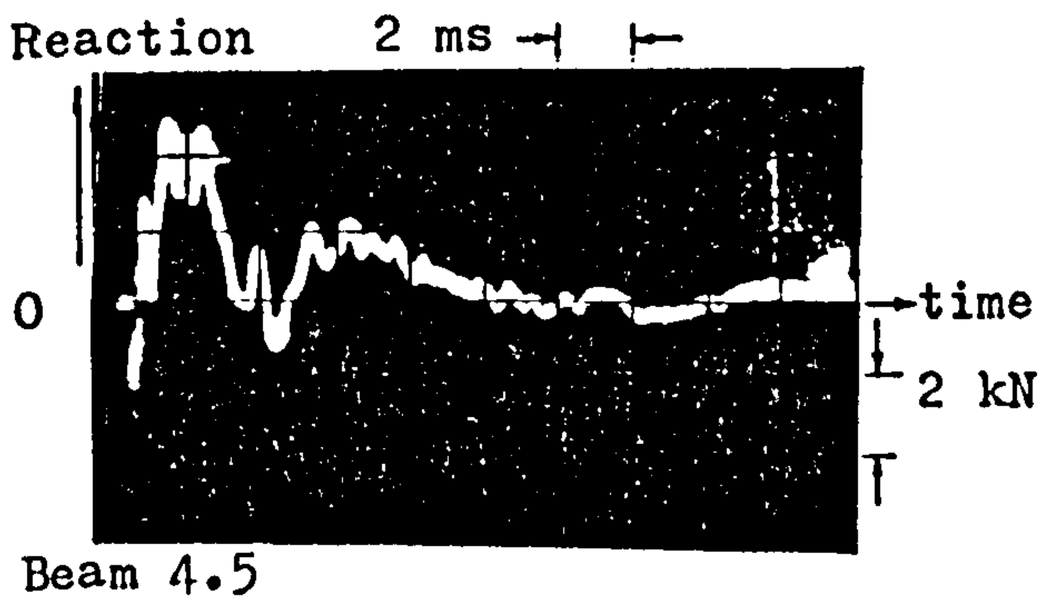

Beam 4.5

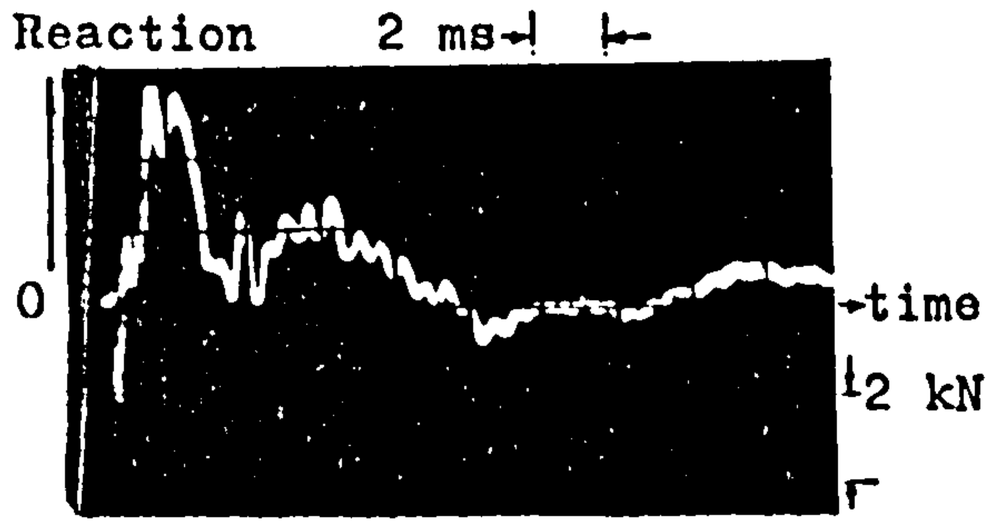

Beam 4.6

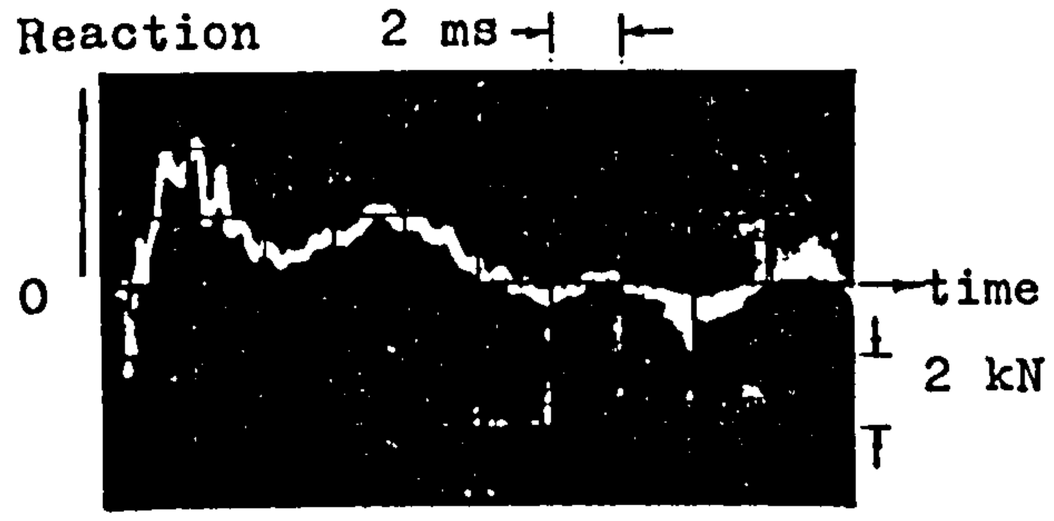

Beam 4.7

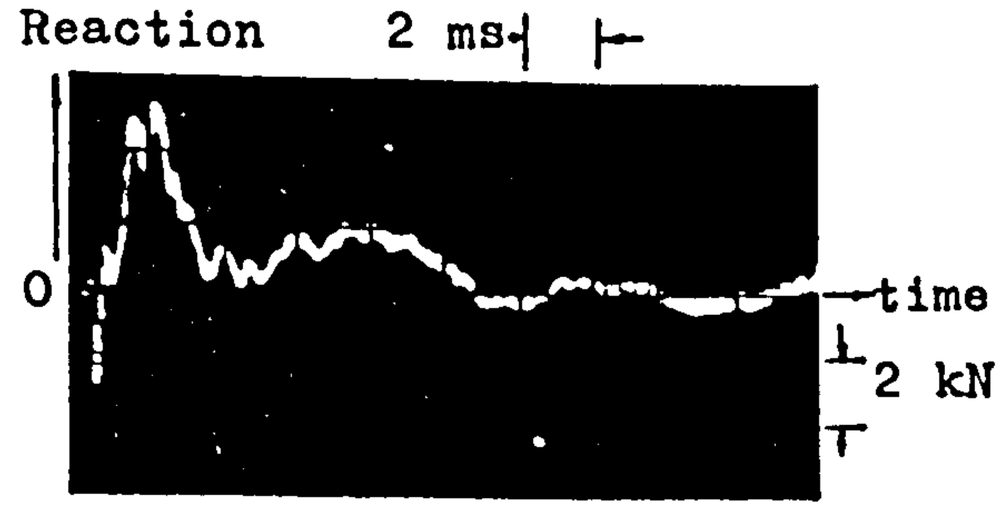

Beam 4.8

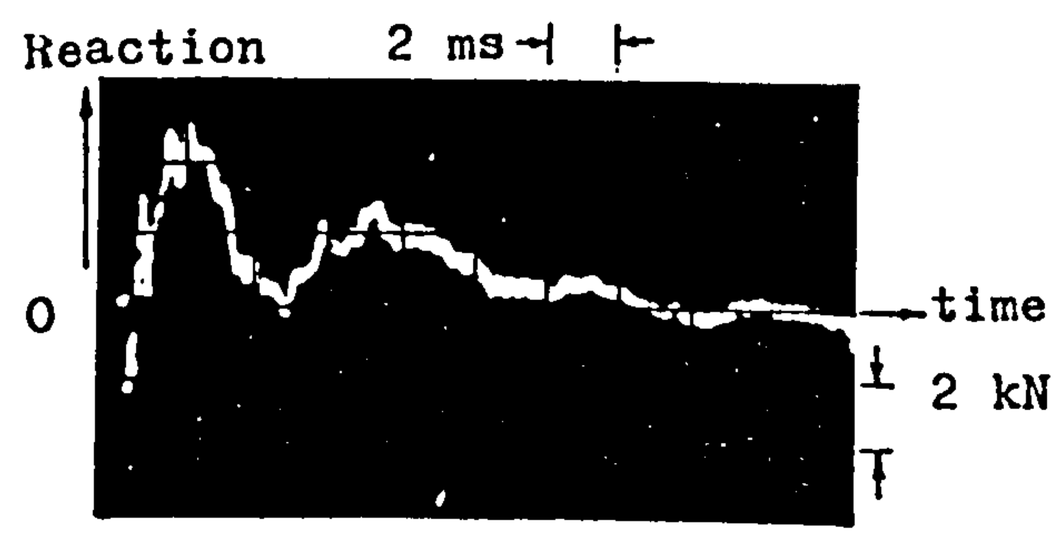

Beam 4.9

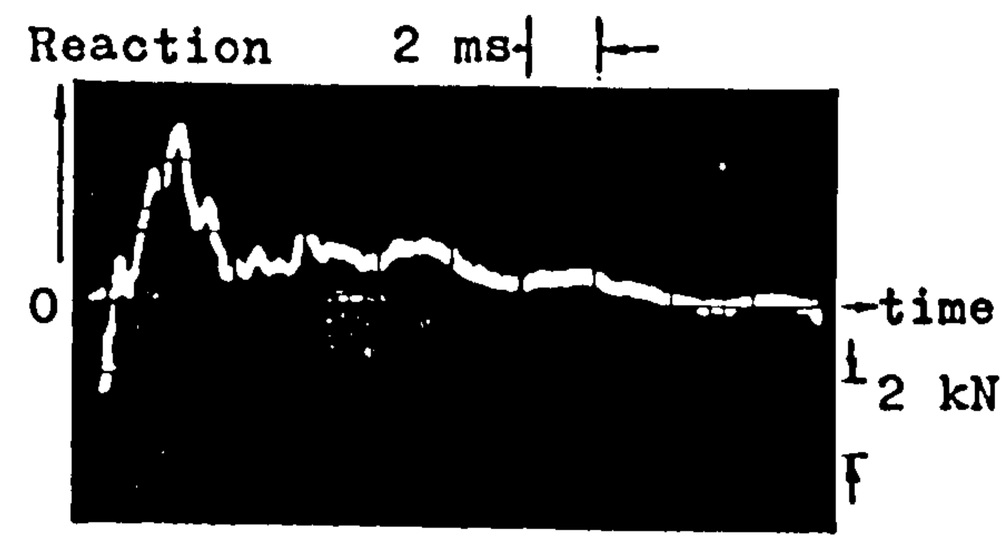

Beam 4.10

Note : Time = 0 at trigger (section 4.3.4).

APPENDIX E REACTION TRACE

APPENDIX F

Load-Deflection Curve - Post- Impact- Static Test

This appendix presents the load-deflection curves for the 32 beams which were tested statically after being impacted. The curves were obtained as described in section 3.7.5. The following notes apply to all the 32 graphs.

(a) The axis marked LC 1 is the load at midspan (section 3.7.4).

(b) The axis marked LVDT is the midspan deflection.

(c) The identification number of the beam is located at the top right-hand corner of the graph preceded by the letter R.

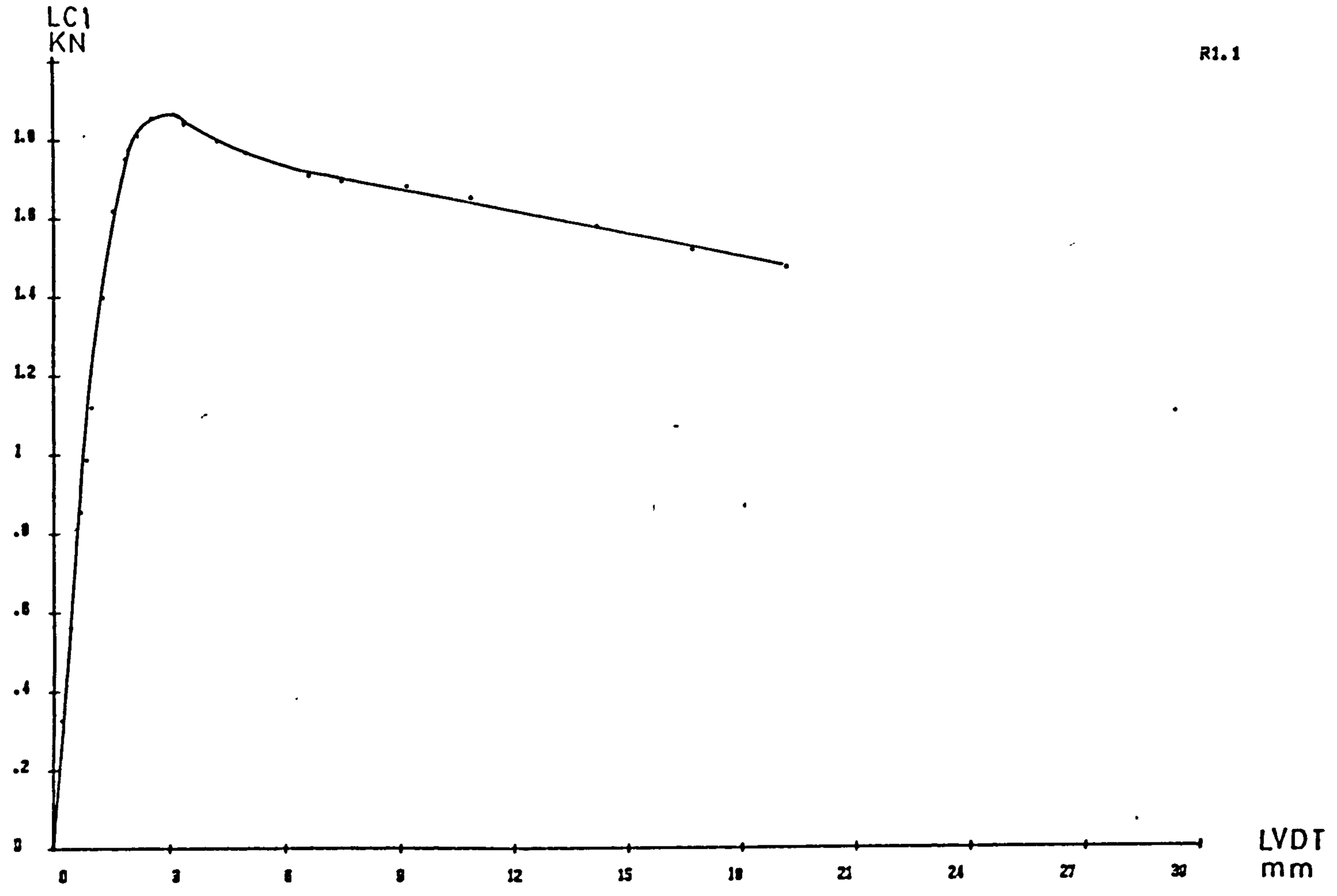

F2

Notes : see page F1.

APPENDIX F LOAD - DEFLECTION CURVE - POST - IMPACT - STATIC TEST

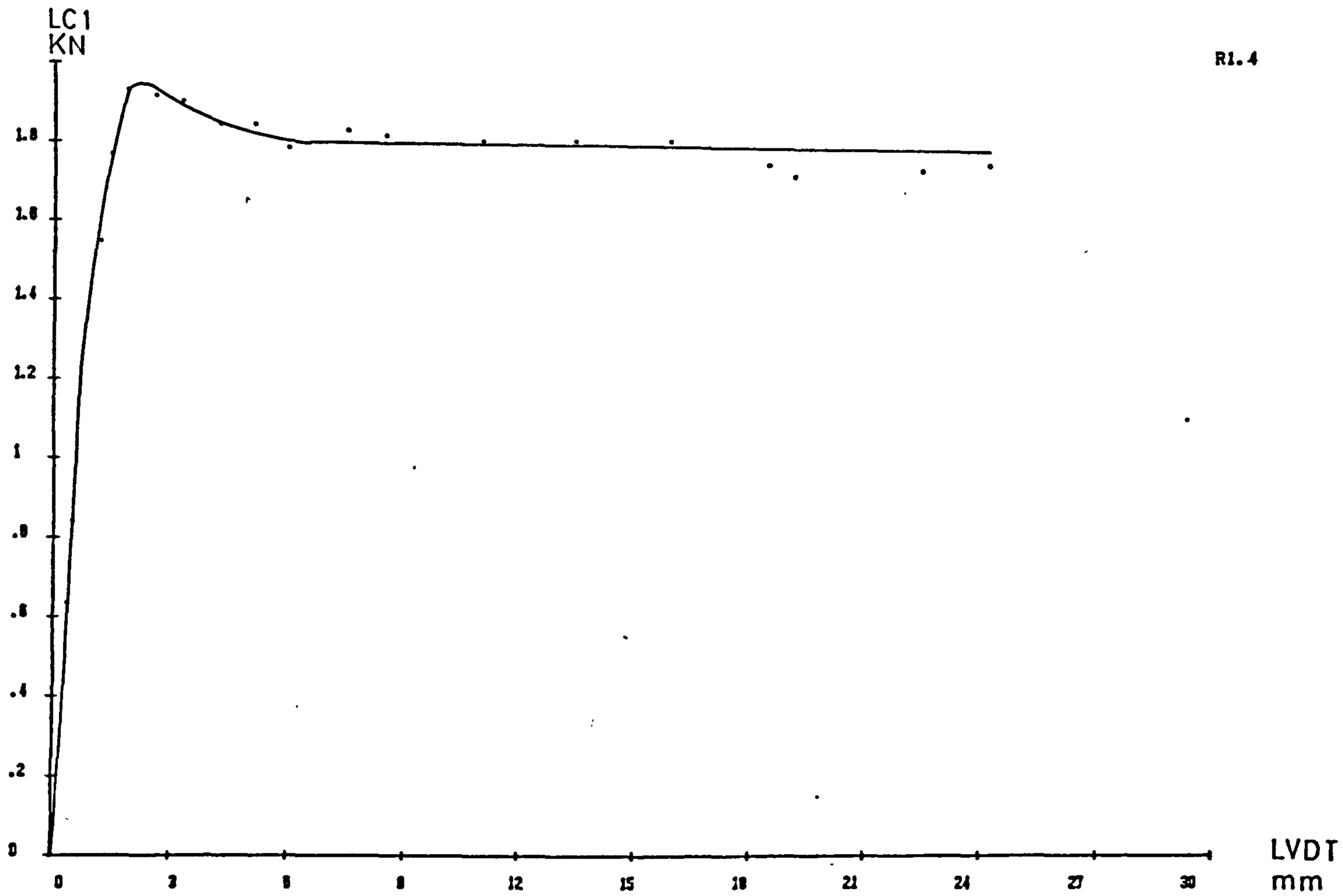

R1.4

Notes : see page F1.

APPENDIX F LOAD - DEFLECTION CURVE - POST - IMPACT - STATIC TEST

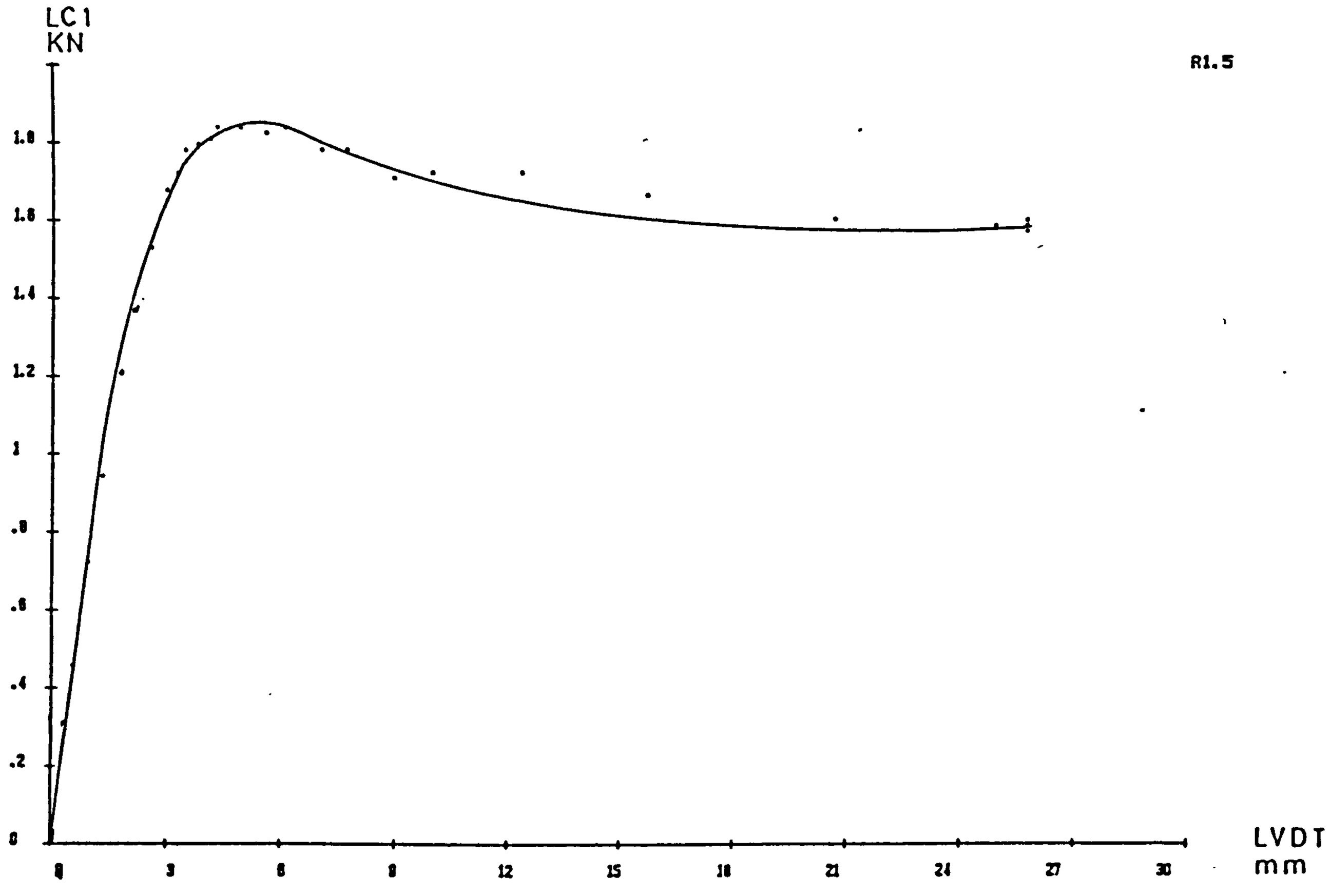

R1.5

F4

Notes : see page F1.

APPENDIX F LOAD - DEFLECTION CURVE - POST - IMPACT - STATIC TEST

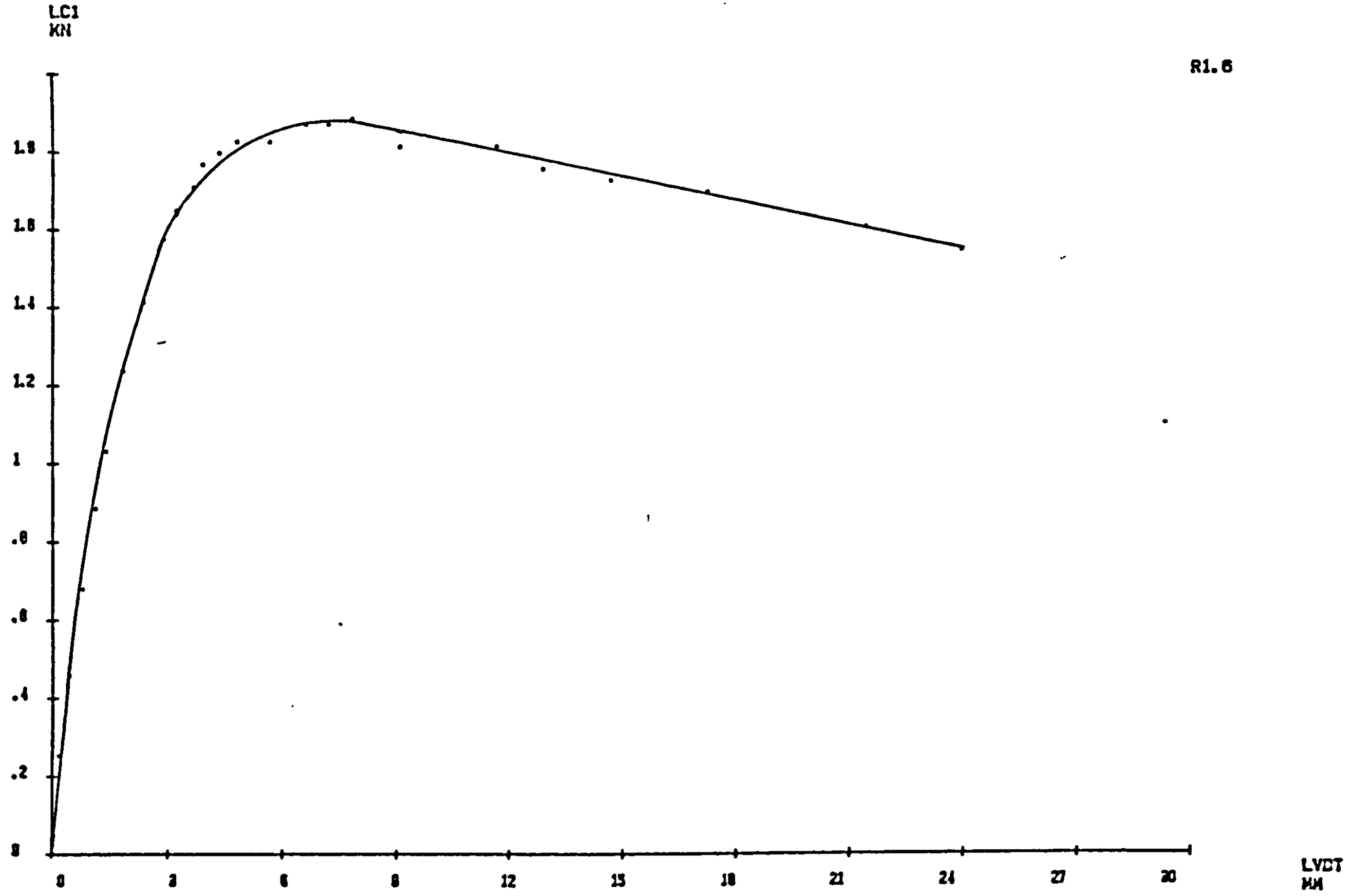

R1.6

Notes : see page F1.

APPENDIX F LOAD - DEFLECTION CURVE - POST - IMPACT - STATIC TEST

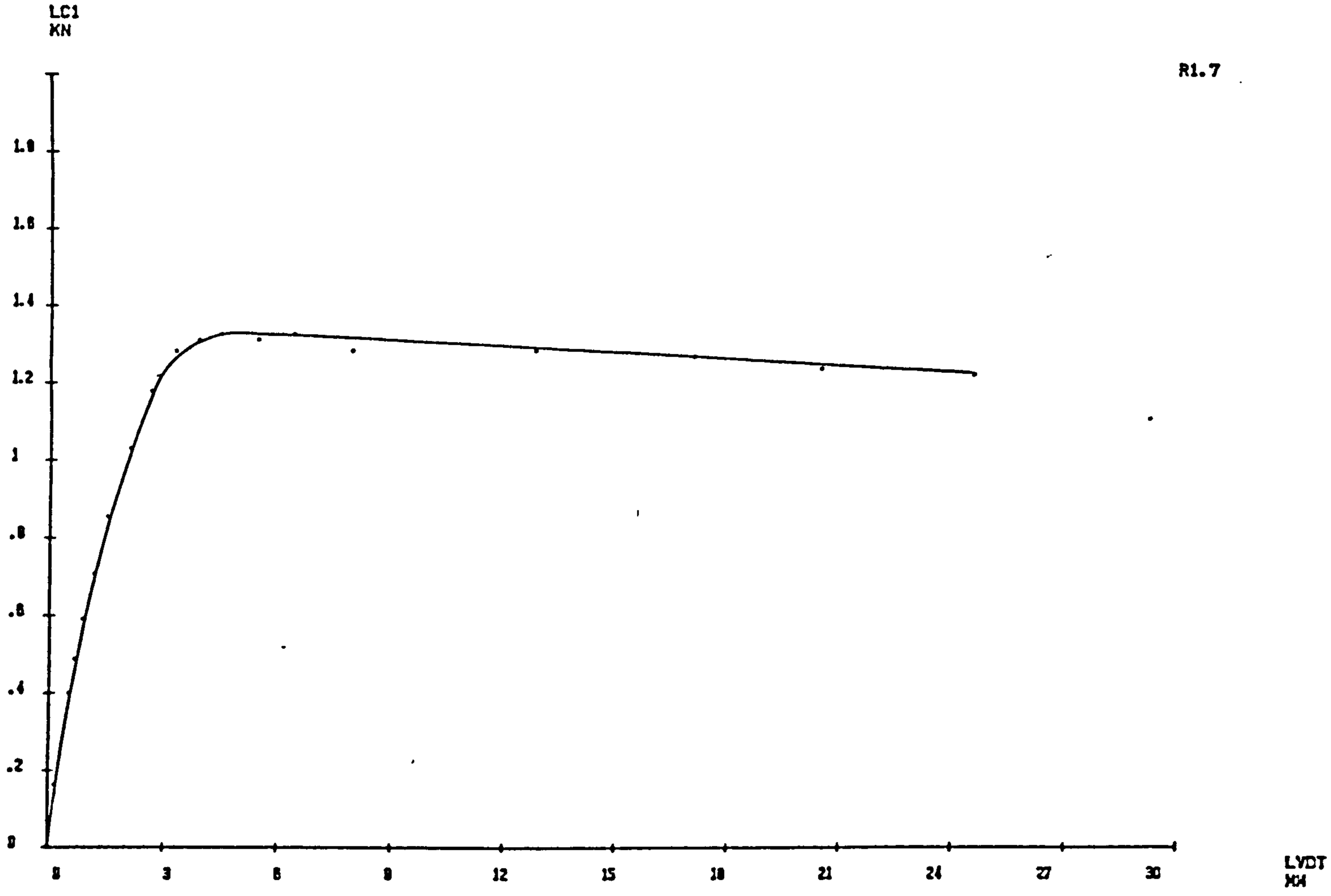

R1.7

Notes : see page F1.

APPENDIX F LOAD - DEFLECTION CURVE - POST - IMPACT - STATIC TEST

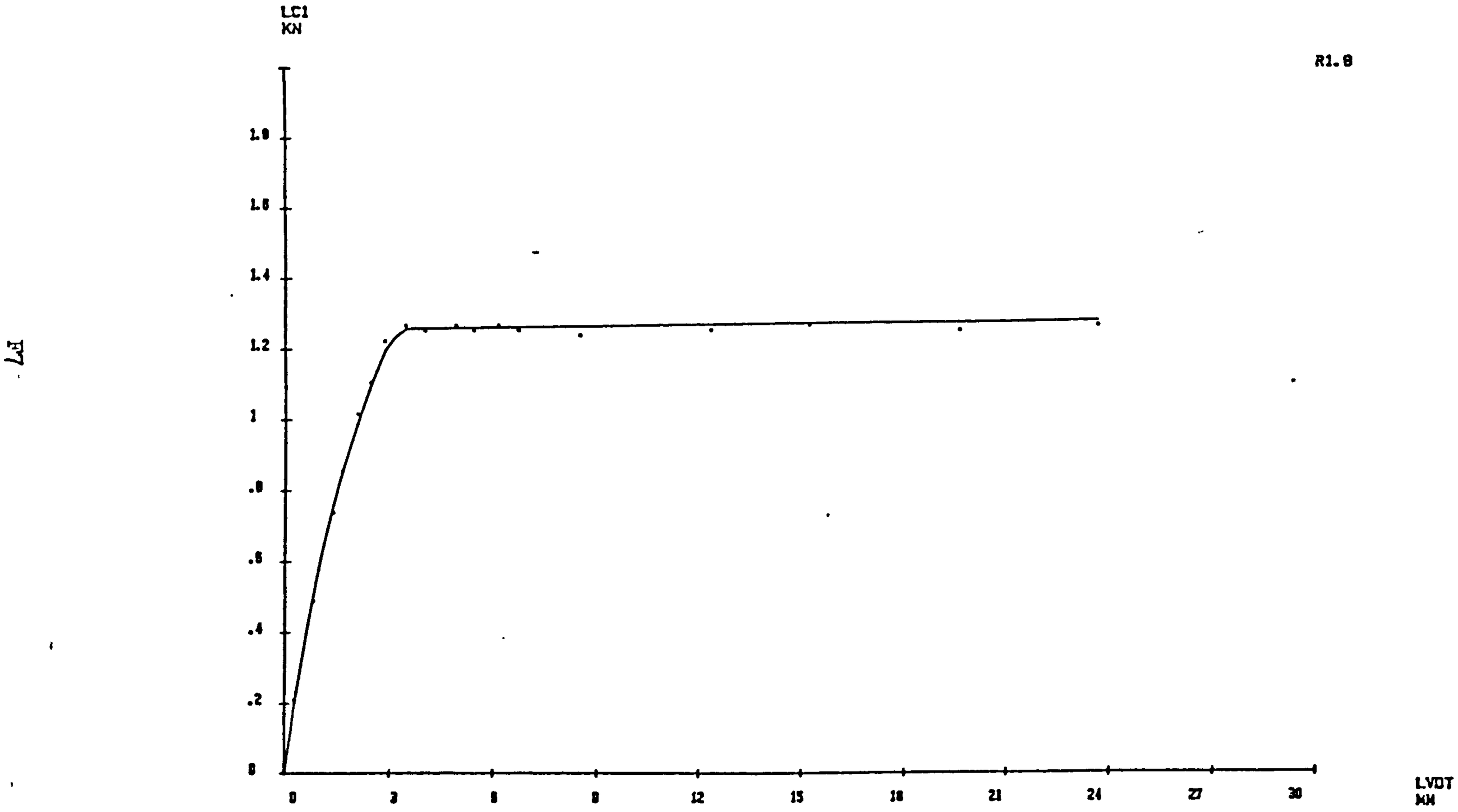

R1.8

Notes : see page F1.

APPENDIX F LOAD - DEFLECTION CURVE - POST - IMPACT - STATIC TEST

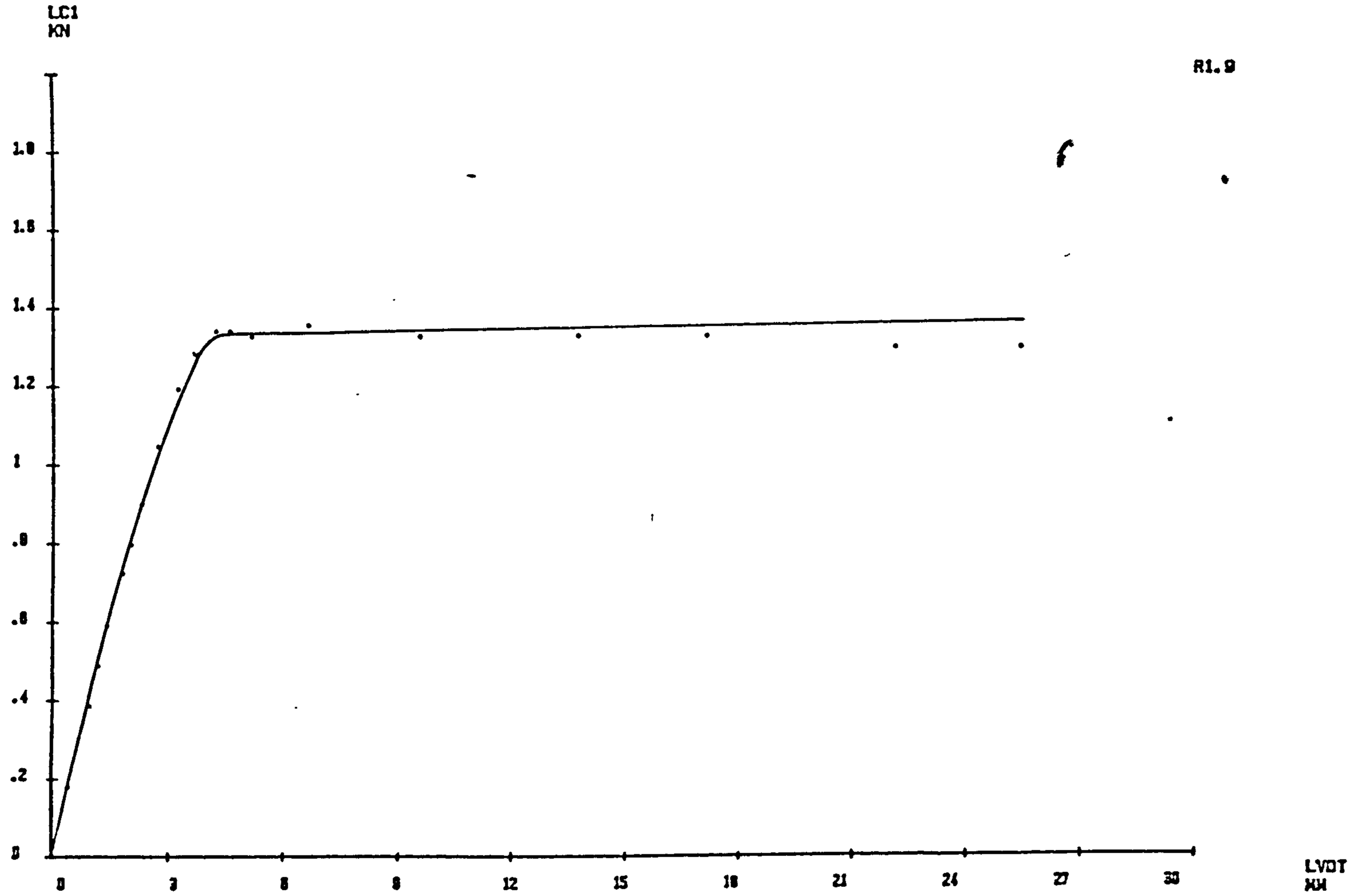

R1.9

Notes : see page F1.

APPENDIX F LOAD - DEFLECTION CURVE - POST - IMPACT - STATIC TEST

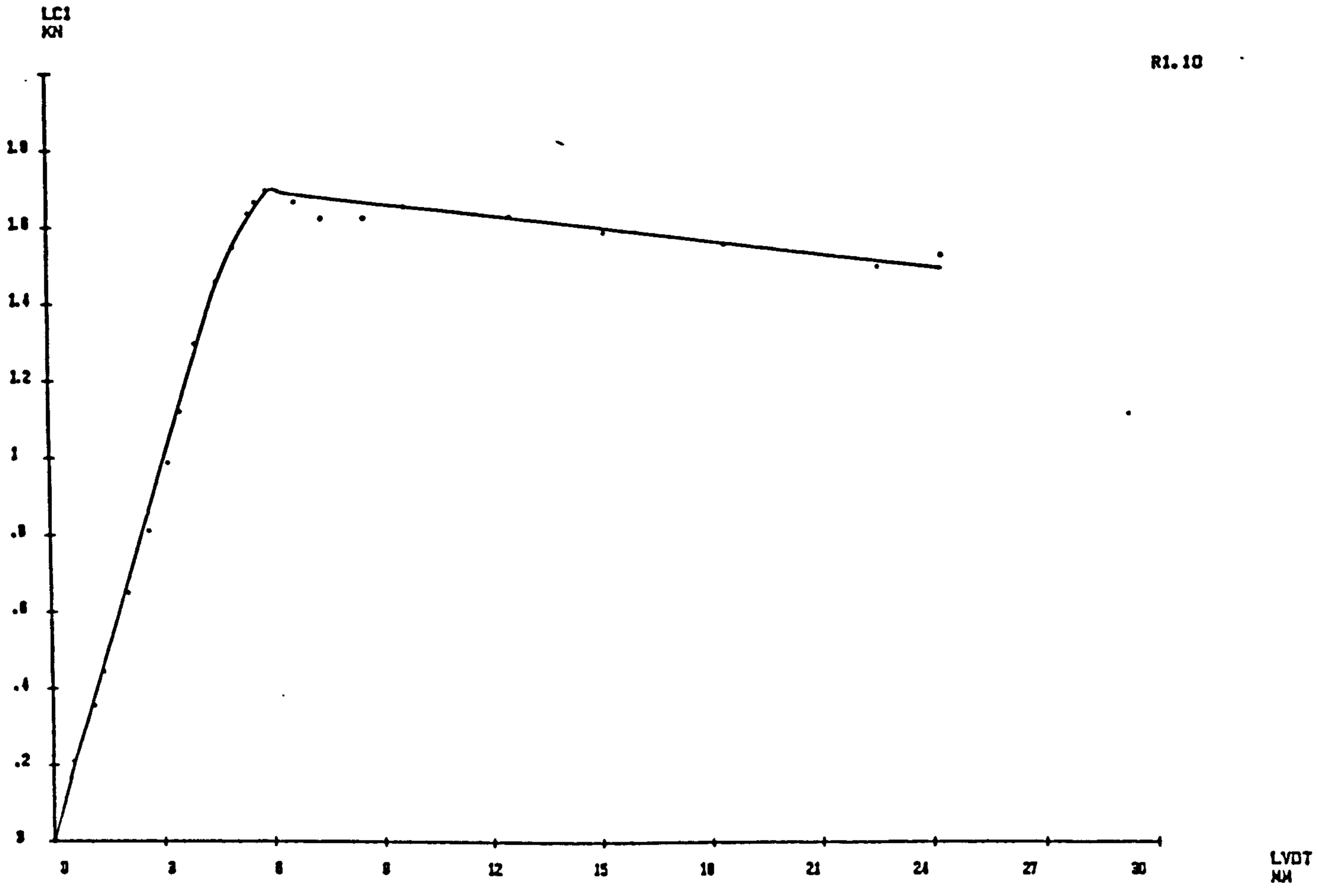

R1.10

Notes : see page F1.

APPENDIX F LOAD - DEFLECTION CURVE - POST - IMPACT - STATIC TEST

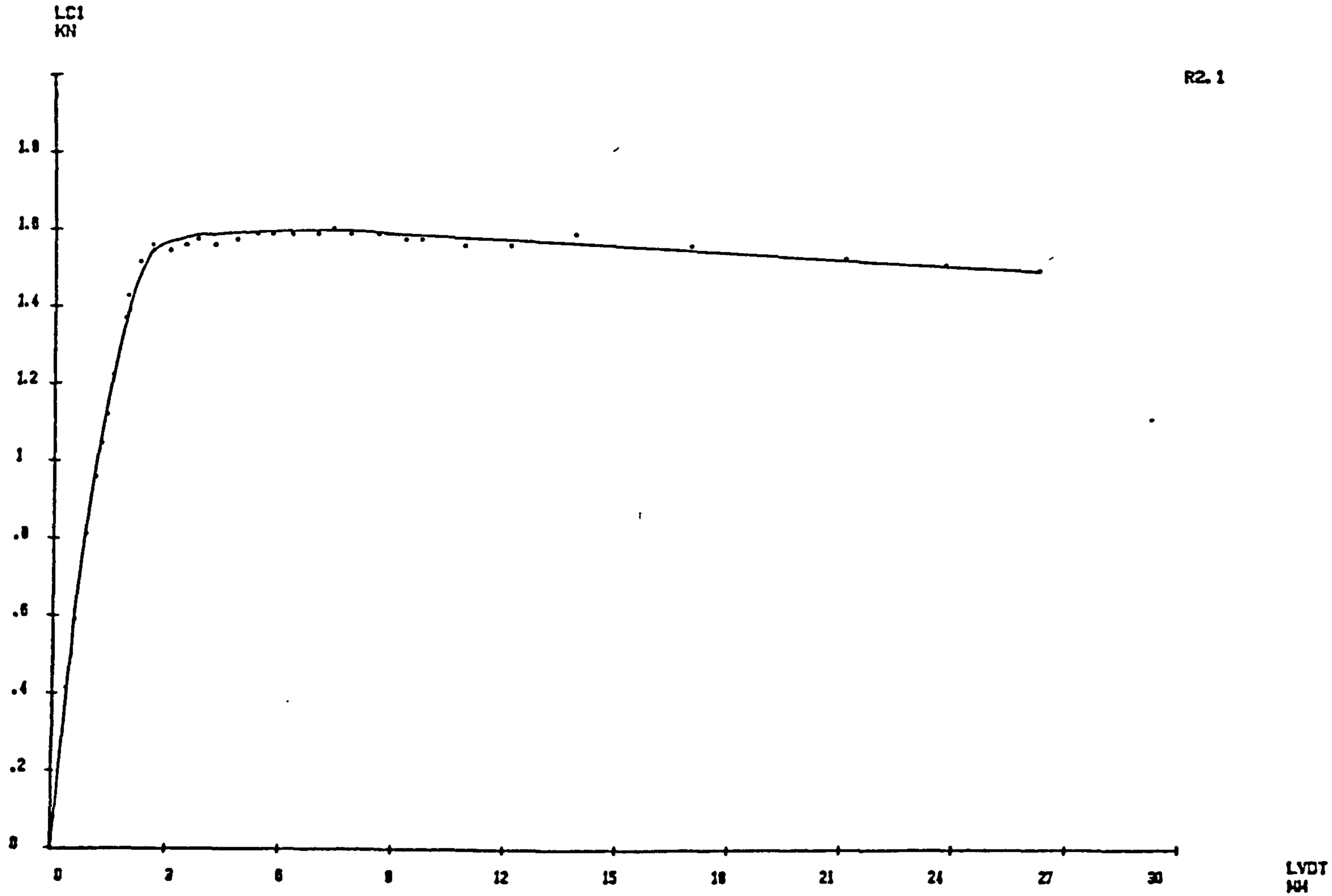

Notes : see page F1.

APPENDIX F LOAD - DEFLECTION CURVE - POST - IMPACT - STATIC TEST

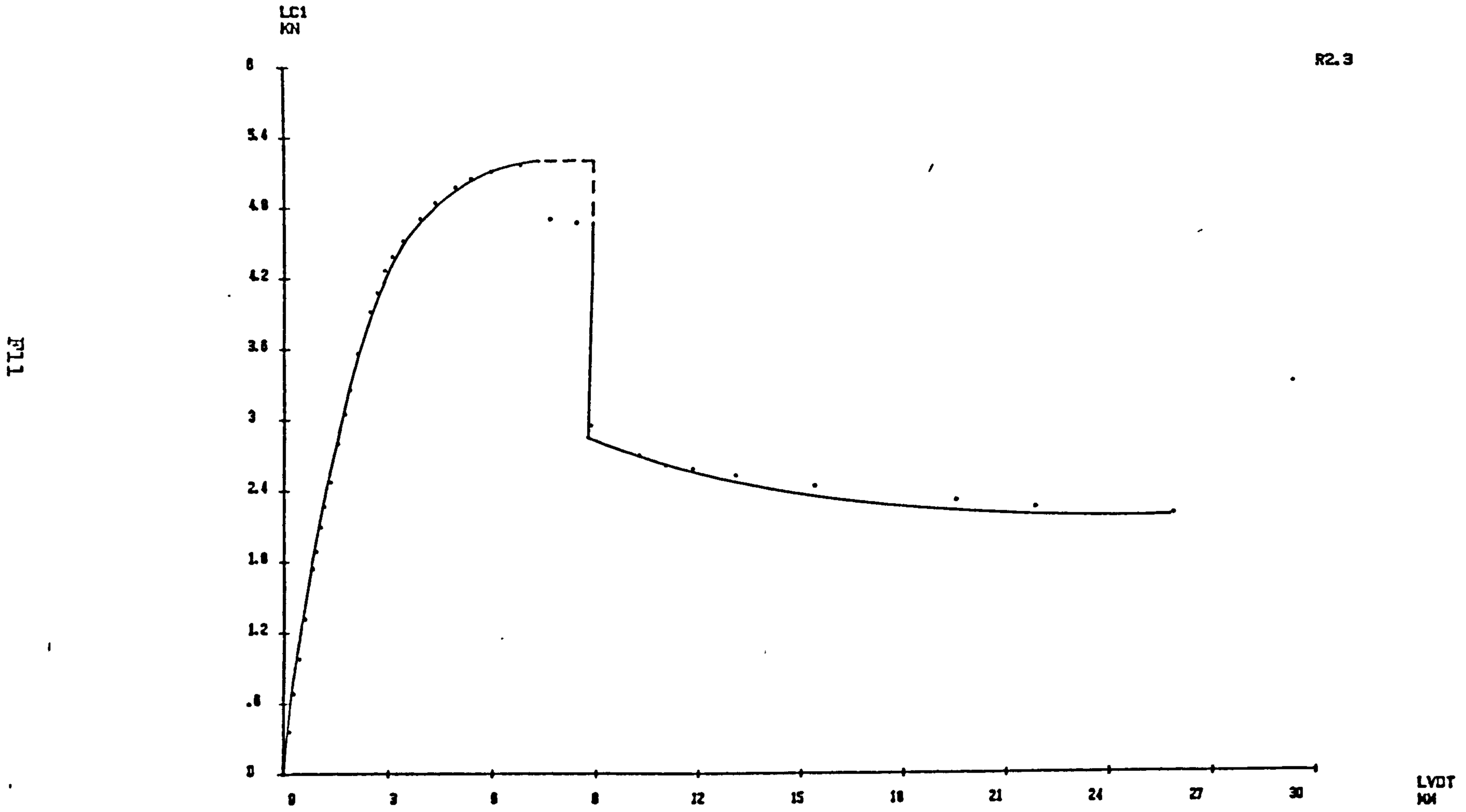

Notes : see page F1.

APPENDIX F LOAD – DEFLECTION CURVE – POST – IMPACT – STATIC TEST

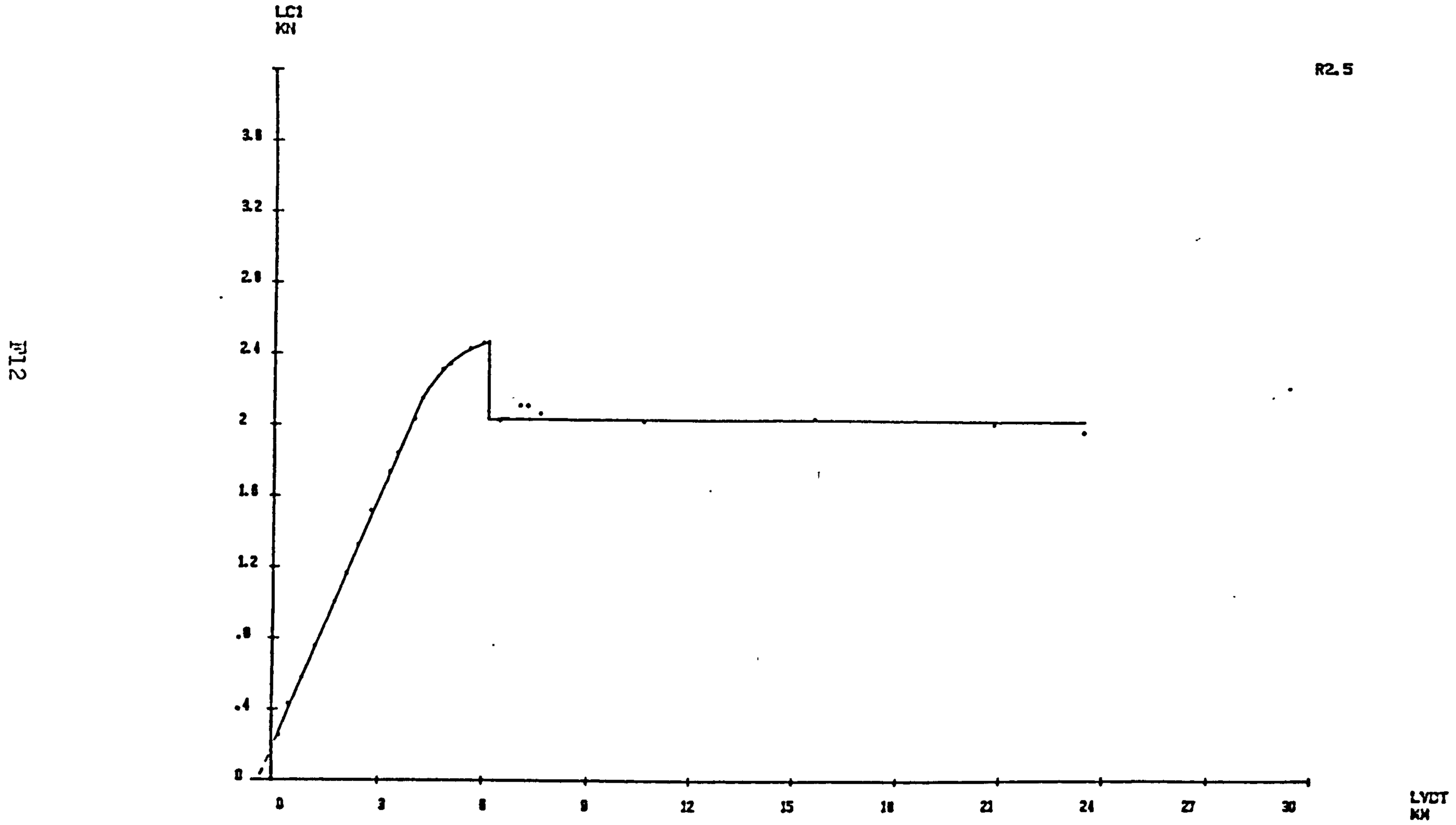

R2.5

Notes : see page F1.

APPENDIX F LOAD - DEFLECTION CURVE - POST - IMPACT - STATIC TEST

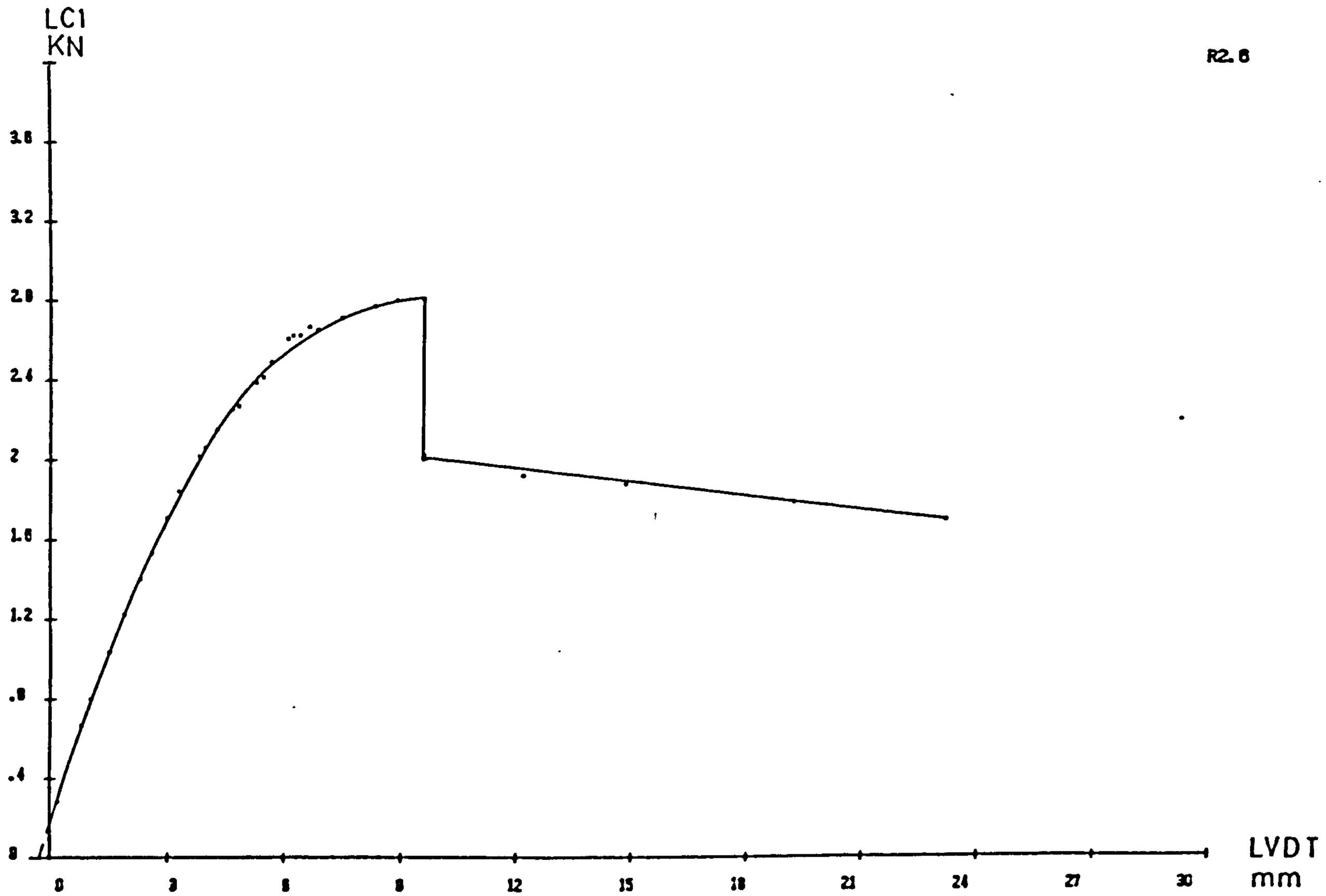

F13

R2.6

Notes : see page F1.

APPENDIX F LOAD - DEFLECTION CURVE - POST - IMPACT - STATIC TEST

R2.7

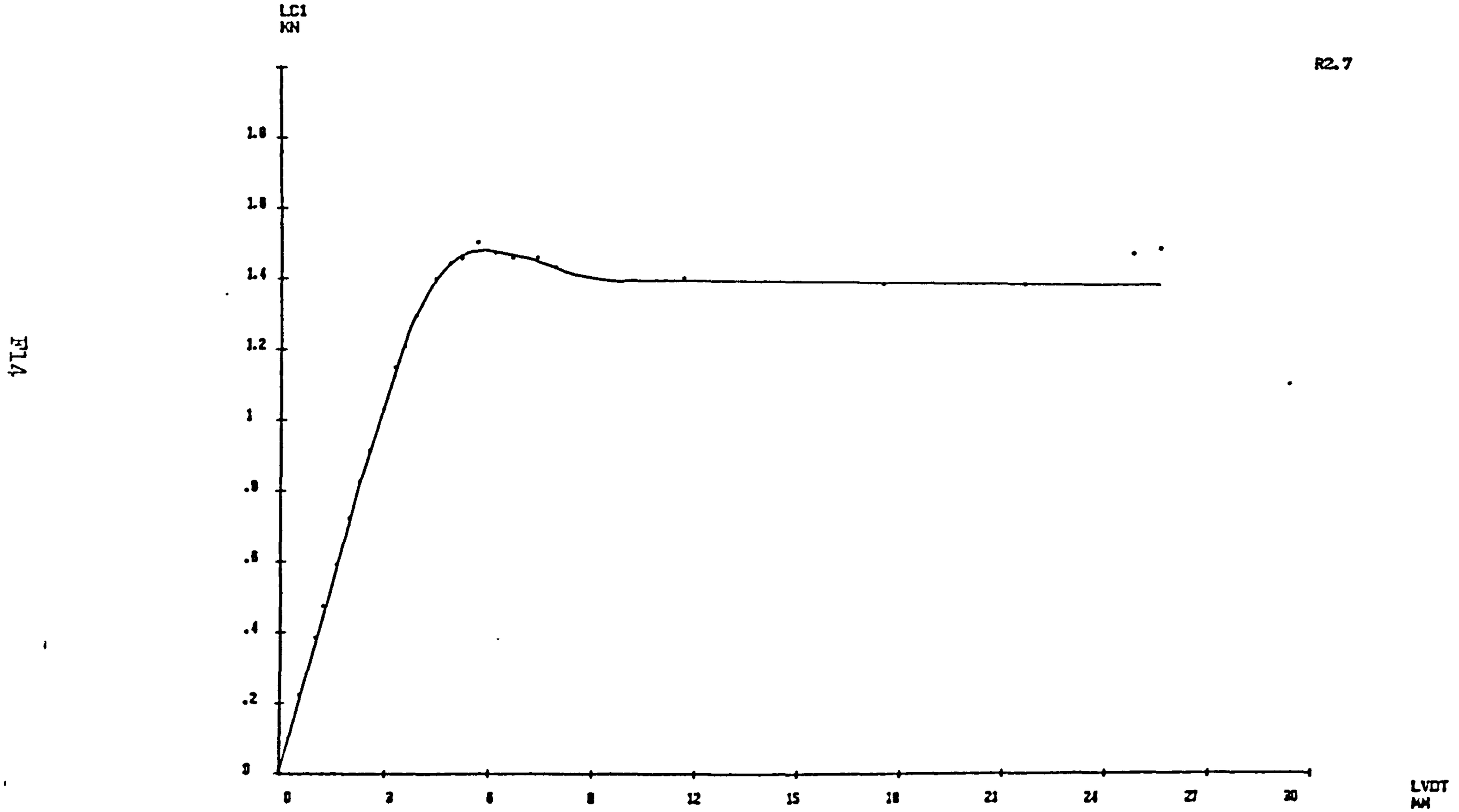

Notes : see page F1.

APPENDIX F LOAD - DEFLECTION CURVE - POST - IMPACT - STATIC TEST

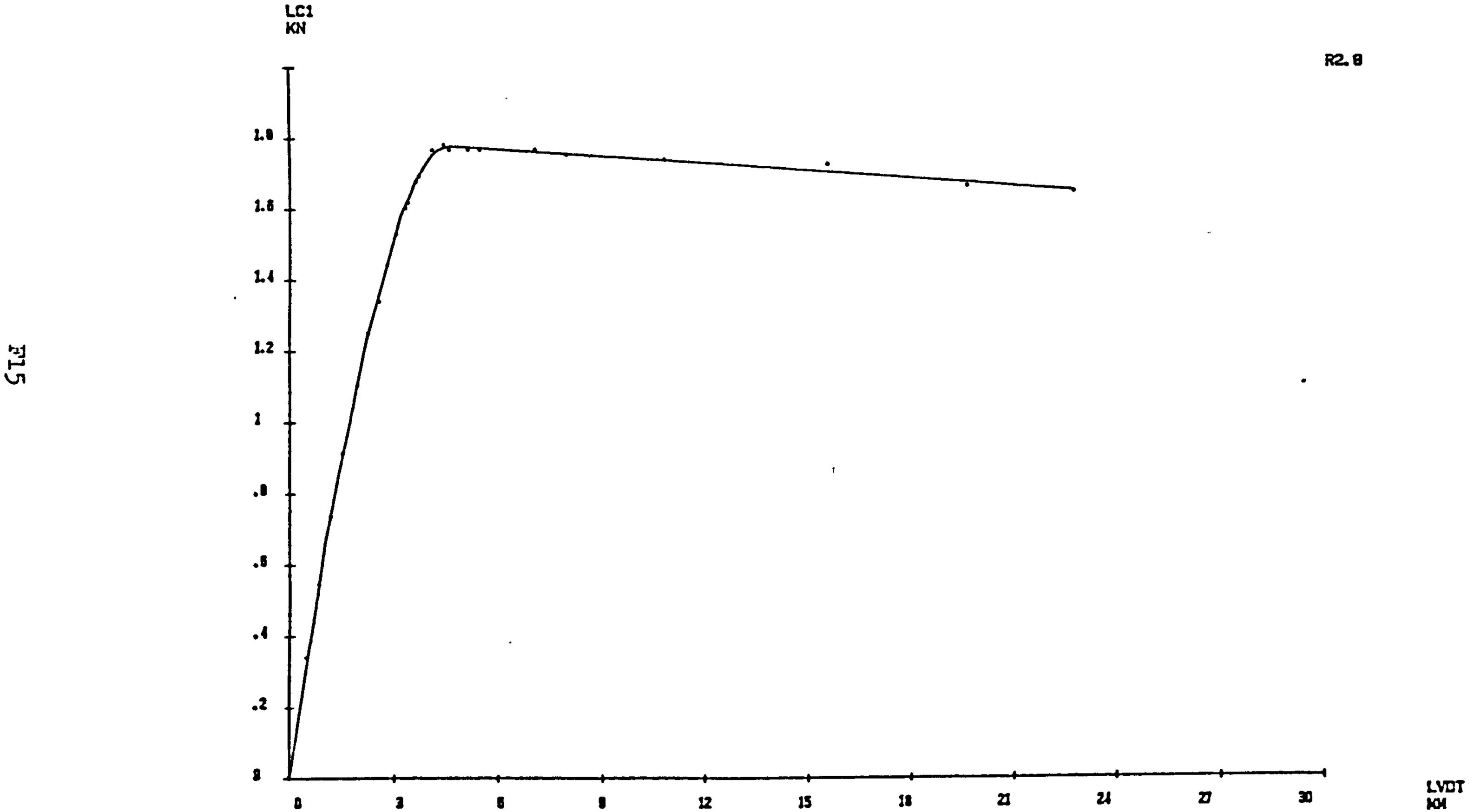

Notes : see page F1.

APPENDIX F LOAD – DEFLECTION CURVE – POST – IMPACT – STATIC TEST

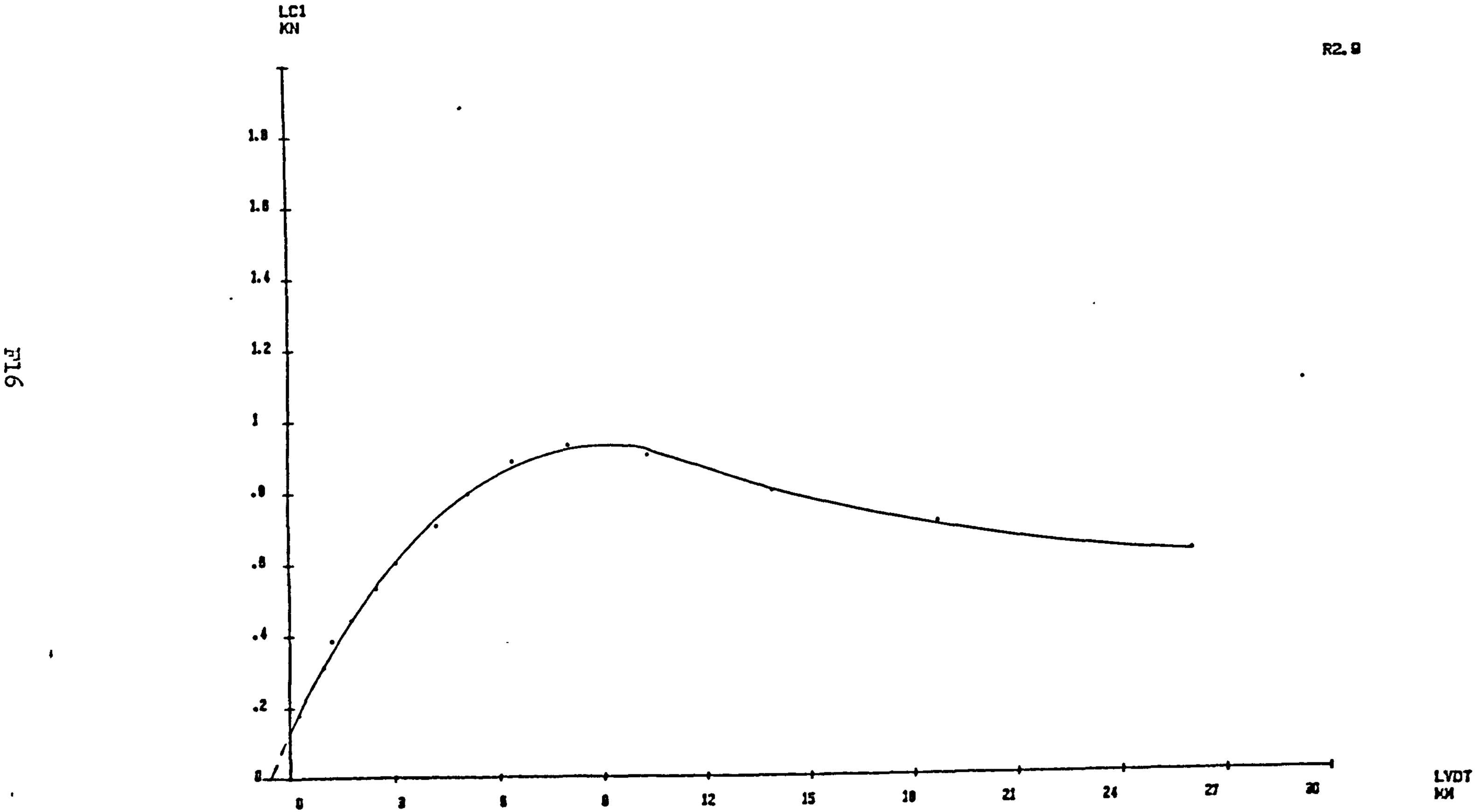

R2.9

F16

Notes : see page F1.

APPENDIX F LOAD - DEFLECTION CURVE - POST - IMPACT - STATIC TEST

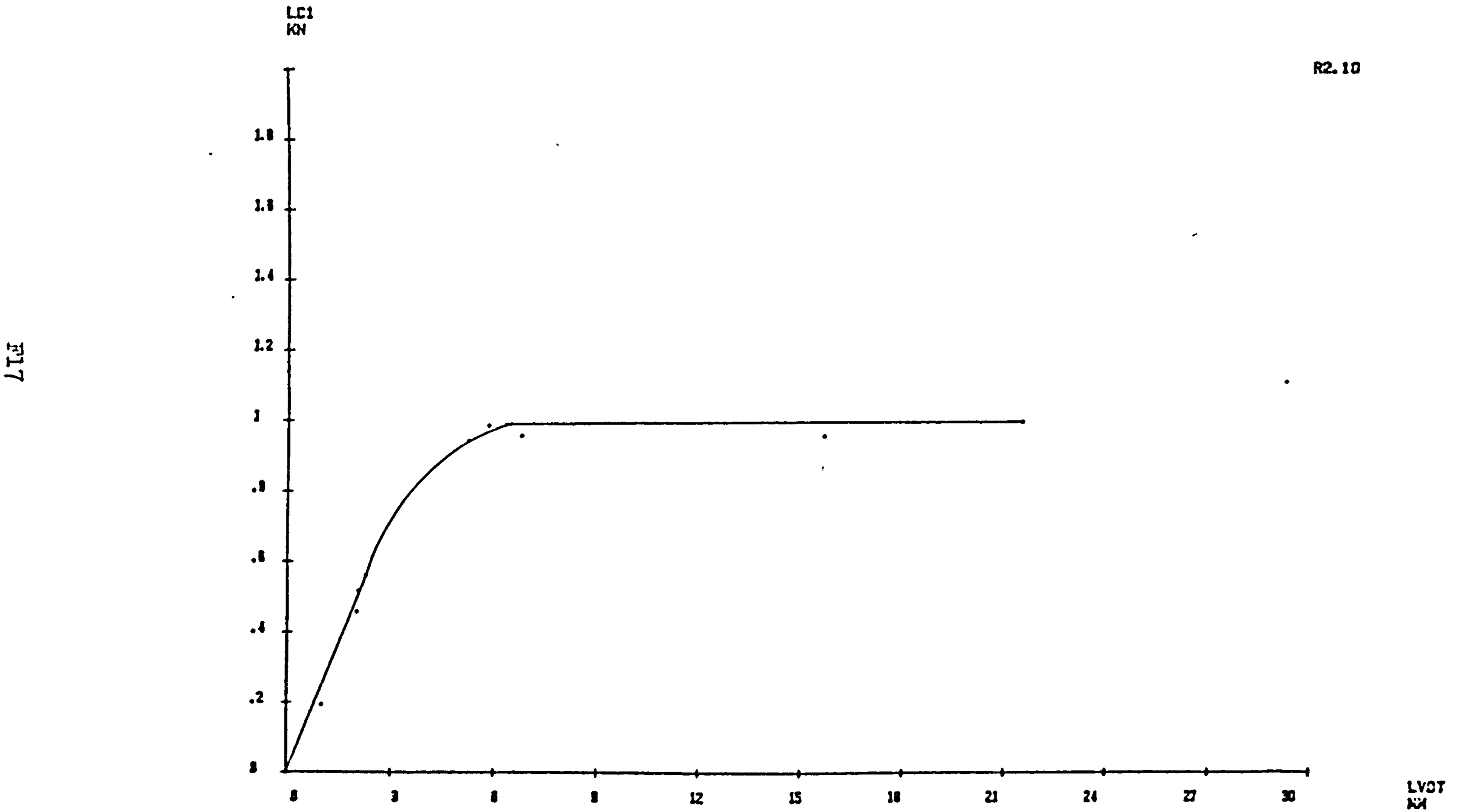

Notes : see page F1.

APPENDIX F LOAD – DEFLECTION CURVE – POST – IMPACT – STATIC TEST

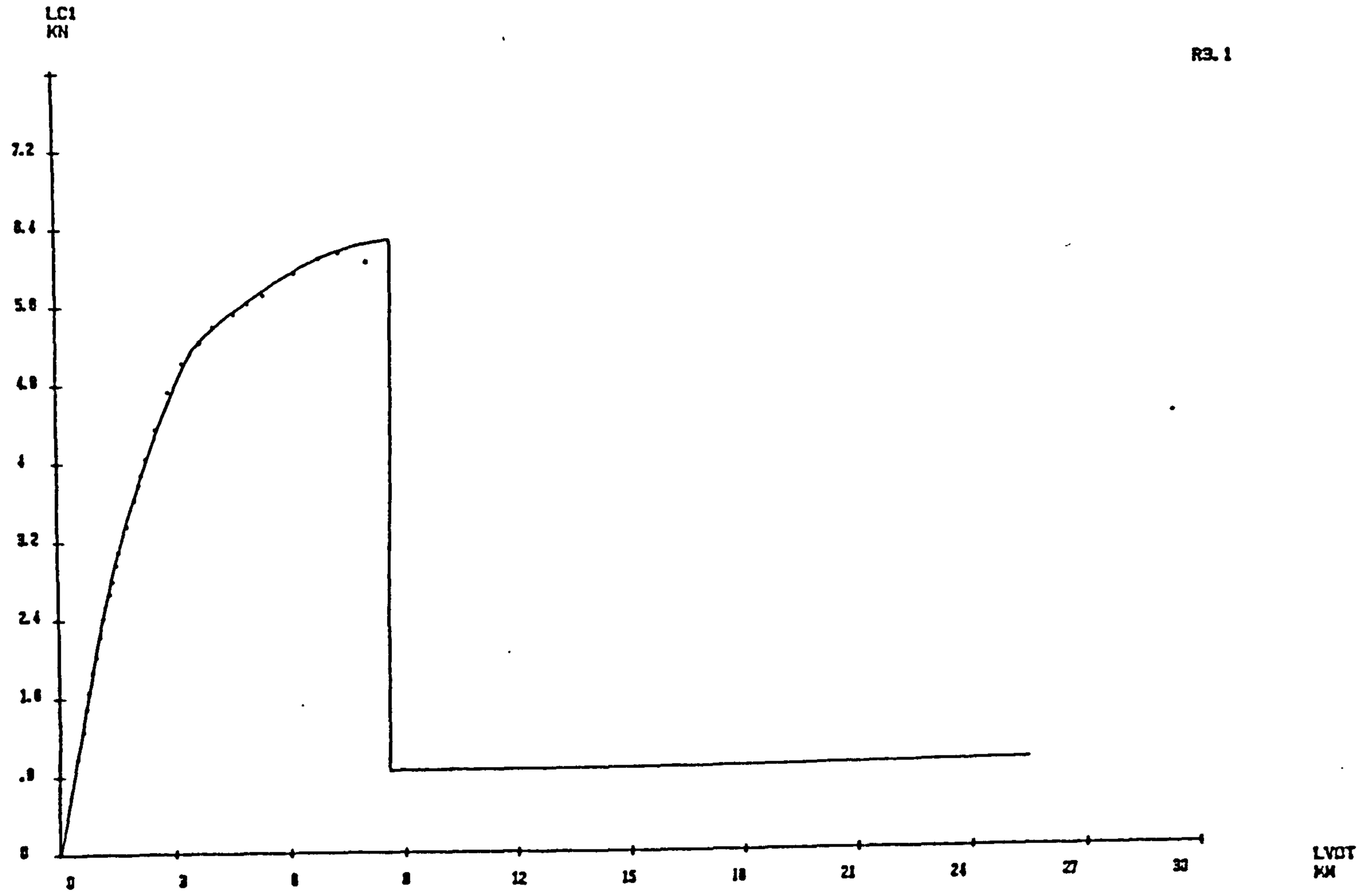

Notes : see page F1.

APPENDIX F LOAD - DEFLECTION CURVE - POST - IMPACT - STATIC TEST

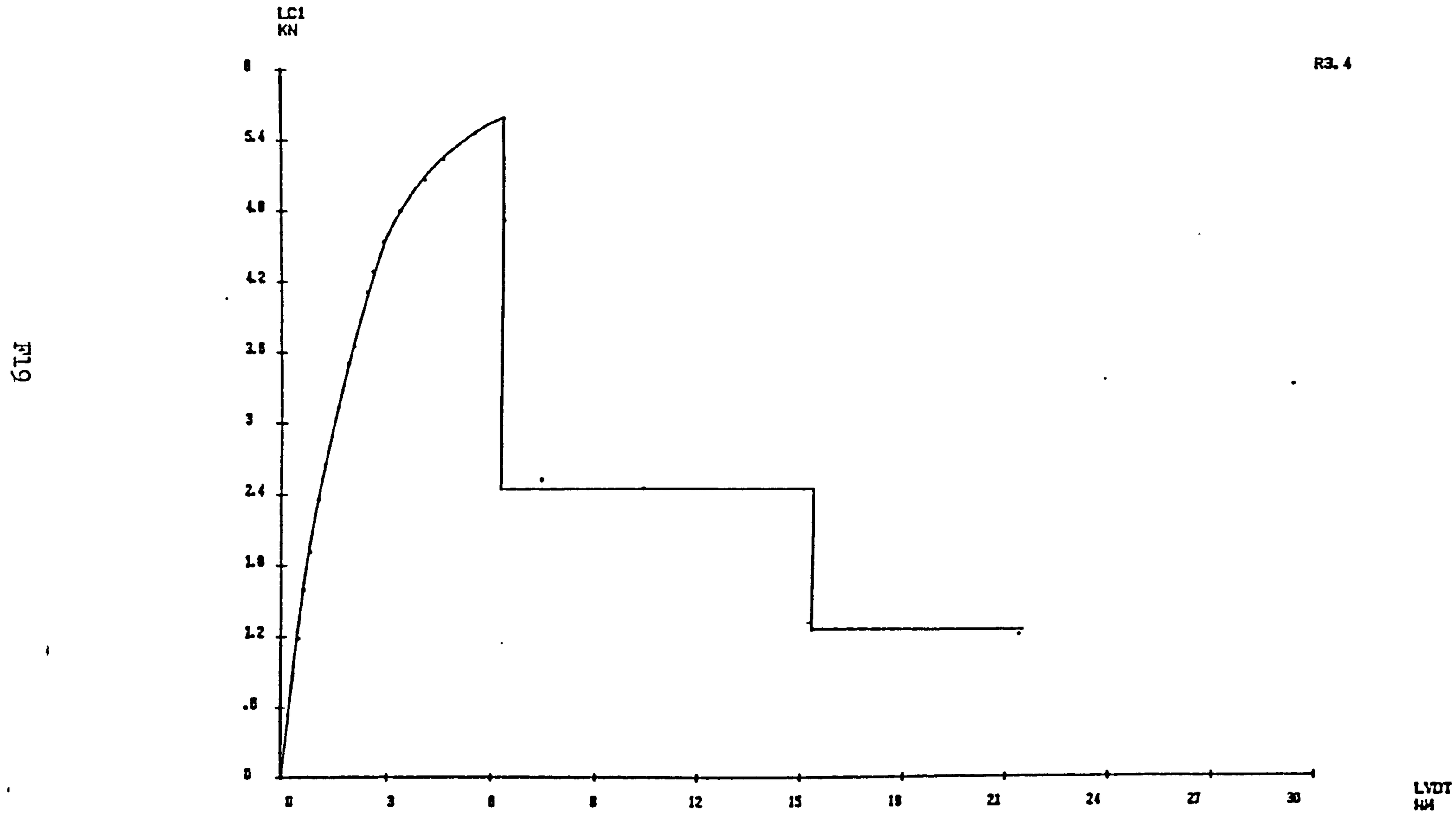

R3.4

Notes : see page F1.

APPENDIX F LOAD - DEFLECTION CURVE - POST - IMPACT - STATIC TEST

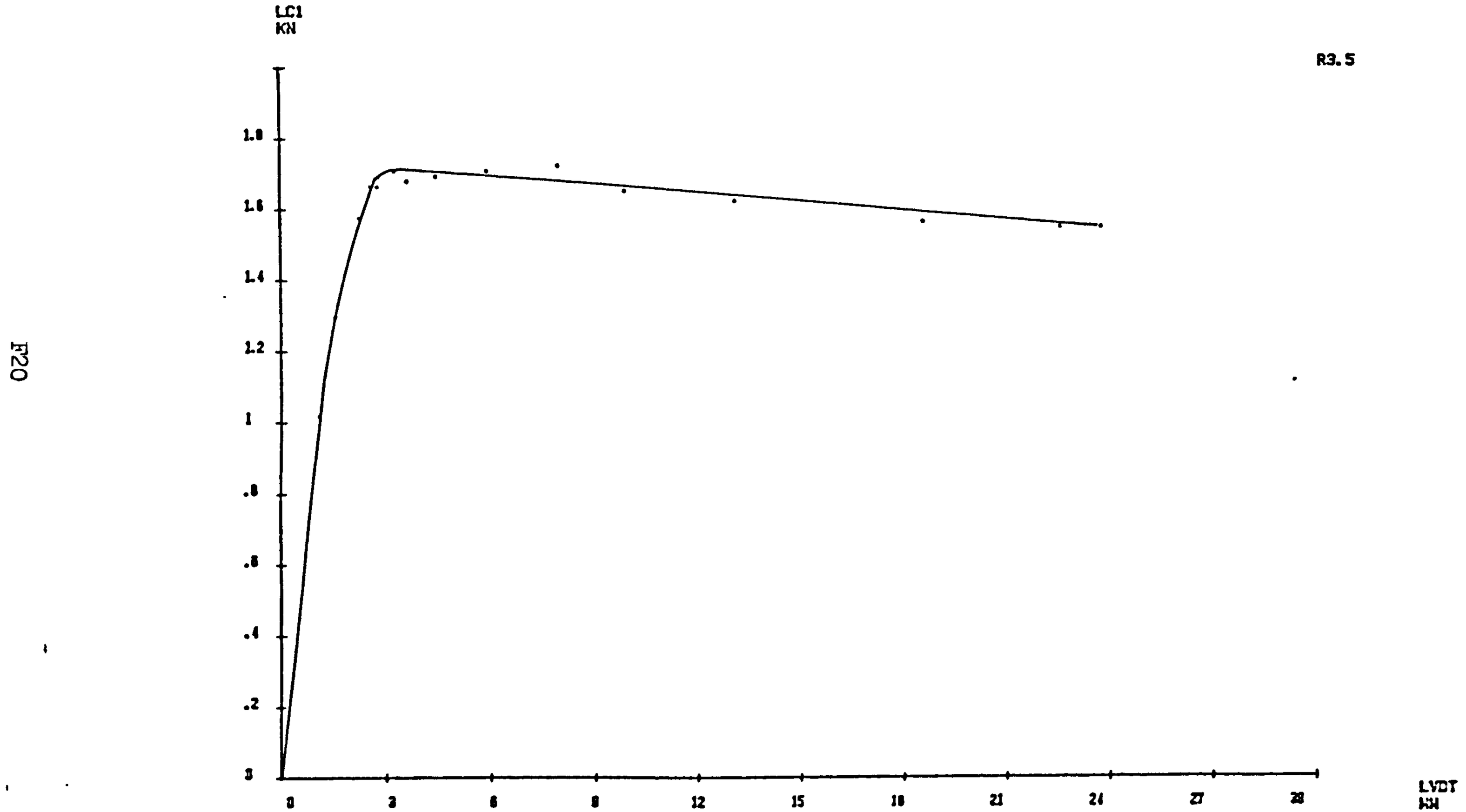

Notes : see page F1.

APPENDIX F LOAD - DEFLECTION CURVE - POST - IMPACT - STATIC TEST

R3.6

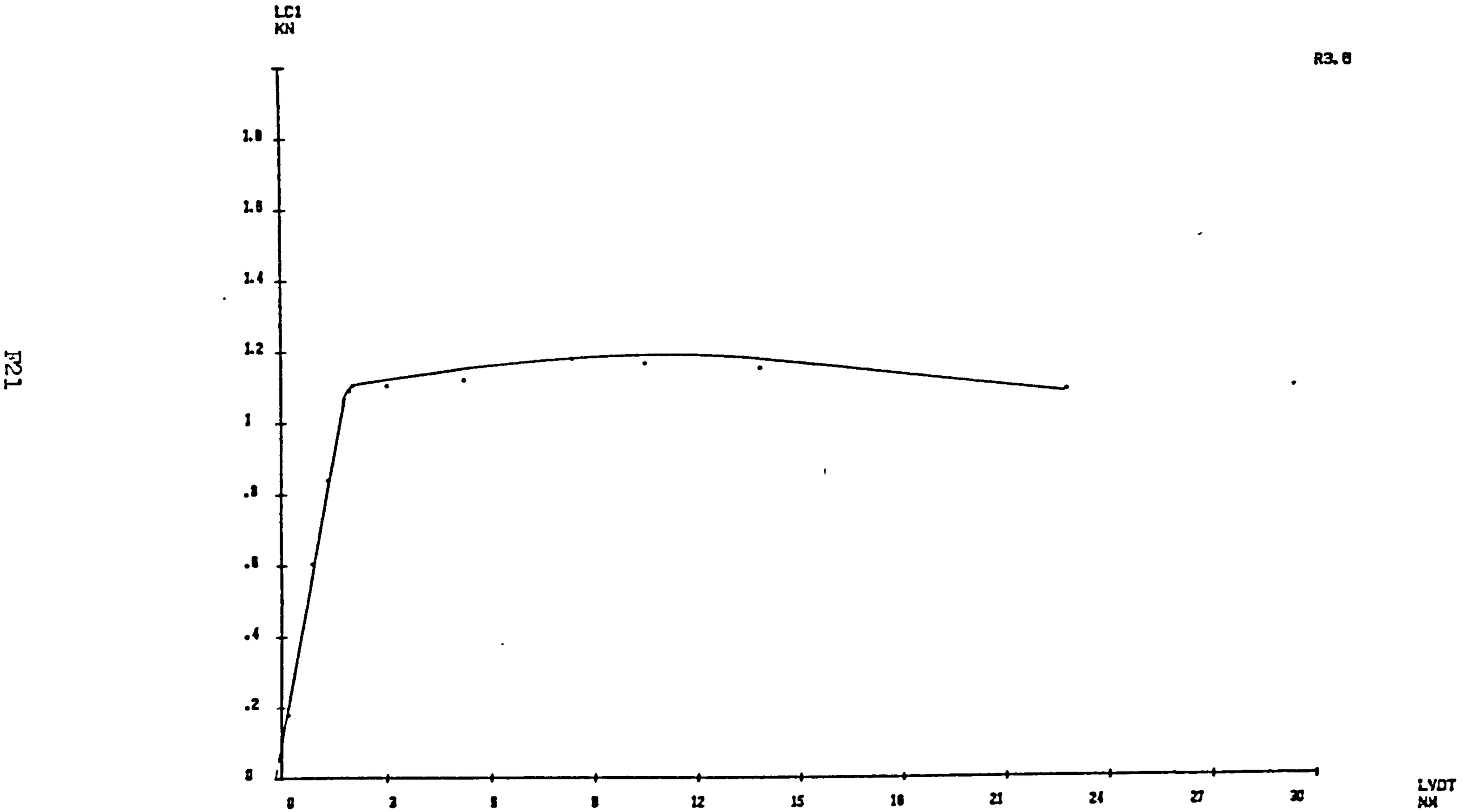

F21

Notes : see page F1.

APPENDIX F LOAD - DEFLECTION CURVE - POST - IMPACT - STATIC TEST

R3.7

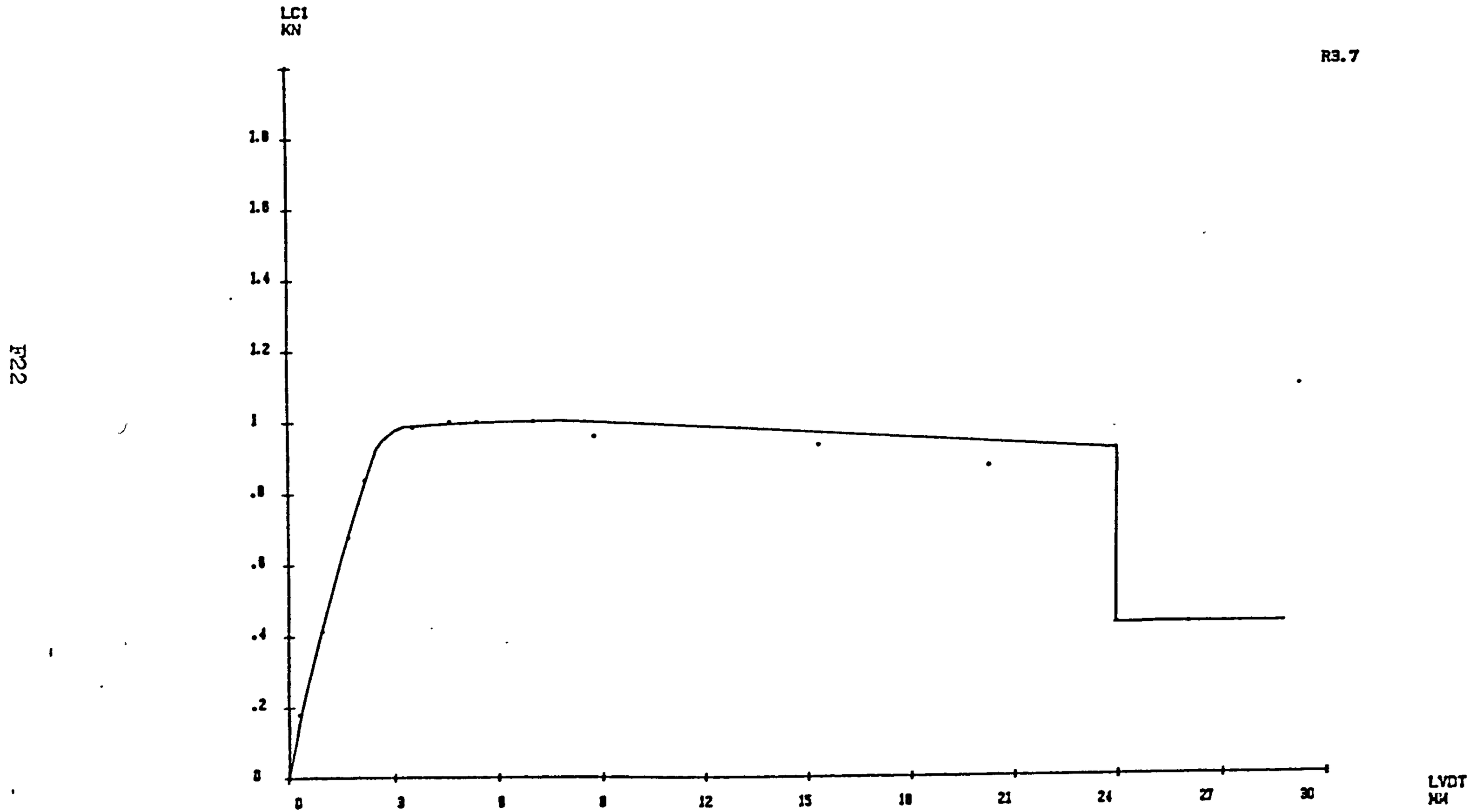

Notes : see page F1.

APPENDIX F LOAD - DEFLECTION CURVE - POST - IMPACT - STATIC TEST

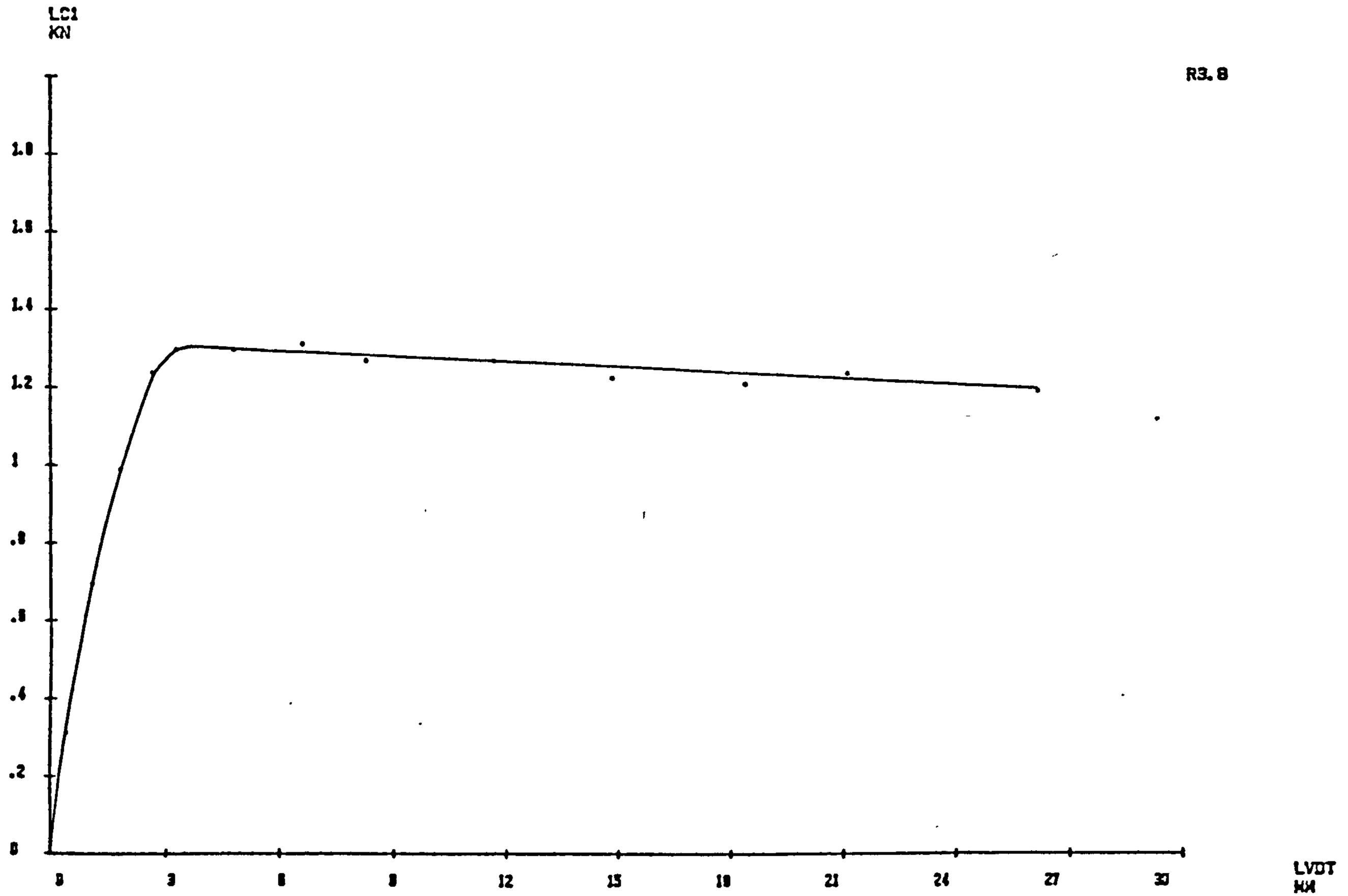

Notes : see page F1.

APPENDIX F LOAD – DEFLECTION CURVE – POST – IMPACT – STATIC TEST

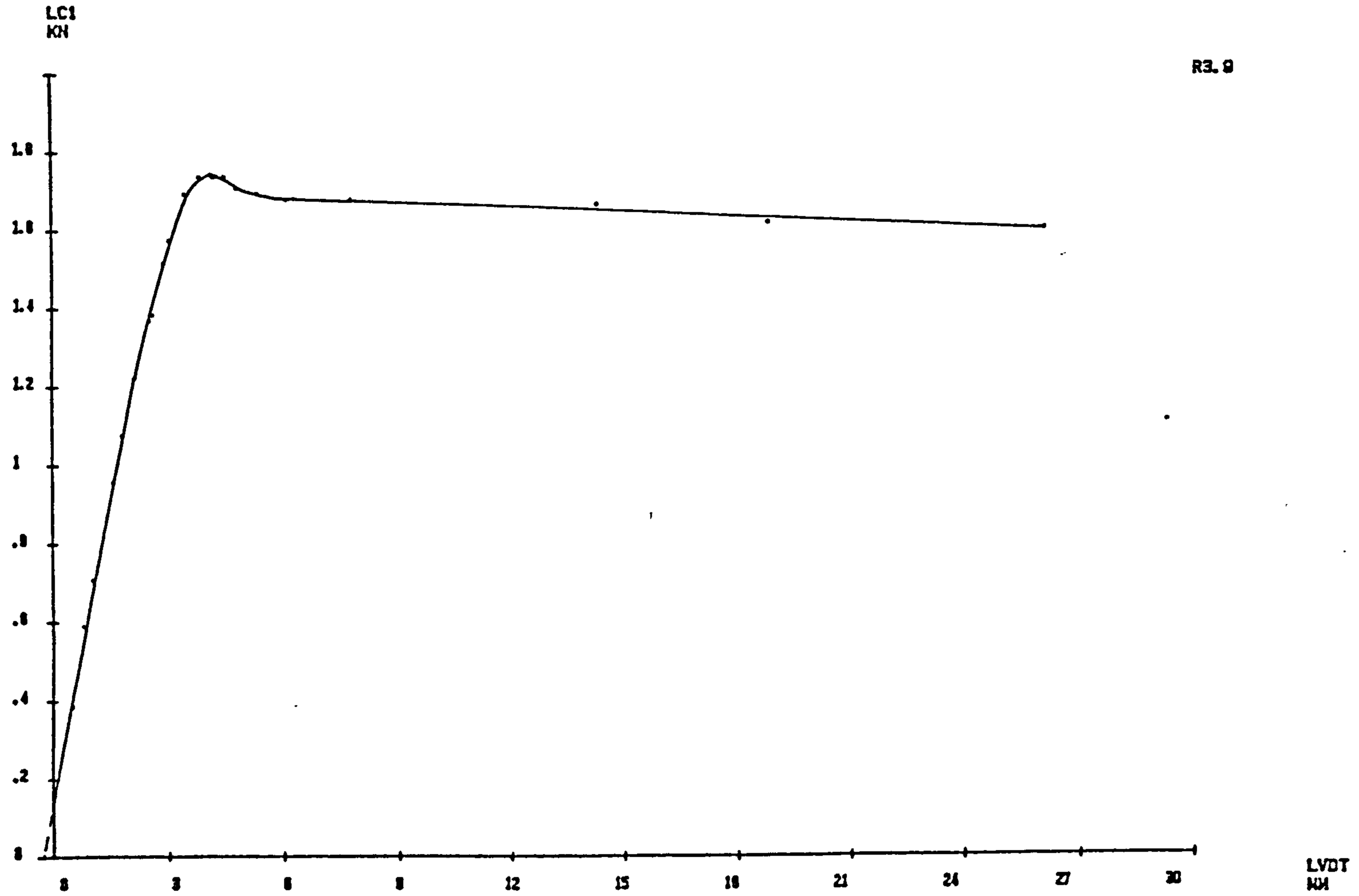

R3.9

Notes : see page F1.

APPENDIX F LOAD - DEFLECTION CURVE - POST - IMPACT - STATIC TEST

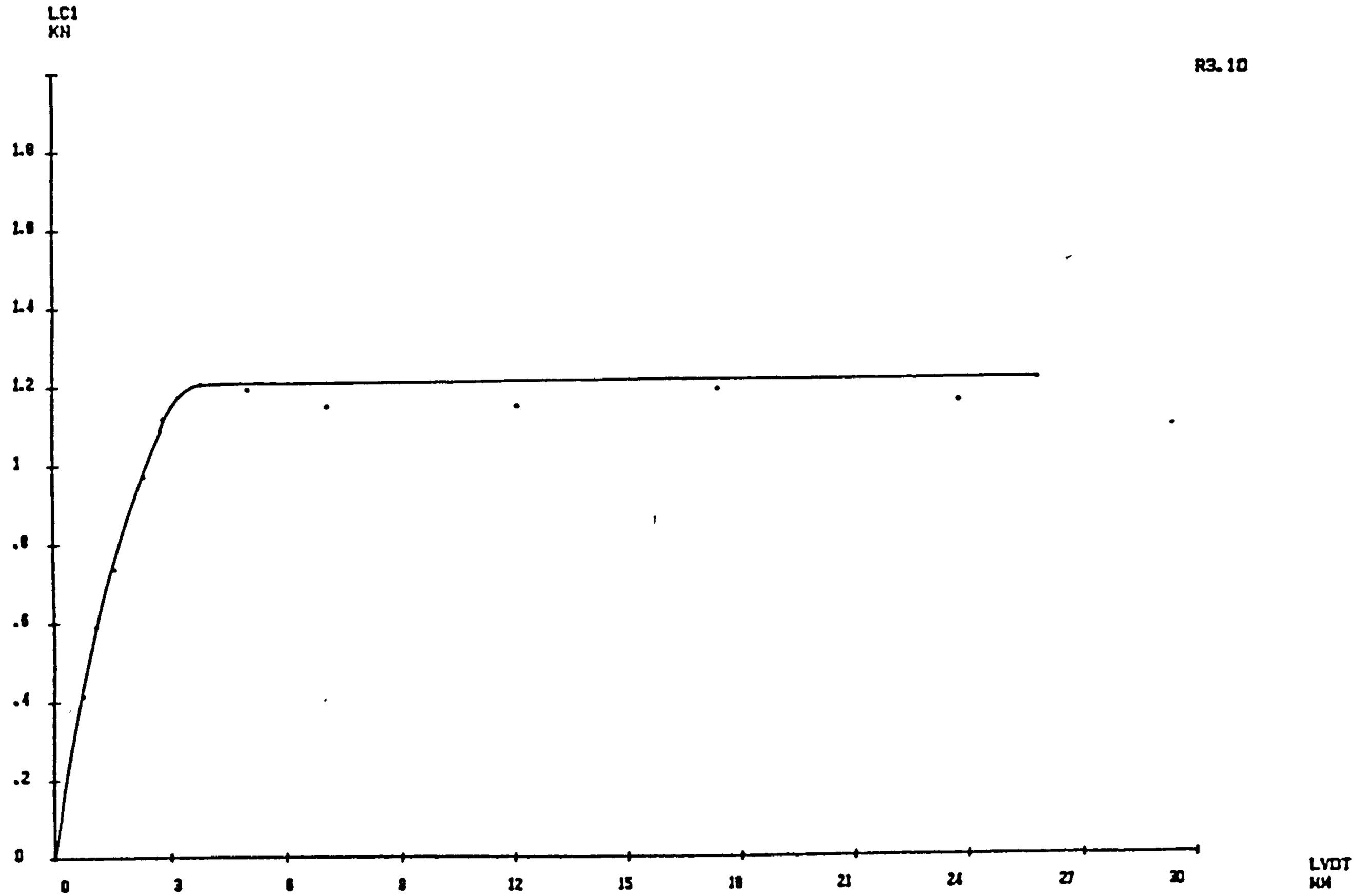

R25

Notes : see page F1.

APPENDIX F LOAD - DEFLECTION CURVE - POST - IMPACT - STATIC TEST

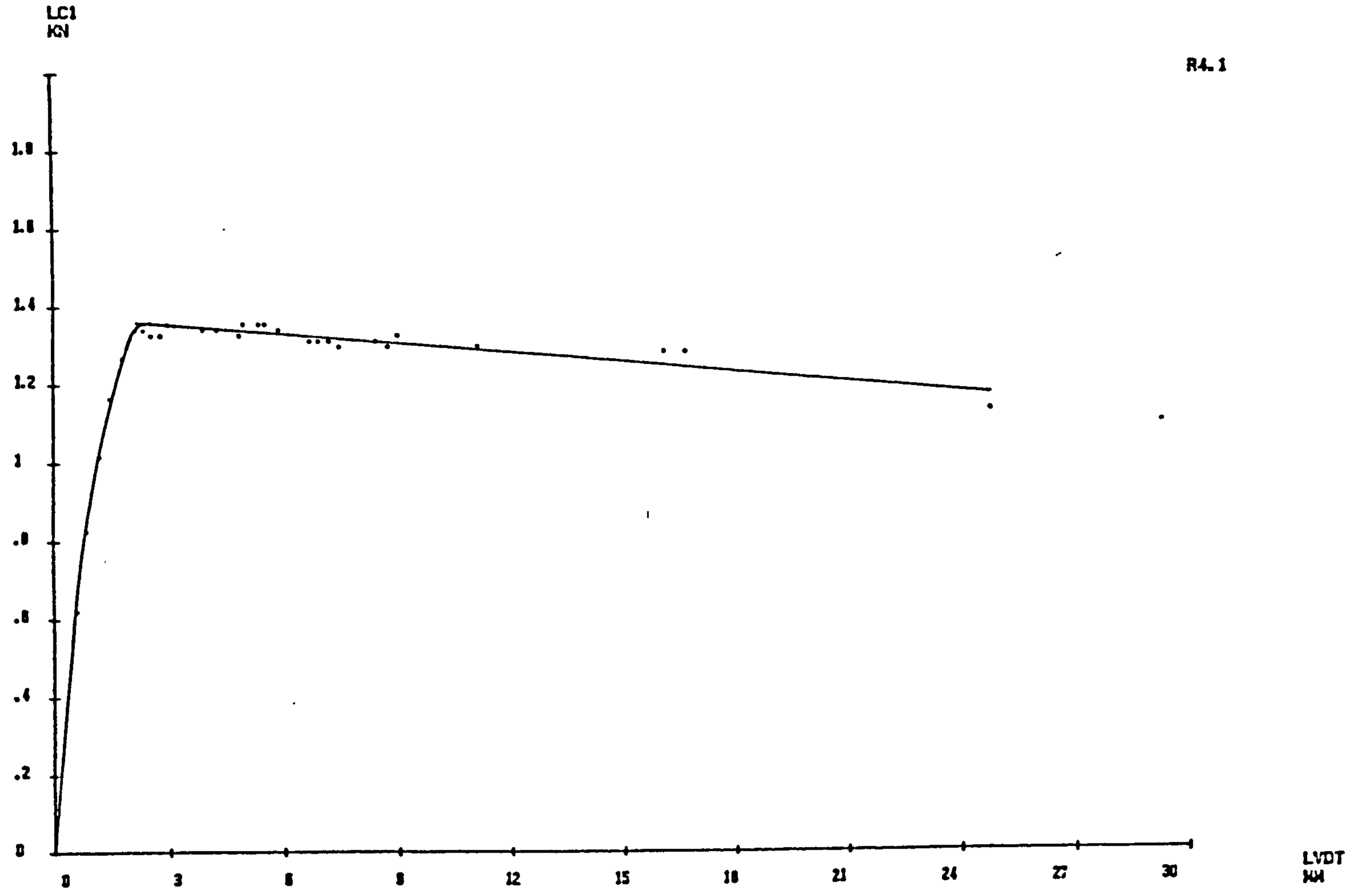

Notes : see page F1.

APPENDIX F LOAD - DEFLECTION CURVE - POST - IMPACT - STATIC TEST

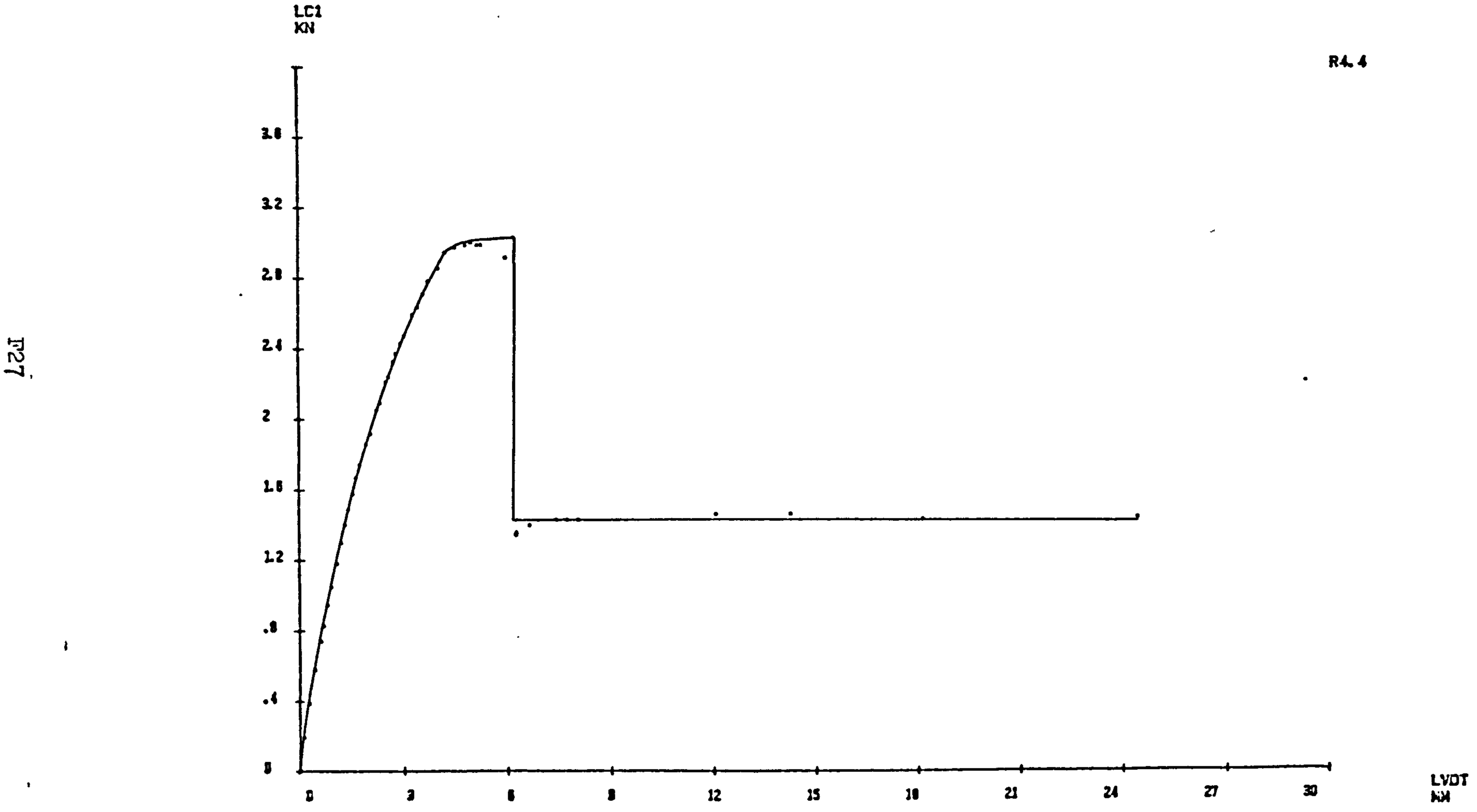

Notes : see page F1.

APPENDIX F LOAD – DEFLECTION CURVE – POST – IMPACT – STATIC TEST

R4.5

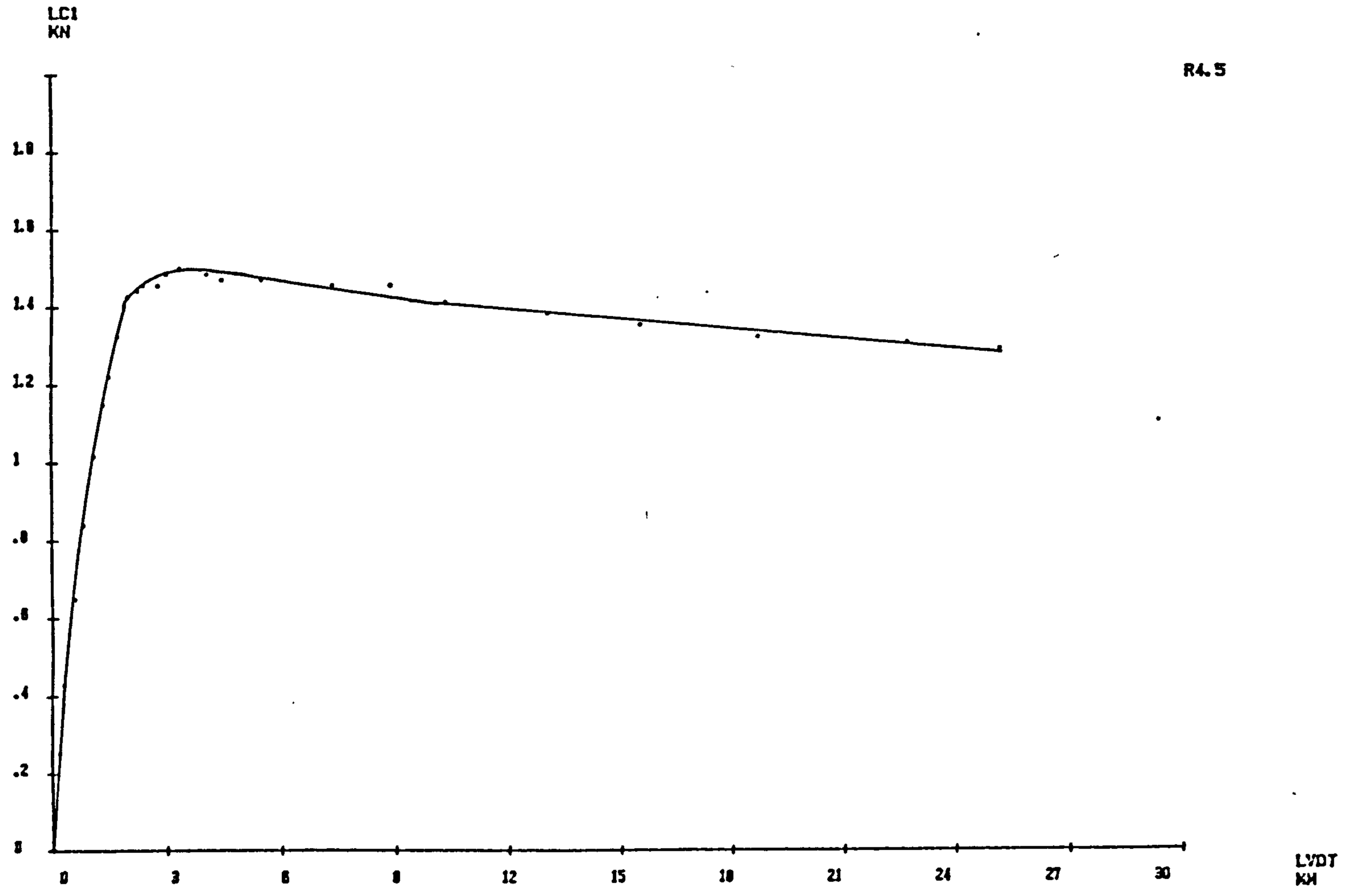

Notes : see page F1.

APPENDIX F LOAD - DEFLECTION CURVE - POST - IMPACT - STATIC TEST

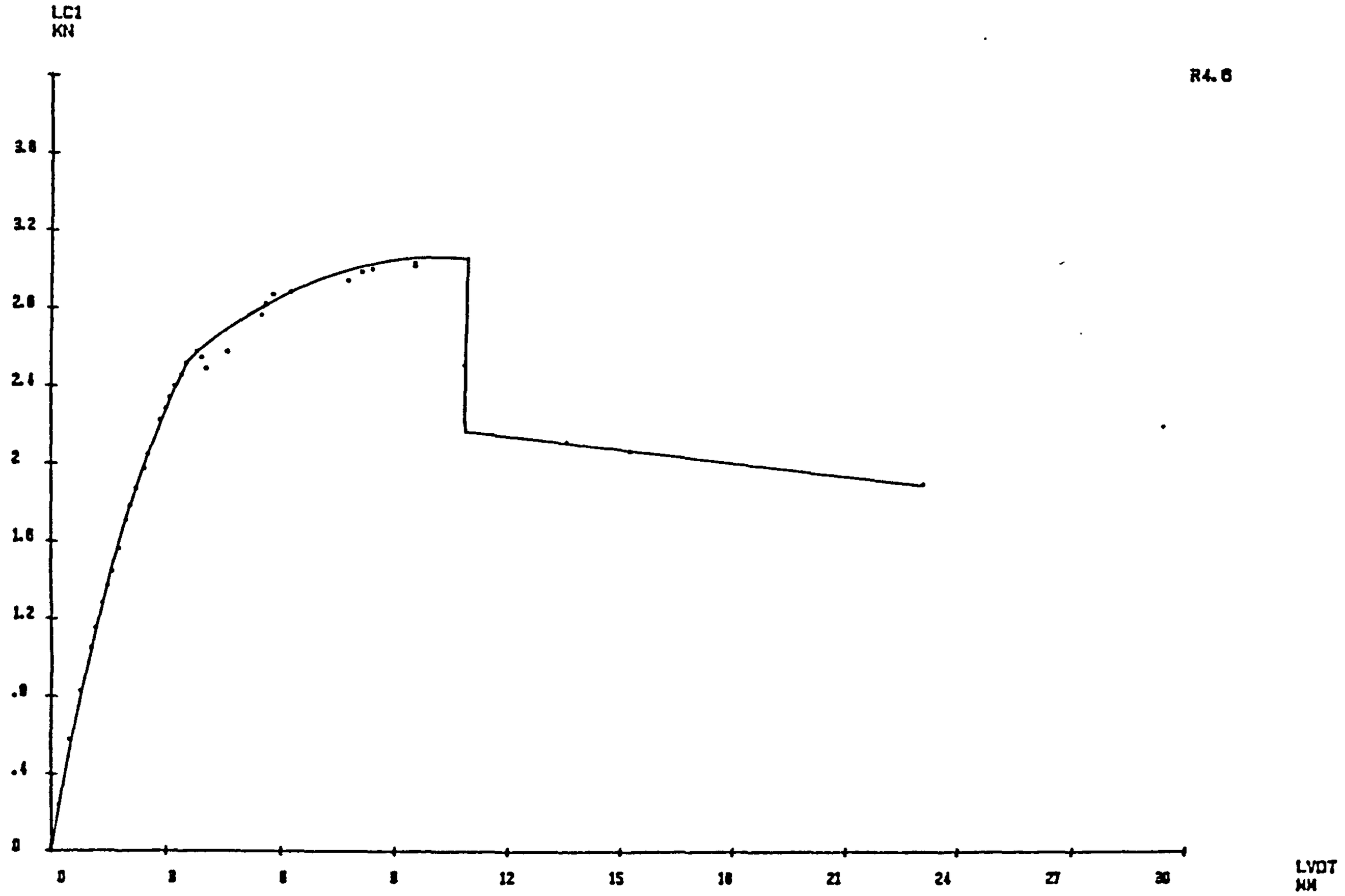

Notes : see page F1.

APPENDIX F LOAD - DEFLECTION CURVE - POST - IMPACT - STATIC TEST

R4.7

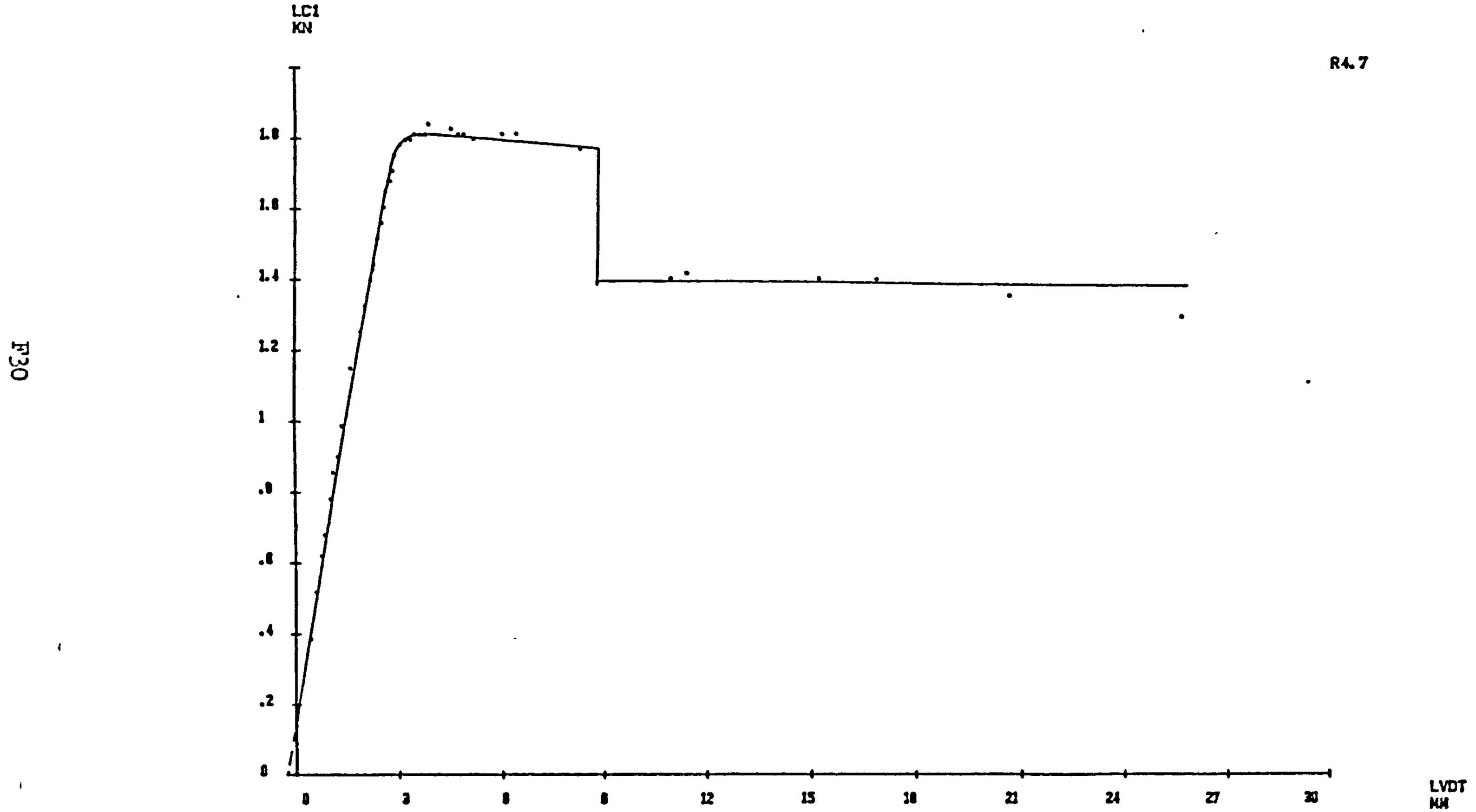

Notes : see page F1.

APPENDIX F LOAD - DEFLECTION CURVE - POST - IMPACT - STATIC TEST

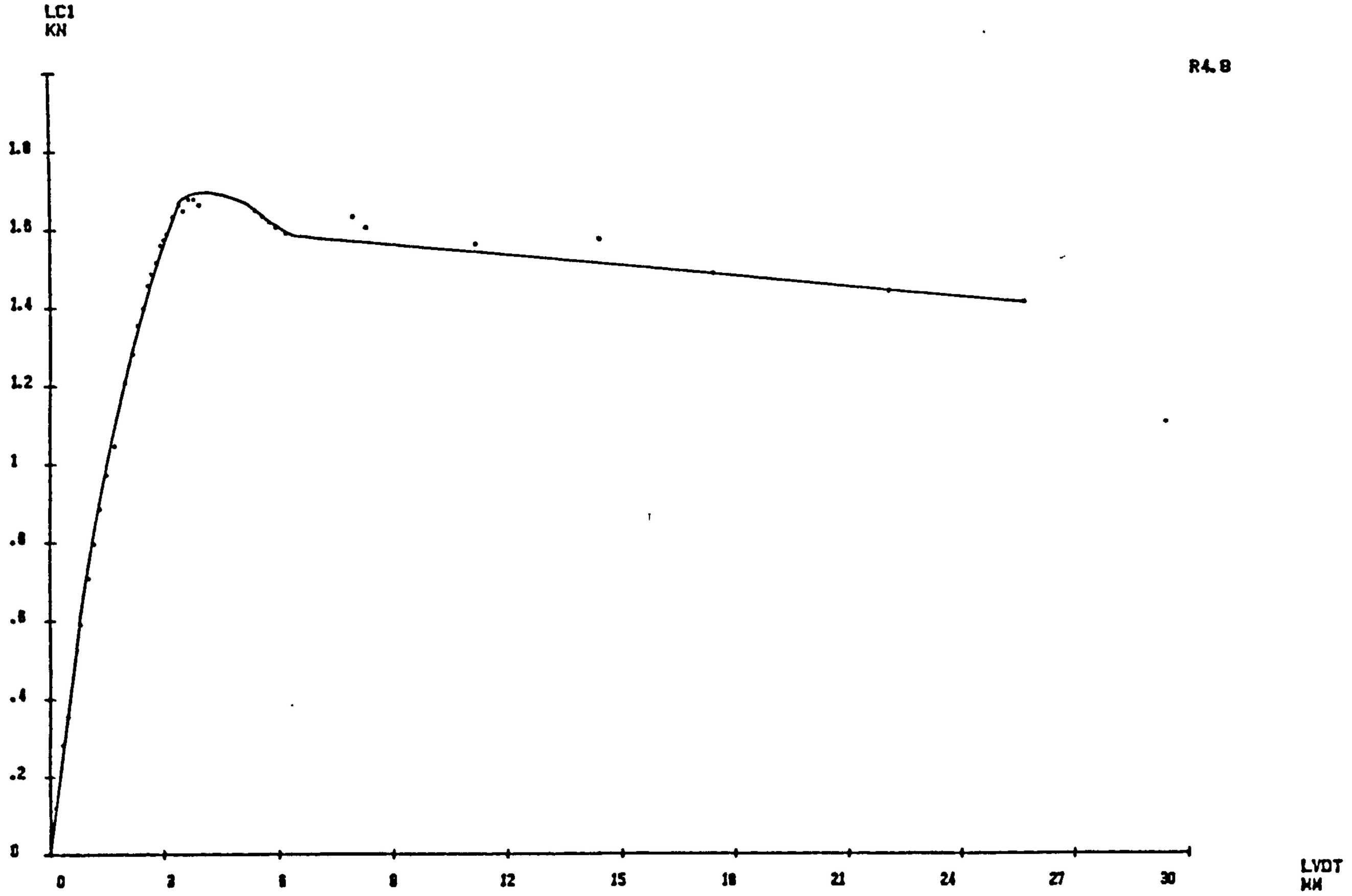

R4.8

F31

Notes : see page F1.

APPENDIX F LOAD - DEFLECTION CURVE - POST - IMPACT - STATIC TEST

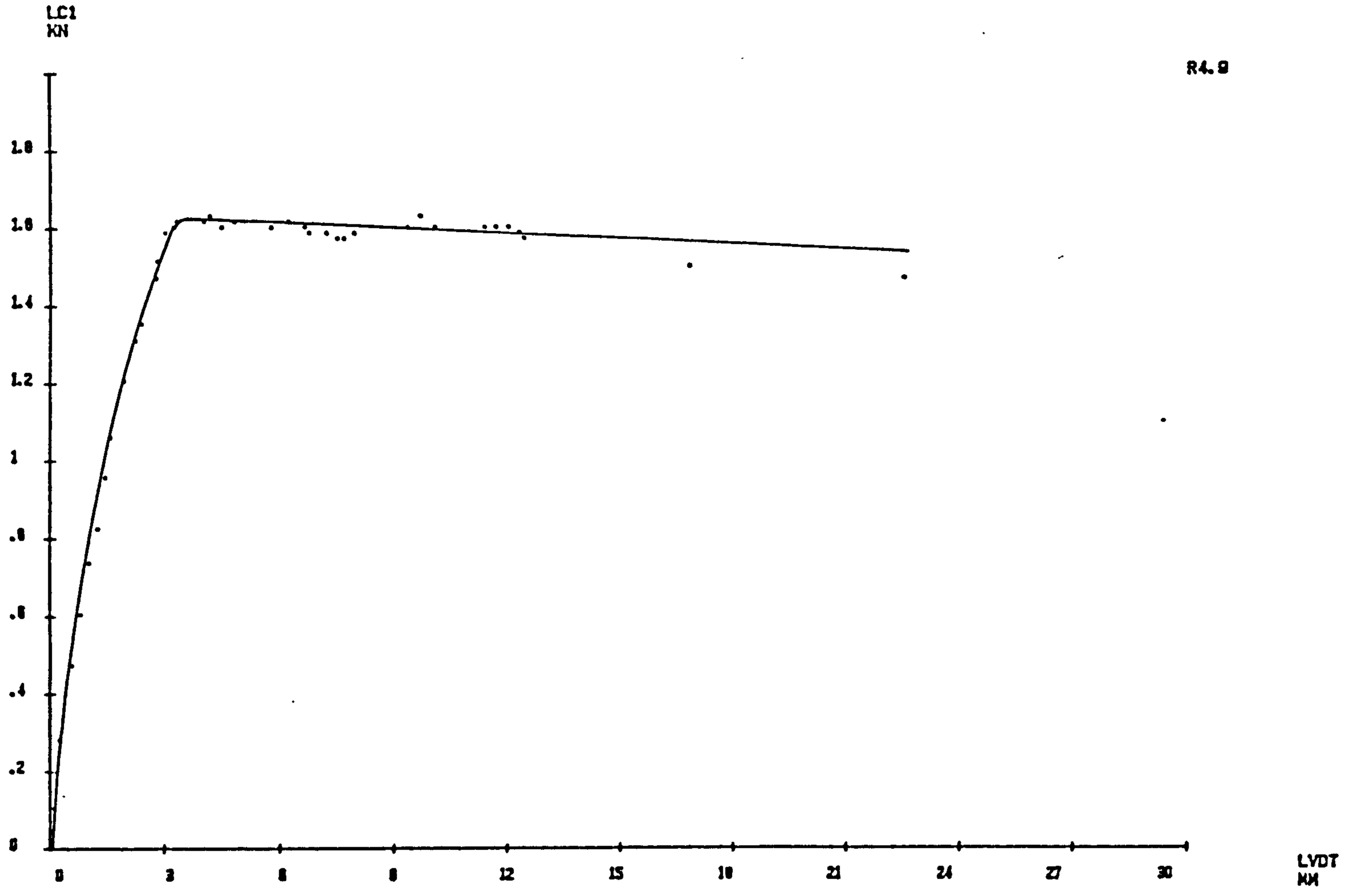

R4.9

Notes : see page F1.

APPENDIX F LOAD – DEFLECTION CURVE – POST – IMPACT – STATIC TEST

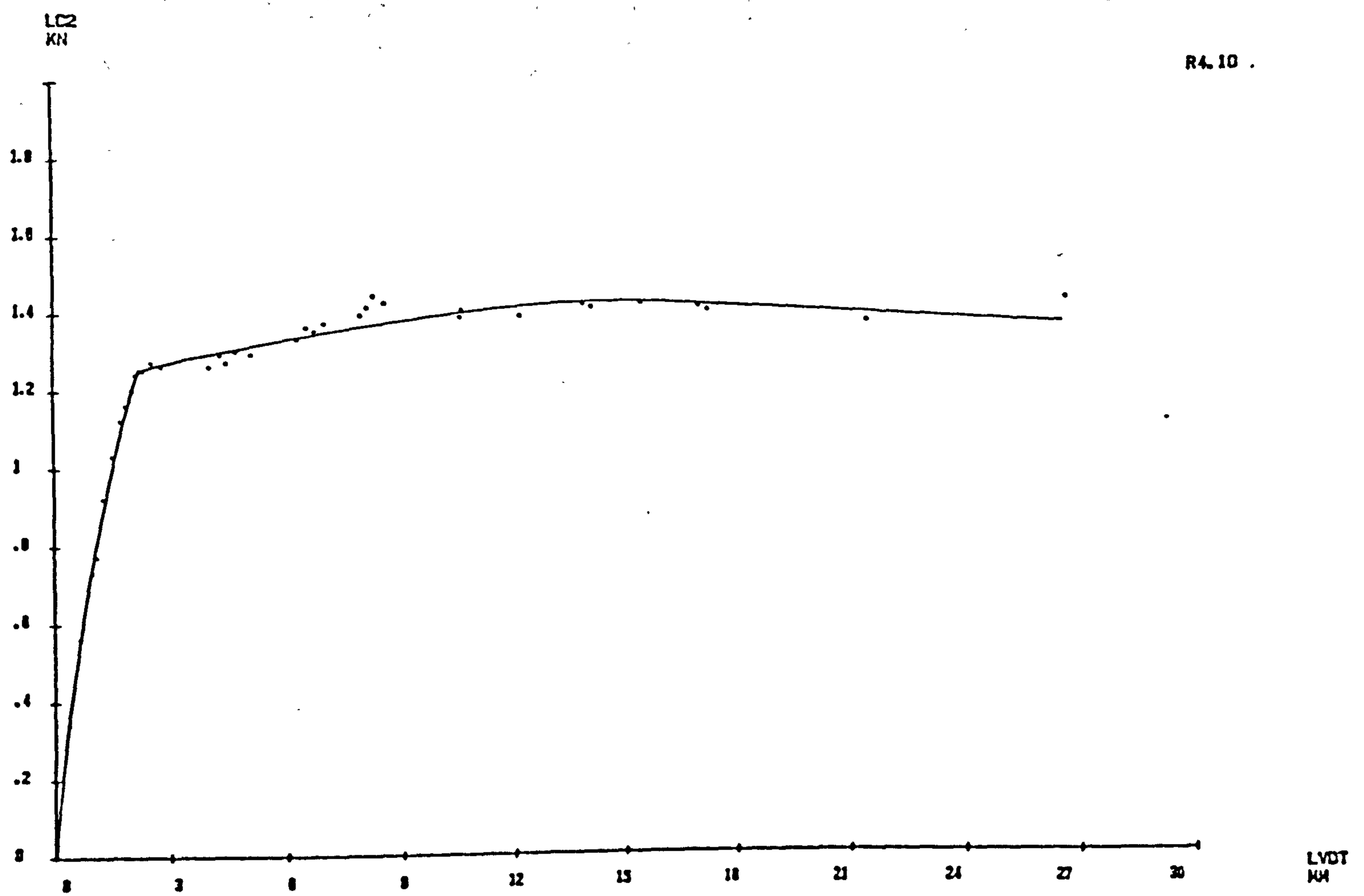

F33

Notes : see page F1.

APPENDIX F LOAD – DEFLECTION CURVE – POST – IMPACT – STATIC TEST

APPENDIX G

Calculation of Ultimate Moment of Resistance, Mp

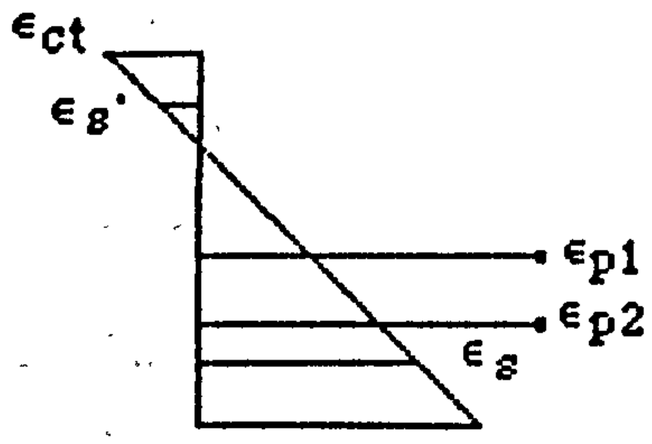

Initial strain diagram

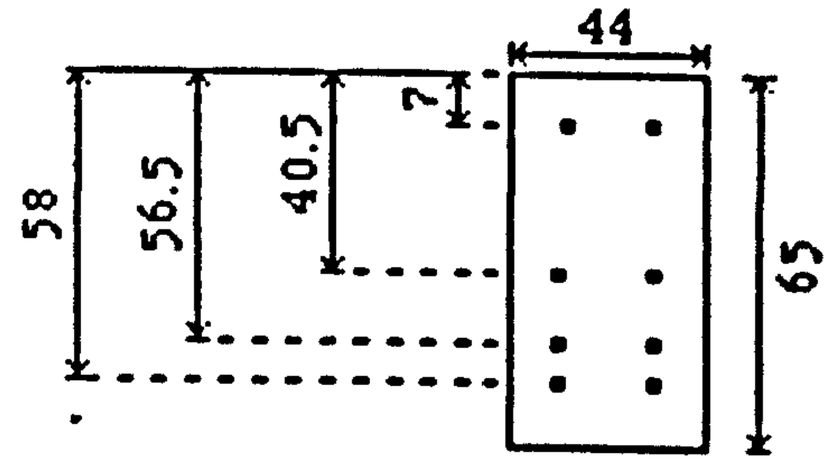

all dimensions in mm

Beam section

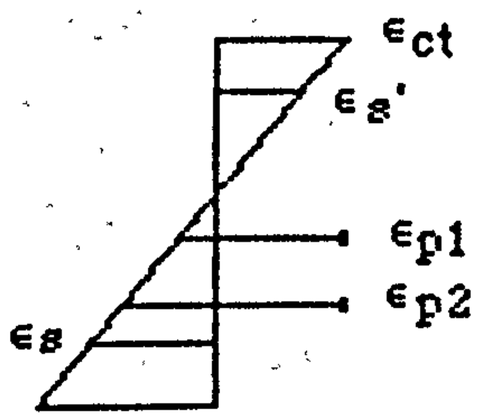

Strain at M_p

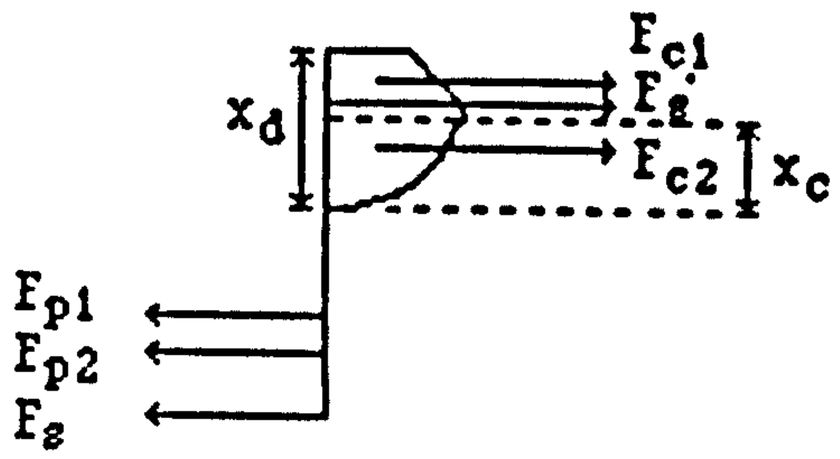

Force at M_p

Notations : see figure 5.1

$A_s = A_s' = 6.28\ mm^2$,

$A_{p1} = A_{p2} = 4.02\ mm^2$,

Assuming loss = 5 %, then

initially, $\epsilon_{p1} = \epsilon_{p2} = 6120\ \mu strain$,

and at ultimate moment, $\epsilon_{p2} = 16000\ \mu strain$.

Try $x_d = 16.5$ mm, then

level	steel strain (μstrain)	steel stress (N/mm^2)	Force (kN)
p1	12050	1956	7.86
p2	16000	2200	8.84
s	10245	350	2.2
s'	2345	-286	-1.80

and for concrete, strain at the top fibre $\epsilon_{ct} = 4075\ \mu strain$.

From section 5.2.1.

f_{ct} = 32 (1-0.15x(1075/2500)) = 29.9 N/mm^2.

x_c = 16.5 x 3000/4075 = 12.2 mm.

therefore,

F_{c1} = (29.9 + 32.0)(16.6 - 12.2)x 44/2 = 5.86 kN.

$F_{c2} = 32x44 \int_0^{12.2} \frac{2x}{12.2} - (\frac{x}{12.2})^2 \, dx$ = 11.45 kN

Σ tensile force = 8.84 + 7.86 + 2.20 = 18.90 kN,

Σ compressive force = 11.45 + 5.86 + 1.80 = 19.11 kN,

i.e a difference of 0.21 kN which is less than 2 % of average, and the forces are considered to be balanced.

Moment due to force F, MF, above top fibre,

MF_{c1} = -44(29.9x4.3^2/2 + 2.1x4.3^2/3) = -0.0127 kNm

$MF_{c2} = -32x44 \int_0^{12.2} (\frac{2x}{12.2} - \frac{x^2}{12.2^2})(16.5 - x) \, dx$ = -0.1016 kNm

MF_s' = -1.80x0.007 = -0.0126 kNm,

MF_{p1} = 7.86x0.0405 = 0.3183 kNm,

MF_{p2} = 8.84x0.0565 = 0.4995 kNm,

MF_s = 2.20x0.058 = 0.1276 kNm.

$\Sigma MF = M_p$ = 0.8185 kNm.

APPENDIX H

Estimation of Strain Rate

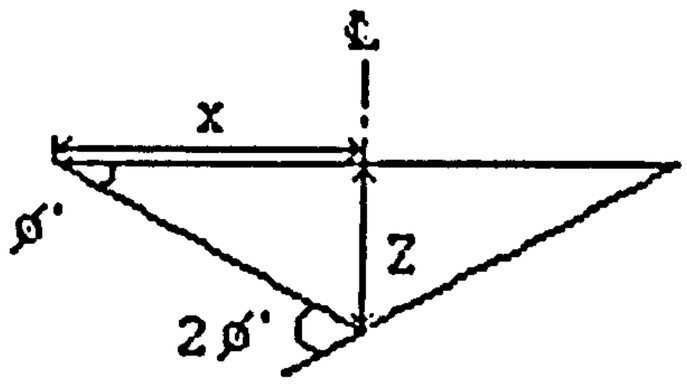

Schematic diagram

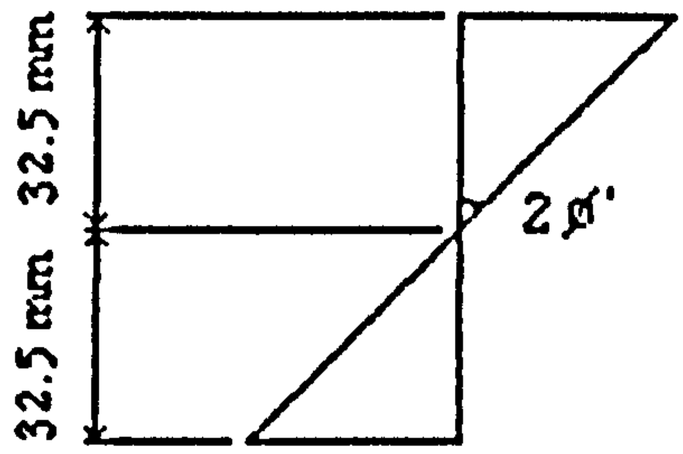

Strain profile at midspan

From the schematic diagram,

$$\dot{\phi}' = \frac{\dot{Z}}{x}$$

From the strain profile,

$$\dot{\epsilon} = \frac{325 \cdot 2\dot{\phi}'}{x}$$

therefore, $\dot{\epsilon} = \frac{32.5\,\dot{Z}}{x^2}$

From table 4.2,

$$\dot{Z}_{max} = 5.30 \text{ m/s}$$

From table 5.2,

$$x_{min} = 0.214 \text{ m}$$

therefore,

$$\dot{\epsilon}_{max} = \frac{32.5 \times 5300}{214^2} = 3.76 \text{ /s}$$

APPENDIX I

Some Results Obtained by Hughes and Speirs[22]

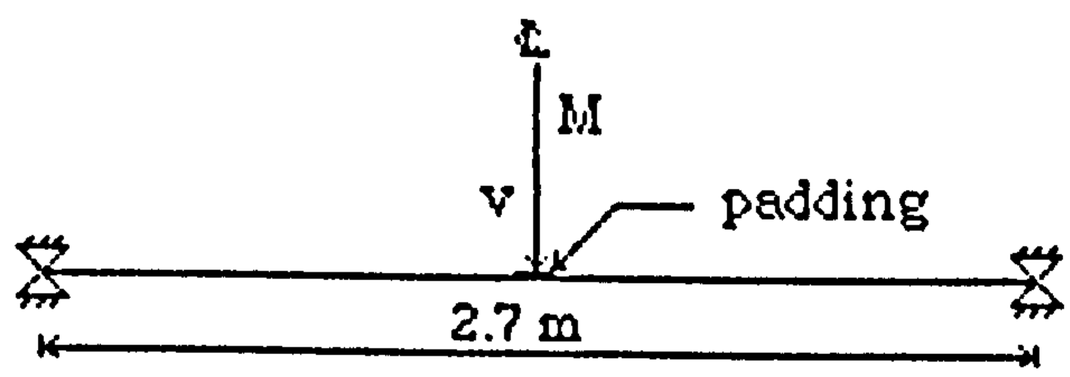

M = Mass of striker,

v = impact velocity.

Beam identification unchanged.

Ultimate moment of resistance (normal and reverse) = 5.4 kNm for series A1,
= 8.9 kNm for series B2,
= 8.9 kNm for series B3.

Mass per unit length of beam = 46.7 kg/m.

Beam type	Test number	Padding type *	M (kg)	v (m/s)	Deflection at midspan(mm)		
					measured ∂_m	predicted ∂_p **	∂_m/∂_p x100%
A1	1	1	98	3.0	40	51	78.4
A1	4	1	58.5	4.2	34	58	58.6
A1	6	2	58.5	3.6	23	43	53.5
B2	14	1	98	5.2	70	93	75.3
B2	17	3	98	5.9	99	120	82.5
B2	19	2	98	5.9	93	120	77.5
B3	20	1	98	3.0	27	31	87.1
B3	21	1	98	4.2	49	61	80.3
B3	22	1	98	5.2	74	93	79.6
B3	23	1	98	5.9	90	120	75.0
B3	26	2	98	2.1	16	15	106.7
B3	27	2	98	3.0	27	31	87.1
B3	28	2	98	3.6	36	45	80.0
B3	29	2	98	4.2	49	61	80.3
							average 78.7

Notes : * padding type 1 - 12mm ply pad
2 - 30 mm steel pad
3 - 6 mm ply pad

** equation 5.36

TABLE I.1 COMPARISON OF MEASURED DEFLECTION WITH PREDICTION